Adaptivity in Solid-State Molecular Organometallic Chemistry

Joe Goodall

Doctor of Philosophy

University of York

Department of Chemistry

March 2024

Abstract

Chapter 1: This chapter introduces the topics pertinent to this thesis, including: *in-crystallo* chemistry; single-crystal to single-crystal transformations; σ-complexes; and C-H activation by organometallic complexes.

Chapter 2: This chapter reports on the *in-crystallo* reactivity of [M(R-PONOP)(L)(CO)$_2$][BAr$^F_4$] complexes with carbon monoxide. The reaction of these complexes with CO gas is shown to produce significant alterations to the 2° microenvironment and 3° periodic structure. Periodic DFT calculations are utilised to understand the non-covalent interactions responsible for these results. The use of MicroED techniques to circumvent crystal-cracking in SCSC transformations is also discussed.

Chapter 3: This chapter reports on the *in-crystallo* synthesis, characterisation, and onward reactivity of a highly reactive, but stable, Rh(III) η^1-σ-alkane complex, supported by a structurally-responsive ligand. The structural-response of the ligand framework is shown to be reversible through substitution of the σ-alkane with propylene. The ligand framework is also shown to facilitate selective H/D exchange at unactivated alkyl C-H positions.

___Declaration___

The work reported in this thesis was carried out by the thesis author at the University of York, under the supervision of Prof. Andrew Weller and Prof. Jason Lynam, unless otherwise stated. I declare that this is an original work, not previously submitted for degree or other qualification at this, or any other, institution. All sources are acknowledged as references.

Joe Goodall

University of York, March 2024

Acknowledgements

First and foremost, I must thank my supervisors *Prof. Andrew Weller* and *Prof. Jason Lynam*. Throughout the three-or-so years of my Ph.D., you have both shown your care and support in countless ways. I'll be forever grateful for all for the dedication you both have shown, and the freedom that you've provided me with. *Andy*: Thank you for all the time you give to the group, not just at work but the walks, the meals at your place and around Yorkshire. All of the Bhindi Bhajis. *Jason:* Thank you for always being accommodating to all the questions I've brought to your door and for your dated taste in music and terrible jokes. I'll never understand any of your references, but that's part of the game at this point.

To all the old Ph.D. students in the Weller groups before me: *David*, *Tim*, *Cameron*, and *James*. You were all truly 'one-of-a-kind,' real individuals, and I genuinely hope our paths overlap again someday. But thankfully you've also all long-since finished and will never read any of this. *David*: Hope the USA is treating you well and you've managed to find a different outfit than the bottomed-up shirt and tight jogging bottoms combo. I've never known someone so committed to catalysis, and frankly I hope you'll never be beaten in that regard. All your 'late-night' NMR sessions spent hiding away, the steadily increasing volume of D&B at 7pm in the lab, and yet you always had time to spare for others. *Tim*: You, and the next person in this list, possess the worst taste in music I have ever had the displeasure of knowing. No one believes you are working in the energy sector, but I do hope you're enjoying your new role, 007-Potter. *Cameron*: Oh Cameron. I so miss our travels to Nisa to scavenge the cheapest possible items for lunch. Sharing

4

a reduced pack of chicken thighs with our bare hands for lunch is one of my most cherished memories of my Ph.D. Your commitment to maximum calorie to price ratio was a sight to behold. I hope that large percentage of your life spent on CrystalMaker has come in useful. *James*: You tolerated me asking mundane questions at you for far too long and always made me feel welcome. You're a real-life BFG, although most of that is in your neck. Thanks for the trial by fire, but the crystals have treated me a lot better in your absence.

To the current and previous PDRAs: *Laurence, Sam, upside-down Matt, Claire, and Kris. Laurence*: On the surface anyone would think you were a normal person. No one would expect all of the mouldy bread, black bananas, and off milk that you consume. Or all the cooking Vlogs you produce in your head with a made-up accent. But knowing all of this, the fact you now work for the government makes a lot more sense. *Sam and upside-down Matt*: I think it's fair to say that no one has moulded and impacted the way I work in the lab more than you two. Congratulations to both of you for being off to embiggen and better things back home. P.S. Don't keep crunching the numbers on your Weetabix orders, life's far too short for Excel. *Claire*: You probably suffered the most of anyone in this list by having me next to you for 2 years in the lab. Thanks for all the help and direction you provided. *Kris*: We all know you went to Canada. Trust me, we *do* believe you.

To the current and previous MChem students: *Baby Matt, Kat, Jack, Orry, and Anna. Baby Matt*: I'm glad that the York Student Cricket Club is finally safe, but I am sad to report the Weller group tea breaks took a strong hit with your departure. *Kat*: Sorry about the project I designed. You persevered and you came out a great

chemist despite me. And then you chose to do a Ph.D., too. You're a glutton for punishment. *Orry and Anna*: All the best with the rest of your project years and whatever you end up doing next.

To the current Ph.D. students: *Helena, Chloe J, Chloe VB, Mat, and Jack*. The group is slipping. *Helena*: For better or for worse, we've been through this whole Ph.D. journey together and we've both almost been the end of the other, more than once. I'll remember your insults, your put-downs, the DCM day, all the glassware you hoarded at CHyM, and the way you'll go to the ends of the world for anyone who means anything to you. Frankly, I'm surprised we made it to the end of our Ph.D.'s. *Chloe J*: Your love for corduroys, PopWorld, and cake, are unmatched. Make sure you get an EPR before you're done. *Chloe VB*: T-1000. As the first from your city to learn to read and write, you're doing pretty well. Don't let the sickness (amine-borane) get to you. *Mat*: When we met on Zoom, I didn't expect that we would bond over explosions, fire, and rocks on the beach. Like cavemen. I certainly didn't expect you'd become one of my closest friends. But you're never getting your AB statue, or a rocket named in your honour. *Jack*: All the best with SMOM. She is a cruel mistress. And I hope the crystals are friendly.

To all those who I have collaborated with: *Drs Graham Tizzard and Mark Warren*: Thank you both for all the help and genius of the crystallographic-type. We even managed to discover ice together. *Dr Alison Edwards*: Thank you for your patience and insight. And for driving me all over NSW. *Dr Arif Sajjad and Prof Stuart Macgregor*: You've both taught me so much about computational chemistry, and really put in a shift for me with your little abacus.

To my family: Thank you for always supporting me throughout my studies, and always trying to take an interest. Your love and prayers have been a great comfort. To my fiancée, *Thea*: The biggest of thanks must go to you. You've always been my biggest fan, pushed me, and been there for me in the lowest points. If I were to dedicate this thesis to anyone, it would be to you. But this is hardly Little Women, so I think you would prefer I didn't.

Finally, as a believer, it is *God* who has got me here in the first place and is the true strength and provision that has seen me through. I've seen You work and the direction You've given me over these last few years. I wish to honour You with this work and whatever comes next.

Abbreviations

a	Unit cell dimension
Å	Ångströms (10^{-10} m)
app.	Apparent
Ar^F	$3,5\text{-}(CF_3)_2C_6H_3$
Ar^{SF5}	$3,5\text{-}(SF_5)_2C_6H_3$
atm.	Atmospheres of pressure (1013 mbar)
ATR IR	Attenuated Total Reflectance Infrared Spectroscopy
b	Unit cell dimension
bar	Unit of pressure (10^5 Pa)
bcp	Bond Critical Point
c	Centi
c	Unit cell dimension
ca.	Circa (approximately)
calc.	Calculated
cf.	Confer (compare)
COA	Cyclooctane
COD	Cycloocta-1,5-diene

COSY   Correlation Spectroscopy

CP   Cross Polarisation

Cy   Cyclohexyl

dcpe   1,2-bis(dicyclohexylphosphino)ethane

dcpm   bis(dicyclohexylphosphino)methane

dcppent   1,5-bis(dicyclohexylphosphino)pentane

dcpprop   1,3-bis(dicyclohexylphosphino)propane

depe   1,2-bis(diethylphosphino)ethane

DFT   Density Functional Theory

dibpe   1,2-bis(di-*iso*-propylphosphino)ethane

dtbpb   1,4-bis(di-*tert*-butylphosphino)butane

dtbpprop   1,3-bis(di-*tert*-butylphosphino)propane

eg   Ethylene glycol

EI   Electron-ionisation

ESI   Electrospray ionisation

EVE   Ethyl vinyl ether

g   Grams

GC   Gas Chromatography

GPC   Gel Permeation Chromatography

HMBC	Heteronuclear multiple-bond coherence
Hz	Hertz (s^{-1})
fac	*Facial*
FWHM	Full-Width Half-Maximum
hfac	hexafluoroacetylacetonate
I	Nuclear spin quantum number
^{i}Bu	*Iso*-butyl
IGMH	Independent Gradient Model with Hirshfeld Partioning
^{i}Pr	*Iso*-propyl
^{i}Pr-PONOP	2,6-(^{i}Pr$_2$PO)$_2$C$_5$H$_3$N
J	Joules (Unit of Energy)
J	Scalar Coupling
k	kilo
K	Kelvin (Unit of Temperature)
kcal	kilocalories (4.184 kJ)
L	Litres
LLHT	Ligand-to-Ligand Hydrogen Transfer
M	Mega
m	milli or metres

M_w	Weight average molecular weight
m/z	mass-to-charge ratio
MAS	Magic Angle Spinning
Me	Methyl
mer	Meridional
MLC	Metal-Ligand Cooperation
MicroED	Microcrystal Electron Diffraction
MOF	Metal-Organic Framework
mol	mole(s)
ms	milliseconds
MS	Mass Spectrometry
NBA	Norbornane
NBD	Norbornadiene
NBE	Norbornene
NMR	Nuclear Magnetic Resonance
NOE	Nuclear Overhauser Effect
NOESY	Nuclear Overhauser Effect Spectroscopy
OTf	trifluoromethylsulphonate
Pa	Pascals (Unit of Pressure)

Ph	Phenyl
PP	Generic chelating diphosphine
ppm	parts per million
ps	picoseconds
Q	Quadrupole moment
QTAIM	Quantum Theory of Atoms in Molecules
R	Generic chemical group
rel.	Relative
R^F-POCOP	$2,6\text{-}\{1,3,5\text{-}(CF_3)_3PO\}_2C_6H_3$
RCP	Ring Critical Point
SC-SC	Single-crystal to single-crystal
SCXRD	Single-crystal X-Ray Diffraction
SEM	Scanning Electron Microscopy
SMOM-Chem	Solid-State Molecular Organometallic Chemistry
^tBu	*Tert*-butyl
^tBu-PONOP	$2,6\text{-}(^tBu_2PO)_2C_5H_3N$
TEM	Transmission Electron Microscopy
THF	Tetrahydrofuran
TMPyz	2,3,5,6-tetramethylpyrazine

TOCSY	Total Correlation Spectroscopy
TRIR	Time-Resolved Infrared Spectroscopy
V	Unit cell volume
Xantphos	4,5-bis(diphenylphosphino)-9,9-dimethylxanthene
Z	Symmetry-independent formula units in unit cell
α	Unit cell angle or crystallographic twin-component ratio
β	Unit cell angle *or* Natural Bite Angle
γ	Unit cell angle
ΔE	Change in energy
ΔG	Change in Gibbs Free Energy
δ	Chemical Shift (in ppm)
η	Hapticity
κ	Denticity or Skew
λ	Wavelength
μ	Micro *or* Bridging
ρ	Electron density at bond critical point
σ-CAM	σ-Complex-Assisted-Metathesis
υ_{CO}	Infrared Stretching Frequency of Carbonyl Ligand
Σ	Summation

Ψ	Wavefunction
Ω	Span
⊂	Subset (encapsulated within)

Table of Contents

Table of Figures

Chapter 1: Introduction

Chapter 1: Introduction

This thesis will discuss *in-crystallo* reactivity and adaptivity of manganese and rhenium organometallics (**Chapter 2**), and a Rh(III) σ-alkane complex (**Chapter 3**). A specific introduction on adaptivity in single-crystals, and ligand adaptivity, will be provided at the beginning of these two chapters, respectively. In this Introduction Chapter, a more general introduction to organometallic solution and *in-crystallo* chemistry is discussed.

1.1 Observation of Reactive Intermediates

Large scale industrial fine-chemicals[1-4] and pharmaceutical[5-7] production is heavily dependent on the use of homogeneous transition metal catalysts. These reactions are carried out in the solution-state, which has a number of benefits for chemical reactivity such as ease of temperature control and dilution by inert solvent media. While the mechanism of these reactions can be determined in the solution-state, the direct observation of reactive intermediate complexes is necessary for catalyst optimisation, but represents significant challenges.[8, 9] This is because these intermediate complexes in 'real-world' reaction mixtures tend to be in small, steady-state concentrations, and rapidly undergo onward reactivity. For example, low valent species, σ-alkane complexes, and oxidative addition products are all common reactive intermediates in alkane dehydrogenation by transition metal catalysts (**Scheme 1.1**), which each play key roles in the reaction mechanism but are unobserved.[10-12] The use of low catalyst concentrations and elevated reaction temperatures, means that observation of the key reactive intermediates is often

difficult, or impossible, to achieve without advanced techniques. As Jack Halpern quoted[13]: "if you can observe it, it is probably not the catalyst."
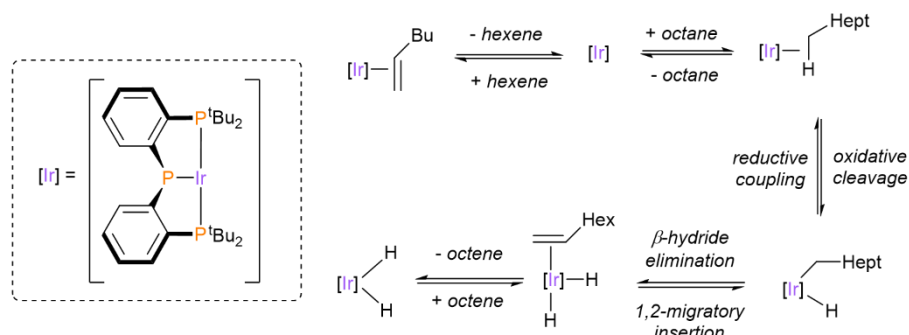
Scheme 1.1: The mechanism of dehydrogenation of *n*-alkanes by an iridium pincer complex includes the formation of highly reactive intermediate species. [12]

1.2a Phosphine Ligands

Phosphine ligands (PR$_3$) are one of the most common types of ligand used in organotransition metal chemistry.[14, 15] Phosphines can act as both σ-donor and π-acceptor ligands and thus can stabilise a wide range of metal oxidation states,[16-19] which is a major reason why they are ubiquitous among catalytic cycles.[7, 19-22] Phosphine σ-donation arises from the overlap of the phosphorus-centred non-bonding orbital (lone pair) with an empty *d*-orbital on the metal, while electron density can be accepted from a filled metal *d*-orbital into the P–R σ*-antibonding orbitals (**Figure 1.1**).
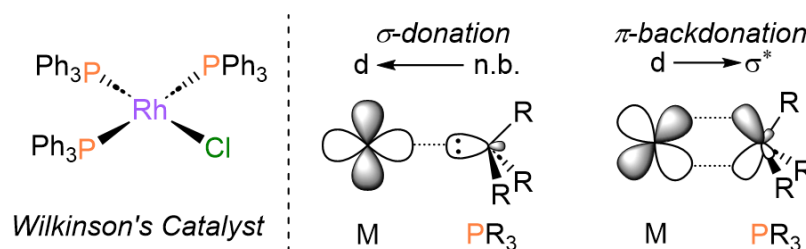
Figure 1.1: *Left*: Wilkinson's Catalyst ([RhCl(PPh₃)₃]), an example of a transition metal-phosphine complex, important in hydrogenation catalysis. *Right*: Bonding description of metal-phosphine complexes.

Alteration of the R-groups on the phosphorus provide a platform to vary to steric profile of the complex. This can be described by the Tolman Cone Angle (θ, **Figure 1.2**).[23] This model assumes an arbitrary M–P distance of 2.28 Å which becomes the apex of a cylindrical cone which is drawn to encapsulate the R-groups of the phosphine.
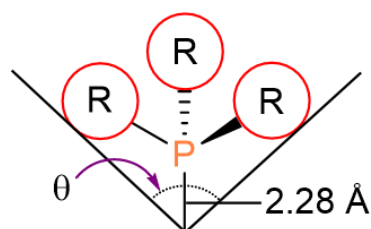
Figure 1.2: Determination of Tolman Cone Angle (θ) [23] of phosphine ligands.

The R-groups also furnish a scaffold to influence the electronic properties of the complex. For example, alkyl groups push more electron density onto the phosphorus centre, enhancing the σ-basicity, increasing from primary, to secondary, to tertiary carbons. Similarly, affixing electron-withdrawing R-groups (aryl < amide < alkoxyl < chloro < fluoro) to the phosphine lowers the P–R σ*-antibonding orbital energy, making these derivatives more effective π-acceptors (**Figure 1.3**). Phosphine

ligands are also valuable in organotransition metal chemistry due to their innate NMR spectroscopic handle: ^{31}P is a spin-½ nucleus, with 100% abundancy.
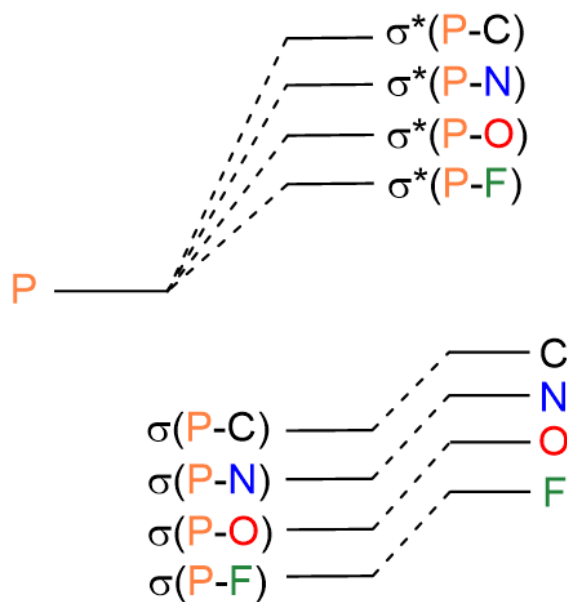
Figure 1.3: Impact on the σ*(P–R) orbital energy with increasing electronegativity of R-group. The increased stability of σ*(P–R) provides a better overlap with filled metal *d*-orbitals, making the phosphine a more effective π-acid.

1.2b Chelating Phosphine Ligands

Within this thesis, chelating phosphines are used exclusively. This includes κ^2-$R_2P(CH_2)_xPR_2$ and κ^3-2,6-$(R_2PO)_2C_5H_3N$ (R-PONOP) ligands (**Figure 1.4**). The 'natural bite-angle' (β), described by Casey and Whitaker,[24] is a value of the preferred chelation angle of chelating bidentate phosphines. The β-value is computationally determined, and independent of the metal-phosphine bonding, solely based on steric considerations of the phosphine backbone. As the phosphine backbone increases in length, the natural bite-angle also increases. The β-angle is not only important for steric influence, but also has a large role to play in the

electronics of the metal centre.[25, 26] For example, the oxidative addition of H_2 by {Rh(diphosphine)$_2$}$^+$ complexes has been shown to be thermodynamically disfavoured when the phosphine backbone contains two methylene units ($\Delta G^0_{-H_2}$ = -0.87 kcal mol^{-1}), and favoured when containing three methylene units ($\Delta G^0_{-H_2}$ = +5.1 kcal mol^{-1}, **Scheme 1.2**).[26] This is explained the ground-state destabilisation of the square-planar Rh(I) starting material by larger bite-angle phosphines.
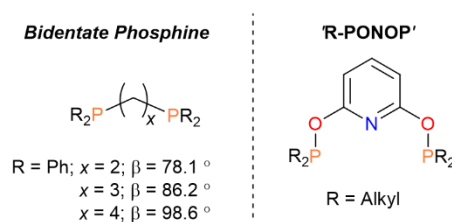
Figure 1.4: Examples of chelating bidentate and R-PONOP phosphine ligands. *Left*: Chelating bidentate phosphines. Associated natural bite angles (β) are listed.[27] *Right*: 'R-PONOP' ligand.
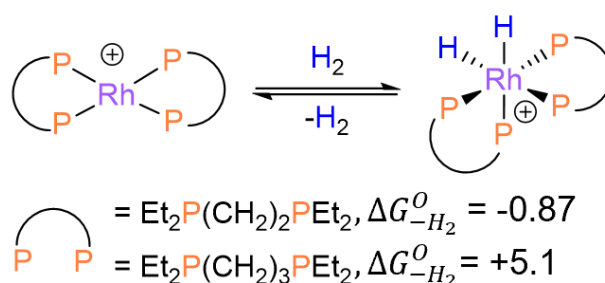
Scheme 1.2: Reversible oxidative addition of H_2 by bis-diphosphine rhodium complexes. Triflate anion omitted for clarity. The Gibbs free energy of the reductive elimination of H_2 ($\Delta G^O_{-H_2}$) becomes more negative with increasing phosphine bite-angle.[26]

Chapter 2 of this thesis will work exclusively with the 'R-PONOP' ligand platform (**Figure 1.4**). The ligand coordinates to metals in a κ^3-fashion through the lone pairs located on the pyridyl nitrogen atom and the two phosphorus atoms, and can be electronically and sterically tuned through variations of the R-groups. This

framework is extremely rigid and is thus restricted to *mer*-coordination geometries, with very little deviation from planar.[28]

1.3 Carbonyl Ligands

Carbon monoxide was one of the earliest ligands used in organometallic chemistry, with the synthesis of nickel tetracarbonyl reported in 1890 (**Figure 1.5**).[29] Metal-carbonyl complexes find a wide range of catalytic applications such as hydroformylation,[30] Fischer-Tropsch,[31] carbonylation[32] and acetic acid synthesis.[33, 34] The nature of metal-carbonyl bonding involves σ-donation through the overlap of the carbon-centred non-bonding orbital (lone pair), the HOMO, of carbon monoxide, with an empty *d*-orbital on the metal (**Figure 1.5**). Carbonyls are potent π-acidic ligands, accepting electron density from the metal through overlap of a filled metal *d*-orbital with the vacant C–O π*-antibonding LUMO orbital (**Figure 1.5**). Carbon monoxide is not a strong nucleophile, which is reflected in relatively weak σ-donation, so π-backbonding is considered to play the major role in metal-carbonyl bonding.[35]
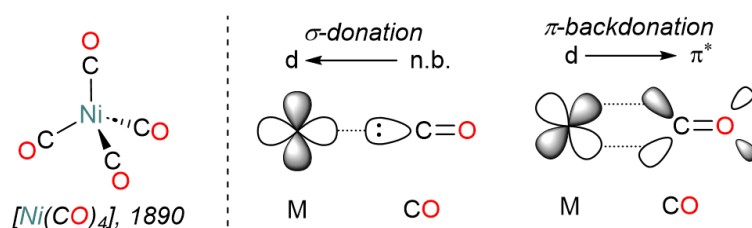
Figure 1.5: *Left*: The structure of nickel tetracarbonyl, first reported in 1890 by Mond.[29] *Right*: Nature of metal-carbonyl bonding, with σ-donation through the carbon-centred lone-pair, and π-backdonation into the C=O π*-antibonding orbital.

The electron donation into the π*-antibonding character orbital lowers the C–O bond order, while increasing the M–C–O bond order. The IR stretch of metal carbonyls is a valuable diagnostic tool. It is utilised by the Tolman Electronic Parameter which is used for assessing the electron donating and withdrawing effects of phosphines, by measuring the A_1 symmetric stretch of $[Ni(CO)_3(PR_3)]$ (**Figure 1.6**).[23] As the phosphine electron donation increases, the M→CO π-backdonation also increases, decreasing the C=O bond order and the vibrational stretching frequency.

	free CO	R = OEt	R = Ph	R = Me	R = ^{t}Bu
A_1 Symmetric CO Stretch	υ_{CO} 2143 cm^{-1}	υ_{CO} 2076 cm^{-1}	υ_{CO} 2069 cm^{-1}	υ_{CO} 2064 cm^{-1}	υ_{CO} 2056 cm^{-1}
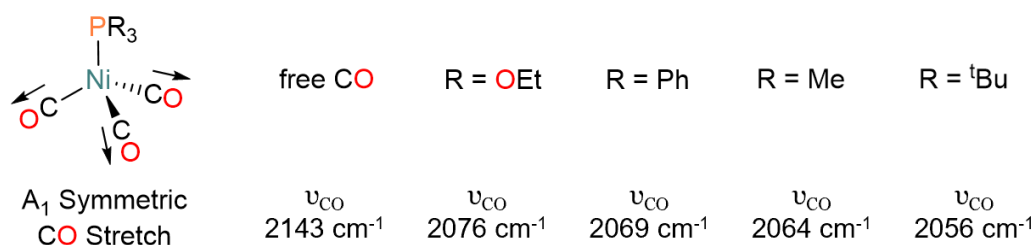
Figure 1.6: The Tolman Electronic Parameter is used to assess the electron donation abilities of phosphines *via* the A_1 symmetric carbonyl stretch of $[Ni(CO)_3(PR_3)]$.[23]

1.4 Weakly-Coordinating Anions

This thesis reports on the direct observation, and isolation of, *cationic* reactive intermediates with very weakly bound ligands. Therefore, careful selection of an anion which will not out-compete the desired ligand for binding to the metal is required. Furthermore, a weakly-coordinating anion must be sufficiently chemically inert to not be prone to reactivity in the presence of reactive organometallic species.[36] Triflate ($[OTf]^-$), hexafluorophosphate ($[PF_6]^-$) and tetrafluoroborate ($[BF_4]^-$) are some of the earliest examples of weakly-coordinating

anions (**Figure 1.7**), however their undesirable coordination chemistry,[37-39] and tendency to undergo decomposition (in the case of $[PF_6]^-$ and $[BF_4]^-$) through fluoride abstraction and hydrolysis is well established.[39-41] Three alternative classes of weakly-coordinating anion have begun to dominate the field in the last 20 years: halogenated alkyl- or arylborates,[42-44] perfluoroalkoxyaluminates,[45] and carborane anions (**Figure 1.7**).[36, 46, 47] Incorporation of highly electron-withdrawing substituents such as fluoride are ubiquitous among weakly-coordinating anions. These substituents induce electron delocalisation across the entire anion, which minimises the basicity, and nucleophilic sites throughout the anion.[48]
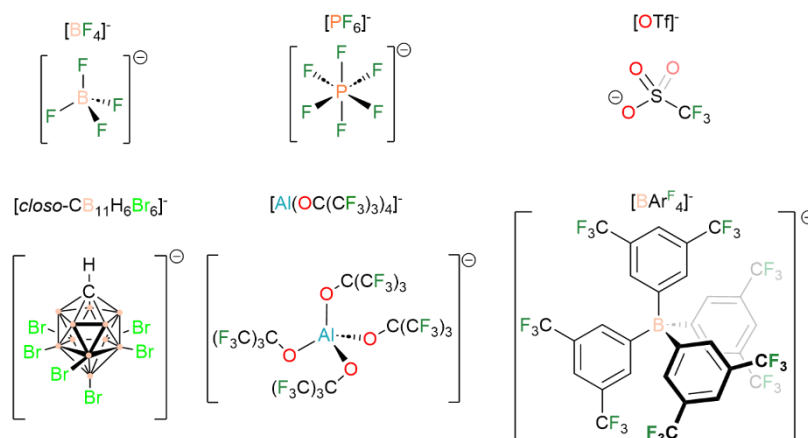
Figure 1.7: Examples of weakly-coordinating anions, including the early examples of $[BF_4]^-$, $[PF_6]^-$ and $[OTf]^-$, through to the modern prototypical $[closo\text{-}CB_{11}H_6Br_6]^-$, $[Al(OC(CF_3)_3)_4]^-$ and $[BAr^F_4]^-$ anions.

The perfluoroalkoxyaluminate are considered to be the least coordinating anions,[36, 45] with carborane anions having a slight tendency to coordinate through their halogen substituents, and borate anions through their π-system (**Scheme 1.3**).[44, 49, 50] However, the borate class possess some notable advantages over the other classes:

ease of synthetic access,[51] solubility, crystallinity,[52] and possession of NMR-active handles.
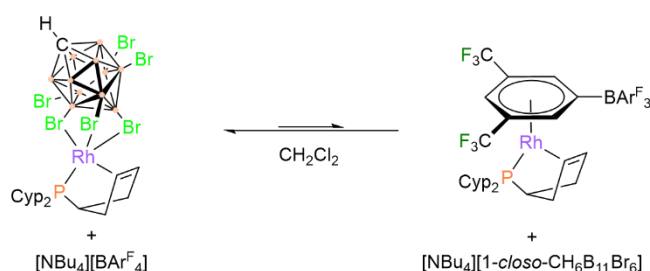
Scheme 1.3: Examples of carborane and $[BAr^F_4]^-$ coordination. In this work, the carborane coordination was the thermodynamic product $[\Delta G^0(298 \text{ K}) = -7.0 \pm 0.5 \text{ kJ mol}^{-1}]$ due to a combination of entropic and solvation effects.[50]

The '$[BAr^F_4]^-$' anion ($[B(3,5-(CF_3)_2C_6H_3)_4]^-$) is the anion which shall be exclusively used throughout the remainder of this thesis. Popularised by Brookhart,[52] $[BAr^F_4]^-$ has been utilised for the stabilisation of highly reactive organometallic complexes, both in solution[43, 53, 54] and in the solid-state.[44, 55] An early example case of the $[BAr^F_4]^-$ anion's utility is the formation of the latent low valent coordination complex $[Mn(depe)_2(CO)][BAr^F_4]$ [depe = $Et_2P(CH_2)_2PEt_2$, **Scheme 1.4**] where the vacant site is masked by polyagostic interactions.[56]
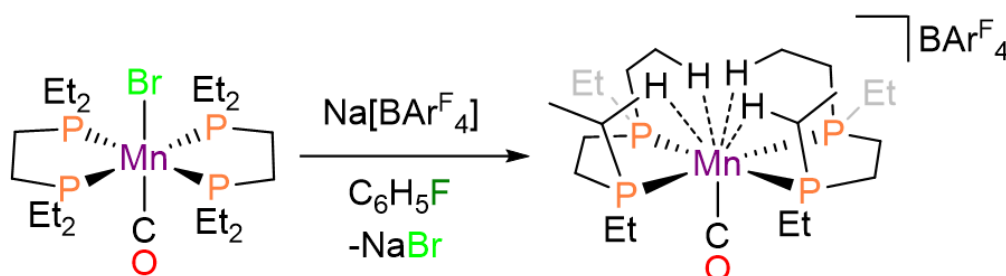
Scheme 1.4: Polyagostic manganese complex stabilised by the $[BAr^F_4]^-$ anion, reported by Kubas.[56]

1.5a σ-Complexes

Coordination complexes featuring an E–H (E = H, C, B, Si, Ge) σ-bond acting as a formally 2-electron donor, *via* a 3-centre-2-electron bond, are known as 'σ-complexes.'[57] These are considered to be the key, first-formed intermediates in many E–H activation mechanisms, such as oxidative cleavage, σ-complex-assisted-metathesis (σ-CAM) and electrophilic activation.[58-60] σ-Interactions are classified as distinct from agostic and anagostic interactions, as these M···H–C interactions are intramolecular, such as the polyagostic species in **Scheme 1.4**.[61]

The simplest, and first reported example of a σ-complex is that of σ-dihydrogen complexes, reported by Kubas in 1984, in the report of [*trans*-M(PR$_3$)$_2$(CO)$_3$(η^2-H$_2$)] (M = Mo, W; R = ^{i}Pr, Cy, **Figure 1.8**).[62] The bonding of these systems is characteristic of η^2-σ-E–H complexes[63] and is reminiscent of the Dewar-Chatt-Duncanson model of alkene bonding.[64] The dihydrogen ligand acts as a 2-electron donor through overlap of the H–H σ-orbital with a vacant metal *d*-orbital. Filled metal *d*-orbitals can also π-backdonate into the H–H σ*-antibonding orbitals (**Figure 1.8**).
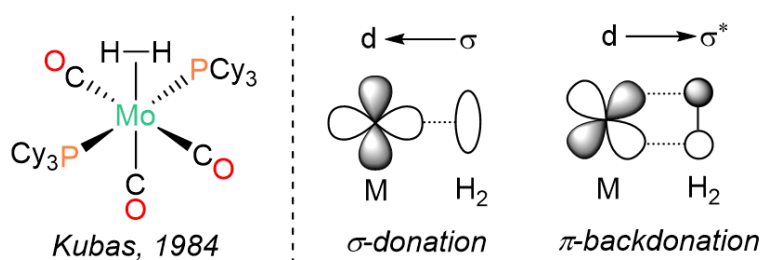
Figure 1.8: *Left*: An example of a σ-dihydrogen complex, [*trans*-Mo(PCy$_3$)$_2$(CO)$_3$(η^2-H$_2$)], published in the original report by Kubas in 1984.[62] *Right*: The bonding model for σ-dihydrogen.

The σ-donation and metal π-backdonation cause elongation of the H–H bond, which at its extreme leads to oxidative cleavage and formation of a dihydride complex. A considerable amount of research has been published on the continuum of σ-dihydrogen, elongated H_2 complexes, compressed dihydrides and dihydrides (**Figure 1.9**).[63, 65, 66] The extent of metal backdonation is increased with metal *d*-orbital radial extension, so the tendency to form dihydride complexes decreases across the period but increases down a group. Incorporating electron withdrawing ligands, or imparting a positive charge on the metal, will favour σ-dihydrogen complex formation, by reducing the backdonation potential of the metal.
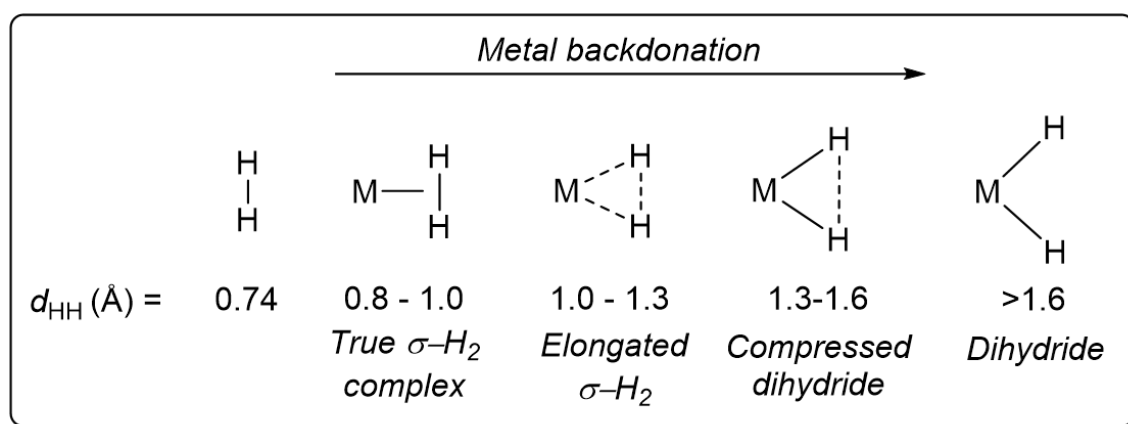
Figure 1.9: Increased metal backdonation to dihydrogen leads to weakening of the H–H bond and its respective elongation, culminating in oxidative cleavage.

Boranes and silanes also form σ-complexes with metals and are often more tightly bound than dihydrogen, due to the increased polarizability of the B–H and Si–H bonds.[67-71] σ-Alkane complexes exist at the other end of the spectrum of stability. The C–H bond is essentially non-polar, non-polarisable, and alkanes possess relatively high steric bulk which disfavours the C–H approach to the metal centre.[72-

[74] Furthermore, the σ(C–H) bond is very low in energy, so finds poor overlap with metal *d*-orbitals, and the σ*(C–H), which is high in energy, is a poor energy match for metal backdonation. For these reasons, σ-alkane complexes tend to have a bond dissociation energy in the region of 15 kcal mol^{-1}.[73, 75] σ-Complexes are not only of academic interest, but also relevant to industrial processes involving transition metal-catalysed E-H bond activation, such as hydroboration, hydrosilylation and alkane dehydrogenation.[12, 60, 70, 71, 76, 77]

The coordination geometries of σ-(E–H) complexes are typically η^1 (binding through *hydrogen-based* σ- and σ*-orbitals) or η^2-E–H (**Figure 1.10**).[60, 78-81] This is considered to be a continuum as the σ-interaction may be located anywhere along the E–H bond.[78]

$$\eta^1\text{-E-H} \qquad \eta^1;\eta^1\text{-E-H} \qquad \eta^2\text{-E-H} \qquad \eta^2;\eta^2\text{-E-H}$$
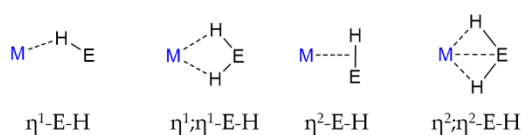
Figure 1.10: Continuum of coordination modes of σ(E–H) (E = C, Si, B, Ge) complexes with metal centres.

1.5b σ-Alkane Complexes Characterised by In Situ Characterisation

Due to the very low bond dissociation energy of σ-alkane complexes and their tendency to undergo onward reactivity, their direct observation is challenging.[58, 73, 82] σ-Alkane complexes tend to have transient lifetimes (ps to hours) in solution, even at low temperatures, and necessitate *in situ* characterisation techniques such as

time-resolved infrared spectroscopy (TRIR)[82, 83] and low temperature NMR spectroscopy (**Figure 1.11**).[43, 54, 84-86] TRIR studies are especially insightful in the case of photolysis of CO-containing complexes as the CO ligands provide a valuable spectroscopic handle.[83, 87] The timescale of TRIR also enables observation of very short lived σ-alkane complexes (ps to μs). Studying σ-alkane complexes through *in situ* NMR spectroscopy requires a significantly longer lived σ-alkane complex (ms to hours), with the bound alkane appearing as a shielded resonance (δ_H 0 to -10) relative to the free alkane.[43, 84]
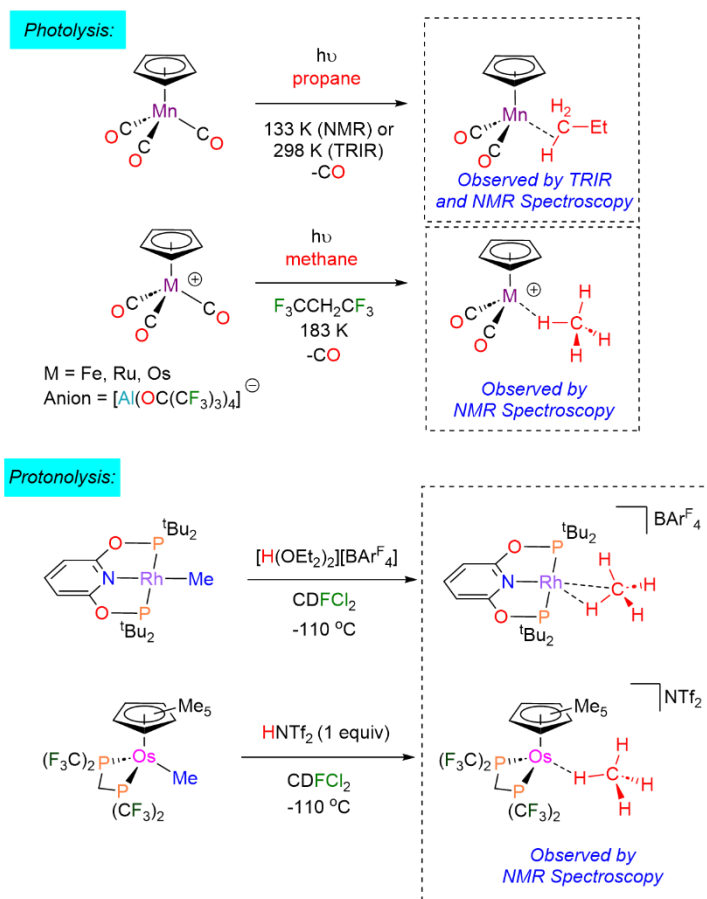
Figure 1.11: Selected examples of solution characterised σ-alkane complexes, formed through photolysis (*top*)[74, 85, 86] and protonolysis (*bottom*).[43, 80]

These studies have provided evidence not only for the formation of σ-alkane complexes, but also for fluxional processes such as ring- and chain-walking,[88, 89] and for onward reactivity such as substitution by water,[90] dinitrogen[90] or solvent,[43] or intramolecular substitution by π-systems or heteroatoms (**Scheme 1.5**).[89, 91] However, these studies have significant limitations: incomplete conversions, especially in photolytic studies; very low temperatures are required for σ-alkane complex lifetimes sufficient for *in situ* NMR spectroscopy; and only small quantities of σ-alkane complex formed (often *ca.* 2 mg).[43, 74, 80, 83-86] Additionally, all σ-alkane complexes studied in solution are ultimately unstable, and isolation of a σ-alkane complex through solution techniques is a goal which has not yet been achieved.[43, 54, 88, 90]
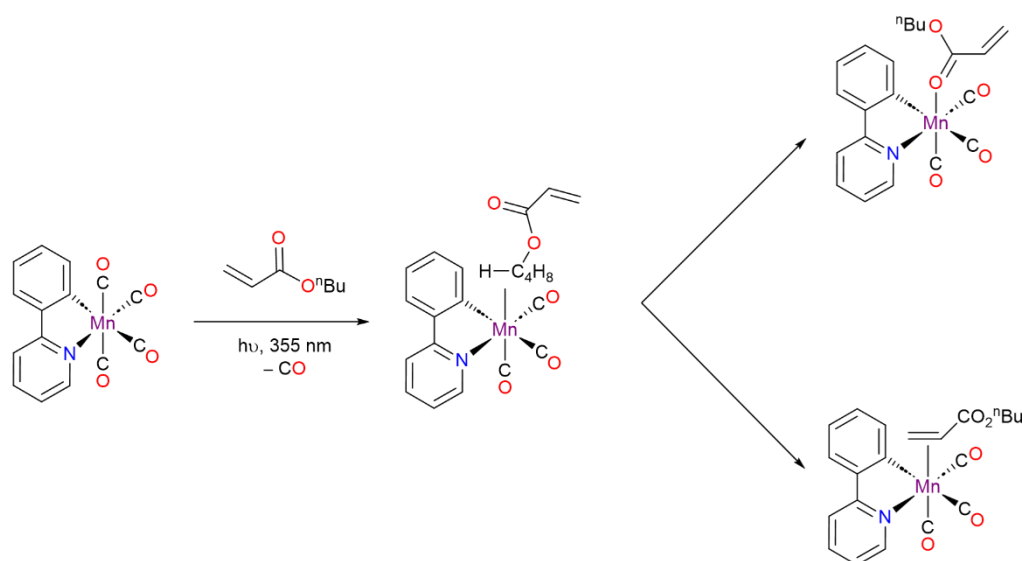
Scheme 1.5: Intramolecular substitution of a σ-alkane complex by a heteroatom or π-system.[89]

1.6.1 'In-Crystallo' Chemistry for Studies of Reactive Intermediates

In this thesis, *in-crystallo* chemistry is defined to be chemistry occurring within crystalline materials through solid/gas or photochemical reactivity, whether the material retains bulk crystallinity after the reaction or not. *In-crystallo* chemistry has many potential benefits to circumvent the above issues regarding decomposition of reactive species in the solution-state, through isolation of active sites.[92, 93] *In-crystallo* chemistry has also been increasingly recognised in chemical transformations.[93-101] This section will highlight some of the successes of *in-crystallo* chemical techniques with organometallic fragments through photocrystallography and solid/gas chemistry, as well as difficulties associated with *in-crystallo* reactivity studies. As this thesis will discuss solid/gas *in-crystallo* chemistry of organometallic complexes, the areas of mechanochemistry[102] and single-crystal to single-crystal (SCSC) transformations of organic substrates[94] fall outside the scope of this section.

1.6.2a Crystal Engineering for 'In Crystallo' Chemistry

In-crystallo reactivity can be investigated and probed *via* a range of solid-state analytical techniques, including solid-state NMR and ATR IR spectroscopies, and powder X-Ray diffraction. However, often the most desirable characterisation technique in inorganic and organometallic chemistry is single-crystal X-Ray diffraction (SC-XRD) to unambiguously assign structural changes. *In-crystallo* reactivity can only be appropriately investigated by SC-XRD techniques if the reaction undergoes a 'single-crystal to single-crystal transformation,' that is, if the starting single-crystalline material diffracts X-Rays, and the single-crystalline

product of the reaction also diffracts X-Rays, and retains short- and long-range order.[103] While recrystallisation may provide a sample which can be solved using SC-XRD techniques, the crystal metrics, space group, the local and repeating environments, and even the species of interest, may change substantially on recrystallisation as the compound may decompose.[95, 104-106] Thus, maintaining single-crystallinity, while not always necessarily integral to understanding the product, is an important challenge to overcome when studying how chemical reactions occur in the solid-state.

1.6.2b Synthetic Methods and Challenges in In-Crystallo Chemistry

In-crystallo photochemistry (or *photocrystallography*) involves photoactivation of a chemical species within a crystalline material. These methods have been utilised to enable crystallographic characterisation of metastable linkage isomers,[107-109] snapshots of intermediates in C–H activation by chlorine radicals,[110] and synthesis of highly reactive metal-nitride and metallonitrene complexes (**Figure 1.12**).[95, 105, 111]
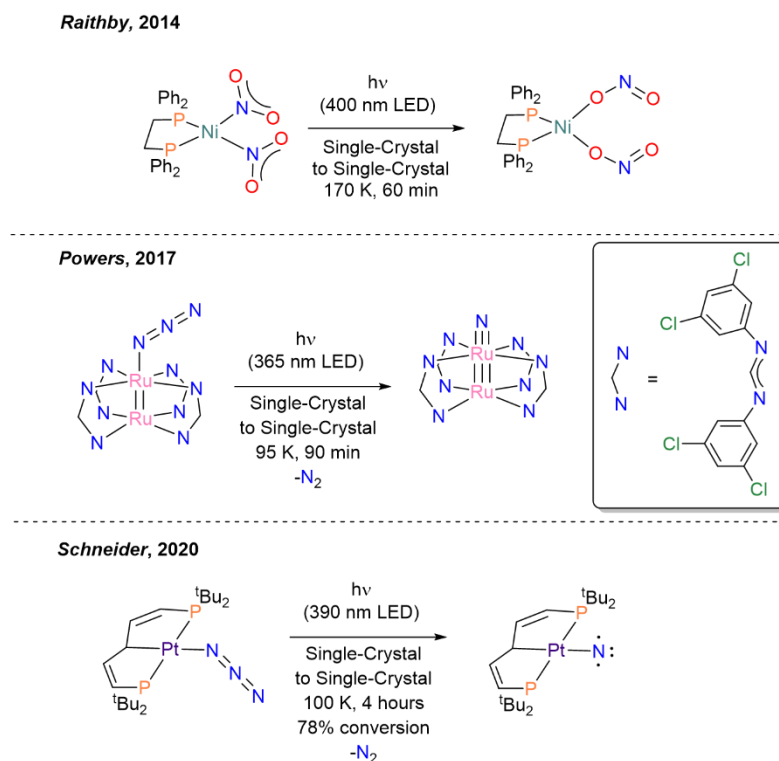
Figure 1.12: Selected examples of photocrystallographic studies of metastable linkage isomers (*top*) and highly reactive metal-nitride (*middle*) and metallonitrene complexes (*bottom*).[95, 108, 111]

Solid/gas *in-crystallo* chemistry involves the addition of a reagent as a gas or vapour to crystalline materials. These methods have been utilised for ligand substitution, carbon dioxide hydrogenation and isolation of highly reactive σ-alkane complexes.[44, 112-115] Solid/gas reactivity has also been applied to industrially relevant alkene and alkyne upgrading processes such as isomerisation and di- and trimerisation (**Scheme 1.6**).[99, 100, 116-118]
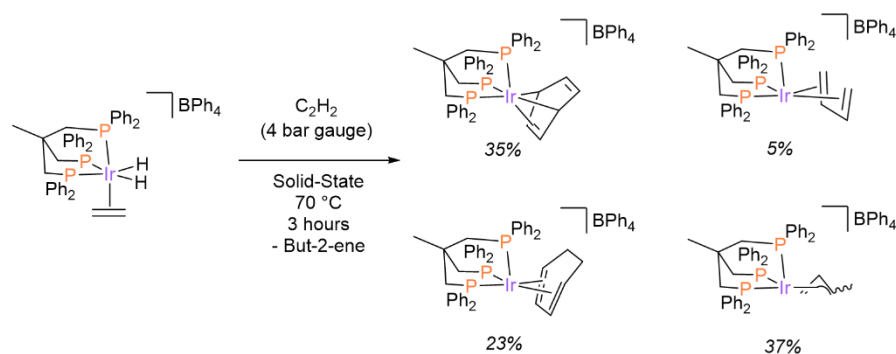
Scheme 1.6: Solid/gas chemistry has been utilised for the oligomerisation of acetylene to benzene, cyclohexa-1,3-diene, buta-1,3-diene and but-2-enes.[117] Listed percentages denote the relative population formed of each complex.

Despite the advantages and advances of *in-crystallo* chemistry, major challenges exist for *in-crystallo* chemistry: permeation of the gas throughout the solid and sufficient flexibility of the solid-state reagent to undergo reactivity in the solid-state confinement.[119, 120] Photocrystallographic techniques also have substantial difficulties with penetration of irradiation through the crystal due to strong internal filtering effects.[93] If these issues are not addressed successfully then the final product will be impure, with significant amounts of the starting material remaining.

To circumvent issues with gas permeation and flexibility within the solid-state, the groups of Fujita,[121] Champness[122] and Sumby[123] have loaded organometallic complexes into porous solid materials, such as clathrates and metal-organic frameworks (MOFs). These studies have focused on the photocrystallography of metal carbonyl complexes and have provided observation of an electronically- and coordinatively-unsaturated 16e Mn(I) complex, *fac-*/*mer*-isomerisation and ligand substitution (**Figure 1.13**).
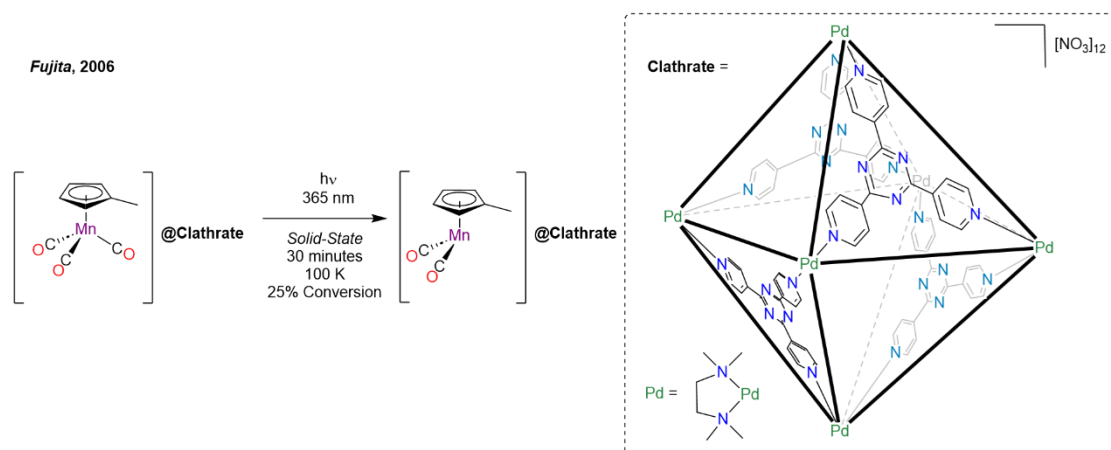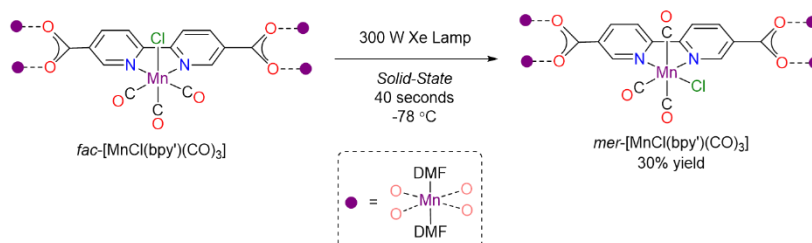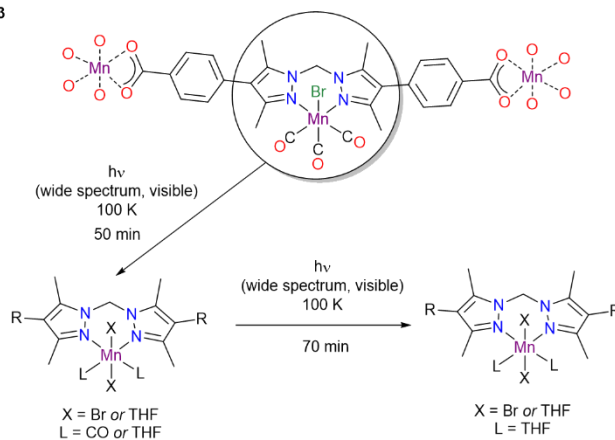
Figure 1.13: *In-Crystallo* reactivity of organometallic complexes in porous solid materials. *Top*: Observation of an electronically unsaturated Mn(I) complex within a clathrate.[121] *Middle*: *Fac/Mer*-isomerisation of a Mn(I) complex within a close-packed MOF.[122] *Bottom*: Ligand substitution within a close-packed MOF.[123]

However, the use of cavities/porous materials has been shown to not be essential to gas permeation by the work of Brammer *et al*. Here, they show that heating single crystals of the non-porous, one-dimensional coordination polymer, $[Ag_4(TMPyz)_3\{O_2C(CF_2)_3CF_3\}_4(EtOH)_2]_n$ (TMPyz = tetramethylpyrazine) causes loss of the bound ethanol ligand through a SCSC transformation (**Scheme 1.7**).[124] Re-coordination of the ethanol ligand was verified by powder X-Ray diffraction techniques, but this step did not retain single-crystallinity. This work therefore showed that product egress, that is the loss of ethanol, is possible through a non-porous solid without degradation to crystalline integrity.
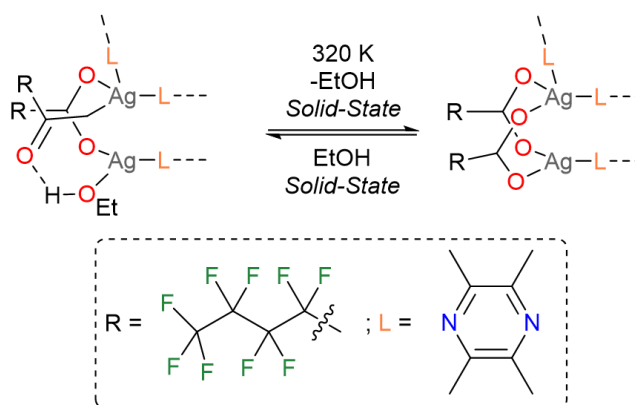
Scheme 1.7: Reversible loss of EtOH to a one-dimensional coordination polymer in a single-crystal to single-crystal transformation reported by Brammer.[124]

Brookhart has studied the addition of gaseous substrates to single crystals of $[Ir(R^F\text{-}POCOP)(N_2)]$ ($R^F\text{-}POCOP = 1,3\text{-}\{(2,4,6\text{-}CF_3C_6H_2)_2PO\}_2C_6H_3$). The gaseous substrates include NH_3, ethylene and CO, and in each case addition leads to the formation of the molecular species where N_2 has been substituted for the incoming ligand (**Scheme 1.8**).[113] The non-porous crystalline material possesses solvent channels filled by toluene (3 toluene molecules per organometallic fragment) which the

authors proposed allows for the gaseous reagents to penetrate the crystal lattice. This work highlights that reactant *ingress*, as well as product egress, is possible without degradation of crystalline integrity in a non-porous solid.
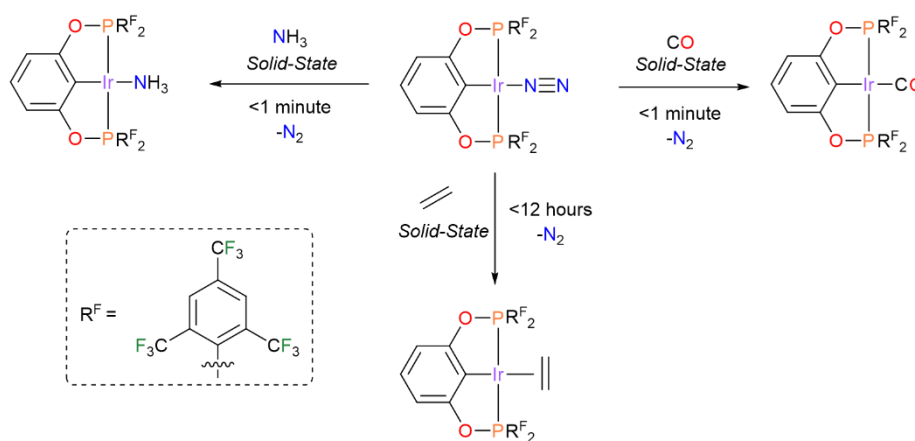
Scheme 1.8: Solid-state reactivity of a fluorinated iridium pincer dinitrogen complex with various substrates. In all cases the dinitrogen ligand is lost and replaced with the incoming substrate.[113]

The Weller group has shown that single crystals of [Rh(dcpm)(NBD)][BAr$^F_4$] [dcpm = bis(dicyclohexylphosphino)methane; NBD = norbornadiene] can reversibly uptake CH_2Cl_2 vapour or Xe gas (**Figure 1.14**).[125] This example is interesting as the encapsulated CH_2Cl_2 or Xe are not bound to the metal as ligands, but encased within the lattice framework, despite this being a non-porous solid (defined in this work as a material with less than 1 Å^3 accessible by a spherical probe of 1.4 Å diameter). The CH_2Cl_2 can be removed by application of vacuum to the crystals for 24 hours, while the Xe is less strongly held and is removed by simply flushing the system with Ar gas for 2 minutes. The unit cell metrics slightly increase with the incoming ligand [starting material: V = 6744.29(8) Å^3; CH_2Cl_2 encapsulated: V =

6855.15(12) Å^3; Xe encapsulated: V = 6809.24(10) Å^3] showing that the crystalline lattice expands and contracts with reactant ingress and 'product' egress to accommodate these substrates, without the displacement or reorganisation of the starting material.
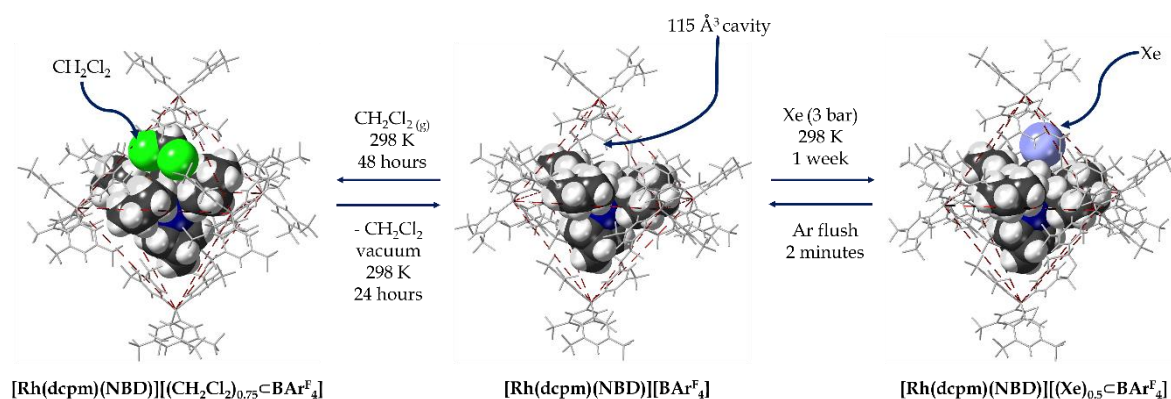
Figure 1.14: Reversible encapsulation of CH_2Cl_2 (*left*) and Xe (*right*) by a non-porous crystalline material ([Rh(dcpm)(NBD)][BAr$^F_4$], *centre*). The [BAr$^F_4$]$^-$ anions are represented as sticks for clarity.

The common thread which connects all of the non-porous solid-state reactivity studies is the presence of fluorous groups. Interhalogen non-covalent interactions are non-specific and non-directional,[126, 127] which enables crystalline structures to undergo plastic deformation without degradation to macroscopic crystalline integrity.

1.7 In-Crystallo Synthesis of σ-Alkane Complexes

In 2012 the Weller group published the first crystallographically characterised, well-defined[128, 129] σ-alkane complex.[44] They showed that addition of hydrogen gas (1 bar gauge pressure, 2 minutes) to single-crystalline samples of

[Rh(dibpe)(NBD)][BAr$^F_4$] (dibpe = ^{i}Bu$_2$PCH$_2$CH$_2$P^{i}Bu$_2$) yielded [Rh(dibpe)(η^2;η^2-NBA)][BAr$^F_4$] (NBA = norbornane, **Scheme 1.9**, **Figure 1.15**) in a SCSC transformation. The σ-alkane complex formed through this reaction decomposes at room temperature in the solid-state to form the amorphous, zwitterionic species [Rh(dibpe){η^6-C$_6$H$_3$(CF$_3$)$_2$}BAr$^F_3$]. Despite the decomposition in the solid-state, this work highlighted that the solid-state could be used to crystallographically characterise σ-alkane complexes for the first time. The crystallographic information provided by this study was essential information for computational insight into the σ-bonding of alkanes with metal centres, allowing for direct comparison between experiment and theory. The stabilisation of this highly reactive σ-alkane complex has been attributed to stabilising C–H⋯F and C–H⋯π non-covalent interactions between the organometallic fragment and the [BAr$^F_4$]$^-$ anion.[55, 130]
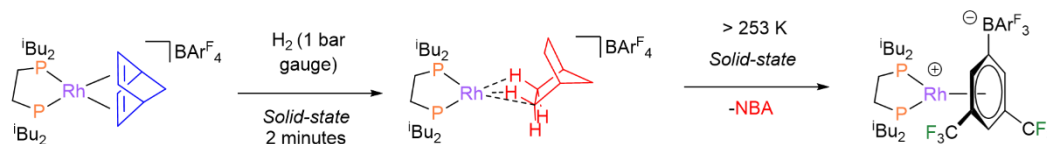
Scheme 1.9: The first report of the synthesis of a well-defined σ-alkane complex was reported by Weller, achieved through solid/gas solid-state reactivity of a rhodium diene precursor.[44]
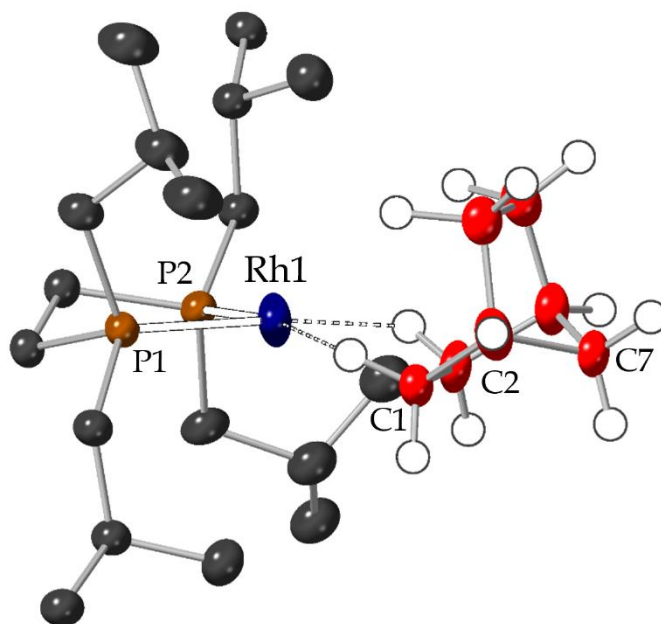
Figure 1.15: Solid-state structure determined by single-crystal X-Ray diffraction of the first well-defined molecular σ-alkane complex, reported by the Weller group in 2012.[44] Displacement ellipsoids are displayed at 50%. The carbons of the NBA fragment are displayed in red and protons on the chelating phosphine are omitted for clarity.

Following the 2012 report by Weller, the group followed up in 2015 on the solid-state synthesis of a more stable σ-alkane complex by variation of the phosphine R-groups from *iso*-butyl to cyclohexyl.[131] The complex in question, [Rh(dcpe)(η^2;η^2-NBA)][BAr$^F_4$] (dcpe = Cy$_2$PCH$_2$CH$_2$PCy$_2$; **Scheme 1.10**), has been shown to be indefinitely stable in the solid-state under an argon atmosphere at ambient temperature.[131, 132] This represents the first example of a σ-alkane complex which is not only isolable, but able to be stored for long periods of time. The long-term stability of this system allowed for onward chemistry of the σ-alkane to be investigated in the solid-state. In 2016 the group published work on the selective exchange of protons on the NBA fragment with deuterium (H/D exchange, **Scheme**

1.11).[132] The work showed that addition of D_2 gas to the rhodium diene precursor led to *endo*-D_4-NBA or *endo-exo*-D_8-NBA, depending on the time of addition (5 minutes or 16 hours). Contrastingly, addition of D_2 gas to the protic σ-alkane complex lead to *exo*-D_4-NBA. This work highlights the potential of *in-crystallo* chemistry to enable selective C–H activation of σ-alkane complexes.
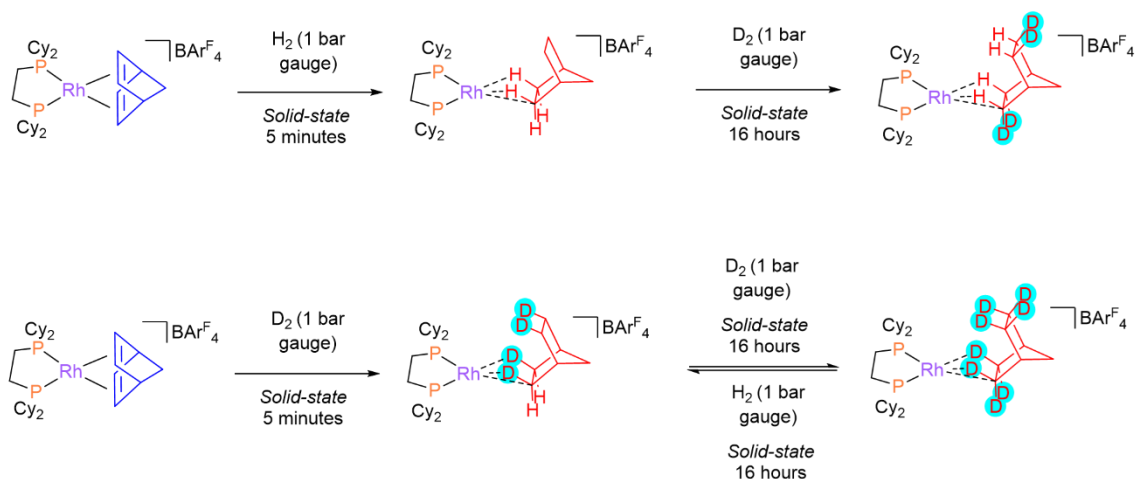
Scheme 1.10: *Top*: Solid-state synthesis of [Rh(Cy$_2$PCH$_2$CH$_2$PCy$_2$)(η^2;η^2-NBA)][BAr$^F_4$], a crystalline σ-alkane complex which is indefinitely stable in the solid-state.[131] *Bottom*: Selective H/D exchange occurring on the NBA fragment in the solid-state.[132]

The diphosphine bite-angle has also been varied by inclusion of alkyl linkers ranging from C_1 to C_5, keeping the R-group constant with cyclohexyls, with marked impact on the hydrogenation products. Hydrogenation of the C_1 variant, [Rh(Cy$_2$PCH$_2$PCy$_2$)(NBD)][BAr$^F_4$], does not lead to the formation of an observable σ-alkane complex, but immediately progresses through to the zwitterionic [Rh(Cy$_2$PCH$_2$PCy$_2$)(η^6-C$_6$H$_3$(CF$_3$)$_2$)BAr$^F_3$] species. Addition of hydrogen to the C_3 and C_4 congeners leads to similar σ-norbornane complexes as seen for [Rh(dcpe)(η^2;η^2-NBA)][BAr$^F_4$] (**Scheme 1.11**), both in terms of stability and

bonding.[79] The C_5 species will be discussed in more detail in the introduction for **Chapter 3** due to the similarity of the product of this reaction with the topic of **Chapter 3**.
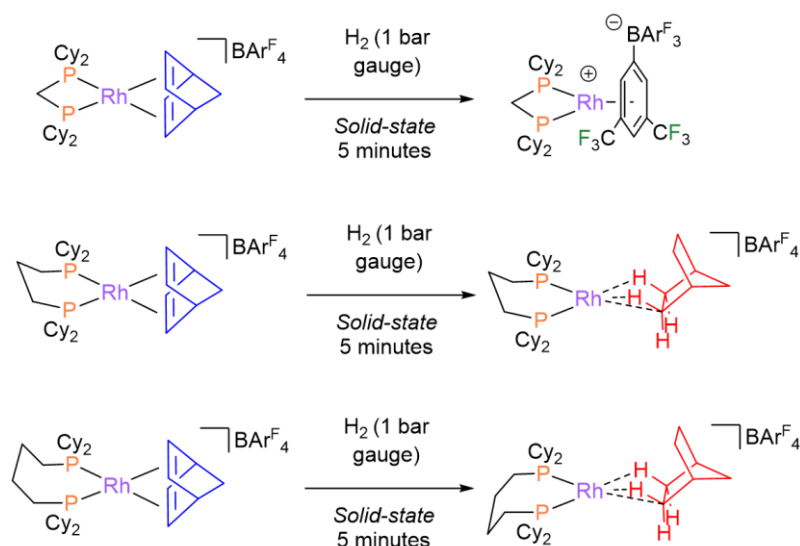
Scheme 1.11: Variation of phosphine bite-angle in the solid-state reactivity of cationic rhodium $\eta^2;\eta^2$-NBD complexes.

Finally, the alkene has been modified to enable access to different σ-alkane complexes. The {Rh(dcpe)}$^+$ scaffold has been utilised for this purpose due to the superior stability of the respective σ-norbornane complex and the robustness of this framework towards SCSC transformations.[104] Variation of the alkene is achieved through displacement of the norbornane ligand *via* SCSC transformations, or through reaction of the 1,2-$F_2C_6H_4$ adduct with the desired alkene. Hydrogenation of single-crystalline samples of these alkene complexes has yielded σ-propane, σ-(2-methyl)butane, and σ-pentane complexes, among others, through solid/gas reactivity (**Scheme 1.12**).[55, 133, 134] The culmination of these studies shows that *in-crystallo* reactivity can harness isolation of a wide range of highly reactive species

which are inaccessible *via* solution techniques for extended timeframes (hours to days) and non-isolable.
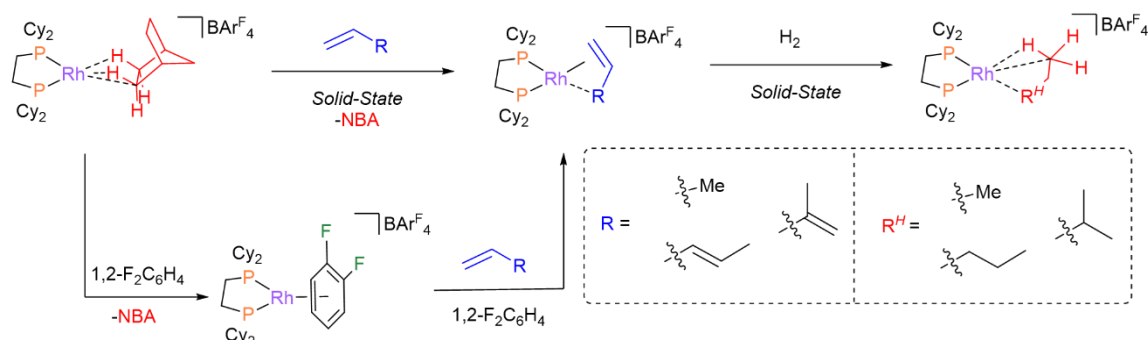
Scheme 1.12: General reaction scheme followed by the Weller group for access to various σ-alkane complexes of {Rh(dcpe)}⁺.

The next chapter will report on the solid/gas reactivity of manganese(I) and rhenium(I) pincer complexes and the impact of non-covalent interactions on the periodic structure of the crystalline material.

1.8 References

1.   J. H. Jones, *Platinum Met. Rev.*, 2000, **44**, 94-105.

2.   R. Tudor and M. Ashley, *Platinum Met. Rev.*, 2007, **51**, 116-126.

3.   M. Stürzel, S. Mihan and R. Mülhaupt, *Chem. Rev.*, 2016, **116**, 1398-1433.

4.   J. H. Phillips, in *Organometallic Chemistry in Industry*, 2020, DOI: https://doi.org/10.1002/9783527819201.ch10, pp. 259-282.

5.   A. Brennführer, H. Neumann and M. Beller, *Angew. Chem. Int. Ed.*, 2009, **48**, 4114-4133.

6. A. C. Flick, H. X. Ding, C. A. Leverett, R. E. Kyne, K. K. C. Liu, S. J. Fink and C. J. O'Donnell, *Biorg. Med. Chem.*, 2016, **24**, 1937-1980.

7. P. Devendar, R.-Y. Qu, W.-M. Kang, B. He and G.-F. Yang, *J. Agric. Food. Chem.*, 2018, **66**, 8914-8934.

8. W. J. Ramsay, N. A. W. Bell, Y. Qing and H. Bayley, *J. Am. Chem. Soc.*, 2018, **140**, 17538-17546.

9. L. A. Hammarback, J. B. Eastwood, T. J. Burden, C. J. Pearce, I. P. Clark, M. Towrie, A. Robinson, I. J. S. Fairlamb and J. M. Lynam, *Chem. Sci.*, 2022, **13**, 9902-9913.

10. I. Göttker-Schnetmann, P. White and M. Brookhart, *J. Am. Chem. Soc.*, 2004, **126**, 1804-1811.

11. A. Kumar, T. M. Bhatti and A. S. Goldman, *Chem. Rev.*, 2017, **117**, 12357-12384.

12. B. M. Gordon, N. Lease, T. J. Emge, F. Hasanayn and A. S. Goldman, *J. Am. Chem. Soc.*, 2022, **144**, 4133-4146.

13. A. S. Goldman, C. R. Landis and A. Sen, *Angew. Chem. Int. Ed.*, 2018, **57**, 4460-4460.

14. J. F. Hartwig, *Organotransition Metal Chemistry: From Bonding to Catalysis*, University Science Books, California, 2010.

15. R. H. Crabtree, *The Organometallic Chemistry of the Transition Metals*, John Wiley & Sons, Inc., Hoboken, New Jersey, 6 edn., 2014.

16. R. B. Bedford, P. B. Brenner, E. Carter, T. Gallagher, D. M. Murphy and D. R. Pye, *Organometallics*, 2014, **33**, 5940-5943.

17. R. J. Burford, A. Yeo and M. D. Fryzuk, *Coord. Chem. Rev.*, 2017, **334**, 84-99.

18. L. Webster, T. Krämer and F. M. Chadwick, *Dalton Trans.*, 2022, **51**, 16714-16722.

19. V. R. Landaeta, T. M. Horsley Downie and R. Wolf, *Chem. Rev.*, 2024, **124**, 1323-1463.

20. N. B. Johnson, I. C. Lennon, P. H. Moran and J. A. Ramsden, *Acc. Chem. Res.*, 2007, **40**, 1291-1299.

21. M. C. Willis, *Chem. Rev.*, 2010, **110**, 725-748.

22. L. D. de Almeida, H. Wang, K. Junge, X. Cui and M. Beller, *Angew. Chem. Int. Ed.*, 2021, **60**, 550-565.

23. C. A. Tolman, *Chem. Rev.*, 1977, **77**, 313-348.

24. C. P. Casey and G. T. Whiteker, *Isr. J. Chem.*, 1990, **30**, 299-304.

25. J. W. Raebiger, A. Miedaner, C. J. Curtis, S. M. Miller, O. P. Anderson and D. L. DuBois, *J. Am. Chem. Soc.*, 2004, **126**, 5502-5514.

26. A. D. Wilson, A. J. M. Miller, D. L. DuBois, J. A. Labinger and J. E. Bercaw, *Inorg. Chem.*, 2010, **49**, 3918-3926.

27. P. W. N. M. van Leeuwen, P. C. J. Kamer and J. N. H. Reek, *Pure Appl. Chem.*, 1999, **71**, 1443-1452.

28. E. Peris and R. H. Crabtree, *Chem. Soc. Rev.*, 2018, **47**, 1959-1968.

29. L. Mond, C. Langer and F. Quincke, *J. Chem. Soc., Trans.*, 1890, **57**, 749-753.

30. R. Franke, D. Selent and A. Börner, *Chem. Rev.*, 2012, **112**, 5675-5732.

31. H. Schulz, *Appl. Catal. A - Gen.*, 1999, **186**, 3-12.

32. D.-M. Yan, C. M. Crudden, J.-R. Chen and W.-J. Xiao, *ACS Catal.*, 2019, **9**, 6467-6483.

33. V. Tomar, P. Kumar, M. Nemiwal and R. K. Joshi, *Inorg. Chem. Commun.*, 2023, **158**, 111488.

34. J. H. Jones, *Platinum Met. Rev.*, 2000, **44**, 94-105.

35. M. Weller, T. Overton, J. Rourke and F. Armstrong, *Inorganic Chemistry*, Oxford University Press, Oxford, 5th edn., 2014.

36. I. M. Riddlestone, A. Kraft, J. Schaefer and I. Krossing, *Angew. Chem. Int. Ed.*, 2018, **57**, 13982-14024.

37. M. B. Humphrey, W. M. Lamanna, M. Brookhart and G. R. Husk, *Inorg. Chem.*, 1983, **22**, 3355-3358.

38. R. M. P. Veenboer, A. Collado, S. Dupuy, T. Lebl, L. Falivene, L. Cavallo, D. B. Cordes, A. M. Z. Slawin, C. S. J. Cazin and S. P. Nolan, *Organometallics*, 2017, **36**, 2861-2869.

39. W. Beck and K. Suenkel, *Chem. Rev.*, 1988, **88**, 1405-1421.

40. R. L. Paul, A. J. Amoroso, P. L. Jones, S. M. Couchman, Z. R. Reeves, L. H. Rees, J. C. Jeffery, J. A. McCleverty and M. D. Ward, *J. Chem. Soc., Dalton Trans.*, 1999, 1563-1568.

41. S. Kannan, M. A. Moody, C. L. Barnes and P. B. Duval, *Inorg. Chem.*, 2006, **45**, 9206-9212.

42. H. Nishida, N. Takada, M. Yoshimura, T. Sonoda and H. Kobayashi, *Bull. Chem. Soc. Jpn.*, 1984, **57**, 2600-2604.

43. W. H. Bernskoetter, C. K. Schauer, K. I. Goldberg and M. Brookhart, *Science*, 2009, **326**, 553-556.

44. S. D. Pike, A. L. Thompson, A. G. Algarra, D. C. Apperley, S. A. Macgregor and A. S. Weller, *Science*, 2012, **337**, 1648-1651.

45. A. Martens, P. Weis, M. C. Krummer, M. Kreuzer, A. Meierhöfer, S. C. Meier, J. Bohnenberger, H. Scherer, I. Riddlestone and I. Krossing, *Chem. Sci.*, 2018, **9**, 7058-7068.

46. Z. Xie, T. Jelinek, R. Bau and C. A. Reed, *J. Am. Chem. Soc.*, 1994, **116**, 1907-1913.

47. S. V. Ivanov, J. J. Rockwell, O. G. Polyakov, C. M. Gaudinski, O. P. Anderson, K. A. Solntsev and S. H. Strauss, *J. Am. Chem. Soc.*, 1998, **120**, 4224-4225.

48. A. Billion, M. Schorpp, R. Feser, M. Schmitt, L. Eisele, H. Scherer, T. Sonoda, H. Kawa, B. Butschke and I. Krossing, *Dalton Trans.*, 2023, **52**, 4355-4370.

49. A. I. McKay, A. J. Martínez-Martínez, H. J. Griffiths, N. H. Rees, J. B. Waters, A. S. Weller, T. Krämer and S. A. Macgregor, *Organometallics*, 2018, **37**, 3524-3532.

50. T. M. Douglas, E. Molinos, S. K. Brayshaw and A. S. Weller, *Organometallics*, 2007, **26**, 463-465.

51.   A. J. Martínez-Martínez and A. S. Weller, *Dalton Trans.*, 2019, **48**, 3551-3554.

52.   M. Brookhart, B. Grant and A. F. Volpe, Jr., *Organometallics*, 1992, **11**, 3920-3922.

53.   J. Campos, R. Peloso, M. Brookhart and E. Carmona, *Organometallics*, 2013, **32**, 3423-3426.

54.   M. D. Walter, P. S. White, C. K. Schauer and M. Brookhart, *J. Am. Chem. Soc.*, 2013, **135**, 15933-15947.

55.   A. J. Bukvic, A. L. Burnage, G. J. Tizzard, A. J. Martínez-Martínez, A. I. McKay, N. H. Rees, B. E. Tegner, T. Krämer, H. Fish, M. R. Warren, S. J. Coles, S. A. Macgregor and A. S. Weller, *J. Am. Chem. Soc.*, 2021, **143**, 5106-5120.

56.   W. A. King, B. L. Scott, J. Eckert and G. J. Kubas, *Inorg. Chem.*, 1999, **38**, 1069-1084.

57.   G. J. Kubas, *Metal dihydrogen and s-bond complexes: structure, theory, and reactivity*, Springer Science & Business Media, 2001.

58.   A. S. Weller, F. M. Chadwick and A. I. McKay, in *Adv. Organomet. Chem.*, ed. P. J. Pérez, Academic Press, 2016, vol. 66, pp. 223-276.

59.   J. Guihaumé, S. Halbert, O. Eisenstein and R. N. Perutz, *Organometallics*, 2012, **31**, 1300-1314.

60.   R. N. Perutz, S. Sabo-Etienne and A. S. Weller, *Angew. Chem. Int. Ed.*, 2022, **61**, e202111462.

61.   M. Brookhart, M. L. H. Green and G. Parkin, *Proc. Natl. Acad. Sci. U.S.A.*, 2007, **104**, 6908-6914.

62.   G. J. Kubas, R. R. Ryan, B. I. Swanson, P. J. Vergamini and H. J. Wasserman, *J. Am. Chem. Soc.*, 1984, **106**, 451-452.

63.   G. J. Kubas, *Chem. Rev.*, 2007, **107**, 4152-4205.

64.   J. Chatt and L. A. Duncanson, *J. Chem. Soc.*, 1953, 2939-2947.

65.   P. G. Jessop and R. H. Morris, *Coord. Chem. Rev.*, 1992, **121**, 155-284.

66.   D. M. Heinekey, A. Lledós and J. M. Lluch, *Chem. Soc. Rev.*, 2004, **33**, 175-182.

67.   C. N. Muhoro, X. He and J. F. Hartwig, *J. Am. Chem. Soc.*, 1999, **121**, 5033-5046.

68.   G. Alcaraz and S. Sabo-Etienne, *Coord. Chem. Rev.*, 2008, **252**, 2395-2409.

69.   G. S. McGrady, P. Sirsch, N. P. Chatterton, A. Ostermann, C. Gatti, S. Altmannshofer, V. Herz, G. Eickerling and W. Scherer, *Inorg. Chem.*, 2009, **48**, 1588-1598.

70.   J. Y. Corey, *Chem. Rev.*, 2016, **116**, 11291-11435.

71.   K. Saha, D. K. Roy, R. D. Dewhurst, S. Ghosh and H. Braunschweig, *Acc. Chem. Res.*, 2021, **54**, 1260-1273.

72.   R. H. Crabtree, *Angew. Chem. Int. Ed.*, 1993, **32**, 789-805.

73.   C. Hall and R. N. Perutz, *Chem. Rev.*, 1996, **96**, 3125-3146.

74.   J. A. Calladine, S. B. Duckett, M. W. George, S. L. Matthews, R. N. Perutz, O. Torres and K. Q. Vuong, *J. Am. Chem. Soc.*, 2011, **133**, 2303-2310.

75.   T. B. Gunnoe, in *Alkane C-H Activation by Single-Site Metal Catalysis*, ed. P. J. Pérez, Springer Netherlands, Dordrecht, 2012, DOI: 10.1007/978-90-481-3698-8_1, pp. 1-15.

76.   R. Martin, M. Kim, A. Asthagiri and J. F. Weaver, *ACS Catal.*, 2021, **11**, 4682-4703.

77.   N. Rothermel, D. Bouzouita, T. Röther, I. de Rosal, S. Tricard, R. Poteau, T. Gutmann, B. Chaudret, H.-H. Limbach and G. Buntkowsky, *ChemCatChem*, 2018, **10**, 4243-4247.

78.   A. Johnson, A. J. Martínez-Martínez, S. A. Macgregor and A. S. Weller, *Dalton Trans.*, 2019, **48**, 9776-9781.

79.   A. J. Martínez-Martínez, B. E. Tegner, A. I. McKay, A. J. Bukvic, N. H. Rees, G. J. Tizzard, S. J. Coles, M. R. Warren, S. A. Macgregor and A. S. Weller, *J. Am. Chem. Soc.*, 2018, **140**, 14958-14970.

80.   P. J. Sempsrott, B. B. Trinh, C. F. Lovitt, N. E. Capra and G. S. Girolami, *Sci. Adv.*, 2023, **9**, eadg8130.

81.   J. Yang, P. S. White, C. K. Schauer and M. Brookhart, *Angew. Chem. Int. Ed.*, 2008, **47**, 4141-4143.

82.   A. J. Cowan and M. W. George, *Coord. Chem. Rev.*, 2008, **252**, 2504-2511.

83.   X.-Z. Sun, D. C. Grills, S. M. Nikiforov, M. Poliakoff and M. W. George, *J. Am. Chem. Soc.*, 1997, **119**, 7521-7525.

84.   S. Geftakis and G. E. Ball, *J. Am. Chem. Soc.*, 1998, **120**, 9953-9954.

85. J. D. Watson, L. D. Field and G. E. Ball, *Nat. Chem.*, 2022, **14**, 801-804.

86. J. D. Watson, L. D. Field and G. E. Ball, *J. Am. Chem. Soc.*, 2022, **144**, 17622-17629.

87. T. E. Bitterwolf, K. A. Lott, A. J. Rest and J. Mascetti, *J. Organomet. Chem.*, 1991, **419**, 113-126.

88. H. M. Yau, A. I. McKay, H. Hesse, R. Xu, M. He, C. E. Holt and G. E. Ball, *J. Am. Chem. Soc.*, 2016, **138**, 281-288.

89. L. A. Hammarback, I. P. Clark, I. V. Sazanovich, M. Towrie, A. Robinson, F. Clarke, S. Meyer, I. J. S. Fairlamb and J. M. Lynam, *Nat. Catal.*, 2018, **1**, 830-840.

90. J. B. Eastwood, L. A. Hammarback, M. T. McRobie, I. P. Clark, M. Towrie, I. J. S. Fairlamb and J. M. Lynam, *Dalton Trans.*, 2020, **49**, 5463-5470.

91. I. J. S. Fairlamb and J. M. Lynam, *Acc. Chem. Res.*, 2024, DOI: 10.1021/acs.accounts.3c00774.

92. R. J. Witzke, A. Chapovetsky, M. P. Conley, D. M. Kaphan and M. Delferro, *ACS Catal.*, 2020, **10**, 11822-11840.

93. K. A. Reid and D. C. Powers, *Chem. Commun.*, 2021, **57**, 4993-5003.

94. F. Hu, X. Bi, X. Chen, Q. Pan and Y. Zhao, *Chem. Lett.*, 2021, **50**, 1015-1029.

95. A. Das, J. H. Reibenspies, Y.-S. Chen and D. C. Powers, *J. Am. Chem. Soc.*, 2017, **139**, 2912-2915.

96.   M. Oliván, A. V. Marchenko, J. N. Coalter and K. G. Caulton, *J. Am. Chem. Soc.*, 1997, **119**, 8389-8390.

97.   M. E. Bowden, B. Ginovska, M. O. Jones, A. J. Karkamkar, A. J. Ramirez-Cuesta, L. L. Daemen, G. K. Schenter, S. A. Miller, T. Repo, K. Chernichenko, N. Leick, M. B. Martinez and T. Autrey, *Inorg. Chem.*, 2020, **59**, 15295-15301.

98.   R. C. Laird, M. A. Sinnwell, N. P. Nguyen, D. C. Swenson, S. V. S. Mariappan and L. R. MacGillivray, *Org. Lett.*, 2015, **17**, 3233-3235.

99.   A. J. Martínez-Martínez, C. G. Royle, S. K. Furfari, K. Suriye and A. S. Weller, *ACS Catal.*, 2020, **10**, 1984-1992.

100.   M. R. Gyton, C. G. Royle, S. K. Beaumont, S. B. Duckett and A. S. Weller, *J. Am. Chem. Soc.*, 2023, **145**, 2619-2629.

101.   R. Kanega, N. Onishi, S. Tanaka, H. Kishimoto and Y. Himeda, *J. Am. Chem. Soc.*, 2021, **143**, 1570-1576.

102.   J.-L. Do and T. Friščić, *ACS Cent. Sci.*, 2017, **3**, 13-19.

103.   H. Ito, M. Muromoto, S. Kurenuma, S. Ishizaka, N. Kitamura, H. Sato and T. Seki, *Nat. Commun.*, 2013, **4**, 2009.

104.   F. M. Chadwick, A. I. McKay, A. J. Martinez-Martinez, N. H. Rees, T. Krämer, S. A. Macgregor and A. S. Weller, *Chem. Sci.*, 2017, **8**, 6014-6029.

105.   A. Das, C.-H. Wang, G. P. Van Trieste, III, C.-J. Sun, Y.-S. Chen, J. H. Reibenspies and D. C. Powers, *J. Am. Chem. Soc.*, 2020, **142**, 19862-19867.

106. T. M. Boyd, B. E. Tegner, G. J. Tizzard, A. J. Martínez-Martínez, S. E. Neale, M. A. Hayward, S. J. Coles, S. A. Macgregor and A. S. Weller, *Angew. Chem. Int. Ed.*, 2020, **59**, 6177-6181.

107. L. E. Hatcher and P. R. Raithby, *Acta Crystallogr., Sect. C: Struct. Chem.*, 2013, **69**, 1448-1456.

108. M. R. Warren, T. L. Easun, S. K. Brayshaw, R. J. Deeth, M. W. George, A. L. Johnson, S. Schiffers, S. J. Teat, A. J. Warren, J. E. Warren, C. C. Wilson, C. H. Woodall and P. R. Raithby, *Chem. Eur. J.*, 2014, **20**, 5468-5477.

109. L. E. Hatcher, J. M. Skelton, M. R. Warren and P. R. Raithby, *Acc. Chem. Res.*, 2019, **52**, 1079-1088.

110. M. I. Gonzalez, D. Gygi, Y. Qin, Q. Zhu, E. J. Johnson, Y.-S. Chen and D. G. Nocera, *J. Am. Chem. Soc.*, 2022, **144**, 1464-1472.

111. J. Sun, J. Abbenseth, H. Verplancke, M. Diefenbach, B. De Bruin, D. Hunger, C. Würtele, J. Van Slageren, M. C. Holthausen and S. Schneider, *Nat. Chem.*, 2020, **12**, 1054-1059.

112. S. Supriya and S. K. Das, *J. Am. Chem. Soc.*, 2007, **129**, 3464-3465.

113. Z. Huang, P. S. White and M. Brookhart, *Nature*, 2010, **465**, 598-601.

114. O. V. Zenkina, E. C. Keske, R. Wang and C. M. Crudden, *Angew. Chem. Int. Ed.*, 2011, **50**, 8100-8104.

115. E. A. Patrick, M. E. Bowden, J. D. Erickson, R. M. Bullock and B. L. Tran, *Angew. Chem. Int. Ed. Engl.*, 2023, **62**, e202304648.

116. A. R. Siedle and R. A. Newmark, *Organometallics*, 1989, **8**, 1442-1450.

117. C. Bianchini, P. Frediani, M. Graziani, J. Kaspar, A. Meli, M. Peruzzini and F. Vizza, *Organometallics*, 1993, **12**, 2886-2887.

118. C. Bianchini, M. Graziani, J. Kaspar, A. Meli and F. Vizza, *Organometallics*, 1994, **13**, 1165-1173.

119. M. D. Cohen and G. M. J. Schmidt, *J. Chem. Soc.*, 1964, 1996-2000.

120. S. D. Pike and A. S. Weller, *Philos. Trans. R. Soc. A*, 2015, **373**, 20140187.

121. M. Kawano, Y. Kobayashi, T. Ozeki and M. Fujita, *J. Am. Chem. Soc.*, 2006, **128**, 6558-6559.

122. A. J. Blake, N. R. Champness, T. L. Easun, D. R. Allan, H. Nowell, M. W. George, J. Jia and X.-Z. Sun, *Nat. Chem.*, 2010, **2**, 688-694.

123. R. J. Young, M. T. Huxley, L. Wu, J. Hart, J. O'Shea, C. J. Doonan, N. R. Champness and C. J. Sumby, *Chem. Sci.*, 2023, **14**, 9409-9417.

124. S. Libri, M. Mahler, G. Mínguez Espallargas, D. C. N. G. Singh, J. Soleimannejad, H. Adams, M. D. Burgard, N. P. Rath, M. Brunelli and L. Brammer, *Angew. Chem. Int. Ed.*, 2008, **47**, 1693-1697.

125. A. J. Martínez-Martínez, N. H. Rees and A. S. Weller, *Angew. Chem. Int. Ed.*, 2019, **58**, 16873-16877.

126. B. K. Saha, S. A. Rather and A. Saha, *Cryst. Growth Des,*, 2016, **16**, 3059-3062.

127. B. K. Saha, R. V. P. Veluthaparambath and V. Krishna G, *Chem. Asian J.*, 2023, **18**.

128. D. R. Evans, T. Drovetskaya, R. Bau, C. A. Reed and P. D. W. Boyd, *J. Am. Chem. Soc.*, 1997, **119**, 3633-3634.

129. I. Castro-Rodriguez, H. Nakai, P. Gantzel, L. N. Zakharov, A. L. Rheingold and K. Meyer, *J. Am. Chem. Soc.*, 2003, **125**, 15734-15735.

130. M. A. Sajjad, S. A. Macgregor and A. S. Weller, *Faraday Discuss.*, 2023, **244**, 222-240.

131. S. D. Pike, F. M. Chadwick, N. H. Rees, M. P. Scott, A. S. Weller, T. Krämer and S. A. Macgregor, *J. Am. Chem. Soc.*, 2015, **137**, 820-833.

132. F. M. Chadwick, T. Krämer, T. Gutmann, N. H. Rees, A. L. Thompson, A. J. Edwards, G. Buntkowsky, S. A. Macgregor and A. S. Weller, *J. Am. Chem. Soc.*, 2016, **138**, 13369-13378.

133. F. M. Chadwick, N. H. Rees, A. S. Weller, T. Krämer, M. Iannuzzi and S. A. Macgregor, *Angew. Chem. Int. Ed.*, 2016, **55**, 3677-3681.

134. A. I. McKay, A. J. Bukvic, B. E. Tegner, A. L. Burnage, A. J. Martínez-Martínez, N. H. Rees, S. A. Macgregor and A. S. Weller, *J. Am. Chem. Soc.*, 2019, **141**, 11700-11712.

Chapter 2 – In-Crystallo Lattice Adaptivity Triggered by Solid/Gas Reactivity of Cationic Group 7 Pincer Complexes

2.1 Introduction

2.1a Lattice Adaptivity in Molecular Crystals

As discussed in **Chapter 1**, organometallic chemists have recently utilised the single-crystalline solid-state to enable the synthesis of extremely reactive complexes which cannot otherwise be studied effectively in solution. These studies are, by design, focused on the coordination chemistry of the metal site, or 1° coordination site. The intermolecular/inter-ion non-covalent interactions, or 2° microenvironment, within the solid-state have been investigated by the Weller and Macgregor groups[1, 2] due to the influence this site has on the 1° coordination site. However, investigations into the impact of the 1° and 2° sites have on the 3° periodic structure of the crystalline lattice in solid-state organometallic chemistry is underexplored (**Figure 2.1**).
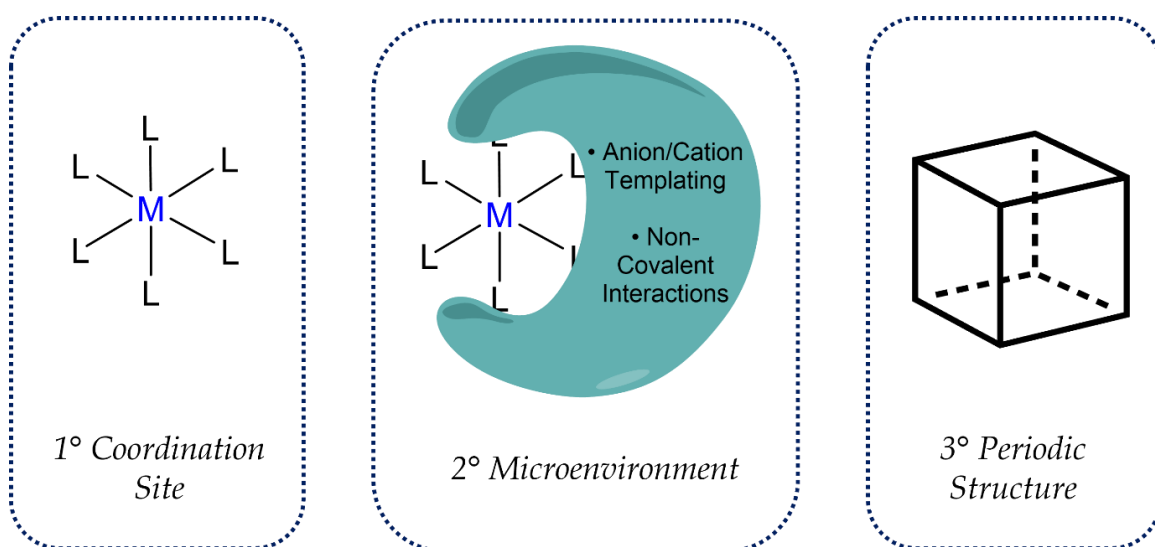
Figure 2.1: *Left*: The 1° coordination site of the metal. *Middle*: The 2° microenvironment, consisting of the local non-covalent interactions. *Right*: The 3° periodic structure.

This is not universally the case in solid-state chemistry, as the study of *lattice adaptivity* within single-crystalline molecular species is an emerging field of study in materials chemistry. This is where external stimuli such as temperature,[3] light,[4, 5] mechanical pressure,[6] and chemical reactivity,[7, 8] can induce changes to the lattice parameters through an *in-crystallo* transformation. This is often accompanied by the alteration, or complete breaking, of one set of (non-)covalent interactions, and a new set of (non-)covalent interactions becomes relevant or dominant.

Structural rearrangements of crystalline materials impart significant mechanical strain on the material. The consequence of this is that lattice adaptations are often *disintegrative*, that is the loss of single-crystallinity.[9] While reactions undergoing *disintegrative* lattice adaptions may retain their ability to diffract X-Rays as powder samples, single-crystal X-Ray diffraction (SC-XRD) data may be unobtainable due to the lack of suitably sized single crystals. This is typically due to crystal cracking along multiple fault lines in the crystal,[10, 11] which gives rise to a loss of macroscopic long-range order, which is also a major reason for loss of single-crystalline diffraction in organometallic single-crystal to single-crystal (SCSC) reactivity. *Restorative* lattice adaptions, that is the retention of single-crystallinity are desirable as an asset to provide insight into the microscopic changes that take place within the transformation and the (non-)covalent interactions which have promoted the transformation.

A partially *restorative* lattice adaption was serendipitously studied by Martinho and co-workers, who were studying a spin-crossover transition in an iron(III) Schiff base complex (**Scheme 2.1**).[12] Spin-crossover transitions are reversible transitions

between spin isomers, for example, thermal interconversion between accessible high and low spin isomers.[12] Heating single-crystals of the complex to 320 K led to the desired spin crossover transition, which was associated with an unexpected *thermosalient effect*, which is an event where crystals can bend, twist, or even explode,[10, 13] which occurs in this example. The thermosalient effect observed here preserved sufficient single-crystalline material during the first cycle of heating to allow for SC-XRD analysis. After four repetitions of the heating/cooling cycles, the crystallites were estimated to have decreased in size by a factor of 1000, necessitating powder X-Ray diffraction techniques for further analysis. The nature of the cause of the thermosalient effect was ascribed to the rapid anisotropic lengthening of the crystallographic *a* and *c* axes [before heating *a* = 10.5910(2) Å; *c* = 18.2420(3) Å; after heating, *a* = 11.931(3) Å; *c* = 19.166(5) Å], with contraction of the *b* axis [before heating *b* = 14.2497(3) Å; after heating *b* = 12.170(3) Å; **Figure 2.2**]. Similar reasonings have been given for other thermosalient events.[13, 14] The authors theorised that the absence of strong non-covalent interactions in the solid-state, namely hydrogen-bonds, rendered the crystals susceptible to the explosive thermosalient event.
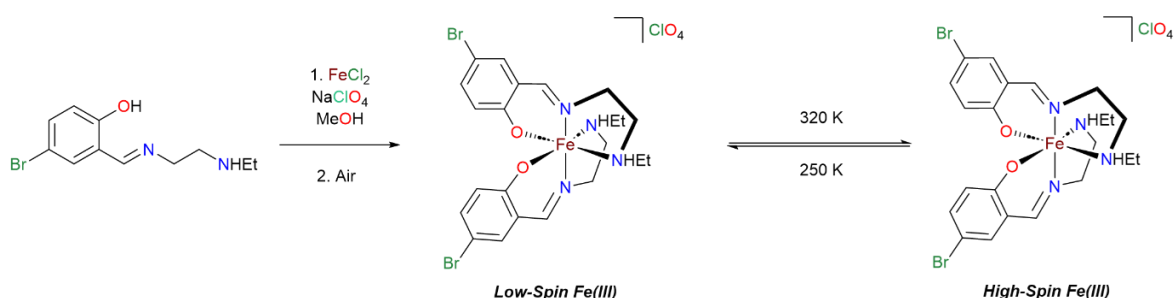
Scheme 2.1: Reaction scheme for the synthesis of an iron(III) Schiff base complex and its associated thermally induced spin-crossover transition.[12]
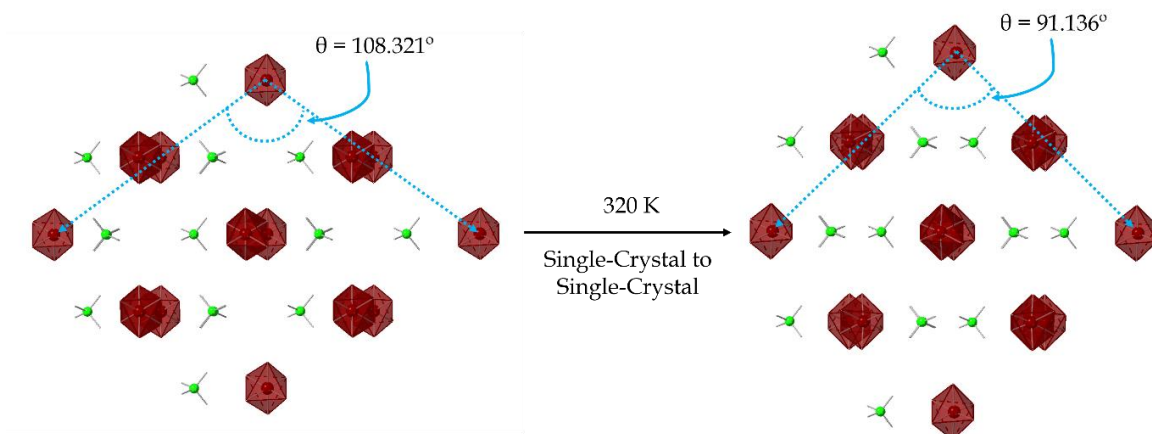
Figure 2.2: Application of heat (320 K) to single-crystals of an iron(III) Schiff base complex causes a thermosalient event to occur. A large distortion in the solid-state packing can be seen along the crystallographic *b*-axis of the structures taken before (*left*) and after (*right*) heating. The iron(III) complex is represented as red polyhedra and the chlorate counterions are represented as green sticks for clarity.

Another example of a reaction which shows *restorative* lattice adaptivity, this time caused by breakage and formation of covalent and non-covalent bonds, as well as large crystallographic parameter changes was published by Tao *et al.*[3] Here, molecular single-crystals of $[Zn(eg)_3][SO_4]$ (eg = ethylene glycol) undergo reversible, thermally induced, elimination of ethylene glycol ligands in two SCSC steps, first forming the helical 1-dimensional coordination polymeric material, $[Zn(eg)_2(\mu\text{-}SO_4)]_n$, then the 3-dimensionally structured material $\{[Zn(eg)_2]Zn(\mu_3\text{-}SO_4)_2\}_n$ (**Scheme 2.2**). Both of these steps are associated with space group changes, starting from the centrosymmetric space group $P\,2_1/n$, to the chiral orthorhombic Sohncke space group $P\,2_12_12_1$, to the polar Sohncke space group $P\,2_1$ (**Figure 2.3**).
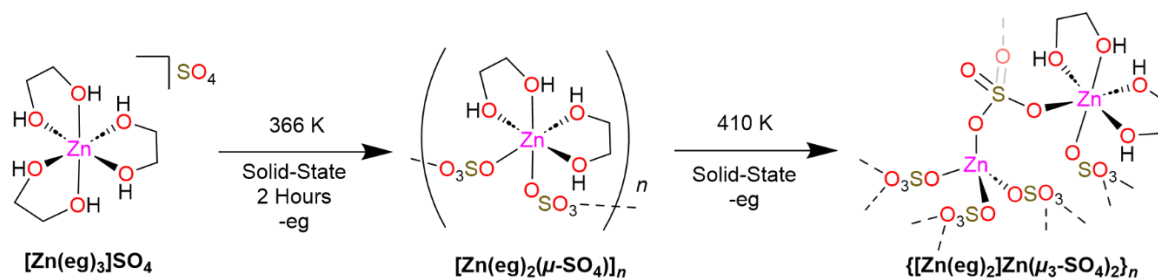
Scheme 2.2: Reaction scheme of the thermally-induced two-step single-crystal to single-crystal elimination of ethylene glycol from Λ/Δ-[Zn(eg)$_3$]SO$_4$. This first forms the intermediate one-dimensional coordination polymer [Zn(eg)$_2$(μ-SO$_4$)]$_n$, which then transforms into the three-dimensional coordination polymer {[Zn(eg)$_2$]Zn(μ_3-SO$_4$)$_2$}$_n$.
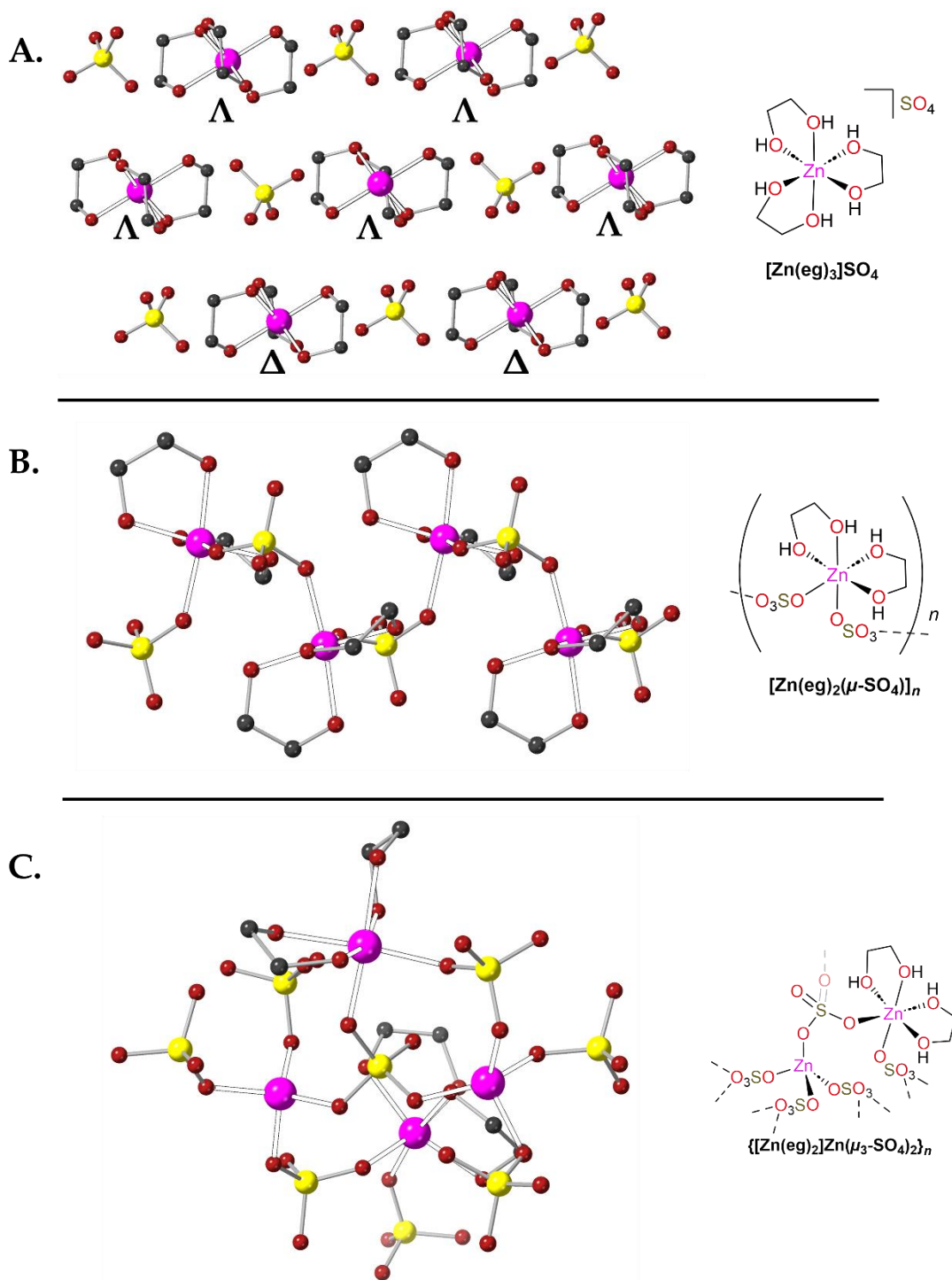
Figure 2.3: Reversible two-step single-crystal to single-crystal transformation reported by Tao *et al.*[3] **A**. Single-crystal structure of [Zn(eg)$_3$]SO$_4$. The Δ and Λ stereoisomers crystallise in parallel directions along the crystallographic *a*-axis. **B**. Solid-state structure of the product of heating single crystals of [Zn(eg)$_3$]SO$_4$ to 366 K. **C**. The solid-state structure obtained by further heating the sample to 422 K.

Overall, the elimination of these chelating ligands causes a 50% decrease in volume, while retaining crystallinity - one of the largest reported changes in volume associated with a restorative lattice adaption. The formation of strong hydrogen bonds between the ethylene glycol and the sulphate anions is attributed to the remarkable crystalline elasticity of this system. The authors note however that the 'single crystals suitable for SC-XRD analysis were carefully chosen from cracked crystals,' highlighting degradation of bulk crystal quality, which is common among SCSC transformations. It is noteworthy that the egress of ethylene glycol from the crystalline material throughout the sequential SCSC transformations may be essential to the formation of material retaining long-range order. The long-range order of the material may be lost throughout the course of the reaction but regained through phase rebuilding of damaged crystals.

2.1b Value of Halogenated Groups in Retention of Macroscopic Crystallinity

As discussed in **Chapter 1.6.2**, halogenated groups appear to be important to retention of macroscopic crystallinity during solid-state reactivity. This has been reflected in lattice adaptivity,[13, 15] as the weak, non-specific, and non-directional nature of interhalogen interactions[16, 17] can assist with solid-state plasticity to overcome the mechanical stresses associated with these transformations.

This has been highlighted by the work of Naumov *et al*, who have studied the crystal flexibility of hexachlorobenzene.[18] The solid-state structure of hexachlorobenzene reveals that the major intermolecular interactions within the

crystal are Cl···Cl and π···π, which operate along different planes. The non-directional and non-specific nature of Cl···Cl interactions means that application of external pressure to the (001) face causes deformation of the macroscopic crystal, without loss of crystallinity. Conversely, application of external pressure along the (100) face leads to breaking of π···π interactions, causing the crystallite to fragment (**Figure 2.4**). This demonstrates that interhalogen interactions can facilitate plasticity within molecular crystals.
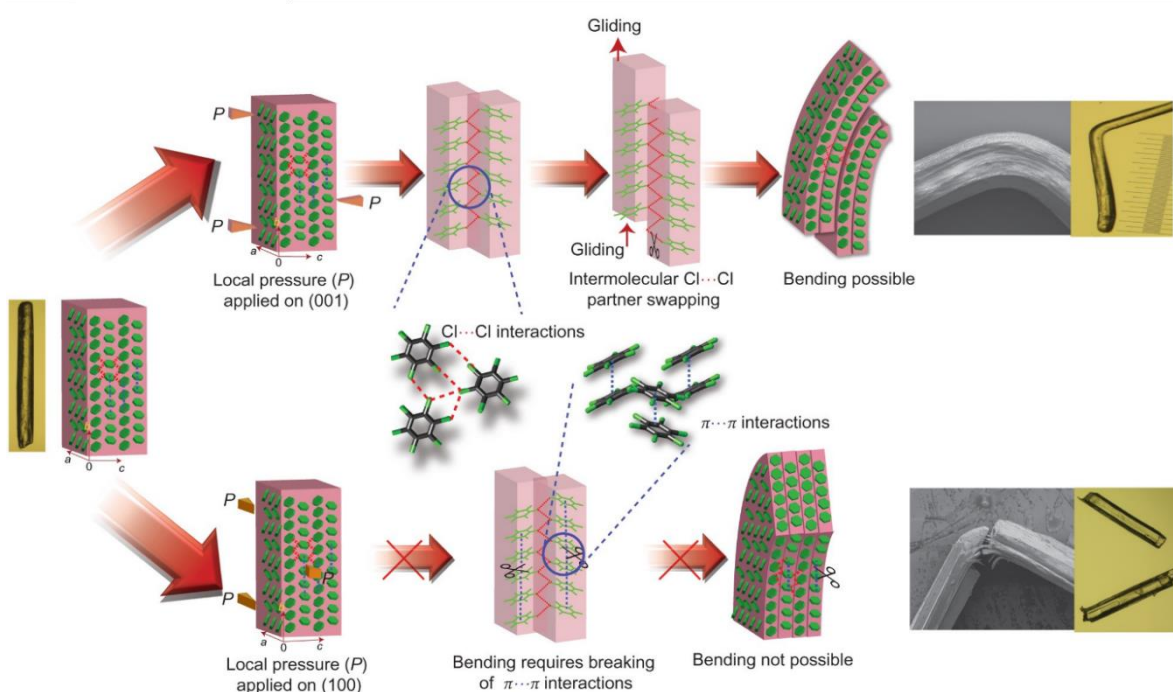
Figure 2.4: Crystals of hexachlorobenzene can be bent when pressure is applied on the (001) face, where intermolecular interactions are dominated by Cl···Cl interactions (*top row*). When pressure is applied to the (100) face, the crystals break as the intermolecular interactions are dominated by π···π interactions (*bottom row*). Image reproduced from ref. 18 with permission.

Lattice adaptivity has also been investigated for a fluorinated organometallic species by the same, and other, authors.[19, 20] The fluorinated organometallic species, [Pd(hfac)(phenylazophenyl)] (hfac = hexafluoroacetylacetonate, **Figure 2.5**), thermally interconverts between five polymorphs.[20] These conversions are associated with both positive and negative thermal expansion coefficients (**Table 2.1**, **Figure 2.6**).

[Pd(hfac)(phenylazophenyl)]
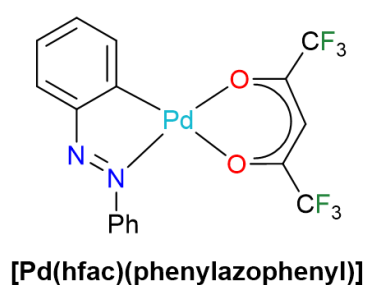
Figure 2.5: Chemical structure of [Pd(hfac)(phenylazophenyl)], which undergoes thermal interconversion between five polymorphs in the solid-state.[19, 20]

Table 2.1: Comparison of unit cell parameters between determined polymorphs of [Pd(hfac)(phenylazophenyl)].

Parameter	Form a	Form β	Form γ	Form ε
Temperature (K)	150	298	358	90
Space Group	$P\bar{1}$	$P\bar{1}$	$P\bar{1}$	$P\bar{1}$
a, b, c (Å)	8.138(4)	7.0160(2)	4.2736(5)	7.7972(2)
	13.173(5)	11.6870(3)	13.5601(2)	13.2030(2)
	16.240(6)	12.4659(3)	14.8046(3)	16.4284(3)
α, β, γ (°)	85.75(2)	63.1390(10)	83.307(8)	94.002(2)
	81.91(2)	84.7600(10)	93.959(9)	87.307(3)
	80.10(2)	80.9950(10)	76.843(7)	100.656(3)
Volume (Å³)	1695.6(12)	900.38(4)	825.66(10)	1657.03(6)
Z	4	2	2	4
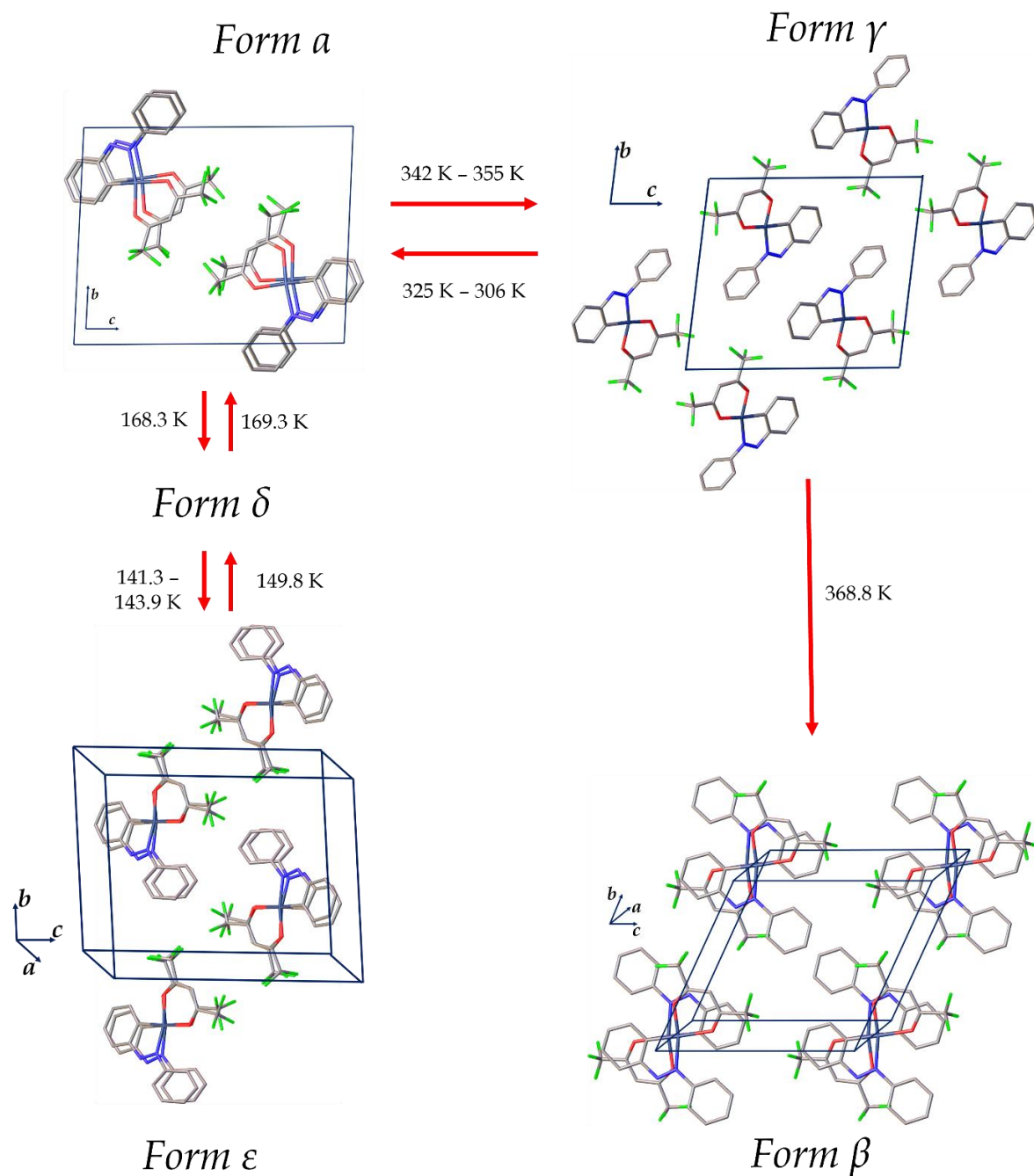
Figure 2.6: Phase transitions and solid-state structures of four of the five determined polymorphs of [Pd(hfac)(phenylazophenyl)]. Forms α and β were determined by single-crystal X-Ray diffraction, while γ and ε where determined by Rietveld refinement of powder X-Ray diffraction data.[20] Form β does not revert to form γ in the solid-state, suggesting this is the thermodynamically preferred polymorph of [Pd(hfac)(phenylazophenyl)].

The authors also noted that the α→γ transition is associated with a thermosalient event where the crystals 'fly off the hot stage,' without cracking of the crystals.[19, 20] This thermosalient effect is due to the anisotropic extension of the crystallographic *a* and *b* axes, with contraction of the *c* axis. The retention of single-crystallinity after a violent thermosalient effect, and the observation of five distinct polymorphs which can interconvert through thermal control, again highlights the function of halogenated groups allowing for flexibility and plasticity of crystalline structures.

2.1c Aims and Objectives

In this chapter, the reaction of two cationic group 7 pincer complexes, [M(R-PONOP)(L)(CO)$_2$][BAr$^F_4$] [M = Mn, R = ^{i}Pr, L = tetrahydrofuran (THF); M = Re, R = ^{t}Bu, L = vacant site; PONOP = κ^3-2,6-(R$_2$PO)$_2$C$_5$H$_3$N; Ar^F = 3,5-(CF$_3$)C$_6$H$_3$], with carbon monoxide in solid/gas reactions is reported. The reactions show significant macroscopic fracturing of the crystals, with microcrystal Electron Diffraction (MicroED) methods required to structurally analyse the resultant microcrystals from the reaction with the manganese congener. The fracturing of the crystals is shown to be due to significant reorganisation of the periodic structures due to changes in the 2° microenvironment. Computational calculations were used to investigate and metricise changes in non-covalent interactions and other inter-ion contributions to the lattice adaption.

2.2. Results and discussion

2.2a Acknowledgements

NMR tensor analysis and related NMR computational calculations were performed by Dr Matthew Conley at the *University of California, Riverside*. Periodic density functional theory (DFT) calculations, IGMH and QTAIM analyses were carried out by Dr M. Arif Sajjad and Professor Stuart Macgregor at *Heriot-Watt University* (now *University of St. Andrews*). The collection, reduction and refinement of microcrystal Electron Diffraction data was carried out by Miss Emily Thompson and Dr Huw Jenkins at the *York Structural Biology Laboratories* at the *University of York*. Solid-state NMR data were collected by Dr Samuel Page at the *University of Durham* Solid-State NMR Service or Dr Matthew Gyton and Dr Laurence Doyle at the *University of York*. Scanning Electron Microscopy (SEM) data were collected by Dr Adam Kerrigan at the *York-JEOL Nanocentre* at the *University of York*. Gel Permeation Chromatography (GPC) data were collected by Mr Mathew Cross at the *University of York*. All other data were collected by the thesis author. The major results of this chapter have been published in the literature (*Chem. Commun.*, 2023, **59**, 10749-10752). [21]

2.2b. Synthesis and Characterisation of [Mn(^{i}Pr-PONOP)(CO)$_3$][BAr$^F_4$]

2.2bi. Project Outline

Several geometric motifs of [BAr$^F_4$]$^-$ anions around cationic organometallic moieties have been shown to successfully sustain SCSC transformations. Namely, an approximately octahedral arrangement of six anions around one cation (**Figure 2.7**),

and an approximately bicapped square prismatic arrangement, where ten anions are organised around two cations (**Figure 2.7**). Both of these arrangements have both supported the formation and isolation of σ-alkane complexes through the stabilising inter-ion non-covalent interactions.[2, 22, 23]

Octahedral   *Bicapped Square Prismatic*
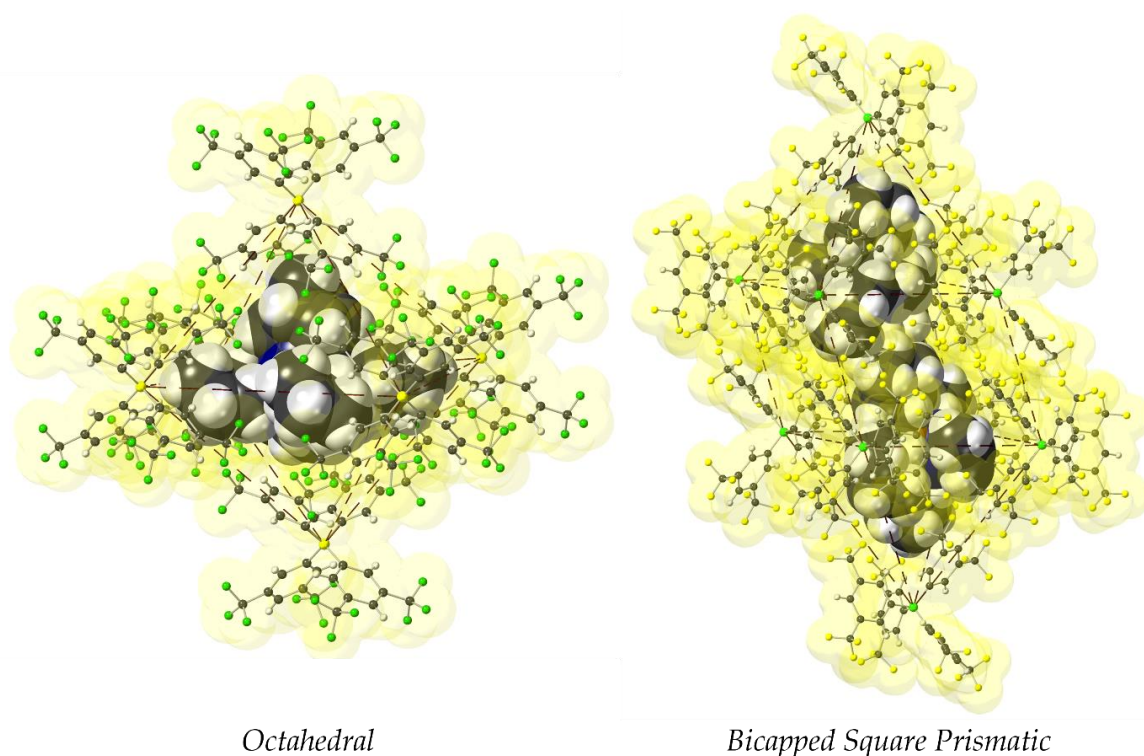
Figure 2.7: Previously published geometric motifs of [BAr$^F_4$]$^-$ anions which have supported the formation of σ-alkane complexes in the solid-state. [BAr$^F_4$]$^-$ anions are mapped with a van der Waals surface (yellow). *Left*: An approximately octahedral motif of six [BAr$^F_4$]$^-$ anions template around one cationic organometallic fragment.[24] *Right*: An appropriately bicapped square prismatic arrangement of ten [BAr$^F_4$]$^-$ anions around two cationic organometallic fragments.[23]

Recently, the Weller group have published research on the solid-state reactivity of [Ir(^{i}Pr-PONOP)(propene)][BAr$^F_4$], in which the R-PONOP ligand scaffold has been

shown to template the bicapped square prismatic framework of anions which appears to be favourable for solid-state reactivity.[25] Looking to expand solid-state molecular organometallic chemistry (SMOM-Chem) beyond group 9 metals, two cationic manganese and rhenium R-PONOP complexes were designed and paired with the $[BAr^F_4]^-$ anion. As noted in **Chapter 1.6.2**, manganese and rhenium complexes have been explored in solid-state chemistry, using photocrystallographic techniques in porous materials such as metal-organic frameworks (MOFs)[26, 27] and clathrates.[28] Here, the solid-state reactivity of non-porous, single-crystalline, molecular species of manganese and rhenium is reported. The solid-state reactivity at the 1° coordination site induces large changes to inter-ion non-covalent interactions (2° microenvironment) which was investigated through periodic DFT calculations. The changes to the 2° microenvironment invoke a lattice adaption in the 3° periodic structure of the crystal, which was characterised by solid-state NMR spectroscopy and single-crystal X-Ray diffraction or microcrystal Electron Diffraction techniques.

2.2bii. Synthesis and Spectroscopic Data

Starting from the previously reported complex, $[MnBr(^iPr\text{-}PONOP)(CO)_2]$,[29] halide abstraction with $Na[BAr^F_4]$ in the weakly-coordinating solvent $1,2\text{-}F_2C_6H_4$ under an atmosphere of carbon monoxide (1 bar gauge pressure at 78 K) led to the formation of $[Mn(^iPr\text{-}PONOP)(CO)_3][BAr^F_4]$ (**[Mn-CO]**). After removal of the solvent *in vacuo*, extraction into CH_2Cl_2 and layering with pentane, **[Mn-CO]** was isolated in 75% yield as a crystalline solid (**Scheme 2.3**).
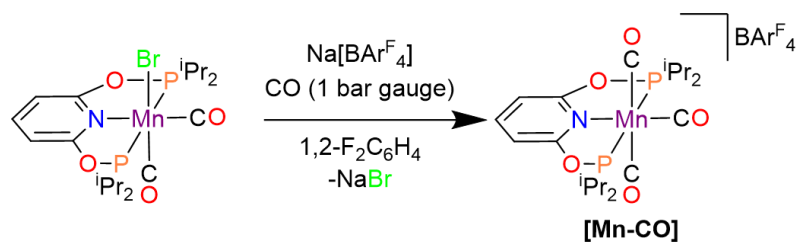
Scheme 2.3: Synthetic route to [Mn(^{i}Pr-PONOP)(CO)$_3$][BAr$^F_4$] (**[Mn-CO]**), starting from [MnBr(^{i}Pr-PONOP)(CO)$_2$].

The solid-state ATR IR spectrum of **[Mn-CO]** reveals two CO stretching bands at v_{CO} 2055 (w, s) and 1970 (s) cm^{-1} (**Figure 2.8**). The separation and intensity of these peaks are indicative of the C_{2v} *mer*-isomer of **[Mn-CO]**,[30-32] as the symmetric stretch of the axial carbonyl ligands (A$_1$-symmetric) is only weakly-allowed due to the minor change in dipole moment. Contrastingly, if the *fac*-isomer were to have formed, the peak separation should be *ca.* 20 cm^{-1}, and both bands be of approximately equal, medium intensity,[30-32] due to the significant increase in dipole moment caused by each of the carbonyl vibrations in this isomer.
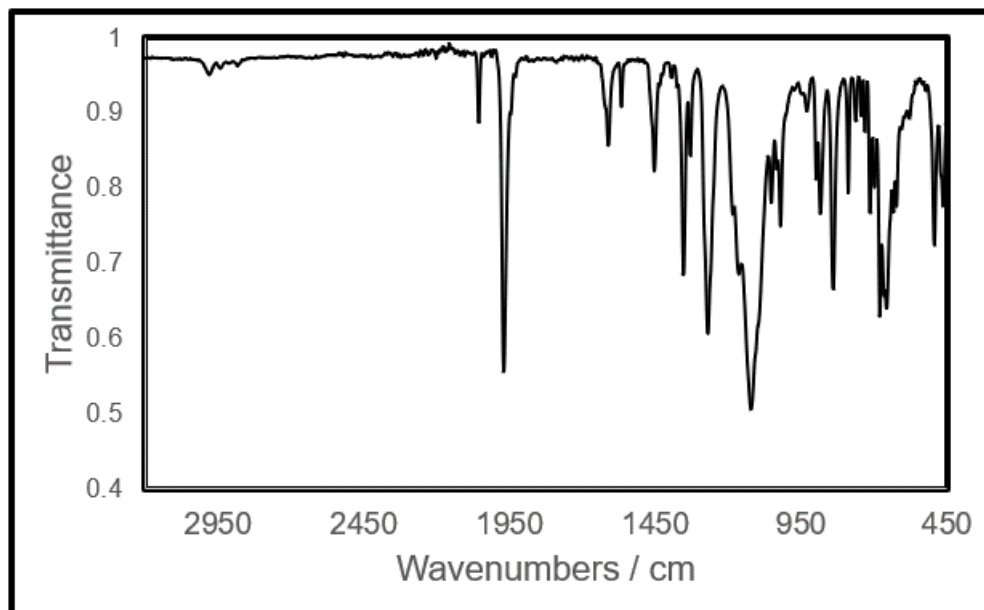
Figure 2.8: ATR IR spectrum of **[Mn-CO]**. Carbonyl stretching bands are observed at v_{CO} 2055 and 1970 cm^{-1}.

[Mn-CO] shows apparent C_{2v} symmetry in solution, with one set of ^{i}Pr resonances in the solution ^{1}H and ^{13}C{^{1}H} NMR (CD$_2$Cl$_2$, 298 K) spectra (**Figure 2.9**). The methine resonance (δ_H 3.00) is observed as a complex triplet of septets in the ^{1}H NMR spectrum due to the magnetically inequivalent ^{31}P environments [3]. The methine signal collapses upon ^{31}P decoupling to a broad septet [^3J(HH) = 7.0 Hz; **Figure 2.9**]. Similarly, the two ^{i}Pr methyl environments (δ_H 1.47, 1.37) are observed as a pair of doublets-of-doublets in the ^{1}H NMR spectrum which collapse to doublets [^3J(HH) = 7.1 Hz, **Figure 2.9**] upon ^{31}P decoupling. The solution ^{31}P{^{1}H} NMR spectrum reveals one broad resonance (δ_P = 225.2, FWHM = 165 Hz) due to quadrupolar broadening from the ^{55}Mn nucleus (I = 5/2, 100% abundant Q = 0.33 x 10^{-24} cm^2).[33]
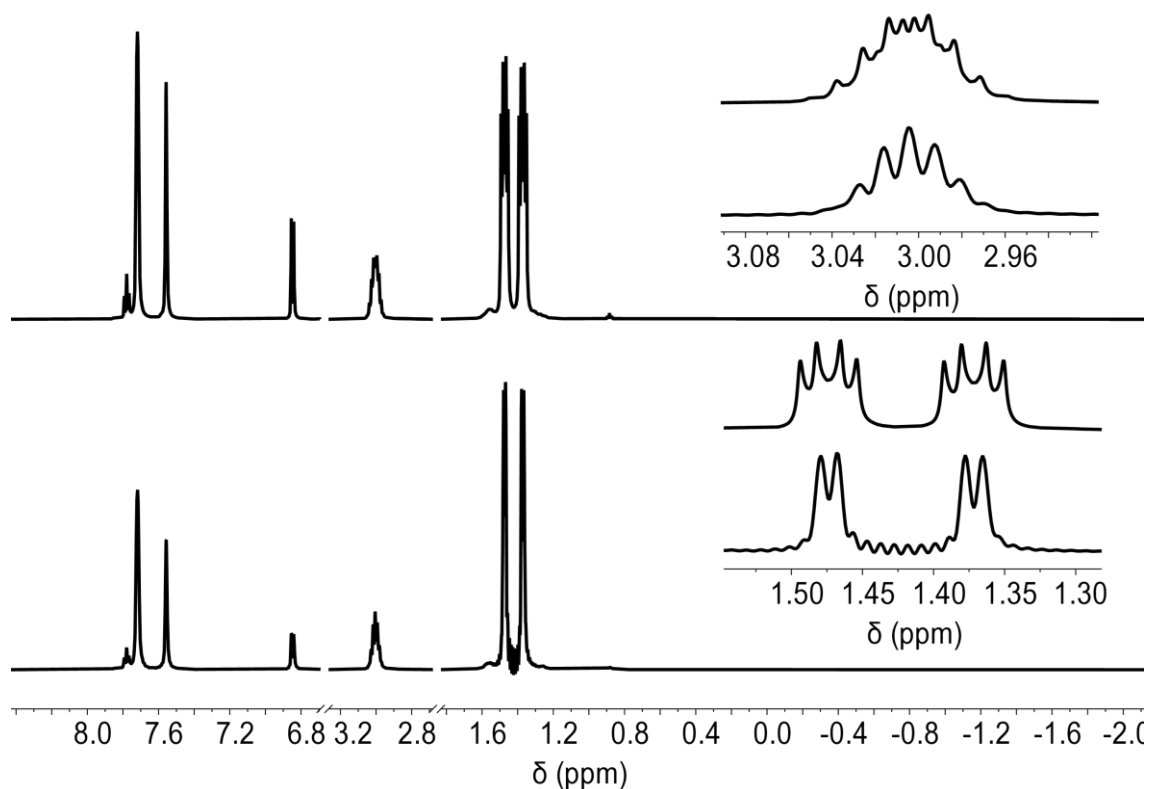
Figure 2.9: Solution ^{1}H (*top*) and ^{1}H{^{31}P} (*bottom*) NMR (600 MHz, CD$_2$Cl$_2$, 298 K) spectra of **[Mn-CO]**. The insets depict the ^{i}Pr methine resonance (δ_H 3.00) and ^{i}Pr methyl environments (δ_H 1.47 and 1.37).

Solid-state ^{31}P{^{1}H} CP MAS NMR spectroscopy (10 kHz spin-rate, 298 K) of **[Mn-CO]** further highlights the ^{31}P-^{55}Mn quadrupolar coupling. This spectrum would be expected to show two resonances due to the crystallographically independent ^{31}P environments. However, at least seven resonances are observed (δ_P 227.5, 226.1, 224.7, 223.2, 221.8, 220.5, 218.5) due to the *trans* ^{31}P-^{31}P coupling, mixed with quadrupolar coupling to the $I = 5/2$ ^{55}Mn nucleus (**Figure 2.10**). The apparent ^{1}J-coupling constants of the *trans*-^{31}P-^{31}P and ^{55}Mn-^{31}P coupling are approximately equal, with coupling constants between $J_{app} \sim 215$ - 300 Hz observed. Similar values

of ^{55}Mn-^{31}P ^{1}J-coupling constants have been reported for *trans*-[MnX(PPh₃)(CO)₄] (X = Ph, Bz), where ^{1}J(MnP) = 245 and 252 Hz.[34, 35]
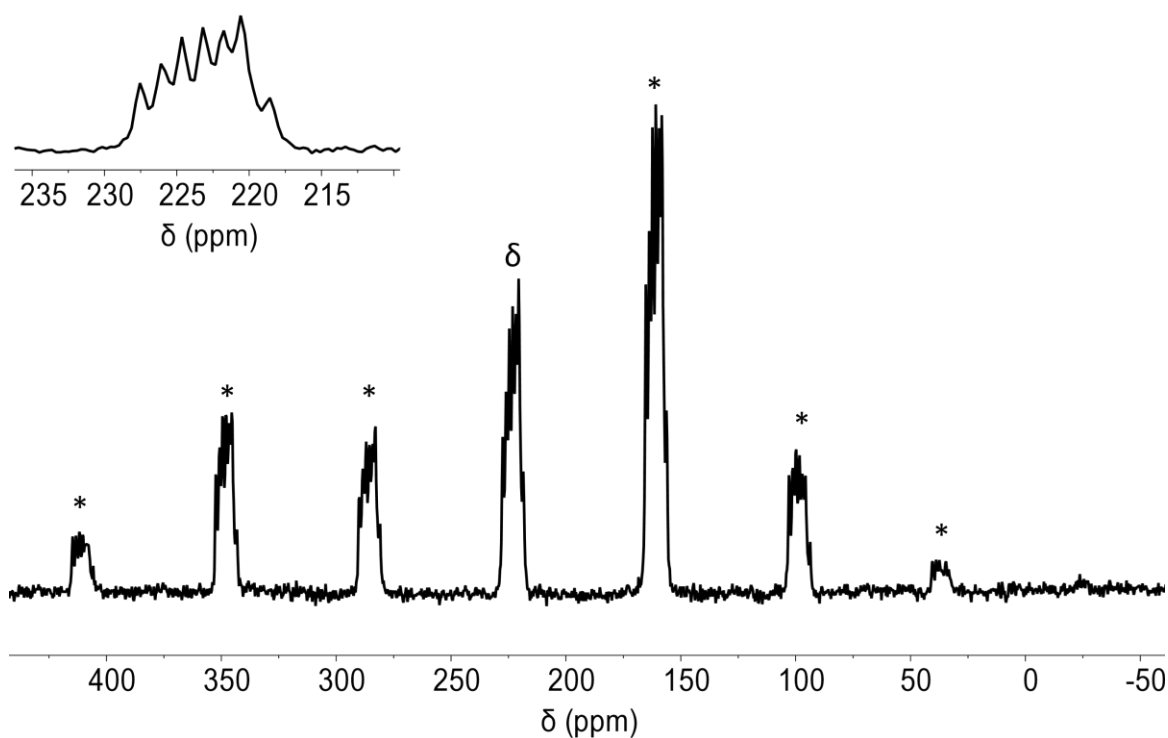
Figure 2.10: Solid-state ^{31}P{^{1}H} CP MAS spectrum of [Mn(ⁱPr-PONOP)(CO)₃][BAr^{F}₄] (162.02 MHz, 10 kHz spin rate, 298 K). Inset depicts fine coupling of isotropic chemical shift. δ denotes isotropic chemical shift. * denotes spinning side bands.

The solid-state ^{13}C{^{1}H} CP MAS NMR spectrum for this compound is devoid of resonances indicative of metal-bound carbonyl ligands, which resonate at δ$_C$ 217.2 and 213.3 in the solution ^{13}C{^{1}H} NMR spectrum. Carbonyl resonances are typically low intensity due to their quaternary nature removing the potential for nuclear spin polarisation transfer (Nuclear Overhauser Effect) from nearby proton relaxation. These peaks are further broadened beyond detection[36, 37] in this sample due to

quadrupole coupling to ^{55}Mn, as well as coupling to the crystallographically inequivalent ^{31}P environments.

2.2biii. Chemical Shift Anisotropy and Chemical Shift Tensor Analysis of [Mn-CO]

The spinning side band intensity in the solid-state ^{31}P{^{1}H} CP MAS NMR spectrum (**Figure 2.10**) indicates a large magnitude and direction of asymmetry of the chemical shift tensors, known as the skew (κ) of the chemical shift tensors [$\kappa = 3(\delta_{22}-\delta_{iso})/\Omega$, where $\Omega = \delta_{11}-\delta_{33}$].[38, 39] The chemical shift tensors were quantified by experiment and theory by computational NMR calculations [PBE0/SDD(Mn)/6-31G** (C, H, O, P, N)]. The experimental spectrum linewidth was broadened to 500 Hz to reduce ^1J(MnP) contributions to the resonances (**Figure 2.11**). The computational NMR calculations were run on a DFT-optimised structure of isolated {Mn(^{i}Pr-PONOP)(CO)$_3$}$^+$. Replicating accurate ^{31}P NMR shieldings and chemical shifts by computation is challenging due to the wide chemical shift range which can span 2000 ppm, so differential from experiment of ≤ 10% has been deemed to be 'excellent.'[40, 41] Given this, the NMR calculations compare very well with the experimental values (**Table 2.2**).

Table 2.2: Experimental and calculated chemical shift tensors for {Mn(^{i}Pr-PONOP)(CO)$_3$}$^+$.

	δ_{iso}	δ_{11}	δ_{22}	δ_{33}	κ	Ω
Experimental	222	429	144	93	-0.70	336
Theory	241	486	151	87	-0.68	400
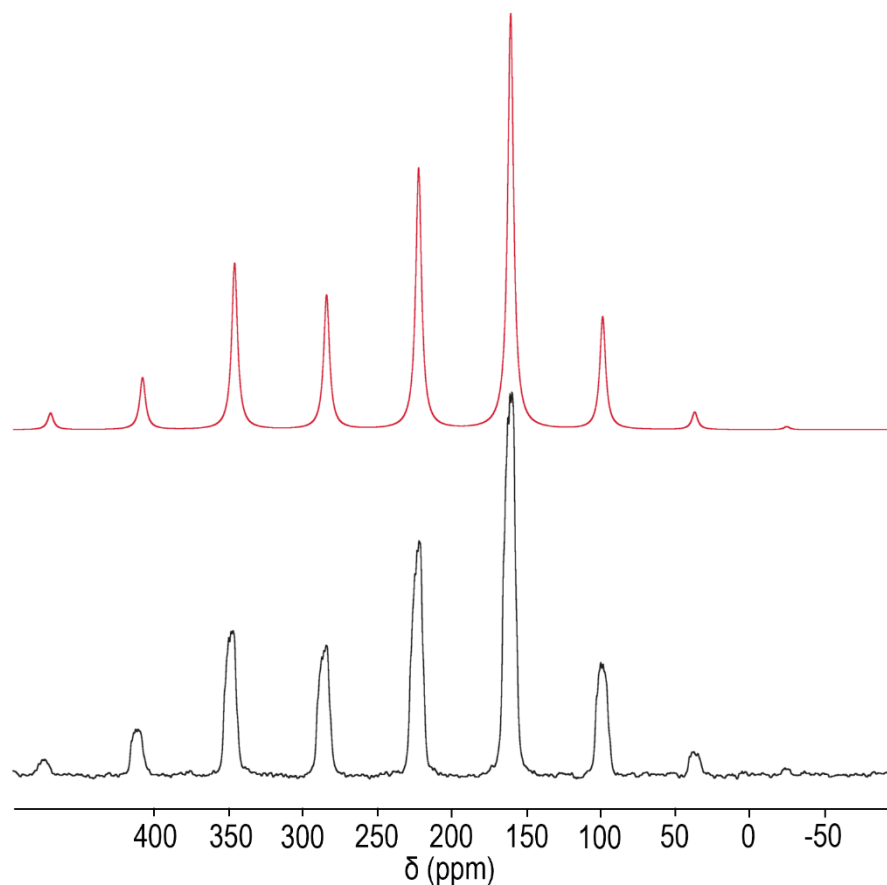
Figure 2.11: Simulated (*top*, red) and experimental (*bottom*, black, with 500 Hz line broadening) solid-state $^{31}P\{^{1}H\}$ CP MAS NMR spectra of $\{Mn(^{i}Pr-PONOP)(CO)_3\}^{+}$ used for quantification of the chemical shift tensors.

The transitions contributing to this were also calculated [PBE0/Mn(TZ2P)/P(DZP)/C,H,O,N(DZ)], with the major contributor ($\hat{L}_{11}$) to the δ_{11} tensor was found to be the coupling between the orthogonal $\sigma(Mn–P)$ and $\sigma^{*}(P–O)$ bonds (**Figure 2.12**). The degree of coupling between the orthogonal orbitals can be quantified by **Equation 2.1**, below.

$$\hat{L}_{11} = \frac{\langle \Psi_{vac}|L_i|\Psi_{occ}\rangle \langle \Psi_{vac}\left|\frac{L_i}{r^3}\right|\Psi_{occ}\rangle}{\Delta E_{vac-occ}}$$

Equation 2.1: Relationship of the integral overlap between two orthogonal orbitals, $\langle \Psi_{vac}|L_i|\Psi_{occ}\rangle \langle \Psi_{vac}\left|\frac{L_i}{r^3}\right|\Psi_{occ}\rangle$, their energy difference, $\Delta E_{vac-occ}$, and the degree of coupling between them, $\hat{L}_{11}$.
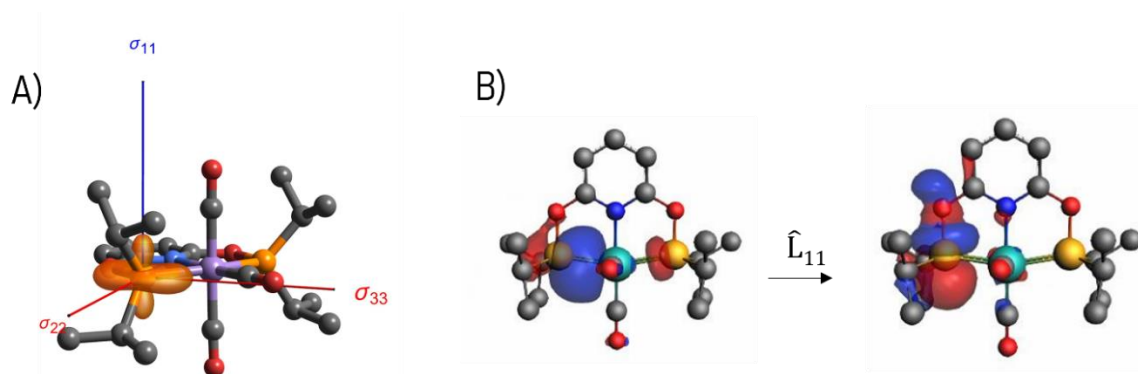
Figure 2.12: A) Orientation of the δ_{11} chemical shift tensor in {Mn(iPr-PONOP)(CO)$_3$}$^+$. B) The orthogonal coupling orbitals responsible for the highest contribution to the δ_{11} chemical shift tensor. *Left*: σ(Mn–P). *Right*: σ*(P–O).

The strong coupling between the orthogonal σ(Mn–P) and σ*(P–O) orbitals is therefore found to be the cause of the asymmetry of the ^{31}P chemical shift tensors of **[Mn-CO]**. This may be due to the integral overlap of these orbitals being significantly larger than that of the δ_{22} and δ_{33}, or, more likely, due to the small energy difference between σ(Mn–P) and σ*(P–O).

2.2biv. Single-Crystal X-Ray Diffraction Analysis of [Mn-CO]

Colourless crystals of **[Mn-CO]** suitable for single-crystal X-Ray diffraction analysis were grown from layering a CH_2Cl_2 solution with pentane at room temperature. The single-crystal X-Ray structure of **[Mn-CO]** collected at 150 K reveals the complex crystallises in the triclinic space group, $P\bar{1}$, where two cationic complexes are encapsulated by ten anions which occupy the bicapped square prismatic arrangement (**Figure 2.13**).
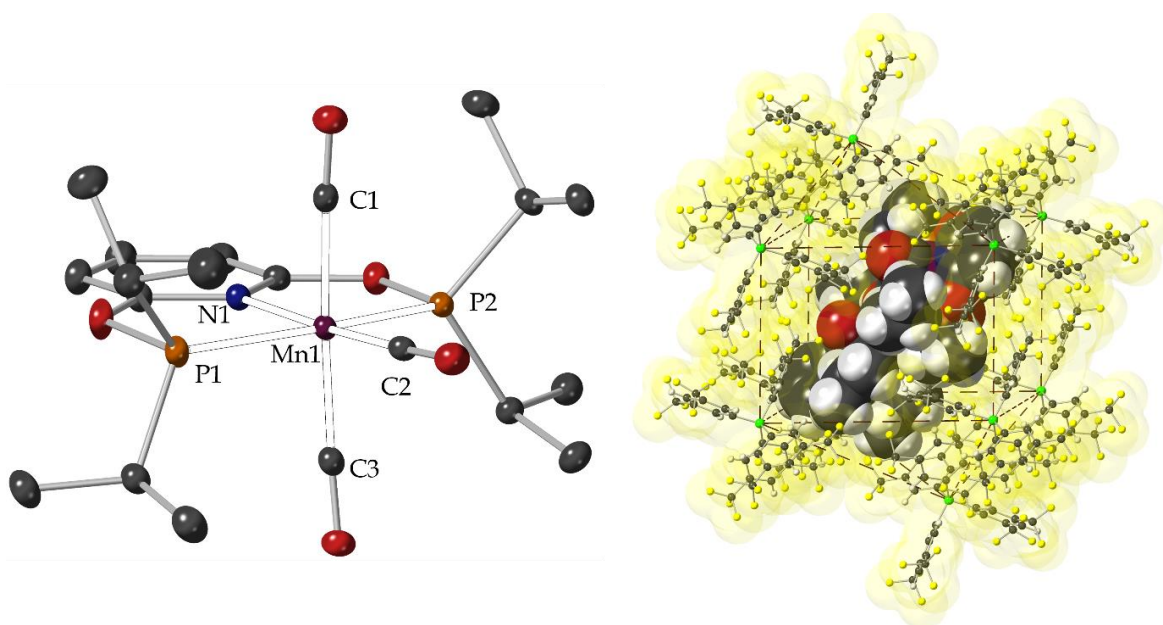
Figure 2.13: *Left*: Single-crystal X-Ray structure of isolated cation of **[Mn-CO]**. Hydrogen atoms omitted for clarity. Thermal displacement ellipsoids displayed at 50%. Selected bond lengths and angles: Mn1-P1 = 2.2505(7) Å; Mn1-P2 = 2.2492(9) Å; Mn1-C1 = 1.8588(19) Å; Mn1-C2 = 1.800(3) Å; Mn1-C3 = 1.8483(19) Å; Mn1-N1 = 2.047(2) Å; P1-Mn1-P2 = 160.50(3)°; C1-Mn1-C3 = 173.99(12)°. *Right*: Packing of [BAr$^F_4$]$^-$ anions around cations in **[Mn-CO]**, forming a bicapped square prismatic arrangement. The anions are mapped with a van der Waals surface (yellow).

The Mn–P bond lengths are crystallographically identical [Mn1-P1 = 2.2505(7) Å, Mn1-P2 = 2.2492(9) Å], as are the axial Mn–C bond lengths [Mn1-C1 = 1.8588(19) Å, Mn1-C3 = 1.8483(19) Å]. The equatorial Mn–C bond is shorter than the axial bonds [Mn1-C2 = 1.800(3) Å] reflecting the weaker *trans* influence of the pyridyl group compared to carbonyl. The axial and equatorial C–O bond lengths are crystallographically identical [C1-O1 = 1.135(2) Å; C2-O2 = 1.148(3) Å; C3-O3 = 1.142(2) Å], therefore detailed interpretation on the reduction in C-O bond order based on the *trans* ligand is not valid from the SC-XRD data. The axial carbonyl ligands are slightly tilted away from parallel [C1-Mn1-C3 angle = 173.99(12)°], pushed forwards from the pyridyl backbone of the ligand.

The donating and accepting properties of the PONOP ligand can be compared to the PNNNP [2,6-(^{i}Pr$_2$PNH)C$_6$H$_3$N] ligand, through the solid-state structure of the cationic species, [Mn(^{i}Pr-PNNNP)(CO)$_3$]Br (**Figures 2.14** and **2.15**), reported by Boncella and co-workers.[29] For this complex, the Mn–P bond lengths are slightly longer, at 2.2626(11) Å. The axial Mn–C bond lengths are 1.851(7) and 1.852(7) Å and the equatorial Mn–C bond length is 1.808(4) Å. The C–O bond lengths are very similar to **[Mn-CO]**, but slightly shortened [C1-O1 = 1.124(10) Å; C2-O2 = 1.134(6) Å; C3-O3 = 1.135(9) Å]. From these data we can suggest that PNNNP and PONOP are likely similar in their σ-donating properties, but PONOP is a stronger π-acceptor. This is also reflected in the ATR IR data for [Mn(^{i}Pr-PONOP)(CO)$_3$]Br, where the CO stretching frequencies are significantly red-shifted (PNNNP v_{CO} = 1996 – 1826 cm^{-1}; PONOP v_{CO} = 2055, 1970 cm^{-1}), implying reduction in C–O bond order compared to **[Mn-CO]**.
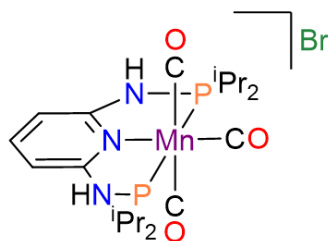
Figure 2.14: Chemical structure of the cationic pincer complex, [Mn(^{i}Pr-PNNNP)(CO)$_3$]Br, reported by Boncella and co-workers.[29]
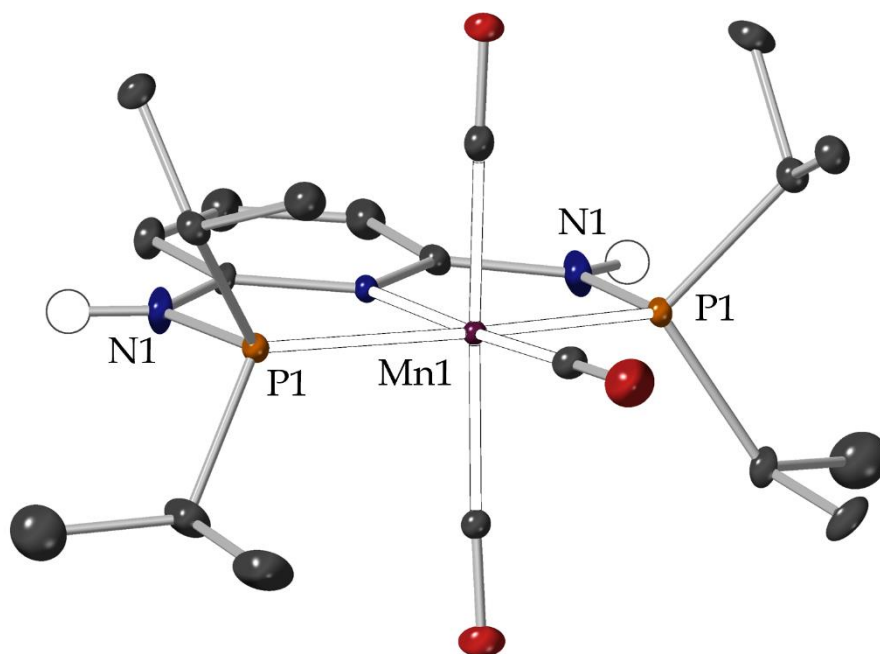
Figure 2.15: Solid-state structure of the cationic component of [Mn(^{i}Pr-PNNNP)(CO)$_3$]Br, reported by Boncella and co-workers.[29] The complex lies on a crystallographic two-fold position, such that both phosphorus atoms and nitrogen atoms are symmetry-related.

2.2bv. Solid-State Photochemistry of [Mn-CO]

As discussed in **Chapter 1.6.2**, the Champness and George groups have investigated the solid-state photochemistry of manganese and rhenium halide carbonyl complexes [MX(diimine*)(CO)$_3$] (M = Mn or Re; X = Cl or Br; diimine* =

5,5'-dicarboxylate-2,2'-bipyridine) supported in a close-packed MOF.[26] Isomerisation from the *fac-* to *mer-* isomers was observed by FTIR and SC-XRD (**Figure 1.13**). Further to this, the Champness and Sumby groups have published further photochemistry of [MnBr(bis-pyazole)(CO)$_3$] supported in a porous, open-packed MOF where carbonyl loss, followed by coordination of THF from the solvent channels of the MOF was observed (**Figure 1.13**).[27]

Inspired by these reports, it was proposed that **[Mn-CO]** would be photochemically active in the solid-state, potentially providing an electronically- and coordinatively-unsaturated species, [Mn(iPr-PONOP)(CO)$_2$][BAr$^F_4$] (**Scheme 2.4**). To assess whether electronic transitions associated with population of an Mn–CO non-bonding or anti-bonding orbital were accessible through UV-excitation, time-dependent DFT [TD-DFT; PBE0/def2-TZVPP/def-ecf(Mn)] calculations were performed on a geometry optimised [BP86/def-SV(P)/def-ecp(Mn)] isolated cation of **[Mn-CO]**. A transition was found at 356 nm, with 73% of the wavefunction corresponding to an excitation from the HOMO -3 (d_{yz}) to the LUMO which is a non-bonding combination of the Mn d_{z^2} orbital and the C–O π*-antibonding orbital (**Figure 2.16**).
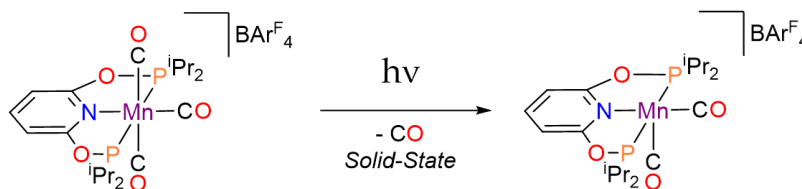
Scheme 2.4: Proposed reaction scheme of photo-induced carbonyl ligand loss in the solid-state from **[Mn-CO]** to yield an electronically- and coordinatively-unsaturated complex.

HOMO -3   *LUMO*
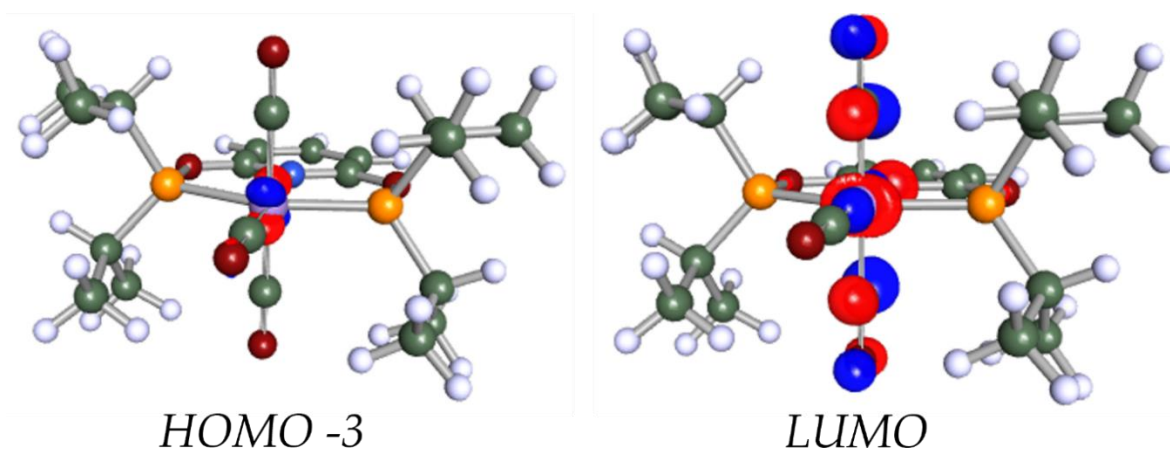
Figure 2.16: Time-dependent DFT calculated orbitals involved in the electronic transition associated with an absorption at 356 nm. The ground-state is dominated by the HOMO -3 (*left*) which is mostly a non-bonding d_{yz} orbital. The excited-state is dominated by the LUMO (*right*) which is a non-bonding combination of the d_{z2} orbital with CO π*-character.

Despite the reports by Champness, Sumby and George, and the promising TD-DFT data, no photochemical reactivity (365 nm LED) was observed in the solid-state for **[Mn-CO]** under a range of conditions: *in vacuo* ($< 1 \times 10^{-2}$ mbar), ethylene, propylene, butene, isobutylene, nitrous oxide, dihydrogen or dinitrogen atmospheres. The difference in photochemistry between this study and the published studies from Champness and Sumby is likely due to the local solid-state environment of the organometallic fragments. Degenerate isomerisation of **[Mn-CO]** would be undetectable if the reactivity were reminiscent of the close-packed MOF example, and the porosity of the open-packed MOF structure gives space for the photoejected carbonyl ligand to diffuse away from the metal fragment without recombination, which is non-trivial in a non-porous molecular solid such as **[Mn-CO]**.

2.2c. Synthesis and Characterisation of [Mn(*iPr*-PONOP)(THF)(CO)$_2$][BAr$^F_4$] •½hexane

2.2ci. Synthesis and Spectroscopic Data

Due to the lack of photoactivity of **[Mn-CO]** preventing formation of an unsaturated species, a complex which could operate as a 'masked' source of the desired low-coordinate species was designed. A carbonyl ligand was replaced by a THF ligand, which is expected to be weakly bound to a Mn(I) centre, allowing for substitution chemistry to be achieved.

Amine-oxides, such as trimethylamine *N*-oxide (TMAO), are known to react with metal-carbonyl complexes to irreversibly form trimethylamine and CO_2 (**Scheme 2.5**).[42] Therefore, a slight excess (1.05 equiv) of TMAO was added to **[Mn-CO]** in THF solution. After thorough removal of the volatiles *in vacuo*, extraction into THF and recrystallisation by layering with hexane, the desired complex, [Mn(*iPr*-PONOP)(THF)(CO)$_2$][BAr$^F_4$]•½ hexane (**[Mn-THF]**) was obtained as bright orange crystals in 65% yield (**Scheme 2.6**).
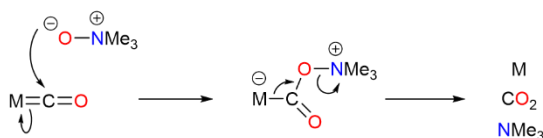
Scheme 2.5: Reaction mechanism of the reaction between trimethylamine *N*-oxide and a metal-carbonyl complex.
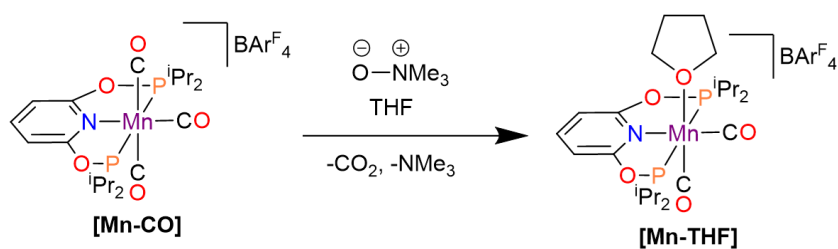
Scheme 2.6: The reaction of **[Mn-CO]** with trimethylamine *N*-oxide in THF solution yields **[Mn-THF]**.

Solution NMR spectroscopic data show that **[Mn-THF]** is fluxional in solution, showing time-averaged C_{2v} symmetry on the NMR timescale at 298 K, as evidenced by a single CO resonance in the solution $^{13}C\{^1H\}$ NMR spectrum (δ_C = 225.7). The solution ^1H NMR (CD$_2$Cl$_2$, 298 K) spectrum of **[Mn-THF]** shows extremely broad and featureless resonances associated with the THF ligand and the ^{i}Pr methine environments (δ_H = 4.0 – 1.5; **Figure 2.17**), which become more resolved at 248 K (**Figure 2.18**). The fluxional behaviour of **[Mn-THF]** is attributed to the de-coordination and recombination of the THF ligand (**Scheme 2.7**), which may be intra- or intermolecular, rather than THF rotation around the Mn–O bond due to the presence of a single well-resolved carbonyl resonance in the solution $^{13}C\{^1H\}$ NMR spectrum. Although, **[Mn-THF]** undergoes slow decomposition in CD$_2$Cl$_2$ to form paramagnetic side products and **[Mn-CO]** through CO scavenging, CD$_2$Cl$_2$ was chosen as the deuterated NMR solvent as all other common deuterated solvents lead to immediate decomposition of the bulk sample. THF-d_8 was not used to ensure resonances associated with the bound THF ligand could be observed.
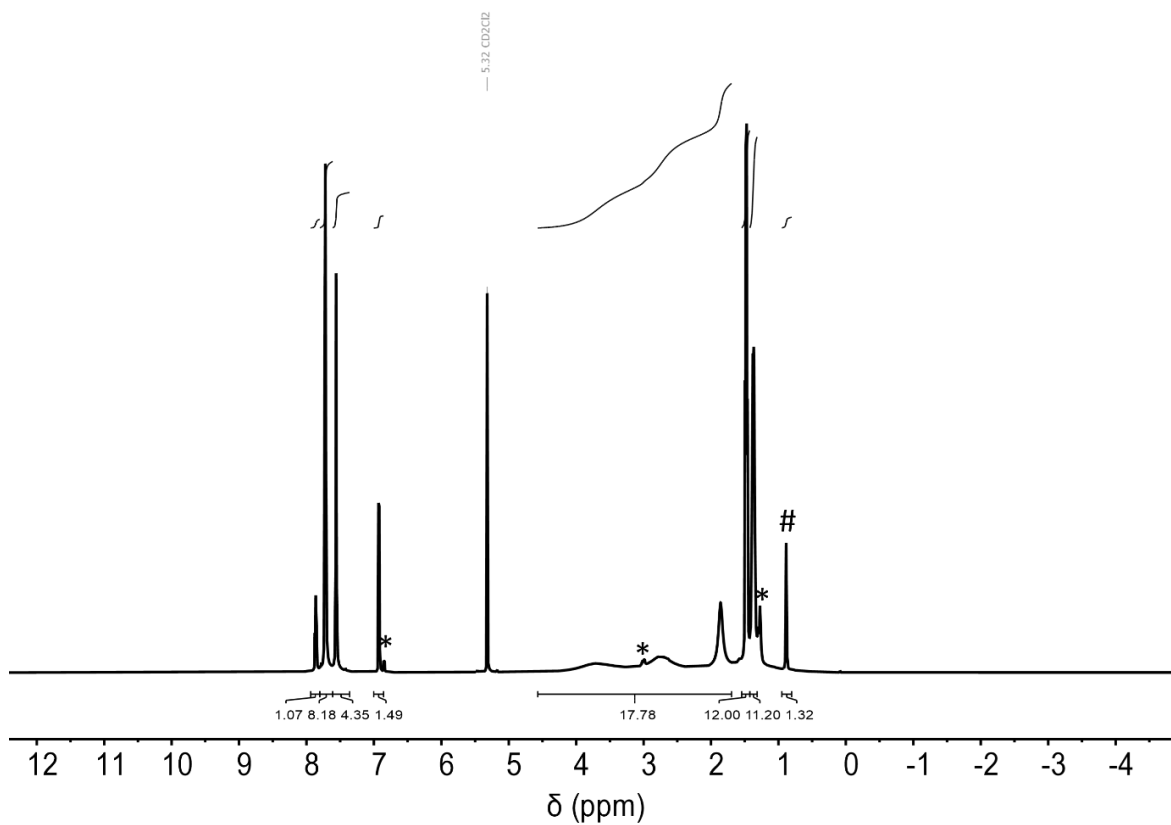
Figure 2.17: Solution ^{1}H NMR (600 MHz, CD$_2$Cl$_2$, 298 K) spectrum of **[Mn-THF]**. * denotes

[Mn-CO] which forms from CO-scavenged decomposition of **[Mn-THF]** in CD$_2$Cl$_2$ solution.

# denotes co-crystallised hexane.
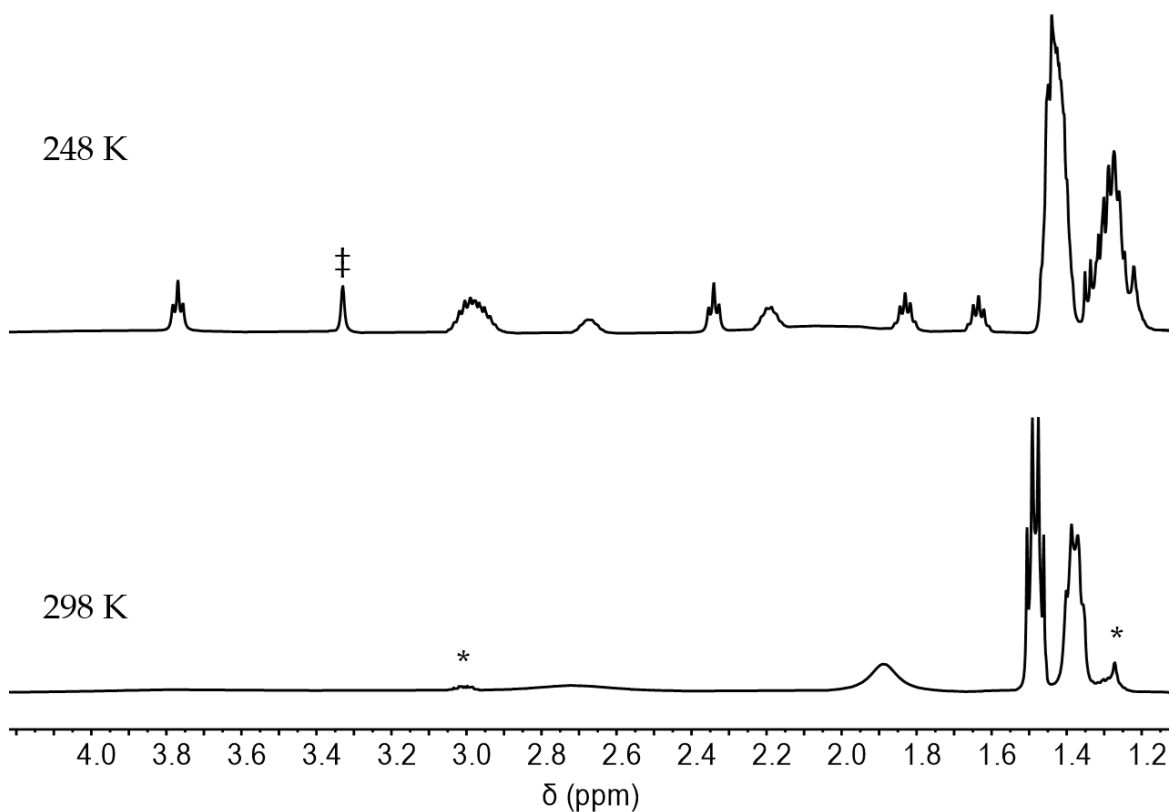
Figure 2.18: Variable temperature ¹H NMR (500 MHz, CD₂Cl₂) spectra of **[Mn-THF]** recorded at 298 K (*bottom*) and 248 K (*top*). In the 248 K spectrum, resonances at δ_H 3.77, 2.34, 1.83 and 1.63 are attributed to the THF ligand, and resonances at δ_H 2.98, 2.66 and 2.19 are attributed to the ⁱPr methine resonances. * denotes **[Mn-CO]** which is formed as a CO-scavenged decomposition product in CD₂Cl₂. ‡ denotes an unknown impurity.
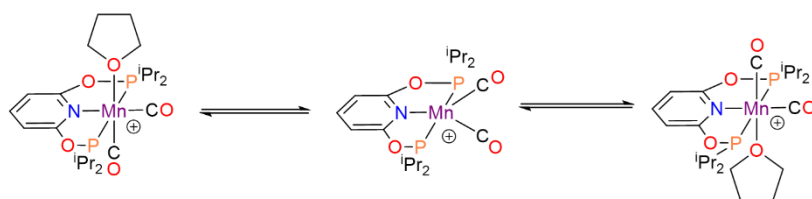
Scheme 2.7: The degenerate isomerisation process of de-coordination and recombination of THF from **[Mn-THF]** which shows time-averaged C_{2v} symmetry on the NMR timescale at 298 K.

The solid-state $^{31}P\{^1H\}$ CP MAS NMR spectrum (10 kHz spin rate, 298 K) of **[Mn-THF]** reveals a broad peak formed of at least four environments (δ_P 234.6, 232.6, 230.8, 227.4) which is best rationalised as two crystallographically independent ^{31}P environments with *trans* ^{31}P-^{31}P coupling (**Figure 2.19**). Due to the reduced local symmetry compared to **[Mn-CO]**, the quadrupolar ^{55}Mn-^{31}P coupling is not clearly resolved. Importantly, the spectrum is devoid of any peaks originating from **[Mn-CO]** showing that the decomposition products observed in the solution NMR spectra are due to reactivity with the solvent and the bulk sample does not contain **[Mn-CO]** starting material or decomposition products in the solid-state.
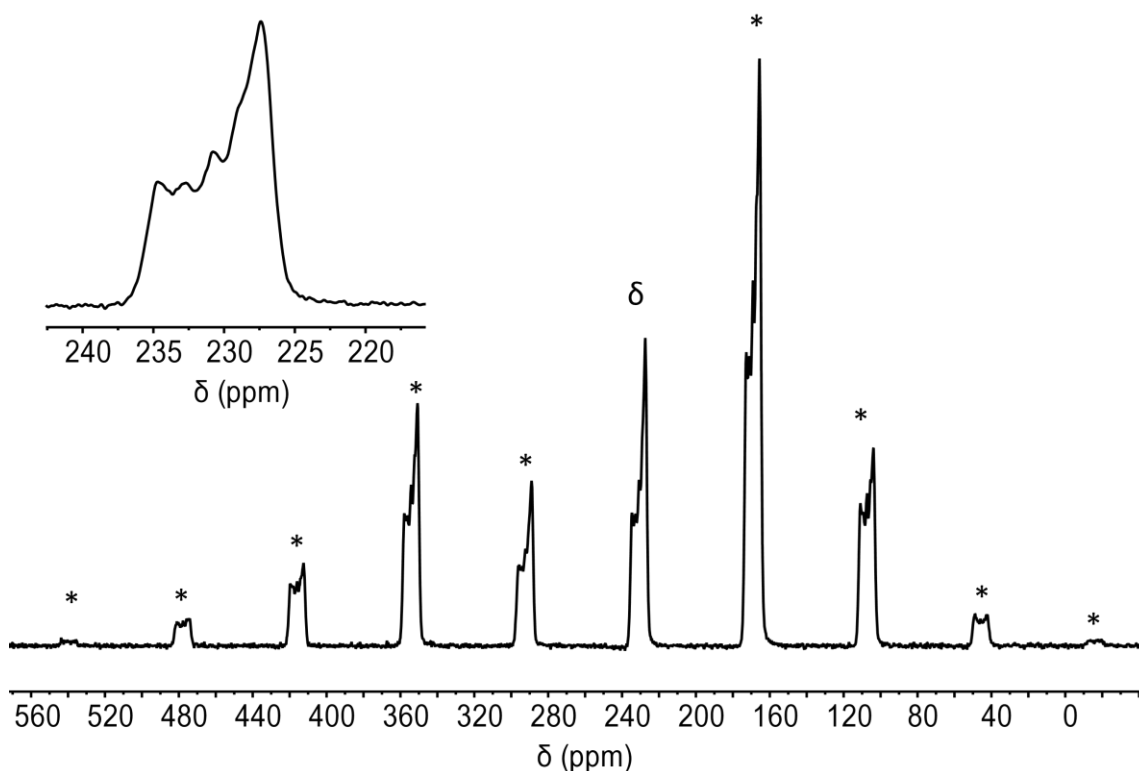
Figure 2.19: Solid-state $^{31}P\{^1H\}$ CP MAS NMR (10 kHz spin rate, 298 K) spectrum of **[Mn-THF]**. Inset depicts the isotropic chemical shift resonance (denoted as δ). * denotes spinning side bands.

The ATR IR (nujol mull) spectrum of **[Mn-THF]** reveals two peaks of approximately equal intensity at v_{CO} 1963 and 1891 cm^{-1} (**Figure 2.20**) for the carbonyl stretching frequencies. The equal intensity of these bands shows that the carbonyl ligands are separated by approximately 90°. The bands are significantly red-shifted with respect to **[Mn-CO]** (*cf.* 2055 and 1970 cm^{-1}) representing the removal of a strongly π-acidic carbonyl ligand, reducing competition for electron density.
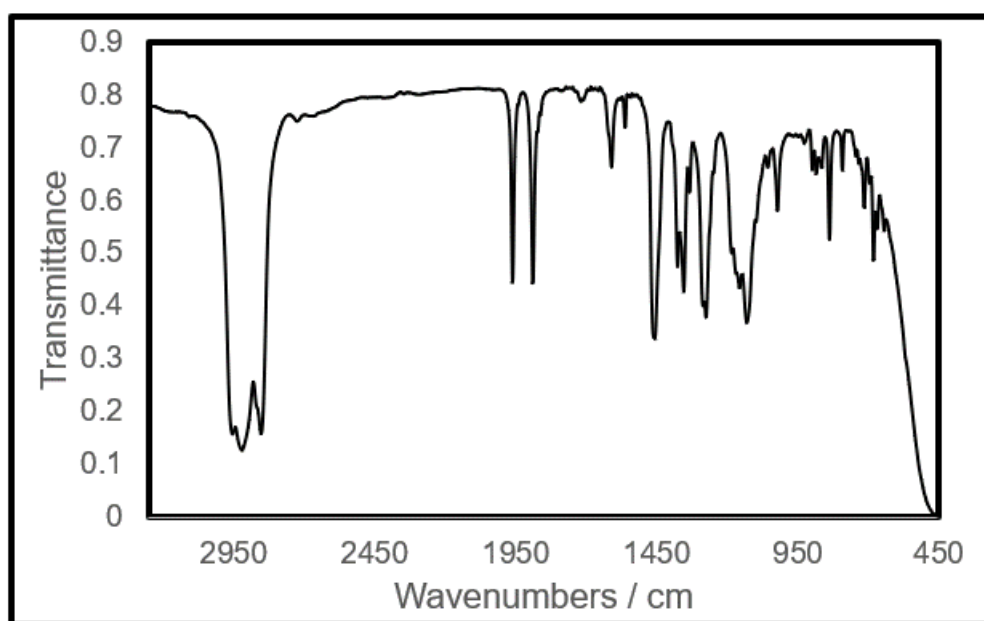
Figure 2.20: ATR IR spectrum of **[Mn-THF]** in a nujol mull. Carbonyl stretching bands are observed at v_{CO} 1963 and 1891 cm^{-1}.

2.2cii. Single-Crystal X-Ray Diffraction Analysis of [Mn-THF]

Bright orange block-like crystals of **[Mn-THF]** suitable for SC-XRD analysis were obtained by layering a THF solution of **[Mn-THF]** with hexane at room temperature. The single-crystal X-Ray diffraction data for **[Mn-THF]** give data for a perfect *pseudo*-merohedrally twinned monoclinic cell (space group $P\,2_1/$n; β = 90°; *a* = 0.5;

where β is the crystallographic angle, and *a* represents the fractional volume of the crystal's minor twin domain, $0 < a \leq 0.5$). A *pseudo*-merohedral twin is a case where a crystal system which should usually not be capable of producing twins, can be twinned due to the unit cell parameters. A monoclinic cell such as $P \ 2_1/n$ can emulate an orthorhombic cell's metric symmetry due to the β angle being very close to, or equal to, 90°. [43, 44]

In the single-crystal X-Ray structure, the THF ligand is found to be *trans* to a carbonyl, as expected based on the strong π-acceptor properties of CO (**Figure 2.21**). As expected based on the ATR IR spectrum (**Section 2.2ci**), the C1-Mn1-C2 angle (carbonyl separation) is 88.0(2)°. Similarly to **[Mn-CO]**, two cations are found within a bicapped square prismatic arrangement of ten $[BAr^F_4]^-$ anions (**Figure 2.21**).
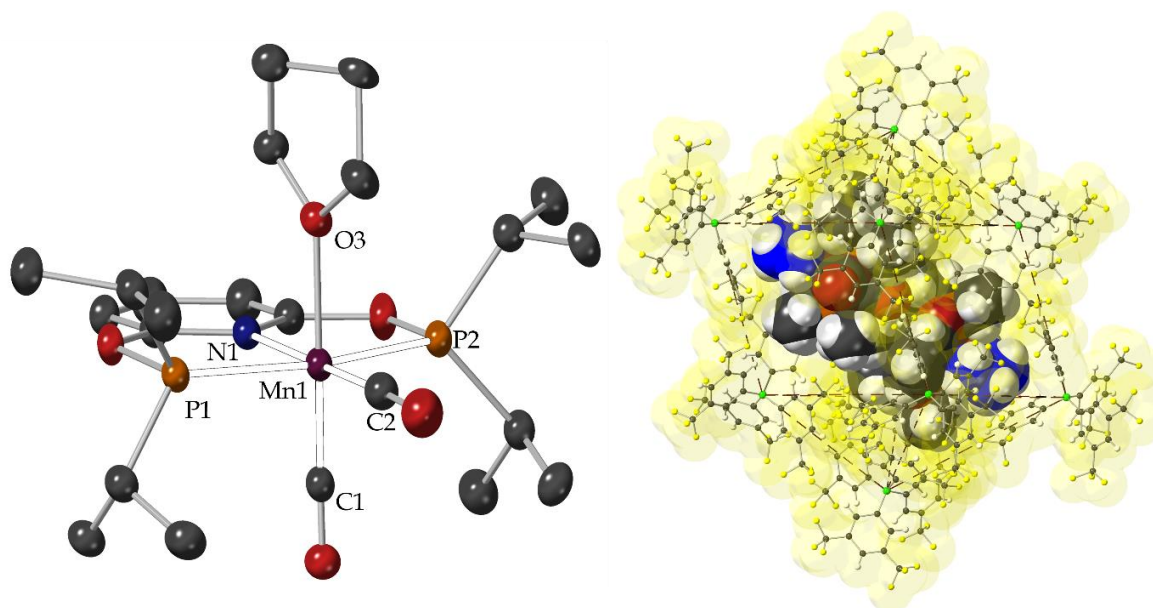
Figure 2.21: *Left*: Solid-state structure of the cationic component of **[Mn-THF]**. Hydrogen atoms are omitted for clarity. Displacement ellipsoids displayed at 50%. Selected bond lengths and angles: Mn1-P1 = 2.2529(14) Å; Mn1-P2 = 2.2569(14) Å, P1-Mn1-P2 = 162.29(6)°; Mn1-N1 = 2.027(4) Å; Mn1-C1 = 1.781(5) Å; Mn1-C2 = 1.789(5) Å; C1-Mn1-C2 = 88.0(2)°; Mn1-O3 = 2.146(4) Å. *Right*: Approximate bicapped square prismatic arrangement of ten [BAr$^F_4$]$^-$ anions around the cationic organometallic fragment. [BAr$^F_4$]$^-$ anions mapped with van der Waals surface (yellow) and THF ligand is represented in blue for clarity.

The unit cell of **[Mn-THF]** contains 2 equivalents of co-crystallised hexane, which due to the twinned data necessitated isotropic modelling and restraining the geometry with bond length and angle restraints. The THF ligand and co-crystallised hexane are not removed under vacuum (< 1 x 10^{-3} mbar) over 72 hours. The axial and equatorial Mn–CO bond lengths are crystallographically identical [Mn1-C1 = 1.781(5) Å, Mn1-C2 = 1.789(5) Å] reflecting similar *trans* influences of THF *vs* pyridyl, with the THF and axial CO ligand almost co-linear [178.75(16)°]. The

backbone of the THF ligand is disordered over two positions and is located within a cleft formed by aryl groups on the [BAr$^F_4$]$^-$ anion (**Figure 2.22**).
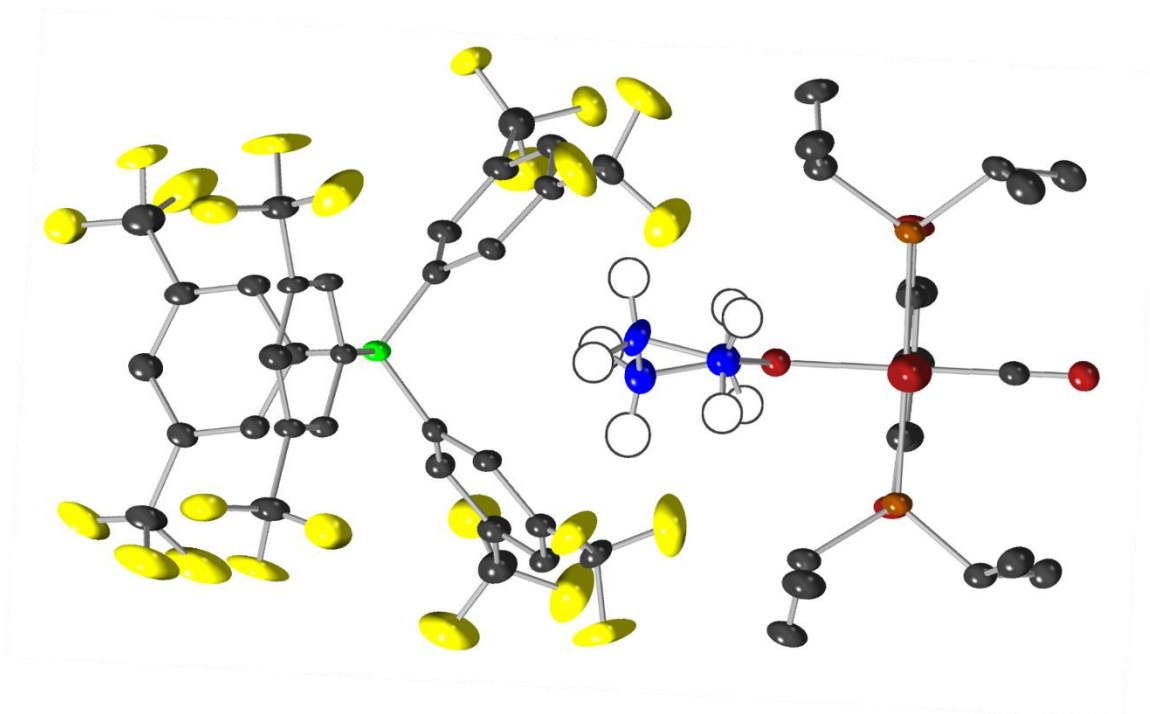
Figure 2.22: The THF ligand of **[Mn-THF]** is located within a cleft of Ar^F groups of a neighbouring [BAr$^F_4$]$^-$ anion in the solid-state. All non-THF hydrogen atoms omitted, and THF carbon atoms are represented in blue, for clarity. Displacement ellipsoids displayed at 50%.

2.2d. Attempted Synthesis of [MnBr(^{t}Bu-PONOP)(CO)$_2$]

In addition to synthesising a 'masked' low coordinate species in the form of **[Mn-THF]**, increasing the steric bulk of the phosphinite R-groups was attempted to produce a species more likely to dissociate CO. The Kirchner group has recently published that the reaction between MnBr(CO)$_5$ and ^{t}Bu-PNNNP [2,6-(^{t}Bu$_2$PNH)C$_5$H$_3$N] yields [Mn(^{t}Bu-PNNNP)(CO)$_2$]Br (**Scheme 2.8**).[45] DFT

calculations revealed that coordination of CO to this electronically- and coordinatively-unsaturated species was endothermic due to the steric bulk of the ^tBu groups.
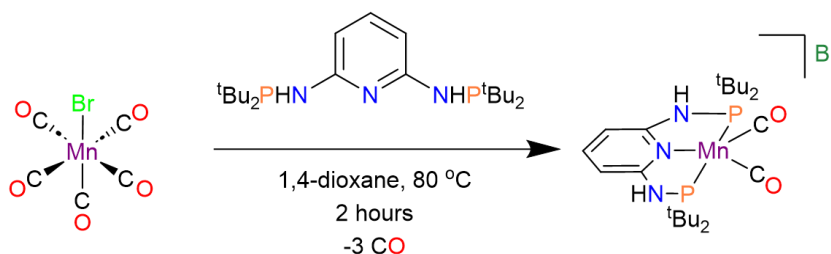
Scheme 2.8: Synthesis of an electronically- and coordinatively-unsaturated Mn(I) complex reported by Kirchner and co-workers.[45]

Owing to this report, ^tBu-PONOP[46] [2,6-($^tBu_2$PO)C$_6$H$_3$N] was combined with with MnBr(CO)$_5$ under a range of experimental conditions. Unfortunately, no repeatable procedure could be realised, and solution NMR spectroscopic studies were hindered by paramagnetic broadening. A small crop of crystals was isolated from one of these attempted syntheses, from which SC-XRD data elucidated [Mn(^tBu-PONOP)(CO)$_2$][MnBr$_3$(THF)] (**Figure 2.23**) as one of the species formed through this reaction. Compared to the Kirchner group's finding, the free bromide anion formed in the reaction of [MnBr(CO)$_5$] and ^tBu-PONOP causes undesirable decomposition, likely representing the weaker P–O bond strength compared to P–N. This decomposition species is similar to that published by the Beller group which was formed as a decomposition product in N-heteroarene hydrogenation by MnBr(CO)$_5$ (**Scheme 2.9**).[47]
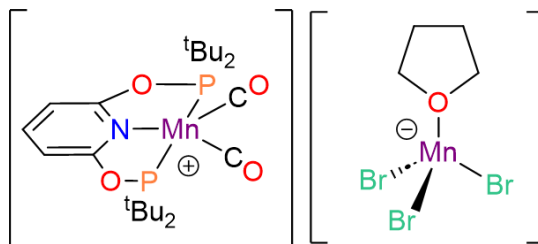
Figure 2.23: Chemical structure of a complex which was observed through reaction of MnBr(CO)$_5$ with ^{t}Bu-PONOP. No repeatable procedure was found for this complex.
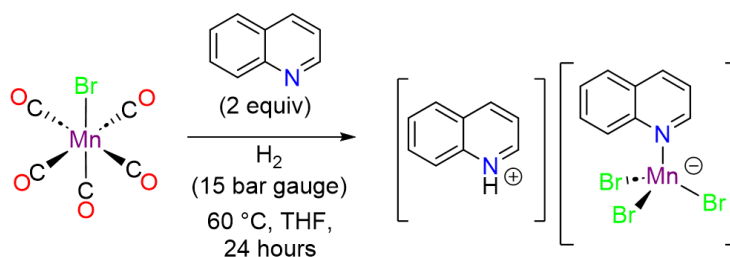
Scheme 2.9: The formation of a Mn(II) anionic decomposition product through stoichiometric hydrogenation of quinoline, reported by Beller.[47]

2.2e. Synthesis of [Re(^{t}Bu-PONOP)(CO)$_2$][BAr$^F_4$]

2.2ei. Synthesis and Spectroscopic Data

The unsuccessful synthesis of [Mn(^{t}Bu-PONOP)(CO)$_2$]Br led to attempts to synthesise the rhenium congener. It was hypothesised that the increased atomic radius from the 3d to 5d metal may facilitate the large steric bulk of the ^{t}Bu-PONOP ligand. Stirring a mixture of ^{t}Bu-PONOP and ReBr(CO)$_5$ in toluene at 95 °C for 18 hours caused a colour change from colourless to bright yellow. The reaction mixture was cooled, dried under vacuum, washed with pentane, and extracted into diethyl ether to give [ReBr(^{t}Bu-PONOP)(CO)$_2$] (**[Re-Br]**, **Scheme 2.10**) as a yellow microcrystalline solid in 70% yield on a gram scale.
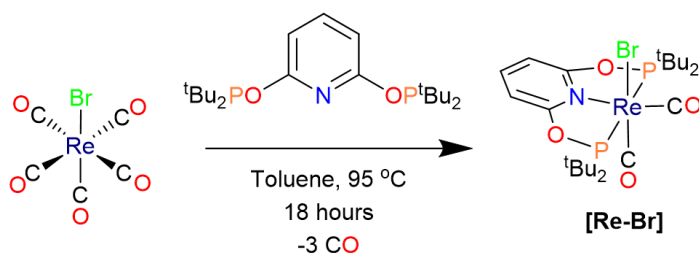
Scheme 2.10: Synthetic route to **[Re-Br]**. Addition of ^tBu-PONOP to ReBr(CO)$_5$ in toluene at 95 °C for 18 hours yields **[Re-Br]** in 70% yield.

The solution ^1H NMR spectrum (C$_6$D$_6$, 298 K) of **[Re-Br]** exhibits C_s symmetry, with two inequivalent ^tBu resonances (δ_H 1.66, 1.32) detected as very strongly coupled virtual triplets which collapse to singlets upon ^{31}P decoupling [δ_H 1.66: $\Sigma\{^3J(PH) + ^5J(PH)\}$ = 15.3 Hz; δ_H 1.32: $\Sigma\{^3J(PH) + ^5J(PH)\}$ = 14.1 Hz]. The solution $^{31}P\{^1H\}$ NMR spectrum reveals a single sharp resonance at δ_P 196.0. The carbonyl resonances are both observed in the solution $^{13}C\{^1H\}$ NMR spectrum as broad signals without distinguishable ^{31}P coupling, at δ_C 206.2 and 198.9.

2.2eii. Single-Crystal X-Ray Diffraction Analysis of [Re-Br]

Crystals of **[Re-Br]** suitable for single-crystal X-Ray diffraction were grown from slow diffusion of pentane into a toluene solution at -30 °C. **[Re-Br]** crystallises in the orthorhombic space group *P* na2$_1$ and the structure reveals a highly distorted octahedral coordination geometry. The bromide ligand is *trans* to a carbonyl but strongly distorted from co-linear [Br1-Re1-C1 = 169.12(16)°] and the pyridyl group is tilted towards the bromide ligand [N1-Re1-Br1 = 82.30(12)°, N1-Re1-C1 = 108.5(2)°, **Figure 2.24**].
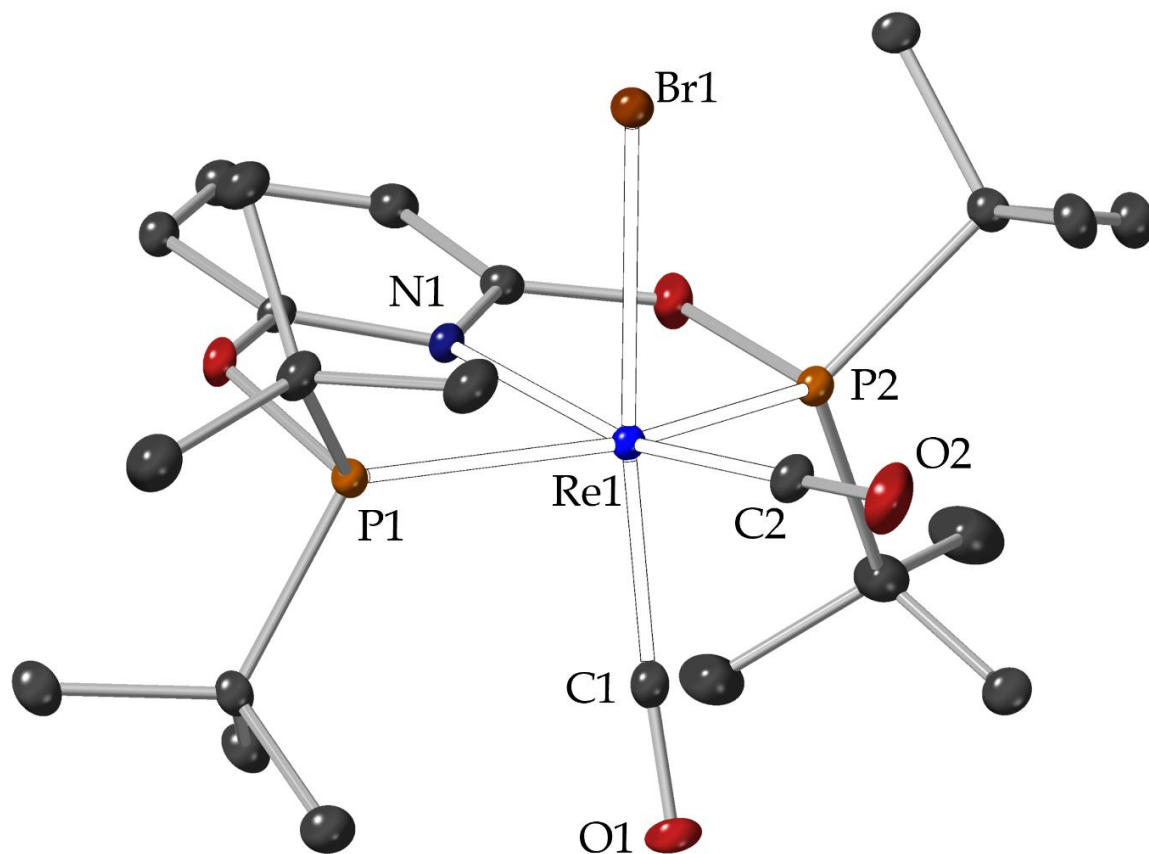
Figure 2.24: Single-crystal structure of **[Re-Br]**. The complex exhibits a strongly distorted octahedral geometry, with a very acute Br–Re–N angle. Hydrogen atoms omitted for clarity. Thermal displacement ellipsoids displayed at 30%. Selected bond lengths and angles: Re1-Br1 = 2.6696(7) Å; Re1-P1 = 2.4036(15) Å; Re1-P2 = 2.4105(16) Å; Re1-C1 = 1.872(5) Å; Re1-C2 = 1.925(6) Å; Re1-N1 = 2.175(5) Å; P1-Re1-P2 = 153.83(5)°; Br1-Re1-N1 = 82.30(12)°; N1-Re1-C1 = 108.5(2)°; C1-Re1-C2 = 84.0(3)°.

2.2f. Synthesis and Characterisation of [Re(*t*Bu-PONOP)(CO)₂][BAr$^F_4$]

2.2fi. Synthesis and Spectroscopic Data

The strongly distorted octahedral geometry of **[Re-Br]** suggested that the steric bulk of the *t*Bu-PONOP ligand scaffold could support a vacant coordination site. **[Re-Br]** was added dropwise to a solution of Na[BAr$^F_4$] in 1,2-$F_2C_6H_4$, causing an immediate colour change from yellow to deep orange/red. The reaction mixture was precipitated with hexane, extracted into CH_2Cl_2, and layered with hexane at room temperature to form bright red block-like crystals of [Re(*t*Bu-PONOP)(CO)₂][BAr$^F_4$] (**[Re]**, **Scheme 2.11**) in 80% yield.
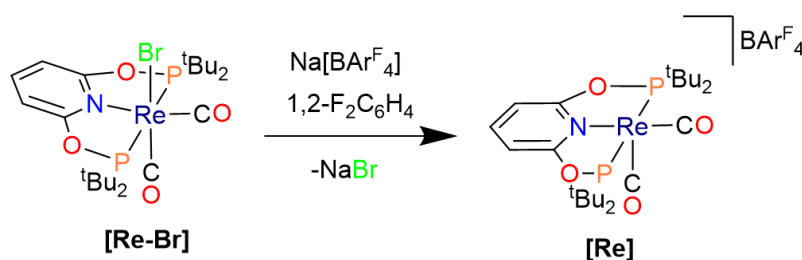
Scheme 2.11: Synthetic route to **[Re]**, by addition of Na[BAr$^F_4$] to **[Re-Br]**.

Only one carbonyl resonance is observed in the solution $^{13}C\{^1H\}$ NMR spectrum [CD_2Cl_2, 298 K, δ_c = 198.8, t, ^2J(PC) = 5 Hz] and one *t*Bu group is observed in the solution ^1H NMR spectrum (δ_H 1.32) as a strongly coupled virtual triplet [$\Sigma\{^3J$(PH) + ^5J(PH)$\}$ = 16.1 Hz] which collapses to a singlet upon ^{31}P decoupling (**Figure 2.25**). The spectra are hence indicative of rapid intramolecular exchange on the NMR timescale to give time-averaged C_{2v} symmetry in solution at 298 K (**Scheme 2.12**).

Infrared spectroscopic data of **[Re]**, both in solution and in the solid-state, show two approximately equal intensity carbonyl stretching bands around 1965 and 1893 cm^{-1} (**Figure 2.26**) which suggests a structure with two inequivalent carbonyl groups separated by ~90°.
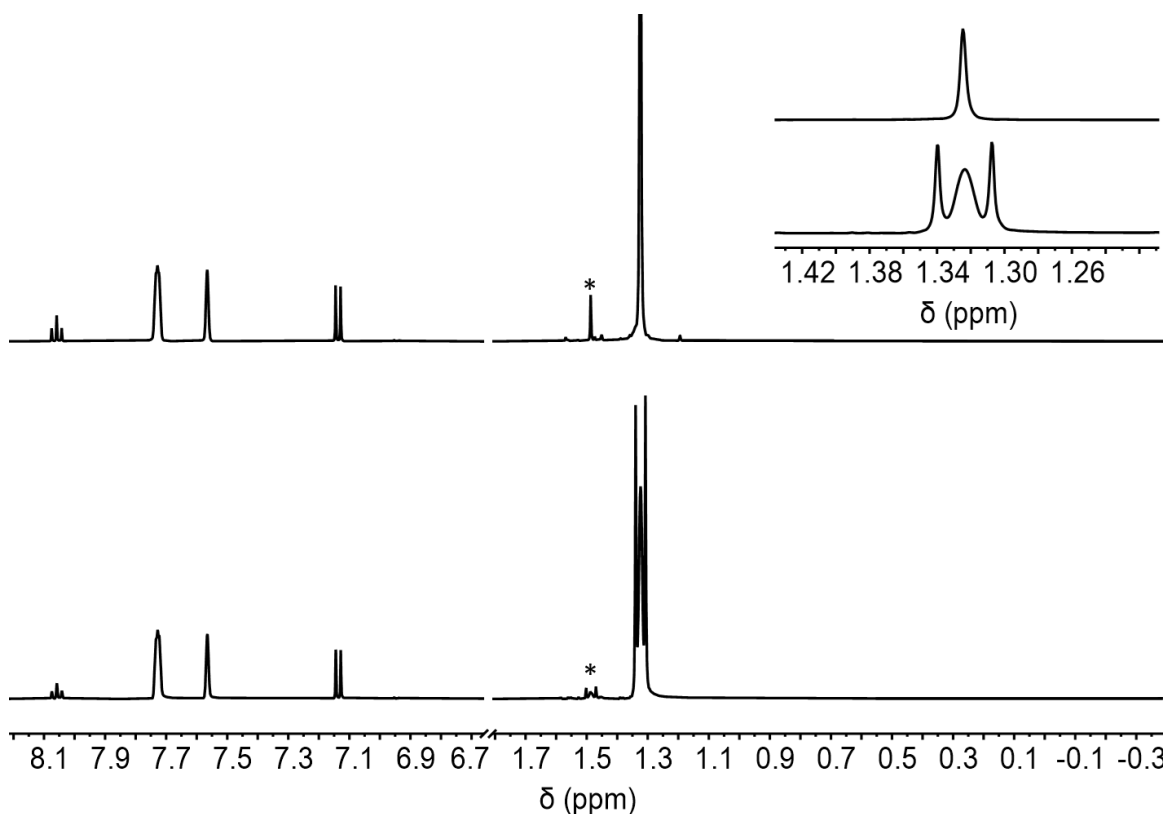
Figure 2.25: Solution ^{1}H (*bottom*) and ^{1}H{^{31}P} (*top*) NMR (500 MHz, CD$_2$Cl$_2$, 298 K) spectra of **[Re]**. The inset depicts the ^{t}Bu methyl resonance (δ_H 1.32). * denotes [Re(^{t}Bu-PONOP)(CO)$_3$][BAr$^F_4$] which forms in solution through CO-scavenged decomposition.
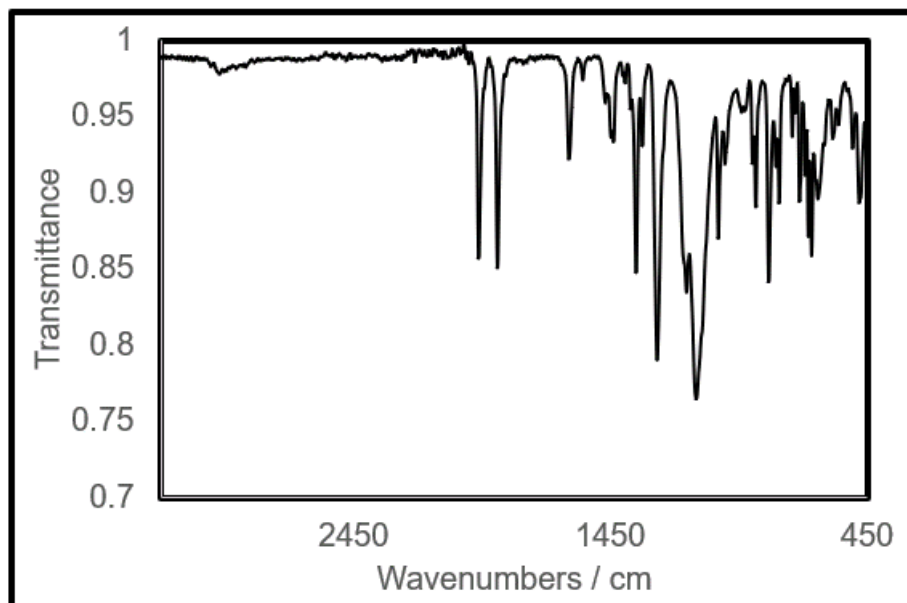
Figure 2.26: ATR IR spectrum of **[Re]**. Carbonyl stretching bands are observed at v_{CO} 1965 and 1893 cm^{-1}.
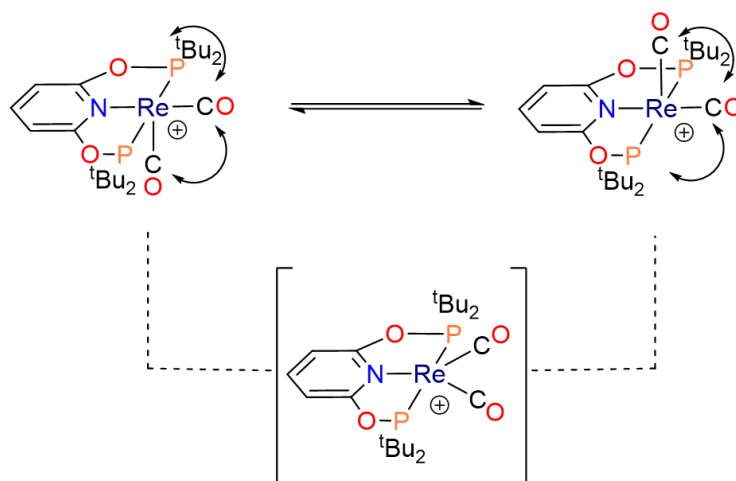
Scheme 2.12: Degenerate isomerisation process of **[Re]** which is rapid on the NMR timescale at 298 K.

2.2fii. Single-Crystal X-Ray Diffraction and DFT Calculations of [Re]

Crystals of **[Re]** suitable for single-crystal X-Ray diffraction experiments were grown by layering a CH_2Cl_2 solution of **[Re]** with hexane at room temperature, to yield bright red, block-like crystals. **[Re]** crystallises in the triclinic space group, $P\bar{1}$. The solid-state structure of the cation reveals a square-based pyramidal structure [τ_5 = 0.26,[48, 49] C1-Re1-C2 = 85.08(16)° at 110 K; **Figure 2.27**]. The *trans*-influence of the pyridyl is displayed by the lengthening of the Re1-C2 bond compared to the Re1-C1 bond which is *trans* to the vacant site [Re1-C1 = 1.863(3) Å *cf.* Re1-C2 = 1.927(4) Å].
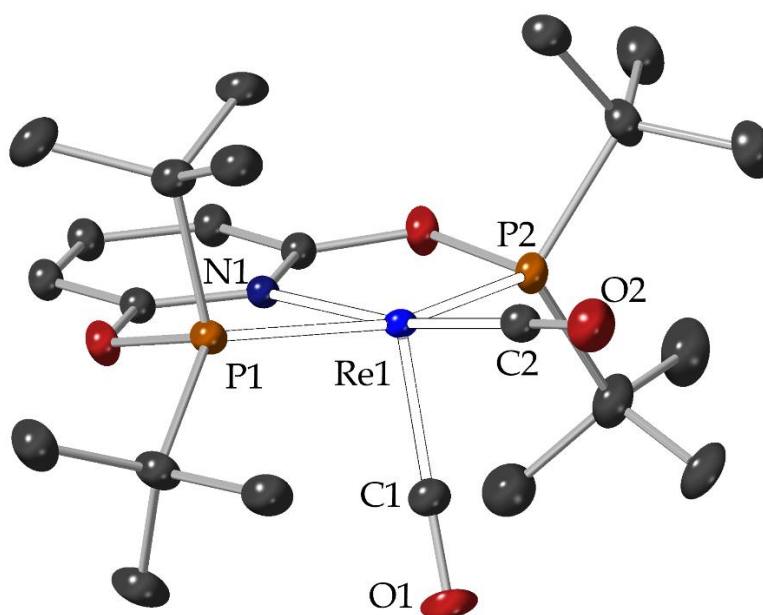
Figure 2.27: Solid-state structure of cationic fragment of **[Re]** collected at 110 K. Hydrogen atoms omitted for clarity and displacement ellipsoids displayed at 50%. Selected bond lengths and angles: Re1-P1 = 2.3845(10) Å; Re1-P2 = 2.3841(9) Å; P1-Re1-P2 = 155.34(4)°; Re1-N1 = 2.150(3) Å; Re1-C1 = 1.863(3) Å; Re1-C2 = 1.927(4) Å; C1-Re1-C2 = 85.08(16)°.

[Re] was investigated with variable temperature SC-XRD studies between 110 K and 298 K. No disorder was found in the carbonyl ligands at 298 K (**Figure 2.28**) showing that the fluxional isomerisation process is not active in the solid-state. The crystallographic, solution NMR and infrared spectroscopic data are supported by computation as (periodic) DFT calculations show that the ground-state structure of **[Re]** is a square-based pyramidal complex which interconverts by a rocking motion. The energy barrier to this rocking transition state is 3.4 kcal mol^{-1} in solution but increases to 19.4 kcal mol^{-1} when calculated within the unit cell of **[Re]**.
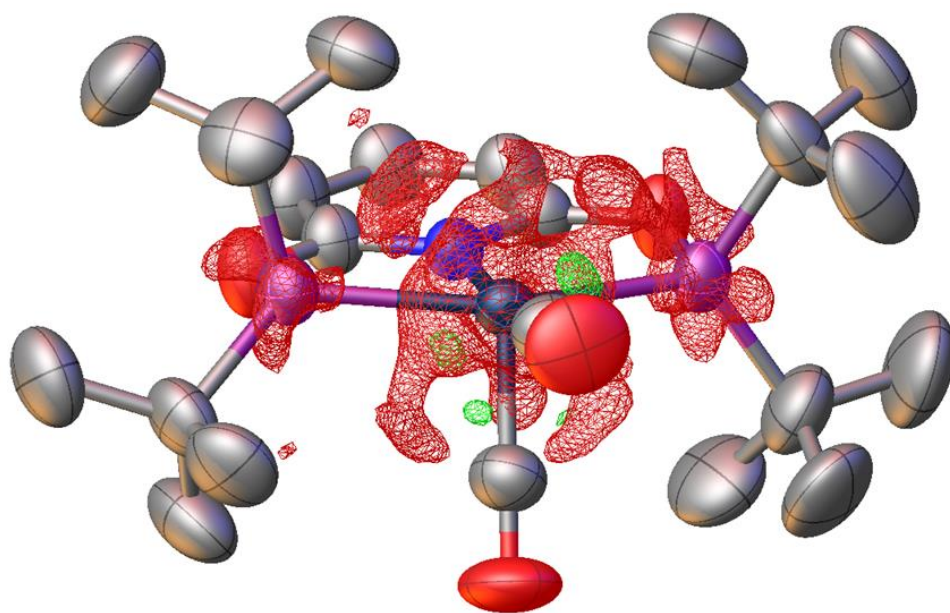
Figure 2.28: Structure of {Re(ᵗBu-PONOP)(CO)$_2$}$^+$ cation as determined by single crystal X-Ray diffraction at 298 K. Hydrogen atoms omitted for clarity. A map of the residual electron density indicates no sign of positional disorder of the carbonyl environments in the solid-state.

Similar to **[Mn-CO]** and **[Mn-THF]**, **[Re]** exhibits a bicapped square prismatic arrangement of ten [BAr$^F_4$]$^-$ around two crystallographically equivalent {Re(^{t}Bu-PONOP)(CO)$_2$}$^+$ cations (**Figure 2.29**). The vacant site of the cation is at the 'surface' of this arrangement of anions, rather than in the centre.
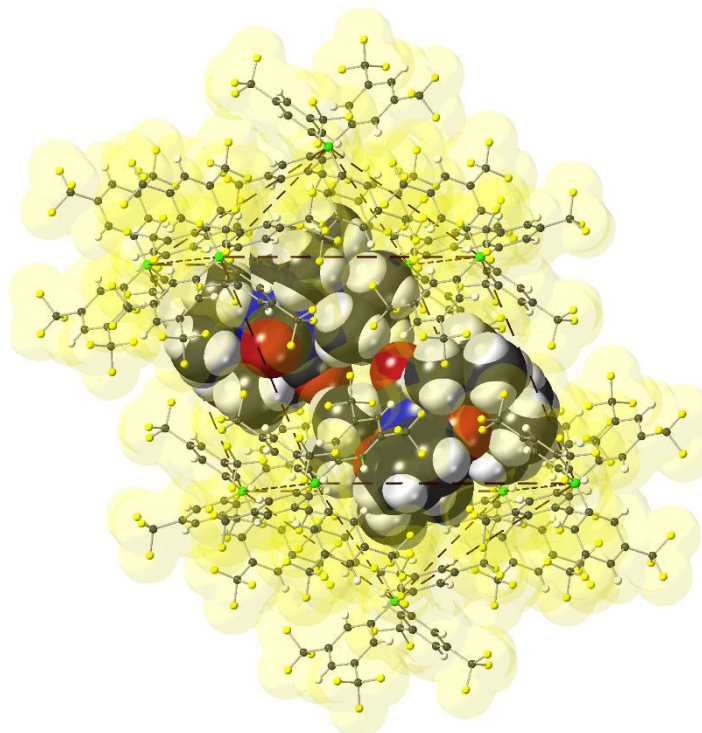
Figure 2.29: Approximately bicapped square prismatic arrangement of ten [BAr$^F_4$]$^-$ anions around two cations found in the solid-state structure of **[Re]**.

Interestingly, the electronically and coordinatively unsaturated rhenium complex has one short Re–C distance [Re1-C22 = 3.122(4) Å] and a compressed Re1-P2-C22 angle compared to the opposite Re1-P1-C7 angle [107.83(13)^o vs 117.49(14)^o; **Figure 2.30**]. This could indicate a C–H agostic interaction[50] present at the vacant site (Re···H distance not directly observed as hydrogen atoms not readily located in X-Ray diffraction data due to the weak scattering power of hydrogen, hydrogen atoms

geometrically placed and allowed to ride on their parent atoms) as has been noted in previous work on close C–H approaches to metal centres.[51] However, the solid-state $^{13}C\{^1H\}$ CP MAS NMR (10 kHz, 298 K) and solution ^1H NMR (CD_2Cl_2, 193 K) spectra are devoid of upfield resonances relative to the ${}^tBu$ methyl groups, which would be expected if an agostic interaction were present.[50, 52, 53] Furthermore, Quantum Theory of Atoms in Molecules (QTAIM)[54, 55] studies could not locate a Re$\cdots$H–C bond path (**Figure 2.31**). DFT geometry optimisation [PBE//def-ecp(Mn/Re)//6-31G**] of the isolated $[Re({}^tBuPONOP)(CO)_2]^+$ cation results in both Re–P–C bond angles becoming equivalent (113.9°) and the Re-C22 distance increasing to 3.43 Å. It is therefore suggested that the contortion of the ${}^tBu$ methyl group towards the rhenium centre is not due to an agostic interaction, but due to steric pressure from the solid-state environment, which has been noted previously.[56]
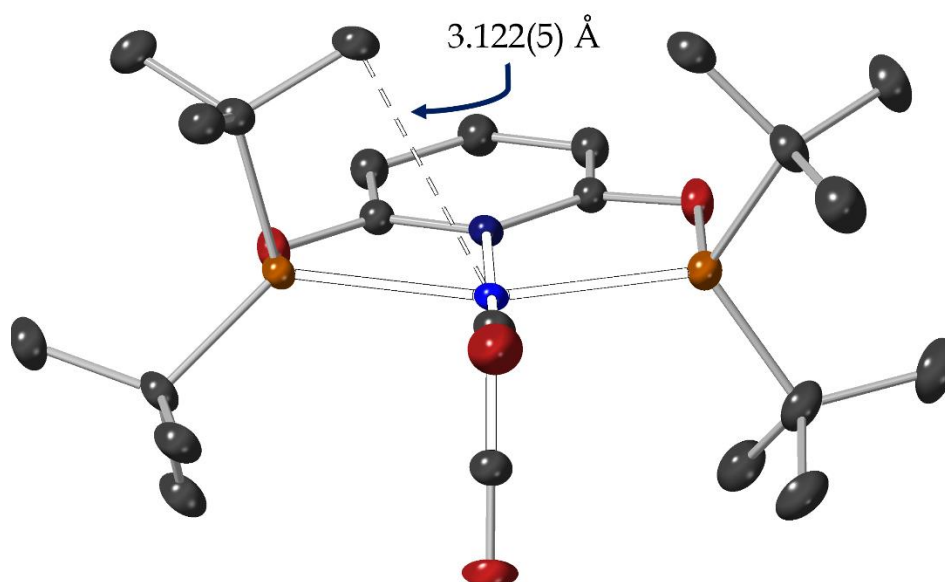
Figure 2.30: The Re–P–C angle is compressed, with one short Re$\cdots$C contact [3.122(5) Å] which could suggest the presence of an agostic interaction.
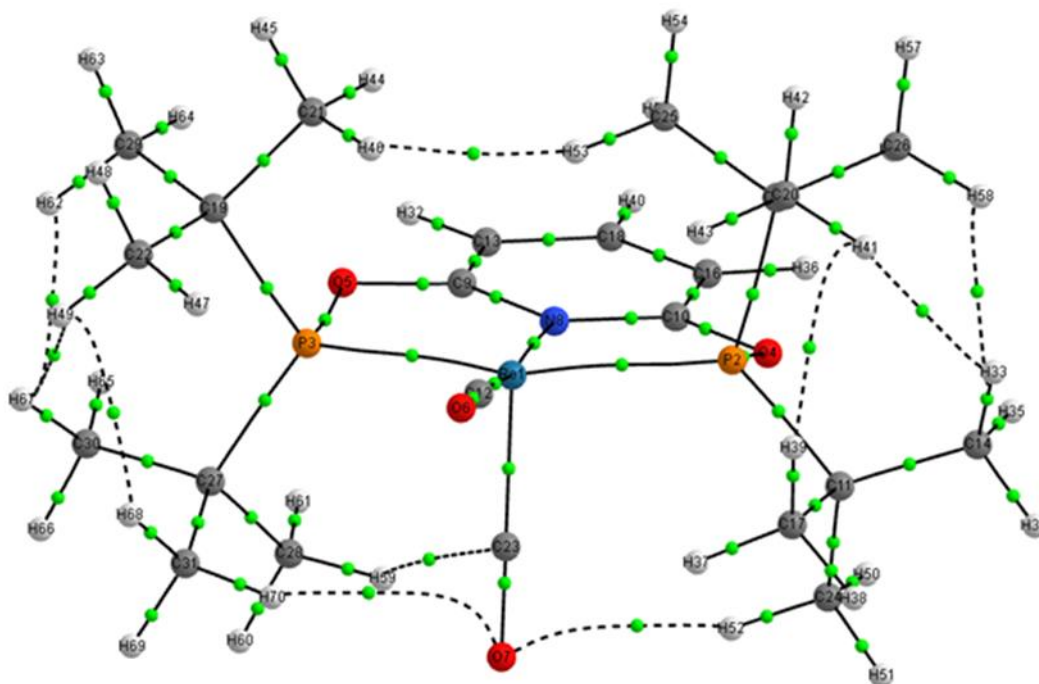
Figure 2.31: Molecular graph for the {Re(^{t}Bu–PONOP)(CO)$_2$}$^+$ cation. Intramolecular non-covalent bond paths are shown with a dotted line, with bond critical points shown in green. Note that atomic labels differ from the rest of the text. QTAIM analysis[54] was employed through the AIMALL program.[57]

2.2fiii. Attempted Synthesis of σ-Dihydrogen Adducts of [Mn-THF] and [Re]

With the wealth of research on the synthesis of σ-dihydrogen adducts of coordinatively unsaturated manganese[58-60] and rhenium complexes[61-65] it was reasoned that dihydrogen should react with **[Mn-THF]** and **[Re]** to yield readily accessible σ-dihydrogen complexes. Treating a solution of **[Re]** in CD$_2$Cl$_2$ with H$_2$ (1 bar gauge, **Scheme 2.13**) lead to no reaction at room temperature as determined by ^{1}H and ^{31}P{^{1}H} solution NMR spectroscopy. Cooling the sample to 193 K enabled observation of a small set of signals (~10% NMR yield) in the ^{1}H solution NMR

spectrum which were consistent with formation of a σ-H_2 adduct: a broad resonance at δ_H -2.85; a new, poorly resolved ^{t}Bu resonance at δ_H 1.39; and a new *meta*-PONOP resonance at δ_H 6.84 (**Figure 2.32**). Additionally, there is a new signal in the ^{31}P{^{1}H} solution NMR spectrum at δ_P 203.0 (*cf.* starting material δ_P 213.2). All the resonances assigned to the σ-H_2 complex were lost when the sample was warmed to 200 K. No reaction of **[Re]** with H_2 was observed in the solid-state as determined by single-crystal X-Ray diffraction.
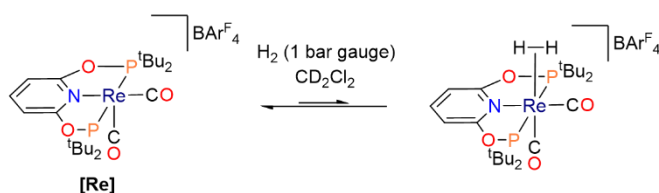
Scheme 2.13: Attempted synthesis of a σ-dihydrogen adduct of **[Re]**. An NMR tube of **[Re]** in CD_2Cl_2 was back-filled with H_2 (1 bar gauge) and analysed by solution NMR spectroscopy. A small conversion (~10%) was achieved at 193 K.
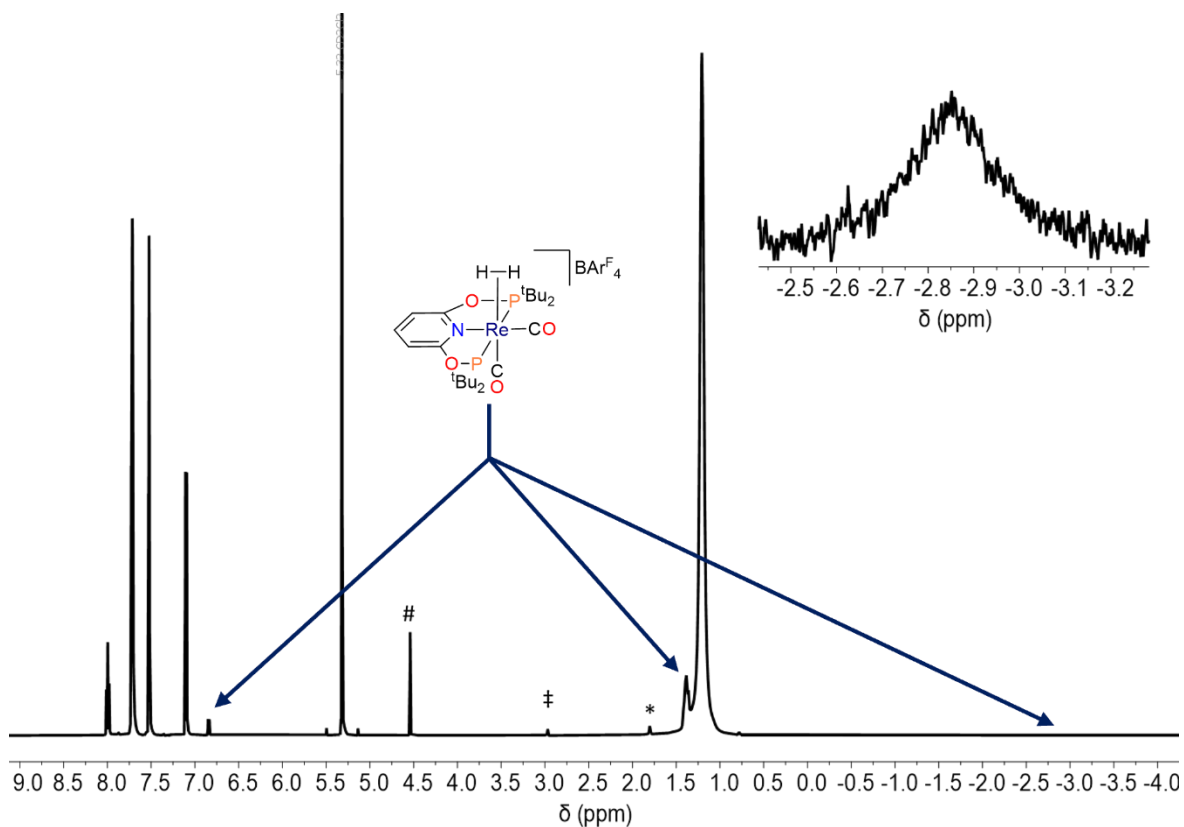
Figure 2.32: ^{1}H solution NMR (500 MHz, 193 K, CD_2Cl_2) of the reaction of **[Re]** with H_2 in CD_2Cl_2. The inset depicts a broad resonance at δ_H -2.85 which is assigned to the σ-H_2 adduct. The *para*-PONOP proton associated with the σ-H_2 complex is coincident with the *ortho*-BAr$^F_4$ resonance. # denotes free H_2, ‡ denotes CD_2HCl which is a solvent impurity and * denotes an unknown impurity.

No reactivity was observed between **[Mn-THF]** and dihydrogen under a range of pressures in solution or in the solid-state. In solution, THF is in a significant excess compared to dissolved H_2 and therefore must outcompete the H_2 for binding at the transient vacant site. In the solid-state, THF may bind more strongly to the manganese centre than H_2, or the activation barrier of decoordination of THF in the

solid-state, followed by THF egress from the crystals, is too high for reactivity to be observed.

2.2g. Lattice Adaptivity Induced by Solid/Gas Reactions of [Mn-THF] and [Re]

2.2gi. Solid-State Reactivity of [Mn-THF] with Carbon Monoxide

Addition of CO (1 bar gauge) to crystalline samples of **[Mn-THF]** (**Scheme 2.14**) causes the material to change in colour from bright yellow to colourless (**Figure 2.33**). It is immediately obvious that the reaction is diffusion controlled as larger crystals react far slower (days to weeks) than finely ground material (28 hours, as determined by solid-state $^{31}P\{^{1}H\}$ CP MAS NMR spectroscopy, *vide infra*). The reaction is a disintegrative solid-state reaction as the crystals are internally shattered, as seen in the scanning electron microscopy (SEM) images before and after CO addition, which show significant cracking on a μm scale (**Figure 2.34**). The internal fracturing of the crystals leaves behind smaller crystalline domains (~50 μm), as shown by SEM, which are far too small to be suitable for SC-XRD studies. The reaction was repeated on a range of crystal sizes (0.1 mm^3 to 2 mm^3) as smaller crystals have been shown to be less susceptible to cracking under solid/gas reactions,[11, 66] however all attempts at finding suitable material for SC-XRD studies from this reaction failed.
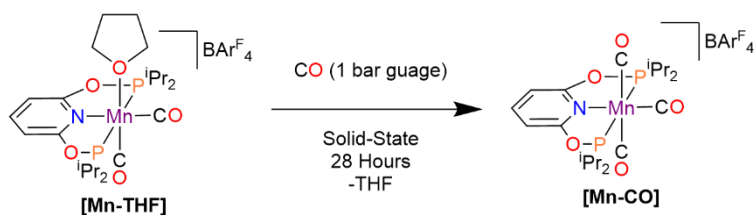
Scheme 2.14: *In-Crystallo* reaction of microcrystalline **[Mn-THF]** with CO to form **[Mn-CO]**. The time of this reaction is highly dependent on crystallite size, with macrocrystalline samples requiring days to weeks.
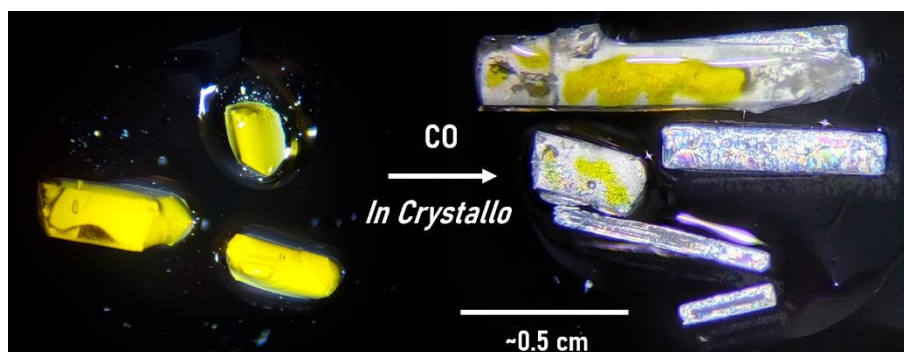
Figure 2.33: Optical microscopy image under plane polarized light of crystals of **[Mn-THF]** before (left) and after (right) exposure to CO (1 bar gauge, 48 hours). The colour change from yellow to colourless is clearly observed. Larger crystals remain yellow at the centre, indicating the reaction is diffusion ordered. Post-exposure to CO crystals can be seen to be extensively cracked internally.
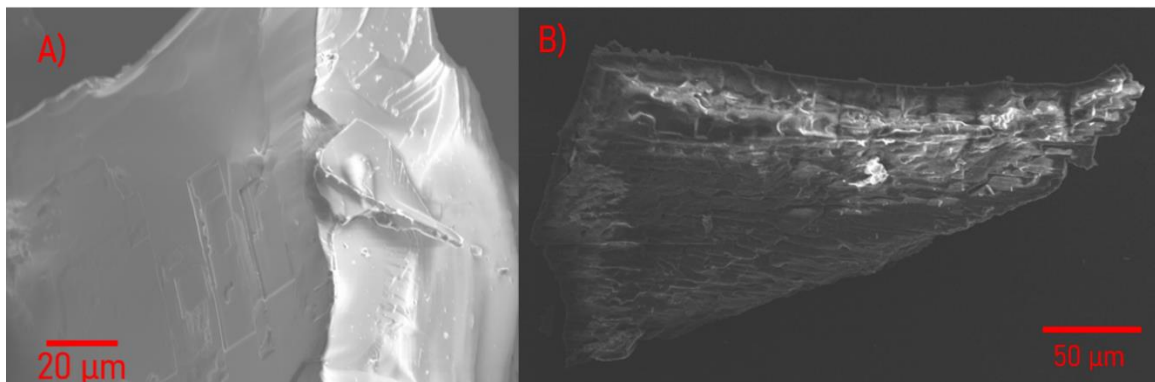
Figure 2.34: Scanning Electron Microscopy (SEM) images of **[Mn-THF]** before (A) and after (B) exposure to CO (1 bar gauge, 28 hours). The surfaces of the crystals are smooth and well defined before exposure to CO. After exposure, splintering and cracking of the crystal is clearly observed.

The solid-state $^{31}P\{^1H\}$ CP MAS and $^{13}C\{^1H\}$ CP MAS NMR spectra (10 kHz, 298 K) show that the reaction quantitatively forms **[Mn-CO]** in the solid-state (**Figure 2.35**). The resonances remain sharp after the reaction indicating that the reaction maintains short-range order. The same pattern of peaks from two crystallographically independent ^{31}P environments, their respective *trans*-coupling and the ^{55}Mn-^{31}P quadrupolar coupling found in **[Mn-CO]**, showing local symmetry is retained in the $^{31}P\{^1H\}$ CP MAS NMR spectrum. Dissolution of the product of this reaction into CD_2Cl_2 shows the clean formation of **[Mn-CO]**, and liberation of free THF and hexane by ^1H and $^{31}P\{^1H\}$ NMR spectroscopy.
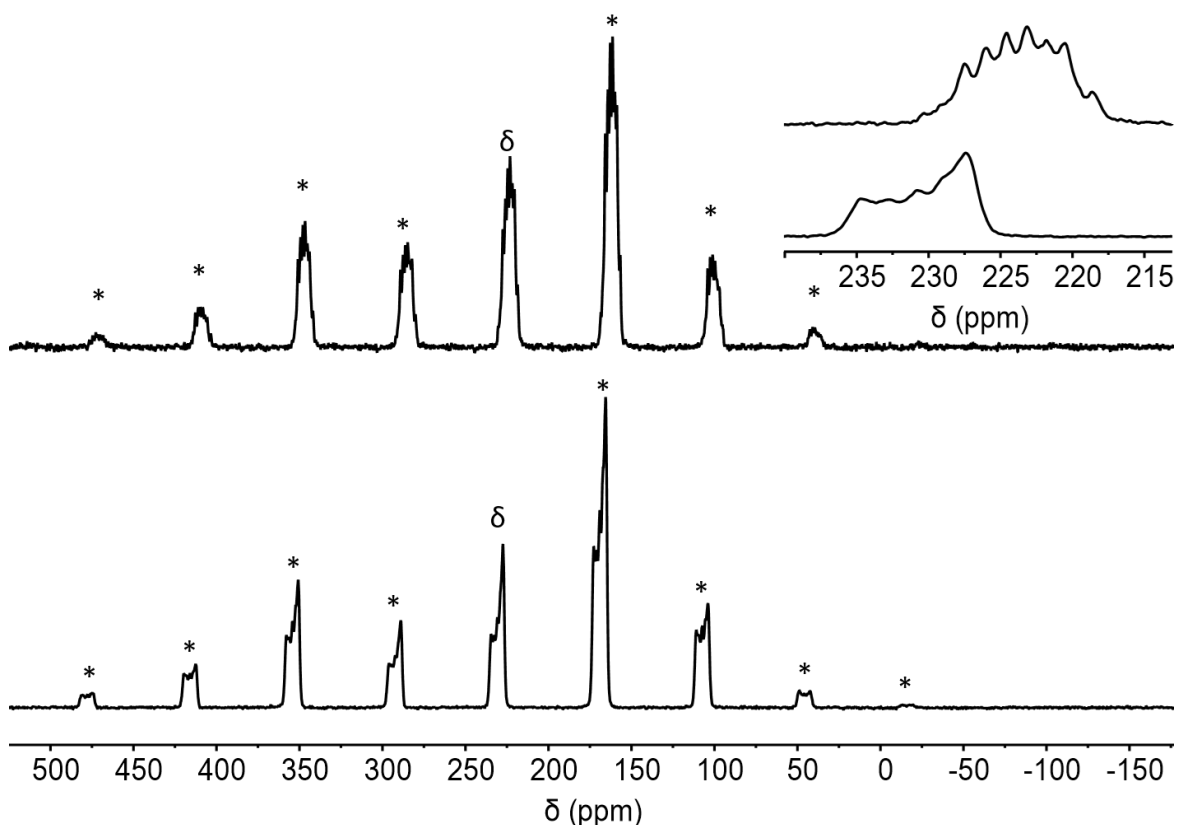
Figure 2.35: Solid-state $^{31}P\{^1H\}$ CP MAS NMR (10 kHz spin rate, 298 K) spectra of **[Mn-THF]** (*bottom*) and **[Mn-CO]** (*top*) formed by addition of CO (1 bar gauge, 28 hours) to **[Mn-THF]** in the solid-state. The inset depicts the isotropic chemical shift resonance (denoted δ). * denotes spinning side bands.

2.2gii. Microcrystal Electron Diffraction Studies

Microcrystal Electron Diffraction (MicroED) is a structure elucidation technique which utilises electrons, rather than X-Rays or neutrons.[67] Electrons interact with chemical matter much stronger than X-Rays or neutrons, meaning extremely thin crystalline samples are required (< 500 nm depth)[68] to allow for the electrons to pass through the sample. This has benefits where macroscopic crystals suitable for SC-XRD analysis cannot be obtained, which was first applied to protein

crystallography. [7, 69-71] Since then, MicroED methods have been utilised in organometallic and main group chemistry to structurally characterise Schwartz's reagent ([{Cp$_2$ZrCl}$_2$(μ_2-H)$_2$]),[72] a copper-carborane cluster,[73] and a rhodium σ-alkane complex (**Figure 2.36**).[74]
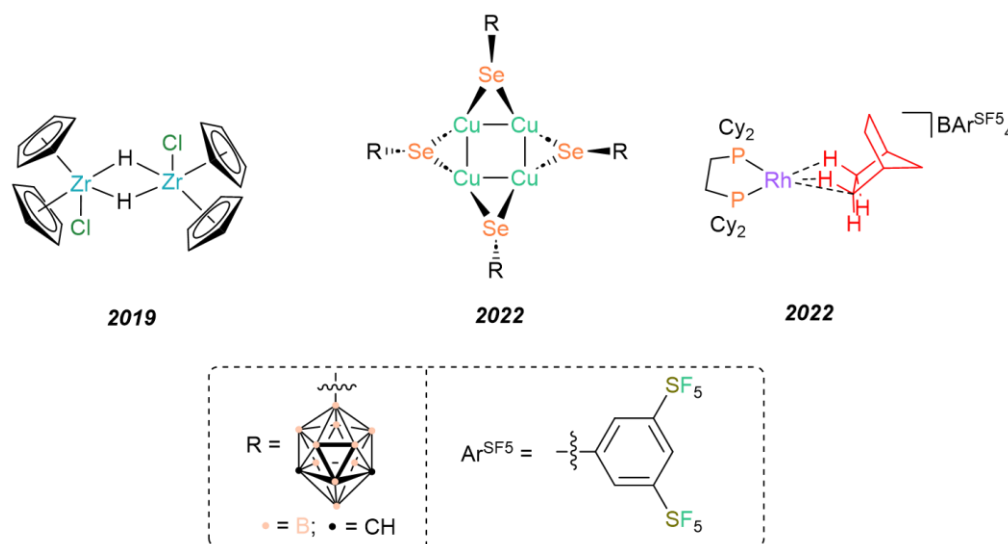
Figure 2.36: Organometallic complexes structurally characterisated by MicroED methods. *Left*: Schwartz's Reagent.[72] *Middle*: A copper-carborane tetramer.[73] *Right*: A Rh(I) σ-alkane complex.[74]

The SEM images of **[Mn-THF]** exposed to CO showed small crystalline domains remaining among a fractured crystal. Therefore, it was hypothesised that the loss in 'macroscopic' long-range order on X-Ray diffraction regimes could be circumvented through MicroED methods.

A microcrystalline sample of **[Mn-THF]** was reacted with CO (1 bar gauge) for 28 hours and deposited onto Quantifoil Cu R2/4 transmission electron microscopy (TEM) grids in an Ar-filled glovebox. The TEM grids were analysed by MicroED

methods[72-75] (**Figure 2.37**). Eight independent datasets collected from regions of fractured crystallites (~1 μm^3, **Figure 2.37**) were merged to give 95.3% completeness with 0.83 Å resolution. The MicroED data confirms the substitution of the THF ligand with CO at the metal centre (**Figure 2.38**). The data and model statistics are standard for electron diffraction data[72-74] (R_{int} = 17.48%, R_1 = 15.14% and wR_2 = 40.84%).
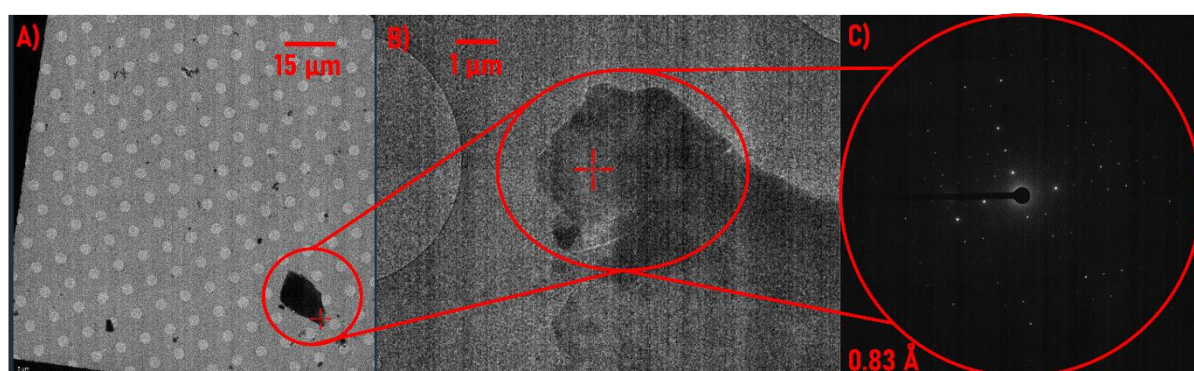
Figure 2.7: Microcrystal Electron Diffraction methods were used to structurally characterise the products of the reaction of **[Mn-THF]** with CO in the solid-state. A) ATLAS view of a larger crystallite, imaged by TEM. B) TEM image of a cracked edge of the larger crystallite from A, which was analysed by MicroED. C) Example diffraction frame from the MicroED analysis. Diffraction peaks are present out to 0.83 Å.
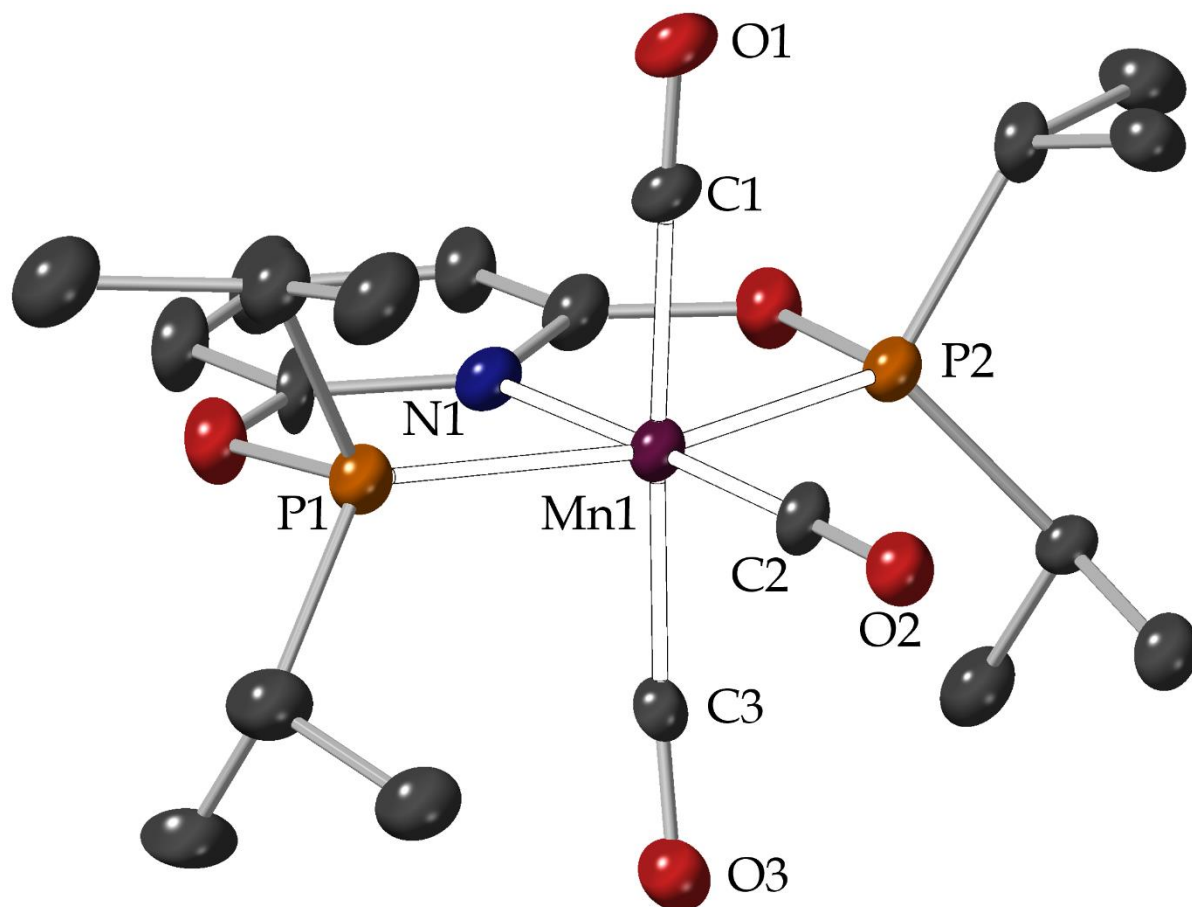
Figure 2.38: Solid-state structure of **[Mn-CO]**, synthesised by addition of CO (1 bar gauge, 28 hours) to **[Mn-THF]** in the solid-state, as determined by MicroED methods. Hydrogen atoms are omitted for clarity. Displacement ellipsoids displayed at 50%.

Also evident within the solid-state structure are significant changes in the 2° microenvironment and 3° periodic structure. The transformation is associated with a space group change from $P\,2_1/n$ to $P\,\bar{1}$, the unit cell volume is reduced by approximately 11% {**[Mn-THF]**: $Z = 4$, $V = 6306.0(2)$ Å^3; **[Mn-CO]**: $Z = 2$, $V = 2835.6(3)$ Å^3; **Table 2.3**} and the THF ligand and co-crystallised hexane are lost. The solid-state structure of **[Mn-THF]** showed that the THF ligand was encapsulated within a cleft formed by a neighbouring [BAr$^F_4$]$^-$ anion (**Figure 2.22**). The

substitution of the THF ligand in **[Mn-CO]** causes this $[BAr^F_4]^-$ anion to 'swing' in and reorientate (**Figure 2.39**). In **[Mn-THF]** the cations were orientated in a herringbone formation perpendicular to the crystallographic *c*-axis (**Figure 2.40**). The cations are rearranged into a parallel formation perpendicular to the crystallographic *a*-axis in the product (**Figure 2.40**). This dramatic transformation is likely largely responsible for the extreme fracturing of the crystals during the reaction. Additionally, the loss of lattice hexane and bound THF from the crystallites, as well as the large energy release from the reaction may play a part in crystal degradation. It is proposed that, despite the extensive restructuring of the material, the fluorus groups on the $[BAr^F_4]^-$ anion is responsible for providing sufficient plasticity for crystallinity to be maintained on a microscopic scale.

Table 2.3: Comparison of selected crystallographic parameters between **[Mn-THF]** and **[Mn-CO]**.

	[Mn-THF]	*[Mn-CO]* *(MicroED)*	*[Mn-CO]* *(Recrystallised, SC-XRD)*
Temperature (K)	150.00(10)	80(2)	149.95(10)
Crystal System	Monoclinic	Triclinic	Triclinic
Space Group	$P\,2_1/n$	$P\bar{1}$	$P\bar{1}$
Z	4	2	2
a, b, c (Å)	19.6838(4), 23.8631(6), 13.4251(3)	13.0245(6), 14.1722(9), 17.0849(12)	12.9543(6), 14.1111(6), 17.0692(8)
α, β, γ (°)	90, 90, 90	105.823(5), 106.400(5), 97.542(5)	105.704(4), 106.445(4), 97.358(4)
Volume (Å³)	6306.0(2)	2835.6(3)	2809.2(2)
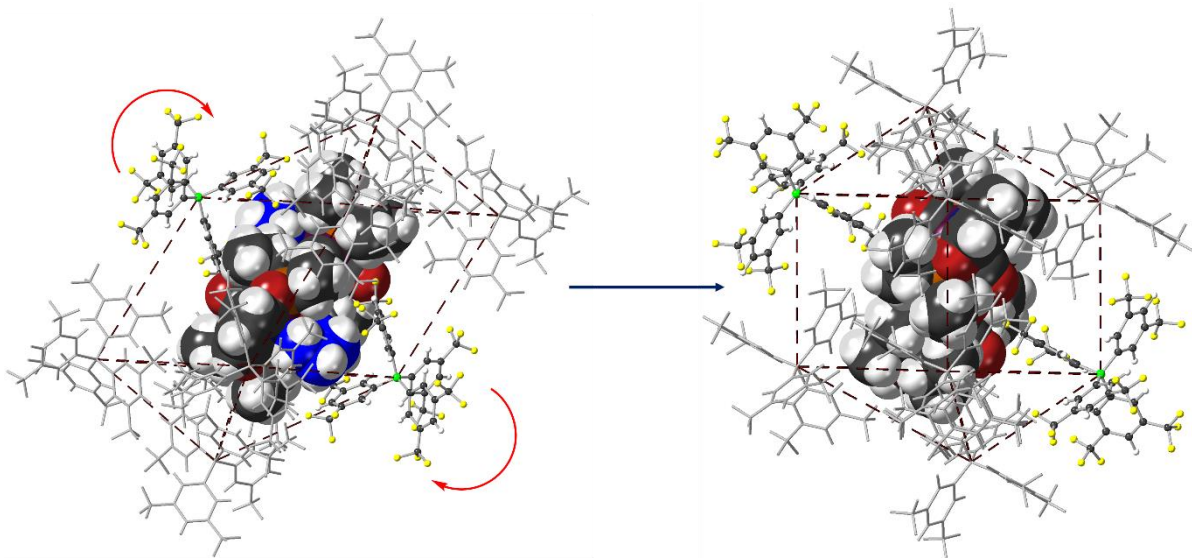
Figure 2.39: Rearrangement of [BAr$^F_4$]$^-$ anion motifs from **[Mn-THF]** (*left*) to **[Mn-CO]** (*right*). The THF ligand (blue) is located in a cleft of Ar^F rings in **[Mn-THF]**. The neighbouring [BAr$^F_4$]$^-$ anion reorientates in **[Mn-CO]**.
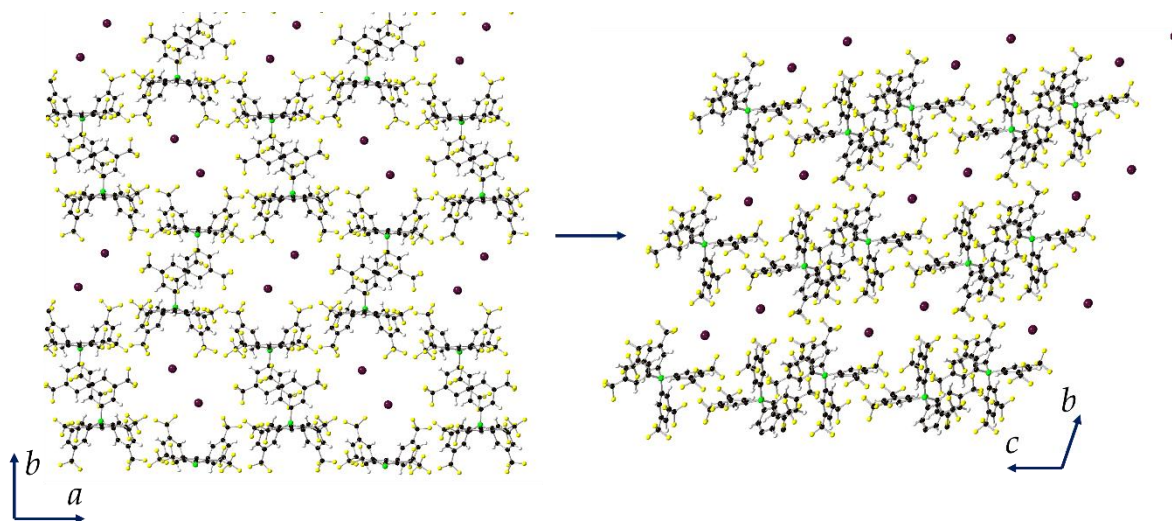
Figure 2.40: Rearrangement of the 3° periodic structure from a herringbone-type arrangement in **[Mn-THF]** (*left*) to a parallel arrangement in **[Mn-CO]** (*right*). Cationic components are represented as purple spheres of arbitrary radius.

2.2giii. Solid-State Reactivity of [Re] with Carbon Monoxide

In a similar fashion to **[Mn-THF]**, addition of CO (1 bar gauge) to **[Re]** (**Scheme 2.15**) causes the sample to change from deep red crystals, to colourless over 4-5 hours. Full completeness of this reaction occurs over approximately 24 hours, as determined by solid-state NMR spectroscopy. This example is also a disintegrative reaction, with significant degradation of crystalline integrity. In contrast to the example of **[Mn-THF]**, the crystalline integrity degradation is not from internal fracturing of the crystals, but the surfaces fragment into microcrystalline material, which could be observed by optical microscopy (**Figure 2.41**). Unfortunately, high resolution SEM images could not be obtained for the material either before or after the reaction due to high electron beam sensitivity of the samples.
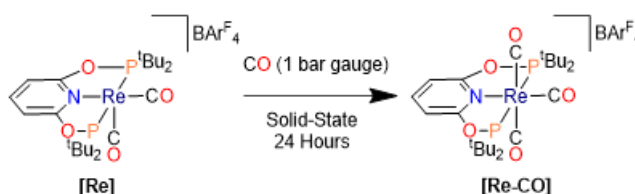
Scheme 2.15: *In Crystallo* reaction of **[Re]** with CO to form **[Re-CO]** in the solid-state.
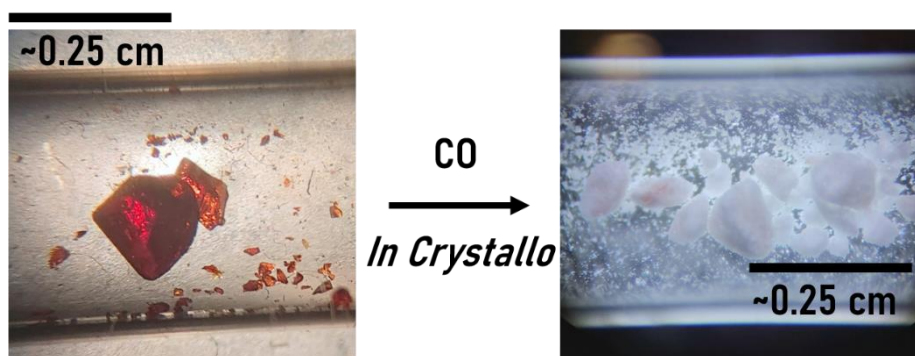
Figure 2.41: Optical microscopy images of **[Re]** (*left*) and **[Re-CO]** (*right*) formed by addition of CO (1 bar gauge, 5 hours) to **[Re]** in the solid-state. The surfaces of **[Re-CO]** formed through this reaction have fragmented into a microcrystalline material.

Despite the surface fracturing and degradation of crystalline integrity, internal long-range order was retained, and structural analysis was achieved using SC-XRD, which confirms the formation of **[Re-CO]** (**Figure 2.42**). The SCSC transformation and crystalline integrity degradation is associated with only a modest impact on the data and model statistics compared to that found for **[Re]** (**[Re]**: R_{int} = 4.01%, R_1 = 4.07%, wR_2 = 10.63%; **[Re-CO]**: R_{int} = 8.89%, R_1 = 5.35%, wR_2 = 14.60%). The coordination of CO to the vacant site of **[Re]** to produce **[Re-CO]** causes the ^{t}Bu methyl group which is in close proximity to the Re centre in **[Re]** to be thrust away from the metal and the Re–P–C angle to be opened [Re–C distances range 3.847(4) – 4.119(8) Å, Re1-P2-C21 = 119.4(4)°]. The axial carbonyl ligands are distorted from co-linear [C1-Re1-C3 = 163.5(2)°] and tilted towards the equatorial carbonyl [C1-Re1-C2 = 80.5(2)°, C2-Re1-C3 = 83.0(2)°].
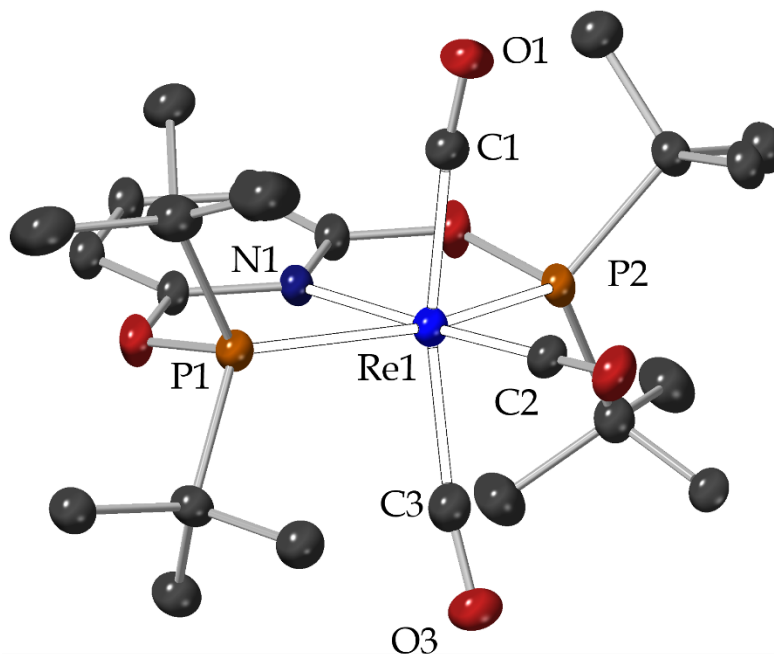
Figure 2.42: Solid-state structure of **[Re-CO]**. Hydrogen atoms omitted for clarity. Displacement ellipsoids displayed at 50%. Selected bond lengths and angles: Re1-P1 = 2.4177(3) Å; Re1-P2 = 2.4212(13) Å; P1-Re1-P2 = 153.65(5)°; Re1-N1 = 2.172(4) Å; Re1-C1 = 1.977(6) Å; Re1-C2 = 1.942(6) Å; Re1-C3 = 2.024(5) Å; C1-Re1-C2 = 80.5(2)°; C2-Re1-C3 = 83.0(2)°.

No change in space group is observed in the SC-XRD data for **[Re]** compared to **[Re-Br]** ($P\bar{1}$), and only a modest change in the 3° periodic structure is noted. The single-crystal X-Ray data for **[Re-CO]** exhibits no space group change occurs (P - 1) and a very modest change in the 3° periodic structure is observed (**Figure 2.43**). The unit cell parameter changes are far smaller than that observed in the transformation of **[Mn-THF]** to **[Mn-CO]** (**Table 2.4**), which is expected based on the smaller change at the 1° coordination site and the related impact on the 2° microenvironment and 3° periodic structure. A slight movement of the three

[BArF4]- anions which were located closest to the vacant site is noted [B···B distances, **[Re]**: 9.214(8) – 14.4679(2) Å; **[Re-CO]**: 9.134(12) – 14.1715(3) Å], but more noticeable is a reordering of the cations {**[Re]**: O1···O1 intermolecular distance = 5.348(9) Å, O1···O1-C1 angle = 107.6(3)°; **[Re-CO]**: O1···O1 intermolecular distance: 3.482(10) Å, O1···O1-C1 angle = 125.5(5)°}.
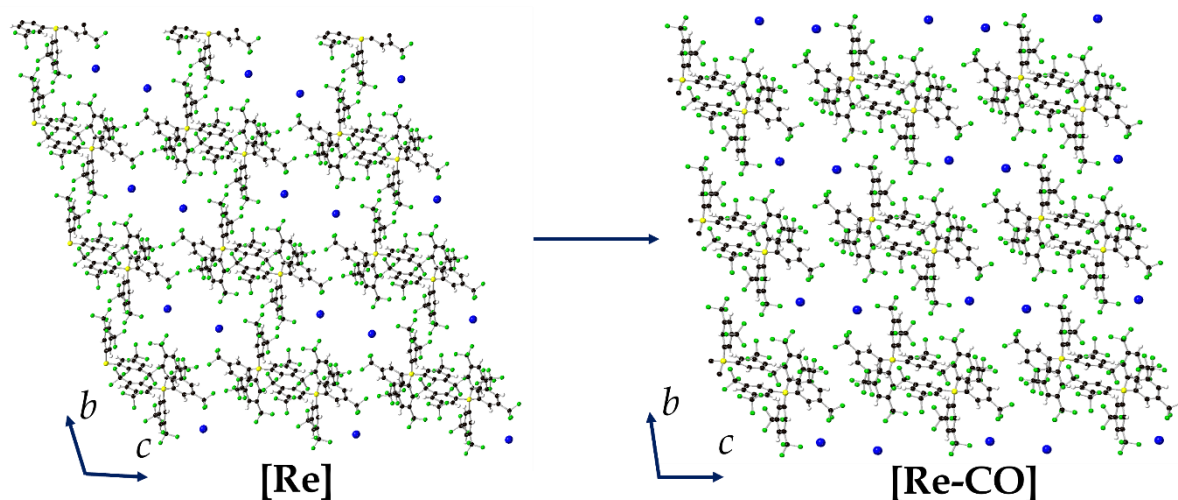
Figure 2.43: Slight change in 3° periodic structure from **[Re]** to **[Re-CO]**. Cations are represented as blue spheres of arbitrary radius.

Table 2.4: Comparison of selected crystallographic parameters between **[Re]** and **[Re-CO]**.

	[Re]	*[Re-CO]*
Temperature (K)	110.00(10)	109.95(10)
Crystal System	Triclinic	Triclinic
Space Group	$P\bar{1}$	$P\bar{1}$
Z	2	2
a, b, c *(Å)*	12.74810(10), 14.4679(2), 17.4995(2)	12.9529(4), 14.1717(3), 16.8449(5)
α, β, γ (°)	107.7110(10), 94.0020(10), 98.7510(10)	97.370(2), 94.209(3), 96.468(2)
Volume (Å³)	3015.62(6)	3034.93(15)

2.2giv. Solid-State NMR Spectroscopy Analysis

The solid-state $^{31}P\{^1H\}$ CP MAS NMR (10 kHz spin rate, 298 K) spectra of **[Re]** and **[Re-CO]** both reveal broad, featureless resonances (**Figure 2.44**) at δ_P 216.3 (**[Re]**; FWHM = 1950 Hz) and 200.6 (**[Re-CO]**; FWHM = 2100 Hz). Importantly, the signal of **[Re]** is not observed in the spectrum for **[Re-CO]**, reflecting that this is a *bulk* transformation, rather than a transformation of a single crystal.
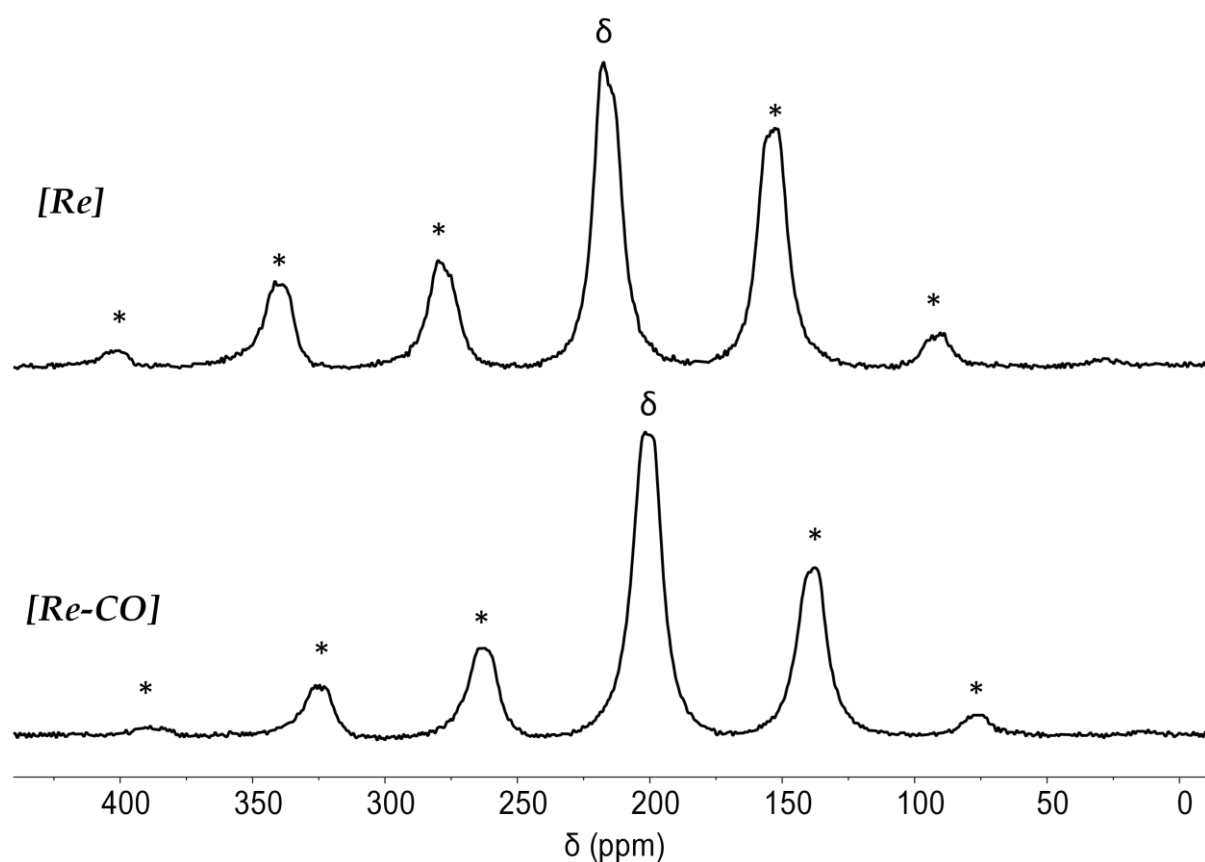
Figure 2.44: Solid-state $^{31}P\{^1H\}$ CP MAS NMR (10 kHz spin rate, 298 K) spectra of **[Re]** (*top*) and **[Re-CO]** (*bottom*). The isotropic chemical shift resonances are denoted by δ. * denotes spinning side bands.

2.2gv. Periodic DFT Investigation of the Nature of Lattice Adaptivity in the Reaction of [Mn-THF] with Carbon Monoxide

Periodic DFT calculations [PBE-D3/DZVP-MOLOPT-SR-GTH(Mn)] were utilised to examine the lattice rearrangement associated with the THF/CO substitution (Mn) reaction. In the first instance, a proto-structure of **[Mn-CO]** was calculated, **[Mn-CO]***, which is a computational model of the structure of **[Mn-CO]** within the unit cell of **[Mn-THF]**. **[Mn-CO]*** was found to be 66.0 kcal mol^{-1} less stable than **[Mn-CO]**, when optimised within the unit cell of **[Mn-THF]**. This shows there is a very large thermodynamic driving force towards lattice reorganisation towards **[Mn-CO]**.

To understand the foundation of this large energy difference of the unit cell, individual ion pairs energies were calculated between one manganese cation and the five nearest neighbours in the bicapped square prism of [BAr$^F_4$]$^-$ anions (the other cation and five anions are crystallographically related by symmetry and so ¼ of the unit cell for **[Mn-THF]** and ½ of the unit cell for **[Mn-CO]** is sufficient for calculations). By calculating the ion pair energies with, and without, Grimme's D3 dispersion correction,[76] dispersion effects could be quantified between the ions. An Independent Gradient Model with Hirshfeld partitioning (IGMH) plot[77] was also calculated for each of the ion-pair interactions to visualise the dominating non-covalent interactions between the ion pairs. The ion-pair (IP) in which the THF ligand is located within the cleft on the local [BAr$^F_4$]$^-$ anion (IP1, **Figure 2.45**) is responsible for the largest ion pair energy, 64.4 kcal mol^{-1}, of which 13.3 kcal mol^{-1} is due to the dispersion energy. The IGMH isosurface highlights the major non-

covalent interactions, which are dominated by THF methylene C–H⋯π interactions to the Ar^F, and minor contributions from THF methylene C–H⋯F and ^iPr C–H⋯F interactions to the Ar^F CF_3 groups (**Figure 2.45**). After THF/CO substitution, the THF⋯Ar^F interactions are lost and only the ^iPr C–H⋯F interactions remain in **[Mn-CO]*** (**Figure 2.45**), reducing IP1 energy by 16.3 kcal mol^{-1}, of which 6.7 kcal mol^{-1} (~40% of the contribution) is due to the loss in dispersion energy. The remainder of the loss in ion pair energy is likely due to inter-ion electrostatic interactions.
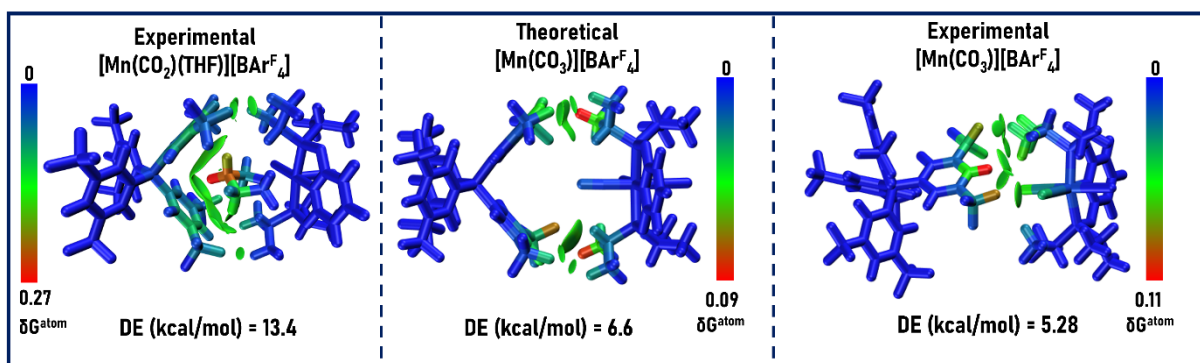
Figure 2.45: Independent Gradient Model with Hirshfeld Partitioning (IGMH) plots for IP1 in **[Mn-THF]** (left), **[Mn-CO]*** (centre) and **[Mn-CO]** (right). Cations and anions are defined as separate fragments; $sign(\lambda_2)\rho$-coloured isosurfaces are plotted with δG^{inter} = 0.003 a.u; relative atomic contributions coloured by %δG^{atom}; DE = dispersion energy.

The ion pair consisting of the pyridyl group's closest approach to the $[BAr^F_4]^-$ anion (IP3) shows the next largest decrease in energy, with a loss of 4.2 kcal mol^{-1}, of which 2.1 kcal mol^{-1} is due to dispersion (**Figure 2.46**). The IGMH plots look very similar for IP3 for **[Mn-THF]** and **[Mn-CO]***, but for **[Mn-THF]** some weak THF methylene C–H⋯F interactions are present which are lost in **[Mn-CO]***. The remainder of the three ion pair energy differences are very small and all exergonic (2.0 – 0.5 kcal mol^{-}

[1]) with minor contributions from dispersion energy (0.3 – 0.1 kcal mol^{-1}). When summed across all five ion pairs the total energy change is +17.6 kcal mol^{-1}, and IP1 is responsible for >92% of this energy.
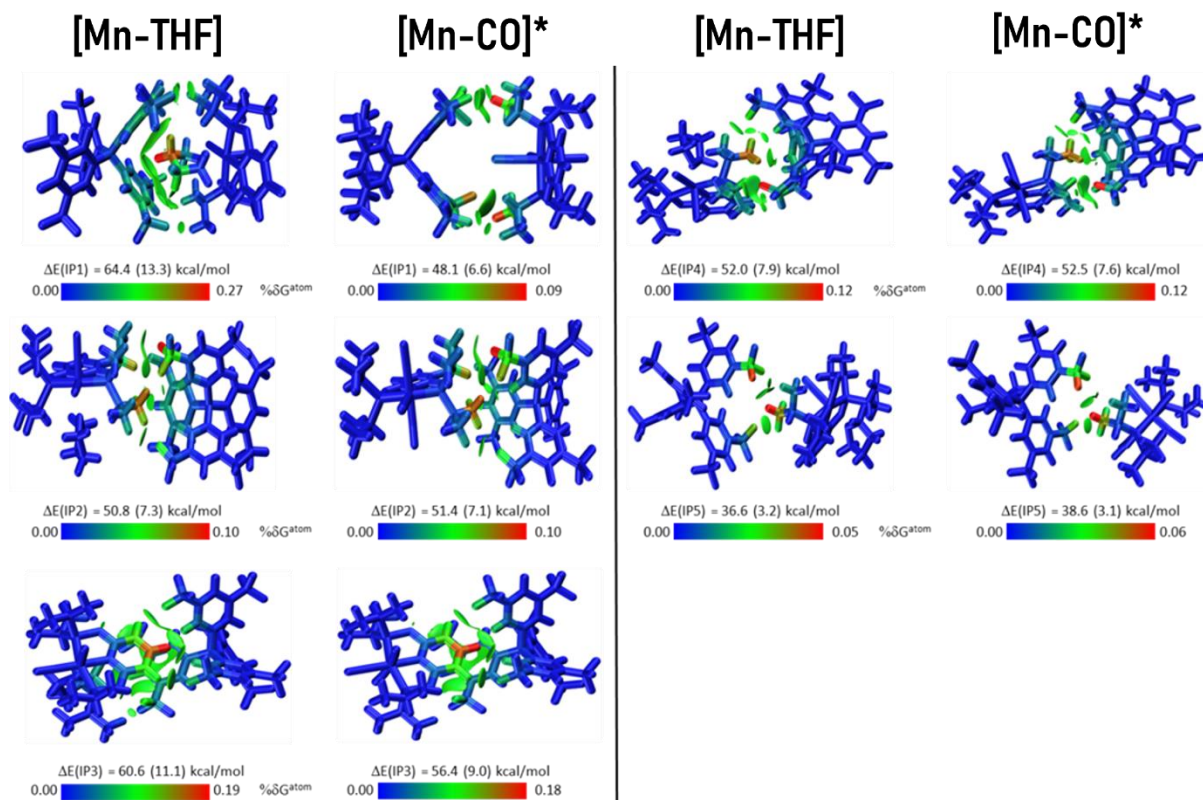
Figure 2.46: IGMH plots for IP1 – IP5 in **[Mn-THF]** and its equivalent in **[Mn-CO]*** after THF/CO substitution. Cations and anions are defined as separate fragments; sign(λ_2)ρ–coloured isosurfaces are plotted with δG^{inter} = 0.003 a.u; relative atomic contributions coloured by %δG^{atom}. The ion–pair interaction energies are also indicated (kcal/mol) with the contribution from dispersion in brackets.
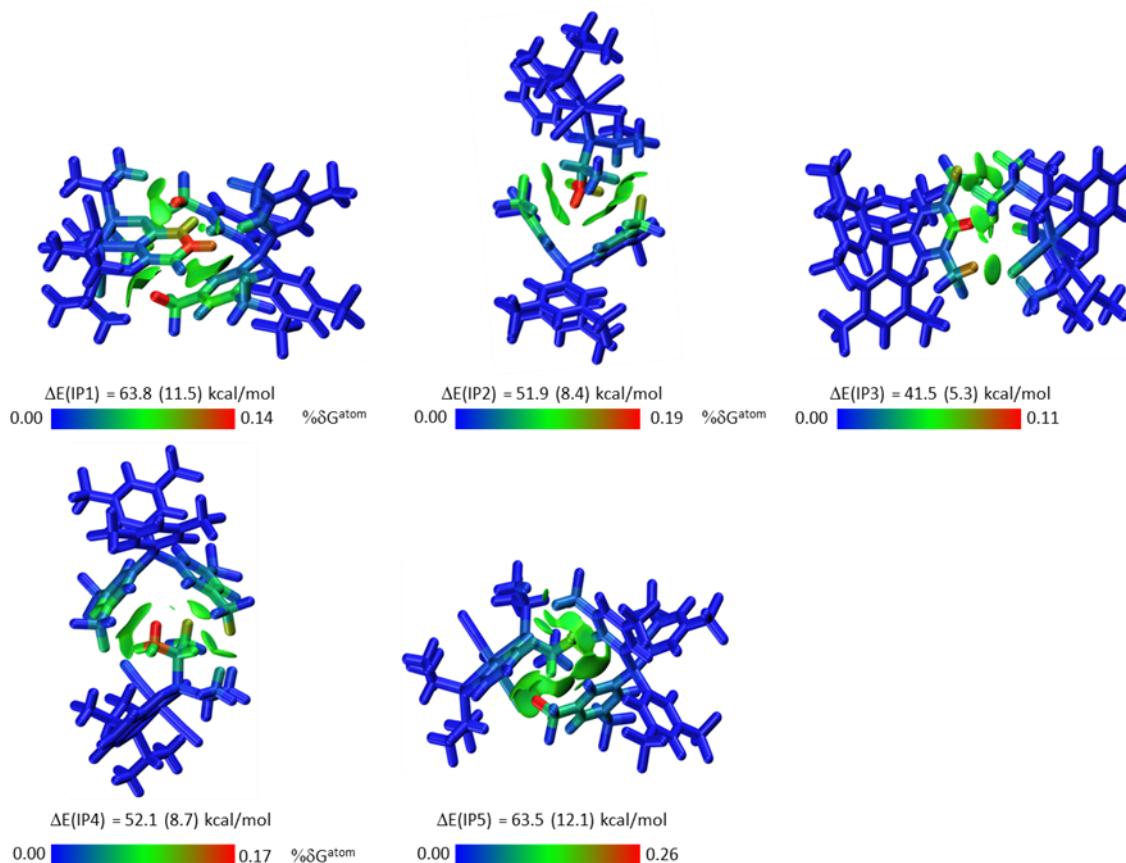
Figure 2.47: IGMH plots for IP1 – IP5 of **[Mn-CO]**. Cations and anions are defined as separate fragments; sign(λ_2)ρ–coloured isosurfaces are plotted with δG^{inter} = 0.003 a.u; relative atomic contributions coloured by %δG^{atom}. The ion–pair interaction energies are also indicated (kcal/mol) with the contribution from dispersion in brackets.

2.2gvi. Periodic DFT Investigation of the Nature of Lattice Adaptivity in the Reaction of [Re] with Carbon Monoxide

The above analysis was also carried out for the CO addition to **[Re]** [PBE-D3/DZVP-MOLOPT-SR-GTH(Re)], by calculating the respective **[Re-CO]** proto-structure, **[Re-CO]***, using the same protocol. **[Re-CO]*** is 15.0 kcal mol^{-1} less stable than **[Re-CO]** when optimised within the unit cell found by experiment. The

thermodynamic driving force favouring lattice rearrangement being significant but less than for **[Mn-THF]/[Mn-CO]** is to be expected given the smaller change around the metal site and expected non-covalent interactions in the solid-state. In this case, the sum of each of the five ion pairs is much smaller (+3.3 kcal mol^{-1}) and the ion pair closest to the added CO, IP1 (**Figure 2.48**), contributes -5.4 kcal mol^{-1}, of which 1.6 kcal mol^{-1} is due to dispersion. The largest contribution to the ion pair energies is the movement of the ^{t}Bu group on the PONOP ligand which was previously in close proximity to the Re centre towards an adjacent [BAr$^F_4$]$^-$ anion (IP2, ΔE = +7.3 kcal mol^{-1}).
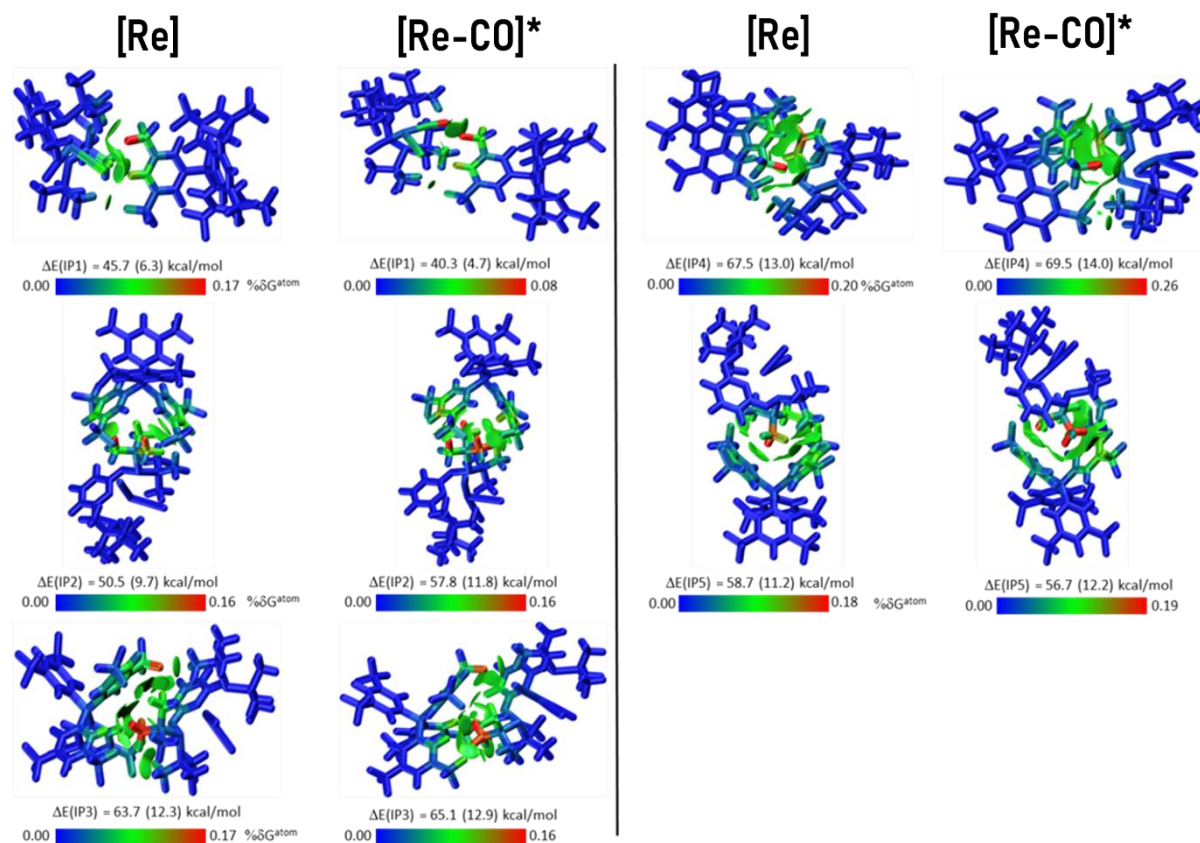
Figure 2.48: IGMH plots for IP1 – IP5 in **[Re]** and its equivalent in **[Re-CO]*** after THF/CO substitution. Cations and anions are defined as separate fragments; $\text{sign}(\lambda_2)\rho$–coloured isosurfaces are plotted with δG^{inter} = 0.003 a.u; relative atomic contributions coloured by $\%\delta G^{\text{atom}}$. The ion–pair interaction energies are also indicated (kcal/mol) with the contribution from dispersion in brackets.

ΔE(IP1) = 40.2 (5.2) kcal/mol

0.00 ▮▮▮ 0.14 %δG^{atom}

ΔE(IP2) = 48.2 (7.1) kcal/mol

0.00 ▮▮▮ 0.09 %δG^{atom}

ΔE(IP3) = 66.2 (14.0) kcal/mol

0.00 ▮▮▮ 0.21

ΔE(IP4) = 67.5 (13.1) kcal/mol

0.00 ▮▮▮ 0.22 %δG^{atom}

ΔE(IP5) = 56.4 (11.9) kcal/mol

0.00 ▮▮▮ 0.19
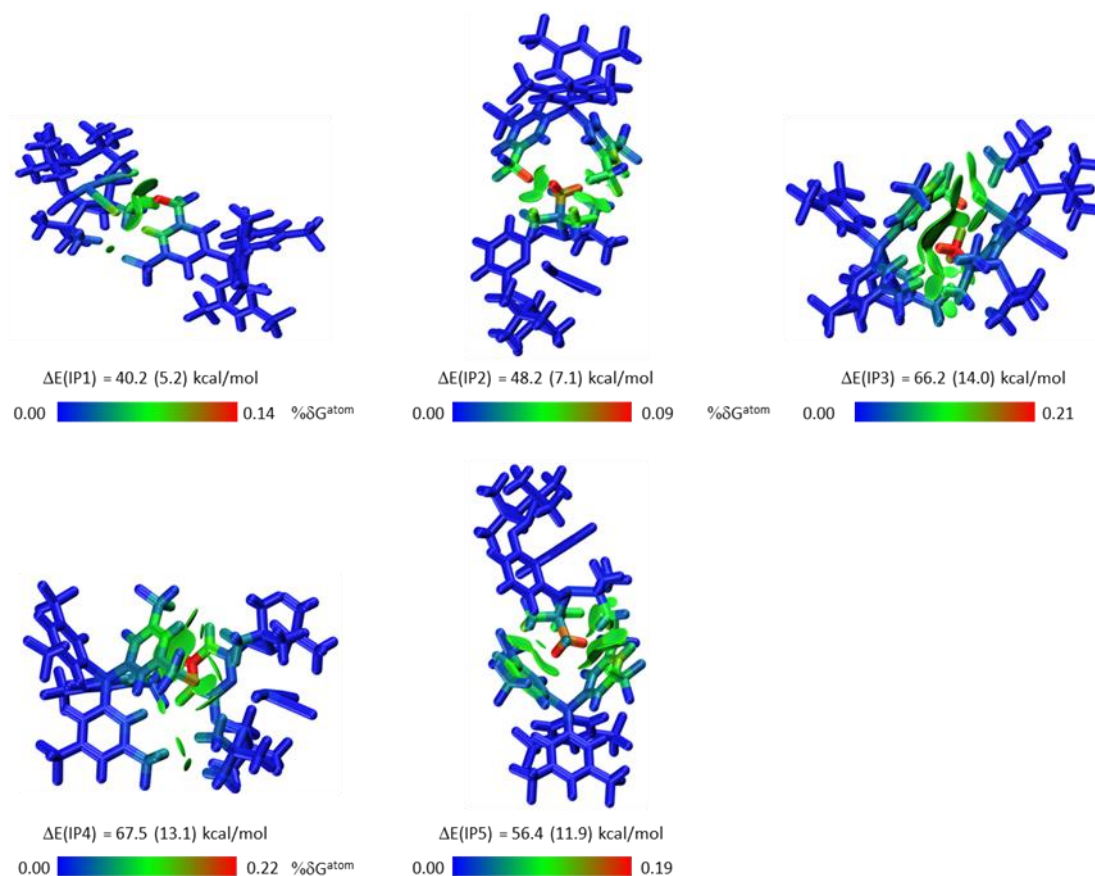
Figure 2.49: IGMH plots for IP1 – IP5 of **[Re-CO]**. Cations and anions are defined as separate fragments; sign(λ_2)ρ–coloured isosurfaces are plotted with δG^{inter} = 0.003 a.u; relative atomic contributions coloured by %δG^{atom}. The ion–pair interaction energies are also indicated (kcal/mol) with the contribution from dispersion in brackets.

It is important to note that the exergonic nature of these reactions, both from the CO binding energy and from the thermodynamics of the lattice rearrangements, may also be a factor in the degradation of macroscopic crystalline integrity in both reactions.

2.2h. Attempts to prevent crystal cracking during the reaction of [Re] with CO

2.2hi. Solvent heat sink

As noted in *Section 2.2gvi* above, the exergonic nature of the CO binding to **[Re]** may have a significant impact on the crystalline integrity of **[Re-CO]**. Previously, it has been reported that a stable, exceedingly insoluble σ-alkane complex, $[Rh(dcpe)(NBA)][BAr^{SF5}_4]$ {NBA = norbornane, Ar^{SF5} = 3,5-$(SF_5)C_6H_3$)}, could be suspended in pentane without rapid, large-scale decomposition *via* anion coordination to form the corresponding zwitterionic complex $[Rh(dcpe)(\eta^6-Ar^{SF5})BAr^{SF5}_3]$.[74] It was reasoned that suspending crystals of **[Re]** in pentane may provide an alternative route for this heat to escape the crystals. Approximately 10 mg of **[Re]** was suspended in 5 mL of pentane, the solvent degassed, cooled to 0 °C and back-filled with CO (1 bar gauge). The suspension was kept at 0 °C for 5 hours. While **[Re-CO]** was formed, the desired retention of macroscopic crystalline integrity was not achieved, as the sample steadily became a white microcrystalline solid over the course of the reaction.

2.2hii. Cationic Lewis Acid polymerisation of ethyl vinyl ether by [Re]

Vinyl ethers, in particular ethyl vinyl ether (EVE), are common substrates for cationic polymerisation reactions.[78-81] Polymerisation of EVE on crystal surfaces has been reported for $[Rh(dcpe)(NBA)][BAr^F_4]$ [dcpe = 1,2-(dicyclohexyl)phosphinoethane, **Scheme 2.16**] which produced a crystalline sample

of a σ-alkane complex which was air tolerant, due to surface passivation from the polymer coating.[80]
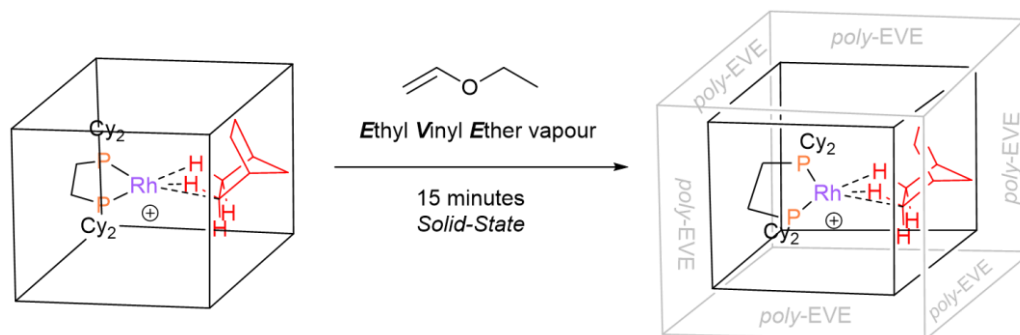
Scheme 2.16: Solid-state reaction between [Rh(dcpe)(NBA)][BAr$^F_4$] with ethyl vinyl ether, forming a crystalline Rh(I) σ-alkane complex encapsulated with poly(ethyl vinyl ether).[80]

The **[Re]** system is pre-configured for crystal surface, cationic Lewis Acid polymerisations, due to the vacant site at the Re centre. It was reasoned that coating the crystalline material of **[Re]** with poly(ethyl vinyl ether) may prevent crystal fracturing during addition of CO.
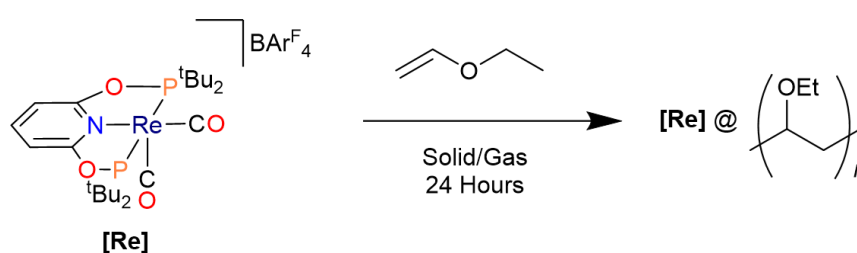
Scheme 2.17: Synthesis route applied to coat single-crystals of **[Re]** with poly(ethyl vinyl ether).

For this reaction, a H-flask was fitted with an adapted J Youngs tap with a needle inserted into the base (**Figure 2.50**).[80] Crystals of **[Re]** were affixed to the needle with

a small amount of silicone vacuum grease. EVE (~0.1 mL) was then vacuum transferred to the opposite side of the H-flask and the apparatus sealed under vacuum (<1 x 10^{-2} mbar). Warming the apparatus to room temperature allowed the EVE to diffuse throughout the H-flask (EVE boiling point = 33 °C), and EVE polymerisation began on the surfaces of the crystals within minutes. Prolonged reaction times (24 hours) causes the polymer to grow large enough to fall from the surface of the crystals and collect at the bottom of the ampoule.
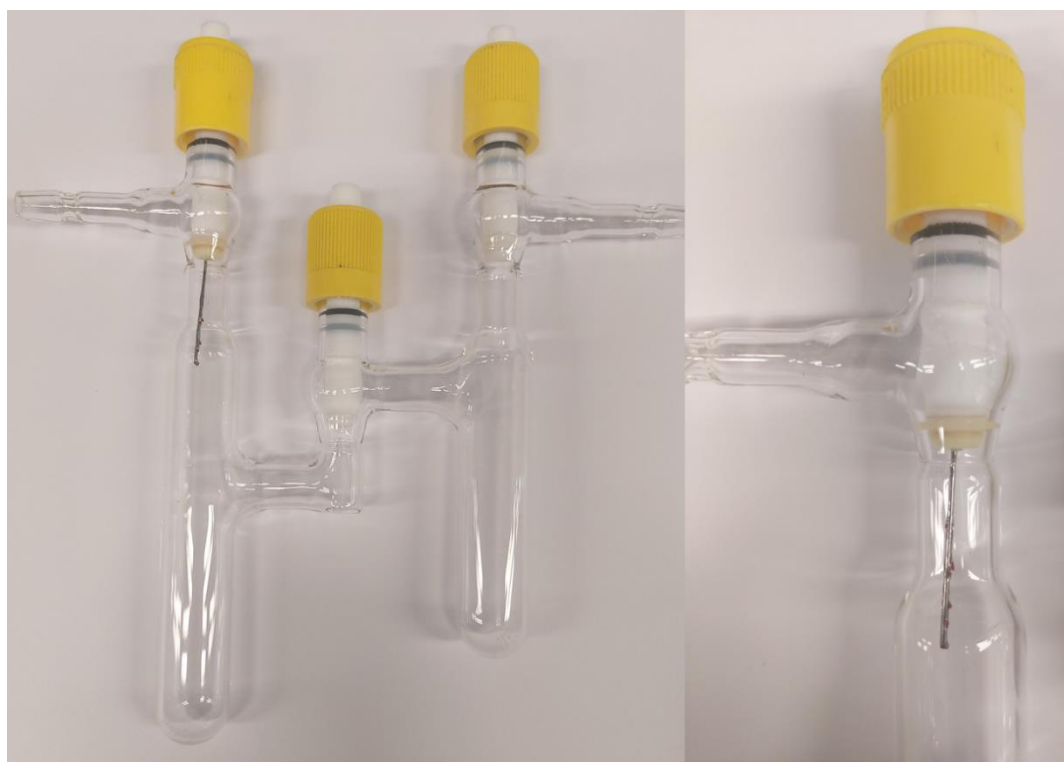
Figure 2.50: H-flask and adapted J Young tap with crystalline samples of [Re-BArF4] mounted using silicone vacuum grease.

Cationic polymerisations in the solid-state should in theory always be living polymerisations due to a lack of termination mechanisms. Therefore, one would expect that the polymers formed through this method would possess highly

homogeneous polymer lengths, ie. a low polydispersity index ($Đ = M_w/M_n$). Gel permeation chromatography (GPC) data of polymer formed on the surfaces of the crystals shows the polymer has a weight average molecular weight (M_w) of ~25800 g mol^{-1} and a polydispersity of 1.1 (**Figure 2.51**). Interestingly, the polymer which condensed at the bottom of the ampoules was much more disperse in nature ($Đ = 2.5$) with an M_w of ~14200 g mol^{-1} (**Figure 2.51**). A proposed mechanism for the cationic Lewis Acidic polymerisation in this case is shown in **Scheme 2.18**.
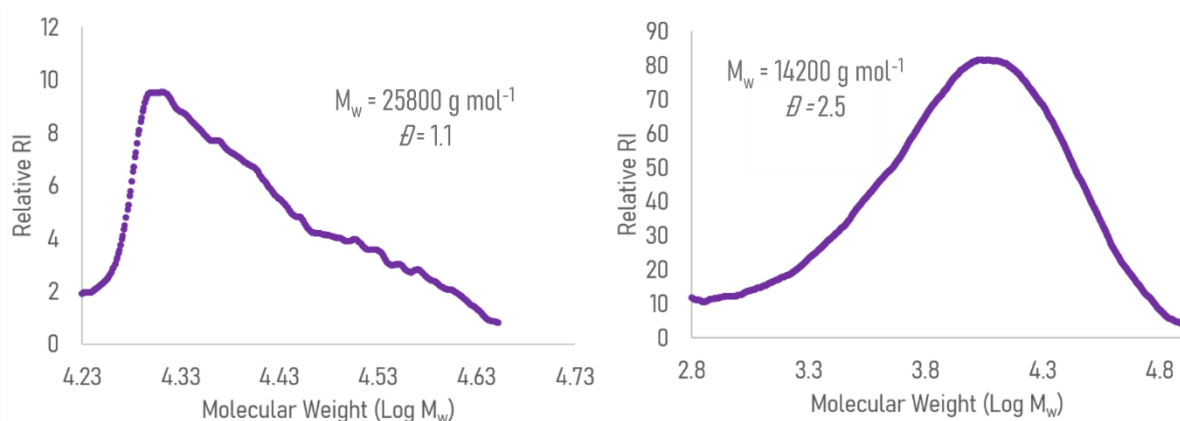
Figure 2.51: Gel Permeation Chromatography (GPC) traces of poly(ethyl vinyl ether) formed from Lewis Acid catalysed solid-state polymerisation. *Left*: Polymer sample remaining on crystalline samples. *Right*: Polymer sample which was no longer attached to the surface of the metal.
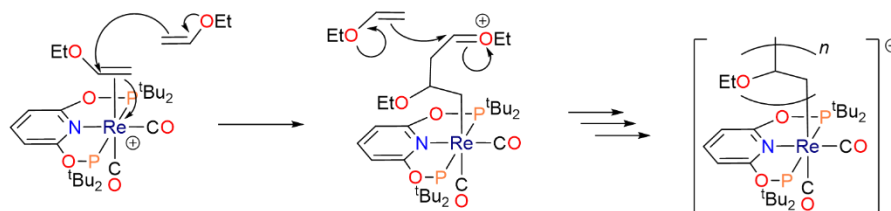
Scheme 2.18: Proposed mechanism of cationic Lewis Acidic catalysed ethyl vinyl ether polymerisation. [BAr$^F_4$]$^-$ anions omitted for clarity.

The polymer-coated crystals were examined by SEM, however, the samples were too beam sensitive for the coating to be imaged. Furthermore, single-crystal X-Ray diffraction experiments on the polymer coated samples were devoid of diffraction peaks, which precluded further experiments with CO addition.

2.3. Conclusions

It has been demonstrated that ionic organometallic systems can be remarkably adaptive in the 2° microenvironment and 3° periodic structure from changes in the 1° coordination site. The coordination sphere of the cationic organometallic fragment induces significant changes in the non-covalent interactions with neighbouring [BAr$^F_4$]$^-$ anions, which causes reorganisation of the 3° periodic structure. The fluorous groups of the [BAr$^F_4$]$^-$ anion are attributed to the retention of bulk crystallinity due to the plasticity they provide, as has been noted in previous work,[18-20] due to the non-specific and non-directional nature of interhalogen interactions.[16, 17] *In silicio* studies of this system involving the use of proto-structures to investigate thermodynamic driving forces to 3° periodic structure alterations is novel and has potential as a predictive tool for lattice adaptivity.

MicroED methods have been utilised to circumvent crystallographic issues associated with the loss of macroscopic long-range order due to crystal cracking. These findings may be applicable to related studies where crystalline integrity is impacted through solid-state reactivity and adaptivity.

2.4 Future Work

This work could be extended to further understand the effects of ligand substitution and addition in the solid-state. For example, reactivity of **[Mn-THF]** with cyclic ethers similar to THF, such as oxetane or 1,4-dioxane, could provide information on how smaller ligand substitutions at the 1° coordination site can influence the 3° periodic structure. Furthermore, **[Re]** could be varied by changing the ^{t}Bu groups of the PONOP ligand to 1-adamantyl groups. In terms of percent buried volume at the metal, the steric bulk of the 1-adamantyl group is similar to that of the ^{t}Bu groups. However, the larger van der Waals radius of the 1-adamantyl group may have significant implications on the solid-state 2° microenvironment and the 3° periodic structure. Finally, the fluorine content of the anion can be altered. The [BPh$_4$]$^-$ anion, and the 3,5-F$_2$C$_6$H$_3$ and F$_5$C$_6$ aryl derivatives synthesised to further investigate the importance of the interhalogen bonds in providing crystal plasticity.

2.5 Experimental

2.5a. General Experimental

All manipulations, unless otherwise stated, were performed under standard Schlenk line and glovebox (<0.5 ppm O$_2$/H$_2$O) techniques under an argon (BOC, N4.8 purity), carbon monoxide (CK Gases, N3.7 purity) or nitrogen atmosphere. Glassware was dried overnight at 140 °C and flame dried under vacuum before use. Pentane, hexane, CH$_2$Cl$_2$ and toluene were dried using a commercially available Grubbs-type purification system (Innovative Technology) and degassed with three freeze-pump-thaw cycles and stored over 3 Å molecular sieves (CH$_2$Cl$_2$ and toluene)

under argon in resealable glass ampoules fitted with PTFE high vacuum stopcocks (Rotaflo HP or J. Young). C_6H_5F (pre-treated with alumina), 1,2-$C_6H_4F_2$ (pre-treated with alumina) and CD_2Cl_2 were dried over CaH_2, vacuum transferred, degassed with three freeze-pump-thaw cycles, and stored over 3 Å molecular sieves. Tetrahydrofuran (THF) was dried over Na/benzophenone, distilled, degassed with three freeze-pump-thaw cycles and stored over 3 Å molecular sieves. Na[BAr$^F_4$],[82] iPr-PONOP,[83] tBu-PONOP,[46] [Mn(iPr-PONOP)Br(CO)$_2$][29] and ReBr(CO)$_5$[84] were synthesised according to literature methods. All other chemicals were from commercial sources and used without further purification. Solution state NMR data were collected on a Bruker AVIIIHD 500 MHz or AVIIIHD 600 MHz Widebore spectrometer at the temperatures specified. The solution ^1H and $^{13}C\{^1H\}$ NMR spectra were referenced to the residual solvent peaks. Assignments were aided with $^1H\{^{31}P\}$ solution NMR data. $^{31}P\{^1H\}$ and $^{11}B\{^1H\}$ solution spectra were referenced externally to 85% H_3PO_4 in D_2O and 5% $BF_3 \bullet OEt_2$ in C_6D_6, respectively. Solid-state NMR samples were prepared in an argon-filled glovebox by pre-loading 60-100 mg of crushed material into a 4.0 mm zirconia solid-state NMR rotor and sealed with Kel-F, vespel or zirconia caps. Solid-state NMR data were obtained on Bruker Avance III HD spectrometers, operating at 100.63 MHz ($^{13}C\{^1H\}$), 100.56 MHz ($^{13}C\{^1H\}$), 162.04 MHz ($^{31}P\{^1H\}$), 161.99 MHz ($^{31}P\{^1H\}$) or 376.5 MHz ($^{19}F\{^1H\}$) at the MAS rates and temperatures specified. All $^{13}C\{^1H\}$ CP MAS spectra were referenced to adamantane where the upfield methine resonance was taken to be δ_C = 29.5 ppm, secondarily referenced to δ_C(SiMe$_4$) = 0.0 ppm. $^{31}P\{^1H\}$ CP MAS spectra were referenced to triphenylphosphine (δ_P = -9.3 ppm relative to H_3PO_4) or calcium

hydrogen phosphate (δ_P = 1.4 ppm relative to H_3PO_4). $^{19}F\{^1H\}$ HPDEC MAS spectra were referenced to CF_3COOH/H_2O (50% v/v, δ -76.54 ppm relative to $CFCl_3$). Solid-state NMR spectra were recorded at varied MAS rates to determine isotropic chemical shifts. Electrospray ionisation mass spectrometry (ESI-MS) was carried out using a Bruker MicrOTOF instrument by Mr Karl Heaton at the *University of York* Centre of Excellence in Mass Spectrometry. ESI-MS for [Mn(^{i}Pr-PONOP)(THF)(CO)$_2$][BAr$^F_4$] was collected using a modified glovebox directly attached to a Bruker HCT-II ion trap. Elemental microanalyses were performed by Dr Graeme McAllister at the *University of York*, or by Ms Orfhlaith McCullough at *London Metropolitan University*.

2.5bi. Preparation of [Mn(^{i}Pr-PONOP)(CO)$_3$][BAr$^F_4$], [Mn-CO]

An ampoule was charged with [Mn(^{i}Pr-PONOP)Br(CO)$_2$] (283 mg) and Na[BAr$^F_4$] (512 mg). Fluorobenzene (30 mL) was vacuum transferred onto the solids. The ampoule was backfilled with CO (1 bar gauge) at 78 K, warmed to room temperature and stirred for 18 hours. The reaction mixture became cloudy during this time, presumably due to NaBr precipitation. The solution was degassed and the product precipitated by addition of pentane (200 mL). The product was isolated *via* cannula filtration. The product was extracted into CH_2Cl_2 (20 mL), cannula filtered, then precipitated with pentane (200 mL). The solids were washed with pentane (3 x 10 mL) and dried *in vacuo* to yield the complex as a microcrystalline white powder (536 mg, 75% yield). Crystals suitable for single-crystal X-Ray diffraction were obtained by layering a CH_2Cl_2 solution with pentane at room temperature.

^{1}H Solution NMR (600 MHz, CD$_2$Cl$_2$, 298 K): δ_H 7.78 (t, $^2J_{HH}$ = 8.1 Hz, 1 H, *para*-PONOP), 7.72 (s, 8 H, *ortho*-BAr$^F_4$), 7.56 (s, 4 H, *para*-BAr$^F_4$), 6.85 (d, $^2J_{HH}$ = 8.0 Hz, 2 H, *meta*-PONOP), 3.00 (virtual m, 4 H, PC*H*Me$_2$), 1.47 (virtual dd, 12 H, PCHC*H$_3$*), 1.37 (virtual dd, 12 H, PCHC*H$_3$*).

^{1}H{^{31}P} Solution NMR (600 MHz, CD$_2$Cl$_2$, 298 K): δ_H 7.77 (t, $^2J_{HH}$ = 7.9 Hz, 1 H, *para*-PONOP), 7.71 (s, 8 H, *ortho*-BAr$^F_4$), 7.56 (s, 4 H, *para*-BAr$^F_4$), 6.85 (d, $^2J_{HH}$ = 7.4 Hz, 2 H, *meta*-PONOP), 3.00 (br sept, $^2J_{HH}$ = 7.0 Hz, 4 H, PC*H*Me$_2$), 1.47 (d, $^2J_{HH}$ = 6.0 Hz, 12 H, PCHC*H$_3$*), 1.37 (d, $^2J_{HH}$ = 6.9 Hz, 12 H, PCHC*H$_3$*).

^{31}P{^{1}H} Solution NMR (242.95 MHz, CD$_2$Cl$_2$, 298 K): δ_P 225.2 (br s, FWHM = 165 Hz).

^{13}C{^{1}H} Solution NMR (150.91 MHz, CD$_2$Cl$_2$, 298 K): δ_C 217.2 (br, equatorial *C*O), 213.3 (br, axial *C*O), 162.9 (virtual t, *ortho*-PONOP), 162.2 (q, $^1J_{BC}$ = 50 Hz, *ipso*-BAr$^F_4$), 145.6 (s, *meta*-PONOP), 135.2 (s, *ortho*-BAr$^F_4$), 129.3 (qq, $^2J_{CF}$ = 32 Hz, $^4J_{CF}$ = 3 Hz, *meta*-BAr$^F_4$), 125.0 (q, $^1J_{CF}$ = 271 Hz, *C*F$_3$), 117.9 (sept., $^3J_{CF}$ = 4 Hz, *para*-BAr$^F_4$), 105.4 (s, *para*-PONOP), 33.0 (virtual t, P*C*H(CH$_3$)$_2$), 17.2 (s, PCH(*C*H$_3$)), 17.0 (s, PCH(*C*H$_3$)).

^{11}B{^{1}H} Solution NMR (192.53 MHz, CD$_2$Cl$_2$, 298 K): δ_B -6.6 (s, BAr$^F_4$).

^{31}P{^{1}H} CP SSNMR (162.06 MHz, 10 kHz spin rate, 298 K): δ_P 227.5, 226.1, 224.7, 223.2, 221.8, 220.5, 218.5.

^{13}C{^{1}H} CP SSNMR (100.66 MHz, 10 kHz spin rate, 298 K): δ_C 164.7, 163.68, 146.5, 138.4, 135.6, 134.6, 132.2, 131.5, 130.5, 125.9, 120.1, 119.3, 106.4, 103.8 (BAr$^F_4$ and PONOP environments), 38.5, 27.8 (methine), 19.7, 17.9, 17.4 (^{i}Pr methyl groups). CO resonance was not observed.

IR (ATR) νCO 2055 (w, s), 1970, (br, s) cm^{-1}.

ESI-MS m/z (CH₂Cl₂) *found* (*calc*): $C_{20}H_{31}MnNO_5P_2$ 482.1066 (482.1058).

Elemental analysis *calc* for $C_{52}H_{43}BF_{24}MnNO_5P_2$: C 46.42; H 3.22; N 1.04; *found*: C 46.34; H 3.17; N 1.12.

2.5bii. Preparation of [Mn(ⁱPr-PONOP)(THF)(CO)₂][BArᶠ₄], [Mn-THF]

Tetrahydrofuran (THF, 5 mL) was added to an ampoule charged with [Mn(ⁱPr-PONOP)(CO)₃][BArᶠ₄] (233 mg) and trimethylamine N-oxide (15 mg). A deep orange solution formed immediately. The solution was stirred at room temperature for 1 hour. The volatiles were thoroughly removed under reduced pressure, the solids taken up in THF (2 mL), isolated *via* cannula filtration and layered with hexane at room temperature to yield the complex as bright orange needles (156 mg, 65% yield).

¹H Solution NMR (600 MHz, CD₂Cl₂, 298 K): δ_H 7.86 (t, $^2J_{HH}$ = 8.0 Hz, 1 H, *para*-PONOP), 7.72 (br s, 8 H, *ortho*-BArᶠ₄), 7.56 (s, 4 H, *para*-BArᶠ₄), 6.92 (d, $^2J_{HH}$ = 8.2 Hz, 2 H, *meta*-PONOP), 4.61-1.70 (extremely broad, 18 H, fluxional THF exchange and overlapping methine environments), 1.48 (virtual m, 12 H, PCHMeC*H₃*), 1.34 (broad virtual m, 11 H, PCHC*H₃*Me). *Note: Fluxionality of THF ligand and decomposition in CD₂Cl₂ solution hindered accurate integration of ¹H spectrum.*

³¹P{¹H} Solution NMR (242.95 MHz, CD₂Cl₂, 298 K): δ_P 231.0 (br s, FWHM = 221 Hz).

^{13}C{^{1}H} Solution NMR (150.91 MHz, CD$_2$Cl$_2$, 298 K): δ_C 225.7 (m, *C*O), 164.5 (virtual t, *ortho*-PONOP), 162.2 (q, $^{1}J_{BC}$ = 50 Hz, *ipso*-BAr$^F_4$), 145.9 (s, *para*-PONOP), 135.2 (s, *ortho*-BAr$^F_4$), 129.2 (q, $^{2}J_{CF}$ = 31 Hz, *meta*-BAr$^F_4$), 125.0 (q, $^{1}J_{CF}$ = 271 Hz, *C*F$_3$), 117.9 (sept., $^{3}J_{CF}$ = 4 Hz, *para*-BAr$^F_4$), 105.3 (s, *meta*-PONOP), 32.0 (s, hexane), 29.5 (br s, methine), 23.1 (s, hexane), 17.3 (br s, PCH(*C*H$_3$)), 14.3 (s, hexane). Bound THF resonances not observed.

^{31}P{^{1}H} CP MAS SSNMR (162.06 MHz, 10 kHz spin rate, 298 K): δ_P 234.6, 232.6, 230.8, 227.4.

^{13}C{^{1}H} CP MAS SSNMR (100.66 MHz, 10 kHz spin rate, 298 K): δ_C 164.4, 158.9 (*ortho*-PONOP and *ipso*-BAr$^F_4$), 143.3, 136.4, 134.7, 132.3, 130.9, 130.2, 124.9, 118.6, 117.4 (overlapping PONOP and BAr$^F_4$ resonances), 104.4 (*meta*-PONOP), 76.8, 68.8, 65.4 (THF resonances), 29.8, 26.7, 25.2, 23.9 (methine resonances), 22.1, 17.9, 16.5, 15.7, 14.2, 12.8 (overlapping ^{i}Pr groups and hexane resonances). CO resonances not observed.

^{19}F{^{1}H} HPDEC MAS SSNMR (376.5 MHz, 20 kHz spin rate, 298 K): δ_F -63.3, -64.8.

IR (nujol) νCO 1963 (s), 1891 (s) cm^{-1}.

ESI-MS m/z (THF) *found (calc)*: C$_{19}$H$_{31}$MnNO$_4$P$_2$ 454.15 (454.11).

Elemental analysis *calc* for C$_{58}$H$_{58}$BF$_{24}$MnNO$_5$P$_2$: C 48.62; H 4.08; N 0.98; *found*: C 48.22; H 4.18; N 0.92.

2.5biii. Synthesis of [ReBr(*t*Bu-PONOP)(CO)$_2$

To an ampoule charged with ReBr(CO)$_5$ (490 mg) was added ^{t}Bu-PONOP (485 mg) in 1,2-difluorobenzene (10 mL). The reaction mixture was heated to 95 °C for 18 hours, turning from colourless to bright yellow. The reaction was cooled to room temperature and the volatiles removed under reduced pressure. The yellow solid was washed with pentane (3 x 10 mL), and extracted into diethyl ether (40 mL) and isolated *via* cannula filtration. The volatiles were removed under reduced pressure and dried *in vacuo* to yield a bright yellow microcrystalline solid. Yield: 607 mg (70%). Crystals suitable for single-crystal X-Ray diffraction were grown from slow vapour diffusion of pentane into a toluene solution at -30 °C.

^{1}H Solution NMR (500 MHz, C$_6$D$_6$, 298 K): δ_H 6.71 (t, $^2J_{HH}$ = 8.1 Hz, 1 H, *para*-PONOP), 6.14 (d, $^2J_{HH}$ = 8.1 Hz, 2 H, *meta*-PONOP), 1.66 (virtual t, 18 H, C(C*H*$_3$)$_3$), 1.32 (virtual t, 18 H, C(C*H*$_3$)$_3$).

^{31}P{^{1}H} Solution NMR (202.53 MHz, C$_6$D$_6$, 298 K): δ_P 196.0.

^{13}C{^{1}H} Solution NMR (125.80 MHz, C$_6$D$_6$, 298 K): δ_C 206.2 (s, equatorial *C*O), 198.9 (s, axial *C*O), 164.7 (virtual t, *ortho*-PONOP), 142.7 (s, *para*-PONOP), 102.6 (virtual t, *meta*-PONOP), 44.7 (virtual t, P*C*(CH$_3$)$_3$), 44.6 (virtual t, P*C*(CH$_3$)$_3$), 32.1 (virtual t, C(*C*H$_3$)$_3$), 28.0 (virtual t, C(*C*H$_3$)$_3$).

IR (ATR) νCO 1933 (s), 1842 (s).

ESI-MS m/z (CH$_2$Cl$_2$) *found (calc)*: C$_{23}$H$_{39}$NO$_4$P$_2$Re 642.1913 (642.1912) [M]$^+$-Br.

Elemental Analysis *calc* for $C_{23}H_{39}BrNO_4P_2Re$: C 38.28; H 5.45; N 1.94; *found*: C 38.58; H 5.63; N 1.91.

2.5biv. Synthesis of [Re(*t*Bu-PONOP)(CO)₂][BAr*F*₄], [Re]

A solution of [Re(*t*Bu-PONOP)Br(CO)₂] (400mg) in 1,2-difluorobenzene (10 mL) was added dropwise to a solution of Na[BAr*F*₄] (567 mg) in 1,2-difluorobenzene (10 mL). After several drops of [Re(*t*Bu-PONOP)Br(CO)₂] solution had been added, the reaction mixture rapidly changed from a cloudy white suspension to a bright red cloudy suspension. After complete addition, the reaction mixture was stirred at room temperature for 1 hour, then precipitated with hexane (200 mL). The reaction mixture was cannula filtered and the solids extracted into CH_2Cl_2 (15 mL). The solution was layered with hexane to yield the product as bright red block-like crystals. Yield: 670 mg (80%).

¹H Solution NMR (500 MHz, CD₂Cl₂, 298 K): δ_H 8.06 (t, $^2J_{HH}$ = 8.25 Hz, 1 H, *para*-PONOP), 7.73 (br m, 8 H, *ortho*-BAr*F*₄), 7.56 (s, 4 H, *para*-BAr*F*₄), 7.13 (d, $^2J_{HH}$ = 8.25 Hz, 2 H, *meta*-PONOP), 1.32 (virtual t, 36 H, C(C*H*₃)₃).

³¹P{¹H} Solution NMR (202.53 MHz, CD₂Cl₂, 298 K): δ_P 214.4.

¹³C{¹H} Solution NMR (125.80 MHz, CD₂Cl₂, 298 K): δ_C 198.8 (t, $^2J_{CP}$ = 5 Hz, *C*O), 166.5 (virtual t, *ortho*-PONOP), 162.2 (q, $^1J_{BC}$ = 50 Hz, *ipso*-BAr*F*₄), 148.8 (s, *para*-PONOP), 135.2 (s, *ortho*-BAr*F*₄), 129.3 (qq, $^2J_{CF}$ = 32 Hz, $^3J_{CF}$ = 3 Hz, *meta*-BAr*F*₄), 125.0 (t, $^1J_{CF}$ = 272 Hz, *C*F₃), 117.9 (sept., $^3J_{CF}$ = 4 Hz, *para*-BAr*F*₄), 105.0 (virtual t, *meta*-PONOP), 43.8 (virtual t, P*C*(CH₃)), 27.5 (virtual t, C(*C*H₃)).

^{31}P{^{1}H} CP MAS SSNMR (162.02 MHz, 10 kHz spin rate, 298 K): δ_P 217.8 (v. broad), 214.5 (v. broad).

^{13}C{^{1}H} CP MAS SSNMR (100.63 MHz, 10 kHz spin rate, 298 K): δ_C 166.1-163.1 (*ortho*-PONOP and *ipso*-BAr$^F_4$), 147.5 (*para*-PONOP), 136.1, 134.9, 133.0, 130.4, 124.8, 117.9 (overlapping PONOP and BAr$^F_4$ resonances), 105.5, 102.6 (*meta*-PONOP), 47.6, 42.2, 41.2, 40.7 (PC(CH$_3$)$_3$), 26.7 (PC(CH$_3$)$_3$).

^{19}F{^{1}H} HPDEC MAS SSNMR (376.5 MHz, 20 kHz spin rate, 298 K): δ_F -62.5, -63.6.

IR (ATR) vCO 1965 (s), 1893 (s).

ESI-MS m/z (CH$_2$Cl$_2$) *found (calc)*: C$_{23}$H$_{39}$NO$_4$P$_2$Re 642.1904 (642.1912).

Elemental Analysis *calc* for C$_{55}$H$_{51}$BF$_{24}$NO$_4$P$_2$Re: C 43.90; H 3.42; N 0.93; *found*: C 44.09; H 3.62; N 0.92.

2.5bv. Formation of [Re(^{t}Bu-PONOP)(H$_2$)(CO)$_2$][BAr$^F_4$]

An NMR tube fitted with a J. Young value was charged with [(^{t}Bu-PONOP)Re(CO)$_2$][BAr$^F_4$] (10 mg). CD$_2$Cl$_2$ (0.6 mL) was vacuum transferred onto the solids and the headspace backfilled with dihydrogen (1 bar gauge). The NMR tube was added to a pre-cooled spectrometer (193 K). [(^{t}Bu-PONOP)Re(H$_2$)(CO)$_2$][BAr$^F_4$] was formed in approximately 5% yield (NMR yield). *Warming the sample above 200 K led to loss of all H$_2$-bound product.*

^{1}H Solution NMR (500 MHz, CD$_2$Cl$_2$, 193 K): δ_H 7.72 (s, 8 H, *ortho*-BAr$^F_4$), 7.52 (s, 4 H, *para*-BAr$^F_4$), 6.84 (d, $^2J_{HH}$ = 8.21 Hz, 0.11 H *meta*-PONOP), 1.39 (b virtual m, 3 H, C(CH_3)$_3$), -2.85 (br, 0.11 H, σ-H$_2$).

Note: Peaks integrated relative to residual BAr$^F_4^-$ protons. Para-PONOP resonance not observed due to overlap with the ortho-BAr$^F_4$ resonances.

^{31}P{^{1}H} Solution NMR (202.54 MHz, CD$_2$Cl$_2$, 298 K): δ_P 203.0.

2.5bvi. Solid-state synthesis of [Mn-CO]

An ampoule was charged with finely ground [Mn(^{i}Pr-PONOP)(THF)(CO)$_2$][BAr$^F_4$]•½ hexane (50 mg), backfilled with CO (1 bar gauge) and sealed for 28 hours (optimised). The volatiles removed under reduced pressure to yield white microcrystalline [Mn(^{i}Pr-PONOP)(CO)$_3$][BAr$^F_4$] in quantitative yield.

^{1}H Solution NMR (600 MHz, CD$_2$Cl$_2$, 298 K): δ_H 7.81 (t, $^2J_{HH}$ = 8.2 Hz, 2 H, *para*-PONOP), 7.71 (s, 8 H, *ortho*-BAr$^F_4$), 7.55 (s, 4 H, *para*-BAr$^F_4$), 6.87 (d, $^2J_{HH}$ = 8.2 Hz, *meta*-PONOP), 3.68 (virtual m, 1 H, OC*H*$_2$), 3.01 (virtual m, 4 H, PC*H*Me$_2$), 1.82 (virtual m, 1 H, OCH$_2$C*H*$_2$), 1.48 (virtual dd, 12 H, PCHC*H*$_3$), 1.38 (virtual dd, 12 H, PCHC*H*$_3$).

^{31}P{^{1}H} Solution NMR (242.95 MHz, CD$_2$Cl$_2$, 298 K): δ_P 225.2 (br s, fwhm = 187 Hz).

^{13}C{^{1}H} Solution NMR (150.91 MHz, CD$_2$Cl$_2$, 298 K): δ_C 162.9 (virtual t, *ortho*-PONOP), 162.2 (q, $^1J_{BC}$ = 50 Hz, *ipso*-BAr$^F_4$), 145.7 (s, *meta*-PONOP), 135.2 (s, *ortho*-BAr$^F_4$), 129.3 (qq, $^2J_{CF}$ = 31 Hz, $^4J_{CF}$ = 3 Hz, *meta*-BAr$^F_4$), 125.0 (q, $^1J_{CF}$ = 272 Hz, CF$_3$), 117.9 (sept., $^3J_{CF}$ = 4 Hz, *para*-BAr$^F_4$), 105.4 (virtual t, *para*-PONOP), 68.2 (br s, OC*H*$_2$CH$_2$), 33.0 (virtual t, PCHMe$_2$), 26.0 (br s, OCH$_2$C*H*$_2$), 17.2 (s, PCHC*H*$_3$), 17.0 (s, PCHC*H*$_3$).

^{31}P{^{1}H} CP MAS SSNMR (162.06 MHz, 10 kHz spin rate, 298 K): δ_P 230.4, 227.5, 226.0, 224.6, 223.2, 221.8, 220.5, 218.6.

^{13}C{^{1}H} CP MAS SSNMR (100.66 MHz, 10 kHz spin rate, 298 K): δ_C 163.3 (*ortho*-PONOP and *ipso*-BAr$^F_4$), 145.1 (*meta*-PONOP), 137.1, 135.3, 133.9, 132.3, 130.6, 129.5, 124.8 (overlapping BAr$^F_4$ and PONOP resonances), 117.2, 104.5, 102.6 (BAr$^F_4$ and PONOP resonances) 67.3 (THF), 37.4, 36.3, 34.8 (methine resonances), 26.6 (THF), 25.3 (hexane), 18.5, 17.3, 16.5, 15.7, 14.0, 13.3 (iPr methyl and hexane resonances).

^{19}F{^{1}H} HPDEC MAS SSNMR (376.5 MHz, 20 kHz spin rate, 298 K): δ_F -59.5, -61.7, -63.4, -64.5, -65.0.

IR (ATR) ν(CO) 2057 (w, s), 1980 (s), 1947 (s) cm^{-1}

ESI-MS (CH$_2$Cl$_2$) *found (calc)*: C$_{20}$H$_{31}$MnNO$_5$P$_2$ 482.1067 (482.1058).

Elemental Analysis *calc* for C$_{52}$H$_{43}$BF$_{24}$MnNO$_5$P$_2$: C 46.42; H 3.22; N 1.04; *found*: C 46.38; H 3.69; N 0.93.

2.5bvii. Solid-state synthesis of [Re-CO]

An ampoule was charged with crystalline [Re(^{t}Bu-PONOP)(CO)$_2$][BAr$^F_4$] (25 mg) and the ampoule backfilled with CO (1 bar gauge). The appearance of the red block-like crystals changed over 24 hours to white crystalline blocks with microcrystalline powder on the surface of the crystals. The ampoule was placed under vacuum and replaced with Ar (0.2 bar gauge). This process was repeated for a total of three vacuum/Ar cycles, yielding [Re(^{t}Bu-PONOP)(CO)$_3$][BAr$^F_4$] in quantitative yield.

^{1}H Solution NMR (500 MHz, CD$_2$Cl$_2$, 298 K): δ_H 7.86 (tt, $^2J_{HH}$ = 8.1 Hz, $^5J_{HP}$ = 0.8 Hz, 1 H, *para*-PONOP), 7.72 (br m, 8 H, *ortho*-BAr$^F_4$), 7.56 (s, 4 H, *para*-BAr$^F_4$), 6.95 (d, $^2J_{HH}$ = 8.2 Hz, 2 H, *meta*-PONOP), 1.49 (virtual t, 36 H, C(CH_3)$_3$).

^{31}P{^{1}H} Solution NMR (202.53 MHz, CD$_2$Cl$_2$, 298 K): δ_P 198.2.

^{13}C{^{1}H} Solution NMR (125.80 MHz, CD$_2$Cl$_2$, 298 K): δ_C 194.7 (t, $^2J_{CP}$ = 9 Hz, axial *C*O), 192.7 (br s, equatorial *C*O), 163.7 (s, *ortho*-PONOP), 162.2 (q, $^1J_{BC}$ = 50 Hz, *ipso*-BAr$^F_4$), 146.5 (s, *para*-PONOP), 135.2 (s, *ortho*-BAr$^F_4$), 129.3 (qq, $^2J_{CF}$ = 31 Hz, $^3J_{CF}$ = 3 Hz, *meta*-BAr$^F_4$), 125.0 (q, $^1J_{CF}$ = 272 Hz, CF$_3$), 117.9 (quint, $^3J_{CF}$ = 4 Hz, *para*-BAr$^F_4$), 105.2 (virtual t, *meta*-PONOP), 44.4 (virtual t, *C*(CH$_3$)$_3$), 29.0 (virtual t, C(*C*H$_3$)$_3$).

^{31}P{^{1}H} CP MAS SSNMR (162.03 MHz, 10 kHz spin rate, 298 K): δ_P 200.3 (v. broad, FWHM = 2100 Hz).

^{13}C{^{1}H} CP MAS SSNMR (100.63 MHz, 10 kHz spin rate, 298 K): δ_c 163.6 (*ortho*-PONOP), 146.0 (*para*-PONOP), 136.2, 135.0, 133.9, 133.1, 131.0, 130.1 (overlapping BAr$^F_4$ resonances) 124.5 (CF$_3$), 119.2, 117.8, 116.6 (overlapping BAr$^F_4$ resonances), 105.0, 102.7 (*meta*-PONOP resonances), 43.9, 42.9, 42.2 (*C*Me$_3$ resonances), 29.6, 29.1, 27.1, 26.5 (methyl resonances).

^{19}F{^{1}H} HPDEC MAS SSNMR (376.5 MHz, 20 kHz spin rate, 298 K): δ_F -61.8, -63.0, -64.3.

IR (ATR) νCO 2050 (s), 1956 (s), 1942 (s)

ESI-MS (CH$_2$Cl$_2$) *found* (*calc*): C$_{24}$H$_{39}$NO$_5$P$_2$Re 670.1877 (670.1861).

2.5bviii. General Preparation of [Re]@poly(ethyl vinyl ether)

Approximately 5 similarly sized crystals of **[Re]** (~1 mg each) were mounted to a specially designed J Young tap using silicone vacuum grease. The J Young tap was fitted into a H-flask. Care was taken to prevent any of the crystals falling from the tap. Ethyl vinyl ether (~0.1 mL) was vacuum transferred to the opposite side of the H-flask. The whole apparatus was placed under vacuum ($<2\times10^{-2}$ mbar) and the ethyl vinyl ether was allowed to warm to room temperature. After the desired reaction time has elapsed, the reaction was quenched by placing the whole apparatus under dynamic vacuum ($<2\times10^{-2}$ mbar) to remove residual ethyl vinyl ether.

2.6 References

1.   S. K. Furfari, B. E. Tegner, A. L. Burnage, L. R. Doyle, A. J. Bukvic, S. A. Macgregor and A. S. Weller, *Chem. Eur. J.*, 2021, **27**, 3177-3183.

2.   A. J. Bukvic, A. L. Burnage, G. J. Tizzard, A. J. Martínez-Martínez, A. I. McKay, N. H. Rees, B. E. Tegner, T. Krämer, H. Fish, M. R. Warren, S. J. Coles, S. A. Macgregor and A. S. Weller, *J. Am. Chem. Soc.*, 2021, **143**, 5106-5120.

3.   Y. Li, B. Zhao, J. P. Xue, J. Xie, Z. S. Yao and J. Tao, *Nat. Commun.*, 2021, **12**, 6908.

4.   L. Zhu, R. O. Al-Kaysi and C. J. Bardeen, *J. Am. Chem. Soc.*, 2011, **133**, 12569-12575.

5.   S. Saha, M. K. Mishra, C. M. Reddy and G. R. Desiraju, *Acc. Chem. Res.*, 2018, **51**, 2957-2967.

6.   D. P. Karothu, J. Weston, I. T. Desta and P. Naumov, *J. Am. Chem. Soc.*, 2016, **138**, 13298-13306.

7.   H. Koshima, N. Ojima and H. Uchimoto, *J. Am. Chem. Soc.*, 2009, **131**, 6890-6891.

8.   O. S. Bushuyev, A. Tomberg, T. Friščić and C. J. Barrett, *J. Am. Chem. Soc.*, 2013, **135**, 12556-12559.

9.   E. Ahmed, D. P. Karothu and P. Naumov, *Angew. Chem. Int. Ed.*, 2018, **57**, 8837-8846.

10.   M. K. Panda, R. Centore, M. Causà, A. Tuzi, F. Borbone and P. Naumov, *Sci. Rep.*, 2016, **6**, 29610.

11.   I. Halasz, *Cryst. Growth Des.*, 2010, **10**, 2817-2823.

12.   A. I. Vicente, A. Joseph, L. P. Ferreira, M. de Deus Carvalho, V. H. N. Rodrigues, M. Duttine, H. P. Diogo, M. E. Minas da Piedade, M. J. Calhorda and P. N. Martinho, *Chem. Sci.*, 2016, **7**, 4251-4258.

13.   P. Naumov, D. P. Karothu, E. Ahmed, L. Catalano, P. Commins, J. Mahmoud Halabi, M. B. Al-Handawi and L. Li, *J. Am. Chem. Soc.*, 2020, **142**, 13256-13272.

14.   C. M. Reddy, G. Rama Krishna and S. Ghosh, *CrystEngComm*, 2010, **12**, 2296.

15.   S. Kusumoto, Y. Kim and S. Hayami, *Coord. Chem. Rev.*, 2023, **475**, 214890.

16.   B. K. Saha, S. A. Rather and A. Saha, *Cryst. Growth Des,*, 2016, **16**, 3059-3062.

17.   B. K. Saha, R. V. P. Veluthaparambath and V. Krishna G, *Chem. Asian J.*, 2023, **18**.

18. M. K. Panda, S. Ghosh, N. Yasuda, T. Moriwaki, G. D. Mukherjee, C. M. Reddy and P. Naumov, *Nat. Chem.*, 2015, **7**, 65-72.

19. M. C. Etter and A. R. Siedle, *J. Am. Chem. Soc.*, 1983, **105**, 641-643.

20. M. K. Panda, T. Runcevski, S. C. Sahoo, A. A. Belik, N. K. Nath, R. E. Dinnebier and P. Naumov, *Nat. Commun.*, 2014, **5**, 4811.

21. J. C. Goodall, M. A. Sajjad, E. A. Thompson, S. J. Page, A. M. Kerrigan, H. T. Jenkins, J. M. Lynam, S. A. Macgregor and A. S. Weller, *Chem. Commun.*, 2023, **59**, 10749-10752.

22. S. D. Pike, A. L. Thompson, A. G. Algarra, D. C. Apperley, S. A. Macgregor and A. S. Weller, *Science*, 2012, **337**, 1648-1651.

23. F. M. Chadwick, N. H. Rees, A. S. Weller, T. Krämer, M. Iannuzzi and S. A. Macgregor, *Angew. Chem. Int. Ed.*, 2016, **55**, 3677-3681.

24. S. D. Pike, F. M. Chadwick, N. H. Rees, M. P. Scott, A. S. Weller, T. Krämer and S. A. Macgregor, *J. Am. Chem. Soc.*, 2015, **137**, 820-833.

25. C. G. Royle, L. Sotorrios, M. R. Gyton, C. N. Brodie, A. L. Burnage, S. K. Furfari, A. Marini, M. R. Warren, S. A. Macgregor and A. S. Weller, *Organometallics*, 2022, **41**, 3270-3280.

26. A. J. Blake, N. R. Champness, T. L. Easun, D. R. Allan, H. Nowell, M. W. George, J. Jia and X.-Z. Sun, *Nat. Chem.*, 2010, **2**, 688-694.

27. R. J. Young, M. T. Huxley, L. Wu, J. Hart, J. O'Shea, C. J. Doonan, N. R. Champness and C. J. Sumby, *Chem. Sci.*, 2023, **14**, 9409-9417.

28. M. Kawano, Y. Kobayashi, T. Ozeki and M. Fujita, *J. Am. Chem. Soc.*, 2006, **128**, 6558-6559.

29. A. M. Tondreau and J. M. Boncella, *Polyhedron*, 2016, **116**, 96-104.

30. I. G. Virrels, M. W. George, J. J. Turner, J. Peters and A. Vlček, *Organometallics*, 1996, **15**, 4089-4092.

31. I. R. Farrell, P. Matousek, M. Towrie, A. W. Parker, D. C. Grills, M. W. George and A. Vlček, *Inorg. Chem.*, 2002, **41**, 4318-4323.

32. B. J. Aucott, A.-K. Duhme-Klair, B. E. Moulton, I. P. Clark, I. V. Sazanovich, M. Towrie, L. A. Hammarback, I. J. S. Fairlamb and J. M. Lynam, *Organometallics*, 2019, **38**, 2391-2401.

33. P. Raghavan, *At. Data Nucl. Data Tables*, 1989, **42**, 189-291.

34. D. Rentsch, PhD, Universitat Zurich, 1997.

35. J. D. Cotton and R. D. Markwell, *Inorg. Chim. Acta*, 1990, **175**, 187-191.

36. D. Rentsch, R. Hany and W. von Philipsborn, *Magn. Reson. Chem.*, 1997, **35**, 832-838.

37. D. Rentsch, L. Nill, W. von Philipsborn, D. R. Sidler, P. J. Rybczynski and P. DeShong, *Magn. Reson. Chem.*, 1998, **36**, S54-S60.

38. J. Herzfeld and A. E. Berger, *J. Chem. Phys.*, 2008, **73**, 6021-6030.

39. J. Mason, *Solid State Nucl. Magn. Reson.*, 1993, **2**, 285-288.

40. K. W. Feindel and R. E. Wasylishen, *Can. J. Chem.*, 2004, **82**, 27-44.

41.   C. Raynaud, E. Norbert-Agaisse, B. R. James and O. Eisenstein, *Inorg. Chem.*, 2020, **59**, 17038-17048.

42.   U. Koelle, *J. Organomet. Chem.*, 1978, **155**, 53-62.

43.   S. Parsons, *Acta Crystallogr D Biol Crystallogr*, 2003, **59**, 1995-2003.

44.   J. G. Wittmann and M. G. Rudolph, *Acta Crystallogr D Biol Crystallogr*, 2007, **63**, 744-749.

45.   M. Glatz, J. Pecak, L. Haager, B. Stoeger and K. Kirchner, *Monatsh. Chem.*, 2019, **150**, 111-119.

46.   S. Kundu, W. W. Brennessel and W. D. Jones, *Inorg. Chem.*, 2011, **50**, 9443-9453.

47.   V. Papa, Y. Cao, A. Spannenberg, K. Junge and M. Beller, *Nat. Catal.*, 2020, **3**, 135-142.

48.   Geom – Geometry Indicies Calculations, http://kchn.pg.gda.pl/geom/ (accessed: 22/03/24).

49.   A. W. Addison, T. N. Rao, J. Reedijk, J. van Rijn and G. C. Verschoor, *J. Chem. Soc., Dalton Trans.*, 1984, 1349-1356.

50.   M. Brookhart, M. L. H. Green and G. Parkin, *Proc. Natl. Acad. Sci. U.S.A.*, 2007, **104**, 6908-6914.

51.   A. C. Cooper, W. E. Streib, O. Eisenstein and K. G. Caulton, *J. Am. Chem. Soc.*, 1997, **119**, 9069-9070.

52.   R. C. Knighton, J. Emerson-King, J. P. Rourke, C. A. Ohlin and A. B. Chaplin, *Chem. Eur. J.*, 2018, **24**, 4927-4938.

53.   J. J. Race, A. L. Burnage, T. M. Boyd, A. Heyam, A. J. Martínez-Martínez, S. A. Macgregor and A. S. Weller, *Chem. Sci.*, 2021, **12**, 8832-8843.

54.   R. F. W. Bader, *Atoms in Molecules: A Quantum Theory*, Clarendon Press, Oxford, 1994.

55.   F. Cortés-Guzmán and R. F. W. Bader, *Coord. Chem. Rev.*, 2005, **249**, 633-662.

56.   G. Ujaque, A. C. Cooper, F. Maseras, O. Eisenstein and K. G. Caulton, *J. Am. Chem. Soc.*, 1998, **120**, 361-365.

57.   AIMAll, http://aim.tkgristmill.com (accessed 22/03/24).

58.   W. A. King, X.-L. Luo, B. L. Scott, G. J. Kubas and K. W. Zilm, *J. Am. Chem. Soc.*, 1996, **118**, 6782-6783.

59.   A. Toupadakis, G. J. Kubas, W. A. King, B. L. Scott and J. Huhmann-Vincent, *Organometallics*, 1998, **17**, 5315-5323.

60.   W. A. King, B. L. Scott, J. Eckert and G. J. Kubas, *Inorg. Chem.*, 1999, **38**, 1069-1084.

61.   M. S. Chinn, D. M. Heinekey, N. G. Payne and C. D. Sofield, *Organometallics*, 1989, **8**, 1824-1826.

62.   C. Bianchini, A. Marchi, L. Marvelli, M. Peruzzini, A. Romerosa, R. Rossi and A. Vacca, *Organometallics*, 1995, **14**, 3203-3215.

63.   D. M. Heinekey, M. H. Voges and D. M. Barnhart, *J. Am. Chem. Soc.*, 1996, **118**, 10792-10802.

64.   D. M. Heinekey, C. E. Radzewich, M. H. Voges and B. M. Schomber, *J. Am. Chem. Soc.*, 1997, **119**, 4172-4181.

65.   G. J. Kubas, *J. Organomet. Chem.*, 2001, **635**, 37-68.

66.   D.-K. Bučar and L. R. MacGillivray, *J. Am. Chem. Soc.*, 2007, **129**, 32-33.

67.   B. L. Nannenga and T. Gonen, *Nat. Methods.*, 2019, **16**, 369-379.

68.   J. A. Rodriguez, D. S. Eisenberg and T. Gonen, *Curr. Opin. Struct. Biol.*, 2017, **46**, 79-86.

69.   J. A. Rodriguez, M. I. Ivanova, M. R. Sawaya, D. Cascio, F. E. Reyes, D. Shi, S. Sangwan, E. L. Guenther, L. M. Johnson, M. Zhang, L. Jiang, M. A. Arbing, B. L. Nannenga, J. Hattne, J. Whitelegge, A. S. Brewster, M. Messerschmidt, S. Boutet, N. K. Sauter, T. Gonen and D. S. Eisenberg, *Nature*, 2015, **525**, 486-490.

70.   E. L. Guenther, Q. Cao, H. Trinh, J. Lu, M. R. Sawaya, D. Cascio, D. R. Boyer, J. A. Rodriguez, M. P. Hughes and D. S. Eisenberg, *Nat. Struct. Mol. Biol.*, 2018, **25**, 463-471.

71.   P. Krotee, S. L. Griner, M. R. Sawaya, D. Cascio, J. A. Rodriguez, D. Shi, S. Philipp, K. Murray, L. Saelices, J. Lee, P. Seidler, C. G. Glabe, L. Jiang, T. Gonen and D. S. Eisenberg, *J. Biol. Chem.*, 2018, **293**, 2888-2902.

72. C. G. Jones, M. Asay, L. J. Kim, J. F. Kleinsasser, A. Saha, T. J. Fulton, K. R. Berkley, D. Cascio, A. G. Malyutin, M. P. Conley, B. M. Stoltz, V. Lavallo, J. A. Rodriguez and H. M. Nelson, *ACS Cent. Sci.*, 2019, **5**, 1507-1513.

73. H. A. Mills, C. G. Jones, K. P. Anderson, A. D. Ready, P. I. Djurovich, S. I. Khan, J. N. Hohman, H. M. Nelson and A. M. Spokoyny, *Chem. Mater.*, 2022, **34**, 6933-6943.

74. L. R. Doyle, E. A. Thompson, A. L. Burnage, A. C. Whitwood, H. T. Jenkins, S. A. Macgregor and A. S. Weller, *Dalton Trans.*, 2022, **51**, 3661-3665.

75. A. Saha, S. S. Nia and J. A. Rodríguez, *Chem. Rev.*, 2022, **122**, 13883-13914.

76. S. Grimme, J. Antony, S. Ehrlich and H. Krieg, *J. Chem. Phys.*, 2010, **132**, 154104.

77. T. Lu and Q. Chen, *J. Comput. Chem.*, 2022, **43**, 539-555.

78. S. Aoshima and S. Kanaoka, *Chem. Rev.*, 2009, **109**, 5245-5287.

79. V. Kottisch, Q. Michaudel and B. P. Fors, *J. Am. Chem. Soc.*, 2016, **138**, 15535-15538.

80. A. J. Bukvic, D. G. Crivoi, H. G. Garwood, A. I. McKay, T. T. D. Chen, A. J. Martínez-Martínez and A. S. Weller, *Chem. Commun.*, 2020, **56**, 4328-4331.

81. H. Watanabe, T. Yamamoto, A. Kanazawa and S. Aoshima, *Polym. Chem.*, 2020, **11**, 3398-3403.

82. A. J. Martínez-Martínez and A. S. Weller, *Dalton Trans.*, 2019, **48**, 3551-3554.

83.   A. Johnson, C. G. Royle, C. N. Brodie, A. J. Martínez-Martínez, S. B. Duckett and A. S. Weller, *Inorg. Chem.*, 2021, **60**, 13903-13912.

84.   M. W. Ndinguri, C. A. Black, A. L. Gosser, S. Reitz, C. Sutphin, F. R. Fronczek and L. E. Cormier, *Inorg. Chim. Acta*, 2021, **520**, 120291.

<u>Chapter 3 – Single-Crystal to Single-Crystal Reactivity of a Stable Rh(III) η¹-σ-Alkane Complex Supported by a Structurally-Responsive Ligand</u>

3.1 Introduction

3.1a Metal-Ligand Cooperation

Metal-ligand cooperation (MLC) is defined as a process in which both the metal and ligand are directly involved in bond cleavage or formation, both are chemically modified, and the coordination sphere of the metal is altered during the course of a reaction.[1] The study of MLC and the design of relevant ligand frameworks has grown into a major field of research in homogeneous catalysis.[1-3] Examples of MLC are even found in nature: [FeFe]-hydrogenase heterolytically cleaves dihydrogen through MLC with a pendant amine moiety, without change in metal oxidation state (**Scheme 3.1**).[4-6]
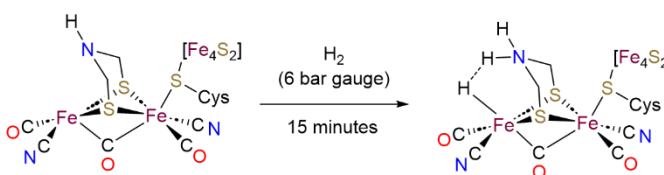
Scheme 3.1: Heterolytic cleavage of dihydrogen by [FeFe]-hydrogenase *via* metal-ligand cooperation.[4-6]

Catalytic processes involving aromatic pincer ligands can invoke MLC mechanisms through disruption, or restoration, of the aromatic system. The Milstein group have pioneered this field over the last 20 years, utilising such aromatisation/dearomatisation for a wide range of catalytic reactions.[1-3, 7-9] The first reported example was the hydrogenation of esters to alcohols by a ruthenium pyridyl pincer complex, where MLC was shown to play a central role in the pathway.[7] The aromaticity of the pyridyl system in the pincer ligand is disrupted

in the starting catalyst (Complex **A**, **Scheme 3.2**), and the aromaticity is restored through hydrogenation of the complex (Complex **B/E**). The aromaticity is then re-disrupted through deprotonation of the neighbouring methylene as the hemiacetal and alcohol are eliminated from complexes **D** and **G**, respectively, to reform complex **A**. This catalytic MLC pathway operates at low loadings of 0.02 mol% of ruthenium complex, under relatively mild conditions (115 °C, 5 atm H_2, 1,4-dioxane solvent). Catalytic hydrogenation of esters bypasses the traditional stoichiometric reductions with metal-hydride reagents such as $Na[BH_4]$ and $Li[AlH_4]$ employed in organic synthesis,[10-12] with no additional reagents required except H_2 gas.
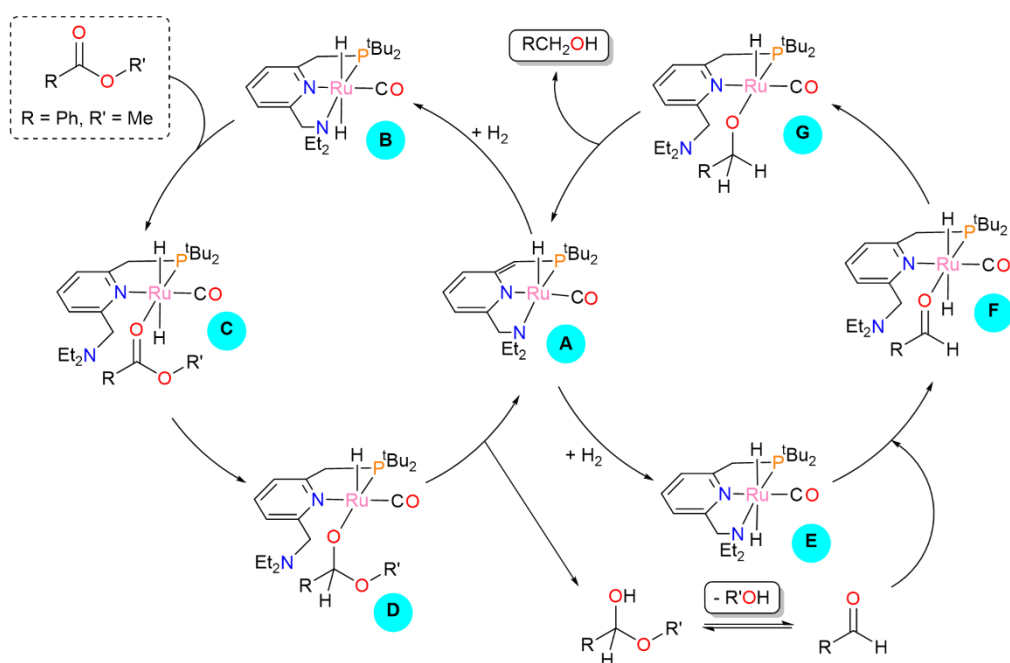
Scheme 3.2: Atom-efficient ester hydrogenation to alcohols through metal-ligand cooperation with a ruthenium pincer complex.[7]

Bond cleavage and formation across M–L (L = B, N, O, S, C, P)[1, 2, 13-19] bonds through a 1,2-addition pathway is a well-known example of MLC. The metal-amine/amide

bond is among the most well-studied within catalytic transformations invoking

MLC. For example, the hydroboration and hydrosilylation of ketones has been

achieved through MLC at a Cu(I) complex (**Scheme 3.3**).[18] The E–H (E = Si or B)

bond is cleaved across the Cu–N(amide) bond, forming a copper-hydride and a Cu–

N(amine) bond through a 1,2-addition. The ketone is then

hydroborated/hydrosilylated through an outer-sphere, 1,2-dipolar addition across

the C=O bond.
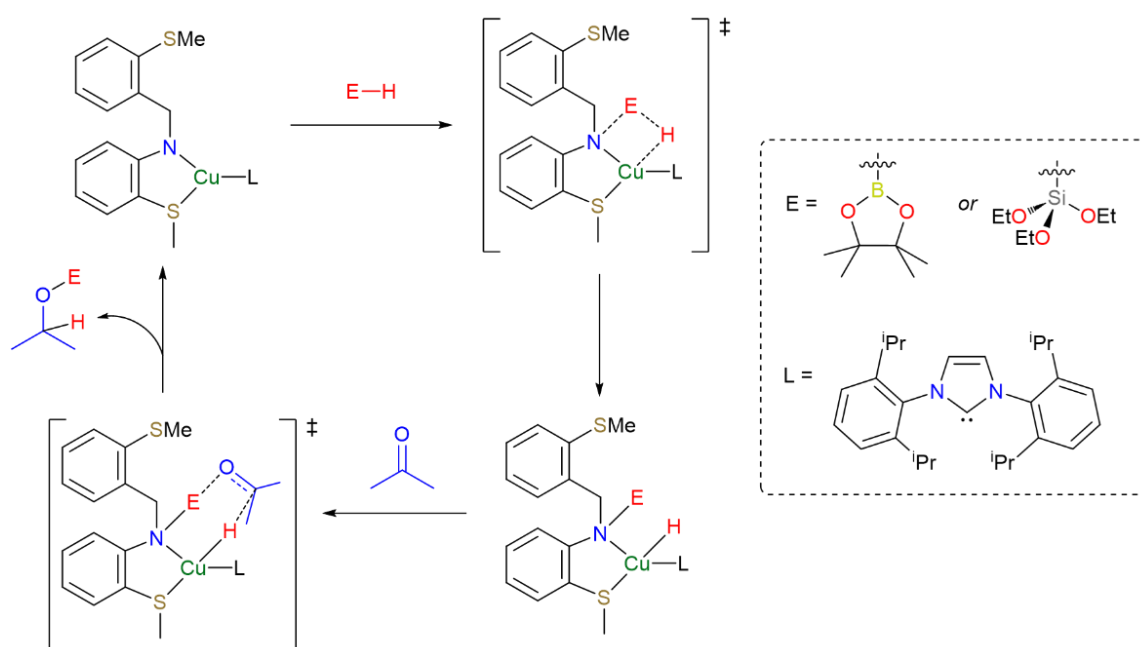
Scheme 3.3: Hydroboration and hydrosilylation of ketones through metal-ligand cooperation at a copper(I) complex.[18]

3.1b Structurally-Responsive Ligands

Ligands which can alter their binding modes through dynamic changes to their

denticity, hapticity or geometry, are referred to as structurally-responsive ligands.[20]

Classic examples of this class of ligand include the ring slippage of indenyl,[21-23]

aryl[24-26] and cyclopentadienyl ligands;[23, 27, 28] hemilabile ligands;[8, 29-34] and more recently, allosteric-type ligands.[35-38] This ligand class has been widely researched in organometallic chemistry, owing to their potential to self-tune the electronic and steric properties to the demands of the metal centre. This self-tuning often establishes a lower energy pathway which can have major improvements on rates of reaction (**Figure 3.1**).[20, 21, 29, 30, 33]
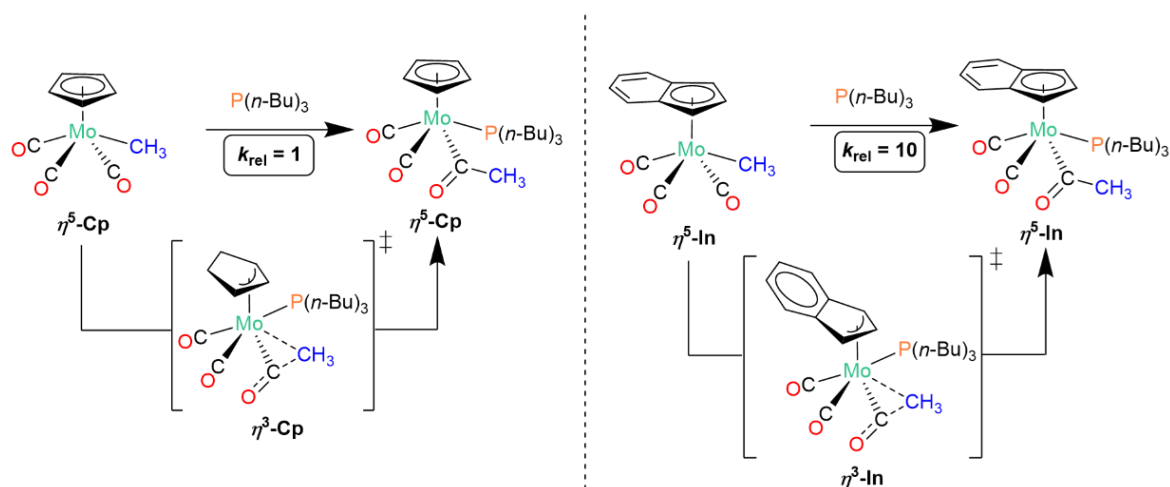
Figure 3.1: Cyclopentadienyl (*left*) and indenyl (*right*) ligands are classic examples of structurally-responsive ligands, which can alter their hapticity to the electronic demands of the metal centre. Indenyl ligands undergo this structural response much more rapidly than cyclopentadienyl,[21] as the formation of the aromaticity in the adjacent phenyl ring provides a lower energy pathway.

An example of structurally-responsive ligands in a catalytic transformation is the application of Xantphos [4,5-bis(diphenylphosphino)-9,9-dimethylxanthene] in palladium-catalysed amination of aryl (pseudo)halides (**Scheme 3.4**).[33, 39] In this work, the hemilabile ether-linkage of Xantphos can bias the pre-equilibrium by forming a κ^3-POP coordination and forcing decoordination of the (pseudo)halide

from the palladium centre. The hemilability of the ether-linkage also plays a role in catalyst stability, increasing catalyst efficiency.
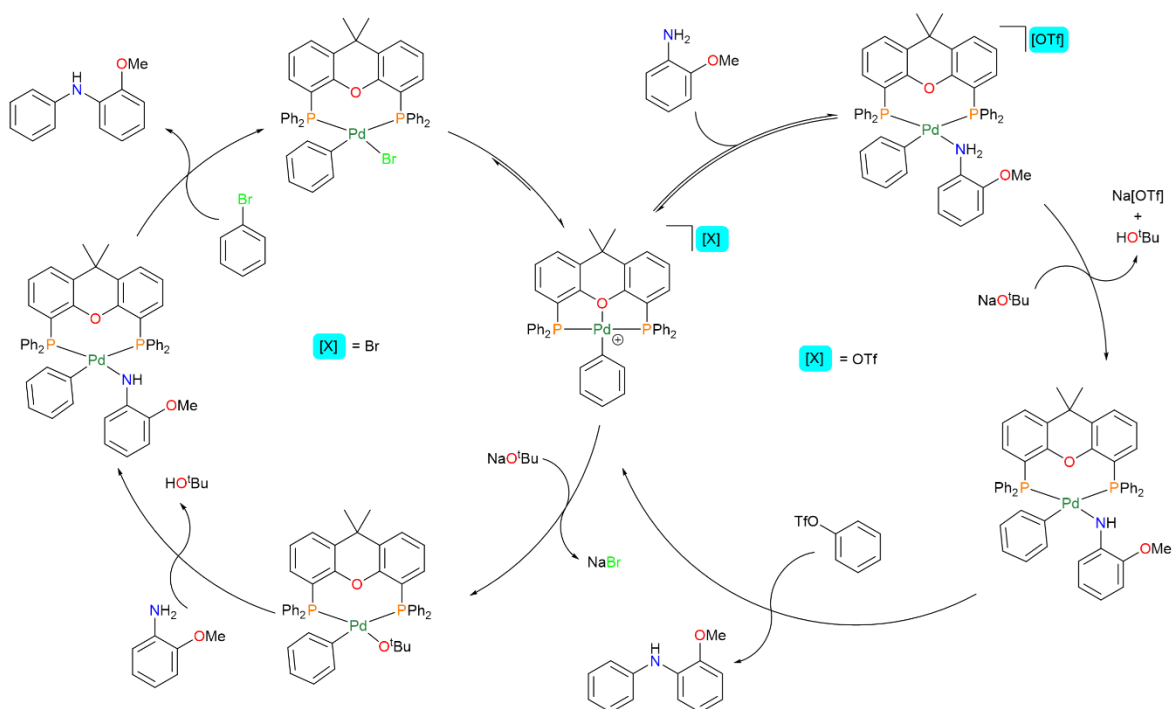
Scheme 3.4: Catalytic cycles for the amination of aryl bromides (*left*) and aryl triflates (*right*) by a palladium-Xantphos complex.[39]

Allosteric ligands are ligands which undergo structural-responses based on external stimuli.[20, 40] An example of this type of structurally-responsive ligand are crown ether-affixed pincer ligands.[40, 41] As shown in **Scheme 3.5**, the crown ether linkage can be hemilabile, masking a vacant site.[35] The supramolecular recognition of alkali metal salts can be used to tune reaction rates of ligand substitution, H/D exchange (**Scheme 3.5**),[35] or alkene isomerisation.[42] The supramolecular recognition of alkali metal salts increases the H/D exchange process shown in **Scheme 3.5** 20- and 250-fold for Na$^+$ and Li$^+$, respectively. This also shows that the small energy difference between the binding of Li$^+$ and Na$^+$ to the aza-15-crown-5 moiety

(typically around 1 kcal mol^{-1})[43] is responsible for an order of magnitude increase in reaction rate.

No Additive, k_{obs} = 1.2 x 10^{-6} s^{-1}

= 0.3 equiv Na$^+$, k_{obs} = 2.4 x 10^{-5} s^{-1}
= 1.2 equiv Na$^+$, k_{obs} = 9.0 x 10^{-5} s^{-1}
= 0.4 equiv Li$^+$, k_{obs} = 2.8 x 10^{-4} s^{-1}
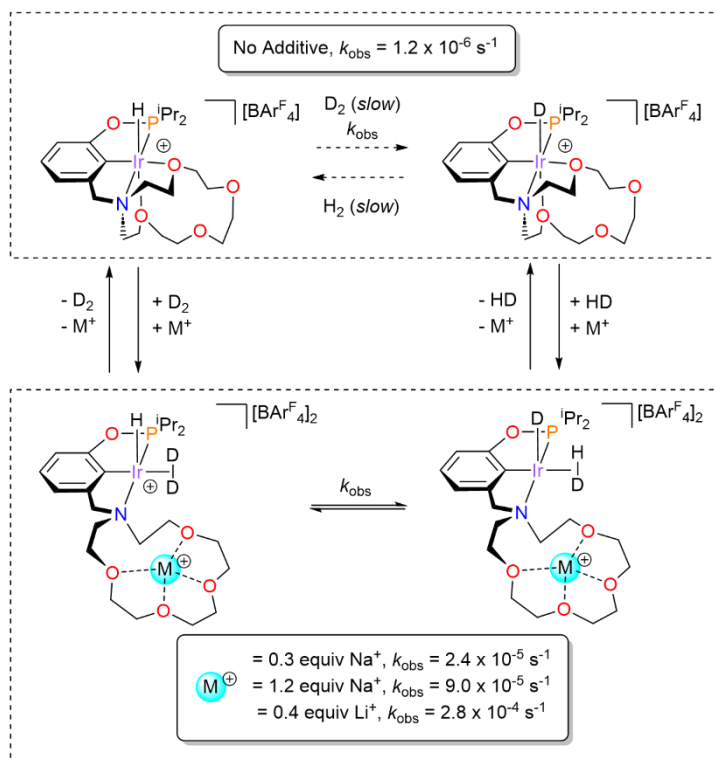
Scheme 3.5: Supramolecular recognition of alkali metals by an allosteric ligand causes marked increase in reaction rate of H/D exchange into an Ir-pincer complex.[35]

3.1c Structurally-Responsive Chelating Bidentate Phospines

As discussed in **Section 1.2b**, the natural bite-angle of chelating bidentate phosphines has a significant impact on the relative energies of oxidation states,[44] and the kinetics and thermodynamics of E–H bond activation.[45] Chelating bidentate phosphines are typically considered to be 'innocent' ligands, that is, they behave as spectator ligands.[46, 47] Wide bite-angle phosphines can, however, be 'non-innocent,'

as C–H bonds in the alkyl backbone can undergo C–H activation, to form a *trans*-spanning PCP-pincer ligand (**Figure 3.2**).[48-53]
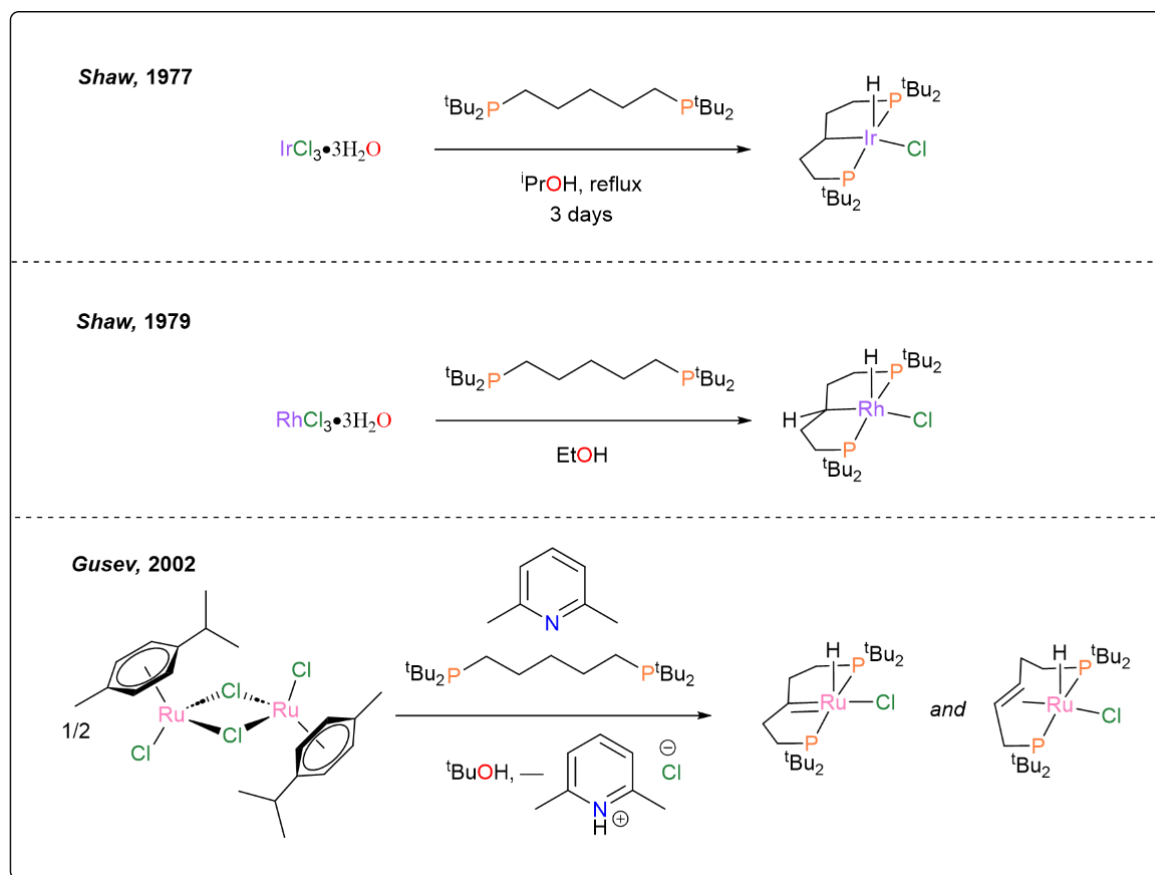
Figure 3.2: C–H activation of wide bite-angle phosphines, reported by Shaw[48, 49] and Gusev.[52]

The installation of a metal-alkyl bond through C–H activation of the phosphine backbone introduces new mechanistic pathways which can be exploited in E–H activation and functionalisation. Hartwig has reported that the cyclometallated precatalyst, $[Ir\{^tBu_2P(CH_2)_2CH(CH_2)_2\}H(NH_2)]$, can be used for deuterium labelling of vinylic groups without double bond isomerisation, using C_6D_6 as the deuterium source.[14] Initial reductive elimination of ammonia is followed by oxidative addition

of a C–D bond of benzene-d_6 (**Scheme 3.6**). Two potential mechanisms which may follow for deuterium incorporation into the phosphine backbone were proposed. Firstly, the deuteride and cyclometallated Ir–C are reductively eliminated (Complex **H**), followed by oxidative addition of the phosphine backbone C–H bond and reductive elimination of C_6D_5H. Alternatively, the cyclometallated alkyl backbone can undergo α-hydride abstraction (Complex **I**), followed by 1,1-migratory insertion of the deuteride and reductive elimination of C_6D_5H. These fundamental mechanistic steps can then be utilised to install the deuterium into vinylic substrates.
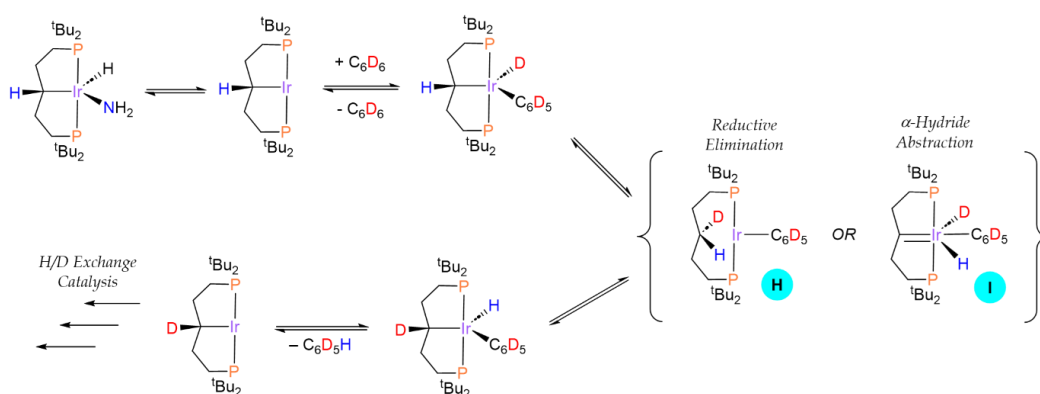
Scheme 3.6: Proposed mechanism by Hartwig for the incorporation of deuterium into the cyclometalated phosphine backbone by benzene-d_6.[14]

Recently, Moret has reported a phosphine backbone structural-response which leads to the activation of H_2 and functionalised phenylacetylenes by a nickel(0) P-(olefin)-P pincer complex though metal-ligand cooperation.[54, 55] In this work, the substrates undergo a 'ligand-to-ligand hydrogen transfer' (LLHT)[56, 57] which is an alternative mechanism to oxidative addition, which was first reported by Eisenstein and Perutz in 2012 (**Scheme 3.7**).[56] Here, C_{sp}–H activation of *para*-fluorophenylacetylene is achieved *via* a concerted mechanism where the C_{sp}–H

bond is broken and forms a new C_{sp3}–H bond with the olefinic pincer in one step (**Scheme 3.8**). The Ni(0) centre is also oxidised to Ni(II) during this step, coordinating new alkyl and alkynyl ligands.
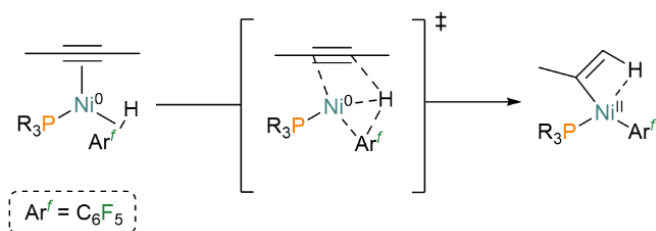
Scheme 3.7: Ligand-to-ligand hydrogen transfer (LLHT) mechanism, first proposed by Eisenstein and Perutz in 2012.[56]
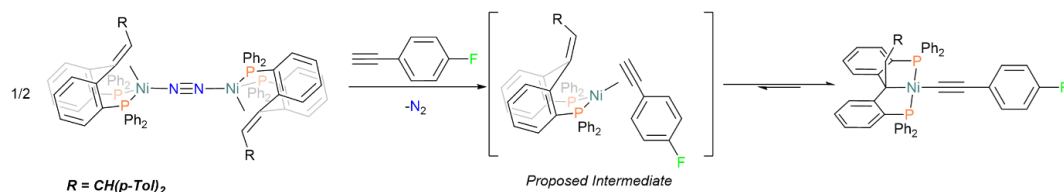
Scheme 3.8: C–H activation of functionalised phenylacetylenes by a nickel(0) P-(olefin)-P pincer complex, reported by Moret.[54] The chelating bidentate phosphine is structurally-responsive during this reaction, forming an alkynyl-alkyl complex.

The Weller group have published a ligand structural-response in *in-crystallo* chemistry. Addition of H_2 to single-crystalline samples of [Rh(dcppent)(diene)][BAr$^F_4$] [dcppent = $Cy_2P(CH_2)_5PCy_2$, diene = norbornadiene or 1,5-cyclooctadiene, Ar^F = 3,5-$(CF_3)_2C_6H_3$] hydrogenates the alkene bonds and concomitantly induces oxidative addition of the phosphine alkyl backbone (NBA complex represented in **Scheme 3.9**).[53] The structural-response of the dcppent ligand framework causes a change in oxidation state from Rh(I) to Rh(III) and significantly alters the coordination geometry, forcing the alkane to adopt an η1-σ-

interaction [P-Rh-P angle increases from 105.03(3)° to 167.43(16)° upon hydrogenation]. The resultant σ-NBA and σ-cyclooctane (COA) complexes were the first examples of crystallographically characterised η^1-σ-alkane complexes, however, both possess noteworthy complications. Crystallographic data for the σ-NBA complex was hampered by significant disorder and the resultant model was of low quality (R_1 = 15.8%; wR_2 = 44.6%). The σ-cyclooctane (COA) complex is chemically unstable, and only formed in ~30% yields before decomposing to undetermined products, hence the SC-XRD model was a superposition of the product and starting material.
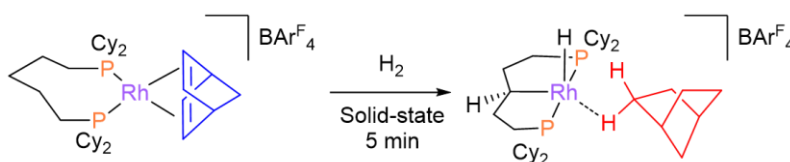
Scheme 3.9: Reaction scheme of the solid-state hydrogenation of [Rh(dcppent)(NBD)][BAr$^F_4$] reported by Weller.[53] The chelating bidentate phosphine alkyl backbone is C–H activated during the hydrogenation process, yielding a Rh(III) η^1-σ-alkane complex supported by a *trans*-spanning PCP pincer ligand.

This chapter will discuss the extension of the phosphine landscape of solid-state molecular organometallic chemistry, using $^tBu_2P(CH_2)_4P^tBu_2$ as the supporting bidentate phosphine. This phosphine is shown to undergo a structural-response to form an η^1-σ-alkane complex supported by a *trans*-spanning PCP pincer ligand. This η^1-σ-alkane complex is shown to be crystallographically well-defined, chemically stable and formed quantitatively on large scales (> 200 mg). The structural-response is shown to be reversible and facilitate H/D exchange through

metal-ligand cooperativity *in-crystallo*. The substitution chemistry of the σ-bound alkane ligand with alkenes is also discussed.

3.2 Results and Discussion

3.2a. Acknowledgements

This project was started by Dr Samantha Furfari (*University of Oxford*), who synthesised the original batches of **dtbpb**, **1-NBD** and **1-NBA**. Dr Alexander Bukvic (*University of Oxford*) collected, reduced, and refined the original single-crystal X-Ray diffraction data for these two complexes at 150 K. Single-crystal X-Ray diffraction data reported in this thesis was recollected, reduced, and refined by the thesis author, at different temperatures. Some of the single-crystal X-Ray diffraction data for **1-Allyl** were collected on the I19 beamline (CY33007) at Diamond Light Source and solved by Dr Graham Tizzard (*UK National Crystallography Service, University of Southampton*). Miss Chloe-Louise Johnson, Dr Kristof Altus (both *University of York*), Dr Matthew Gyton (*University of York*, now *University of Wollongong*), Dr Graham Tizzard, and Dr Mark Warren (*Diamond Light Source, Ltd.*) aided with practical considerations at the I19 beamline at Diamond Light Source. All DFT calculations, including IGMH, NCI and QTAIM analyses, were carried out by Dr M. Arif Sajjad and Professor Stuart Macgregor at *Heriot-Watt University* (now *University of St. Andrews*). Solid-state NMR data were collected by Dr Samuel Page at the *University of Durham* Solid-State NMR Service, or Dr Matthew Gyton at the *University of York*. Gas chromatography electron-ionisation mass spectrometry data were recorded by Mr Karl Heaton at the *University of York* Centre of Excellence in

Mass Spectrometry. Elemental analyses were carried out by Ms Orfhlaith McCullough at *London Metropolitan University*.

3.2b. Project Outline

Solid-state molecular organometallic chemistry has been explored for a wide range of [Rh(PP)(NBD)][BAr$^F_4$] complexes, where PP = bidentate chelating phosphine.[53, 58, 59] Solid/gas hydrogenation of species supported by wide bite-angle phosphines, such as 1,4-bis(di-cyclohexylphosphino)butane (dcpb) and dcppent (**Section 3.1c**), has led to interesting properties of the resulting σ-alkane complex. For example, [Rh(dcpb)($\eta^2;\eta^2$-σ-NBA)][BAr$^F_4$] was reported to be unstable with respect to application of dynamic vacuum (< 1 x 10^{-3} mbar),[53] which is unique among previously reported solid-state σ-norbornane complexes.[53, 58, 59]

The *in-crystallo* hydrogenation of [Rh(dtbpprop)(NBD)][BAr$^F_4$] [dtbpprop = 1,3-bis(di-*tert*-butylphosphino)propane] led to divergent selectivity in σ-alkane binding.[60] While all other reported Rh-$\eta^2;\eta^2$-σ-norbornane complexes with the [BAr$^F_4$]$^-$ anion[61] bind to the Rh centre through the methylene *endo*-C–H positions,[58, 59, 62] the dtbpprop ligand framework induces binding through the methylene *exo*-C–H positions (**Figure 3.3**). This is proposed to be due to small changes in the non-covalent interactions between the cation and the local [BAr$^F_4$]$^-$ octahedral microenvironment (**Figure 3.3**).
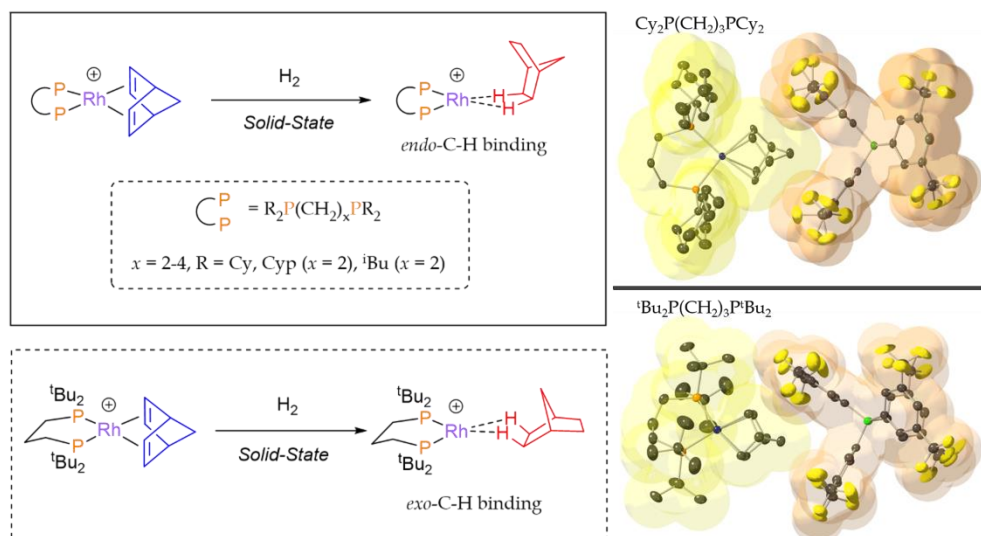
Figure 3.3: The dtbpp ligand framework induces different selectivity in Rh-σ-norbornane binding from all previously explored chelating bidentate phosphines.[60] The position of the neighbouring [BAr$^F_4$]⁻ anion is attributed to the change in selectivity (*right*).

In the work discussed in this **Chapter**, the unique reactivity and properties of σ-alkane complexes supported by a wide-bite angle phosphine, with *tert*-butyl groups is explored. The previously reported[63] 1,4-bis(di-*tert*-butylphosphino)butane (dtbpb) was synthesised and combined with the {Rh(NBD)}[BAr$^F_4$] motif.

3.2bi. Synthesis and Characterisation of dtbpb

The chelating bidentate phosphine ligand used in this study, $^tBu_2P(CH_2)_4P^tBu_2$ (**dtbpb**), was synthesised by an adaptation of two literature preparations by Mecking and Nobbs.[63, 64] This preparation avoids the use of ^tBuLi, an anaerobic aqueous workup and Kugelrohr distillation,[63] or borane protection/deprotection stages,[64] which have previously been reported (**Figure 3.4**).

Di-*tert*-butylphosphine was deprotonated by ^{n}BuLi in THF at -78 °C to yield a bright yellow solution of ^{t}Bu$_2$PLi. Dropwise addition of a 1,4-dibromobutane solution to the cooled ^{t}Bu$_2$PLi solution formed a cloudy suspension. The reaction mixture was warmed to room temperature, the volatiles were then removed, and the product extracted into hexane. The hexane extractions required multiple filtrations through pads of celite to remove residual LiBr precipitate. After removal of the volatiles under reduced pressure and drying *in vacuo*, this procedure yielded **dtbpb** as a white powder in good yields on gram-scale (85%, **Figure 3.4**).
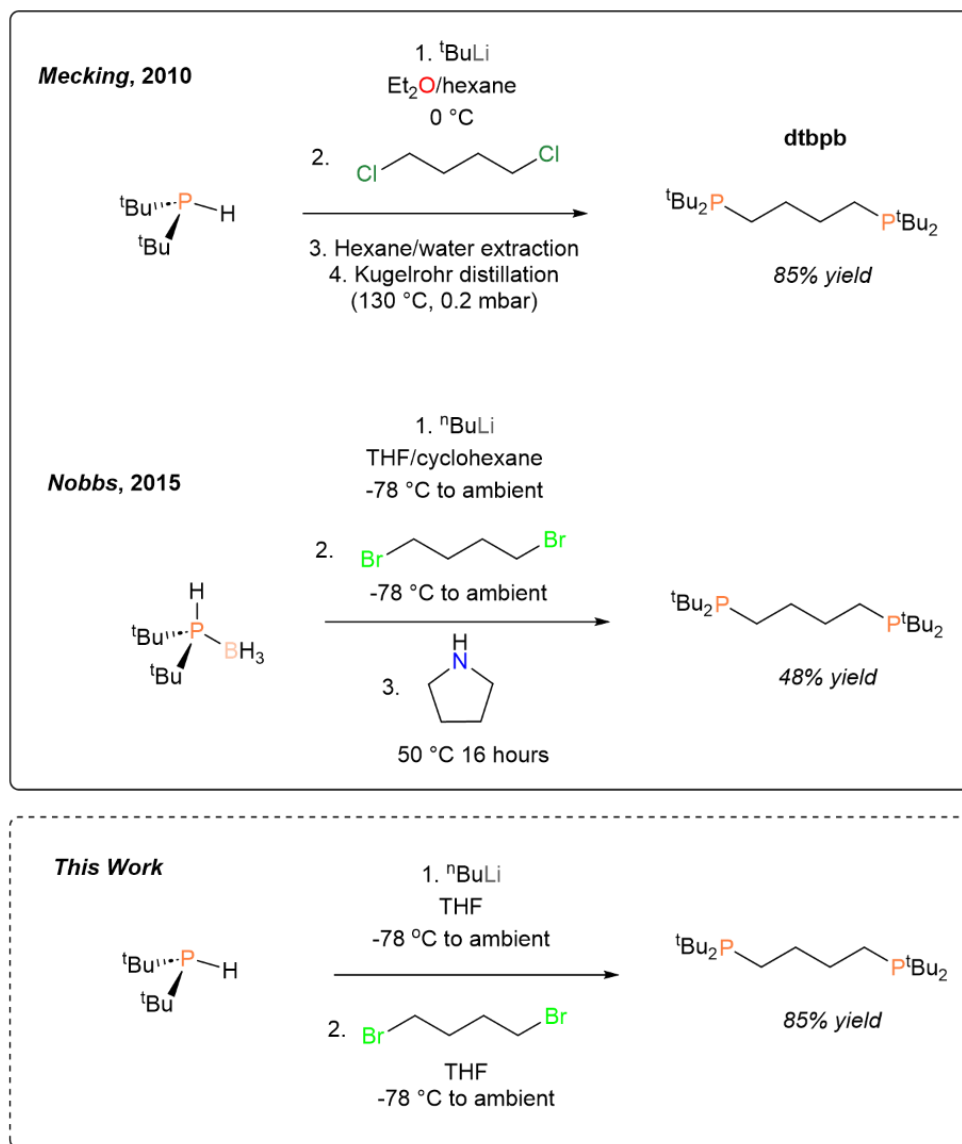
Figure 3.4: Synthetic routes to **dtbpb** reported by the Mecking and Nobbs groups, compared to the synthetic route reported in this work. This work avoids ^{t}BuLi, an aqueous workup, Kugelrohr distillation, or borane protection/deprotection.

The solution $^{31}P\{^1H\}$ NMR (C_6D_6, 298 K) spectrum of **dtbpb** reveals a sharp singlet at δ_P 27.3. The solution ^1H NMR (C_6D_6, 298 K) spectrum reveals the alkyl backbone protons resonate as second-order multiplets at δ_H 1.80 (4 H) and 1.41 (4 H) which simplify on ^{31}P decoupling (**Figure 3.5**). The ^{t}Bu methyl protons are observed as a

doublet, which collapse to a singlet upon ^{31}P decoupling, at δ_H 1.11 [36 H, ^3J(PH) = 10.6 Hz; **Figure 3.5**]. These data are consistent with previously reported NMR spectroscopic data for this compound.[63, 64]
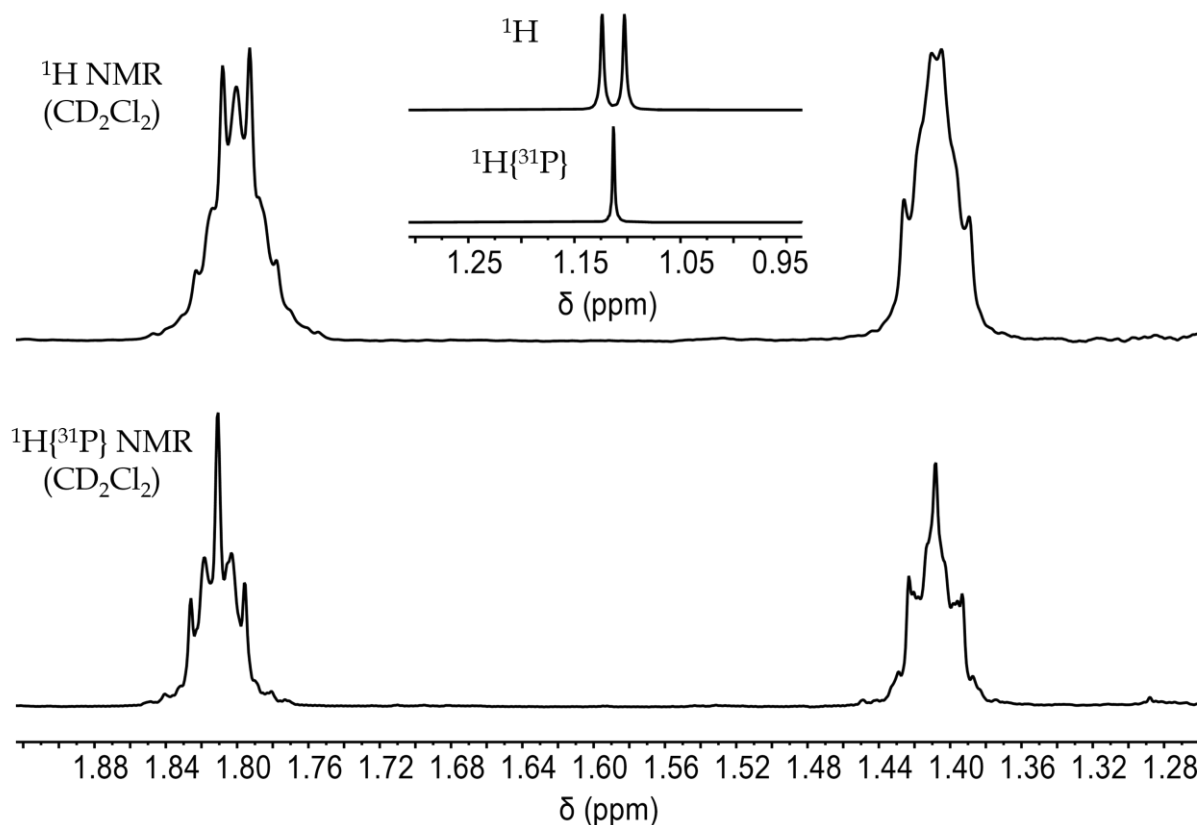
Figure 3.5: Solution ^{1}H NMR (500 MHz, CD$_2$Cl$_2$, 298 K) spectra of **dtbpb**, highlighting the phosphine backbone proton resonances (*main trace*) and ^{t}Bu methyl resonances (*inset*).

3.2c Synthesis and Characterisation of [Rh(dtbpb)(NBD)][BAr$^F_4$]

3.2ci Synthesis and NMR Characterisation

A solution of **dtbpb** in CH$_2$Cl$_2$ was added dropwise to a solution of [Rh(NBD)$_2$][BAr$^F_4$][60] in CH$_2$Cl$_2$, which caused a slight colour change from bright red to a dark plum red. After stirring at room temperature for 2 hours, the product was precipitated from the reaction mixture with hexane. The product was then extracted

into fresh CH_2Cl_2 and isolated by recrystallisation by layering with hexane, to yield

dark red block crystals of [Rh(dtbpb)(NBD)][BAr$^F_4$] (**1-NBD**) in good yield on gram-

scale (80%, **Scheme 3.10**).
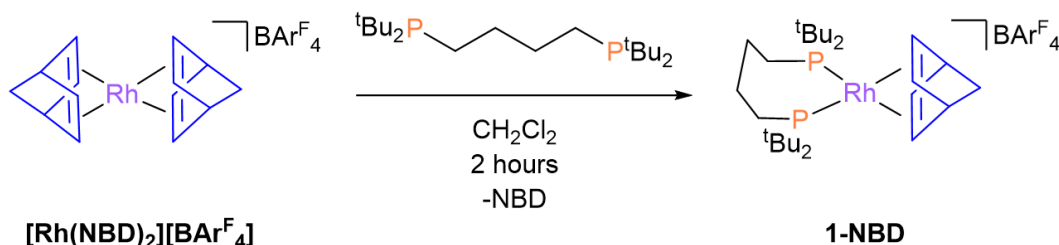
Scheme 3.10: Reaction scheme for the synthesis of **1-NBD** by addition of **dtbpb** to [Rh(NBD)$_2$][BAr$^F_4$].

Solution NMR (CD$_2$Cl$_2$, 298 K) spectroscopic data for **1-NBD** show the complex

possesses C_{2v} symmetry. The solution ^{31}P{^{1}H} NMR spectrum reveals a doublet at

δ_P 34.7 [J(RhP) = 147 Hz]. Two broad methylene phosphine backbone resonances

are observed in the solution ^{1}H NMR spectrum at δ_H 1.92 and 1.79 (4H each, **Figure**

3.6). A single ^{t}Bu methyl environment is observed at δ_H 1.40 [d, J(PH) = 12.6 Hz].

The alkene protons are observed as a complex multiplet at δ_H 5.05 which does not

simplify upon ^{31}P decoupling, suggesting that the coupling is due to a mixture of

^2J(RhH) and intra-NBD proton-proton coupling.
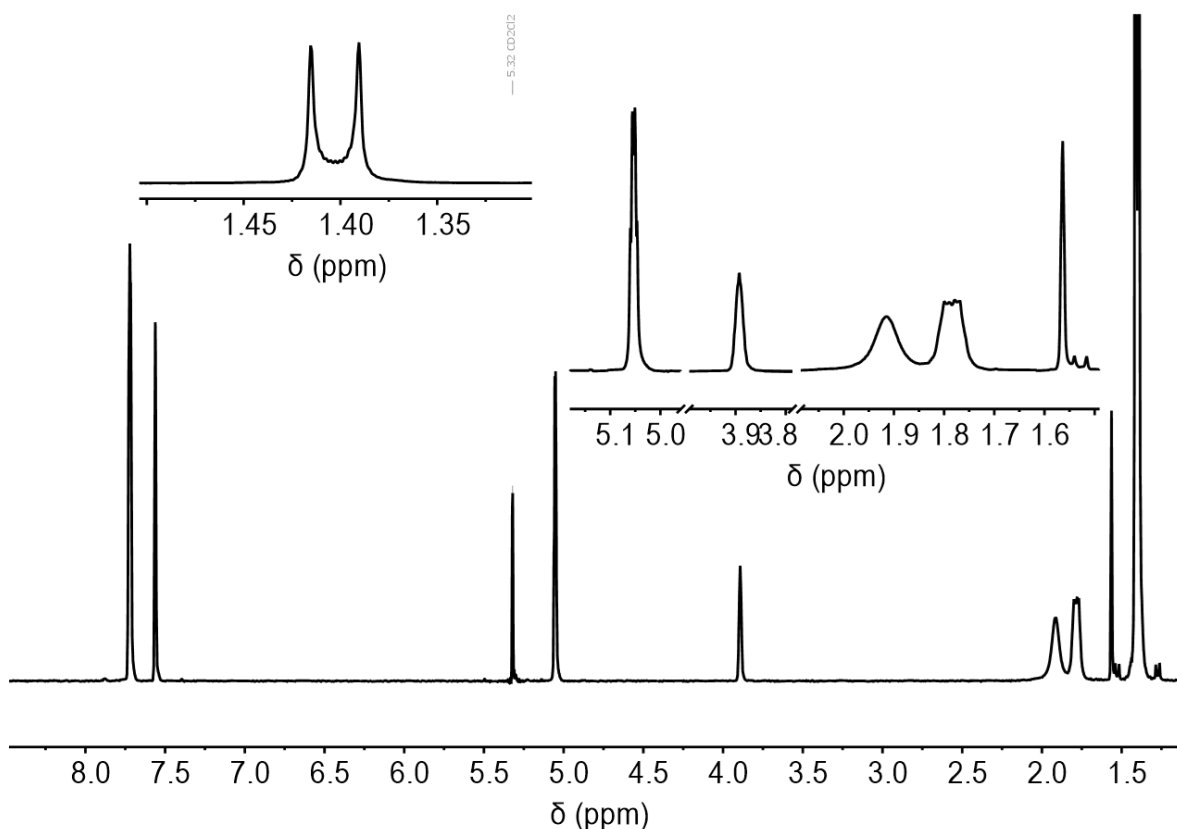
Figure 3.6: Solution ^{1}H NMR (500 MHz, CD$_2$Cl$_2$, 298 K) spectrum of **1-NBD**. Insets depict the ^{t}Bu methyl resonance (*top*, *left*) and phosphine alkyl backbone resonances (*right*).

The solid-state ^{31}P{^{1}H} CP MAS NMR (298 K, 10 kHz spin rate) spectrum shows two crystallographically inequivalent ^{31}P environments at δ$_P$ 42.8 [d, *J*(RhP) = 148 Hz] and 25.0 [d, *J*(RhP) = 148 Hz, **Figure 3.7**]. Resonances attributed to the alkene carbons are found in the solid-state ^{13}C{^{1}H} CP MAS NMR (298 K, 10 kHz spin rate) spectrum at δ$_C$ 77.1, 75.4, 51.0, and 48.2 (**Figure 3.8**), highlighting that unlike in solution, the alkene carbon atoms are inequivalent. The bridge CH$_2$ is observed at δ$_C$ 63.8 and the bridgehead CH positions overlapping with the alkene resonance at δ$_C$ 51.0.
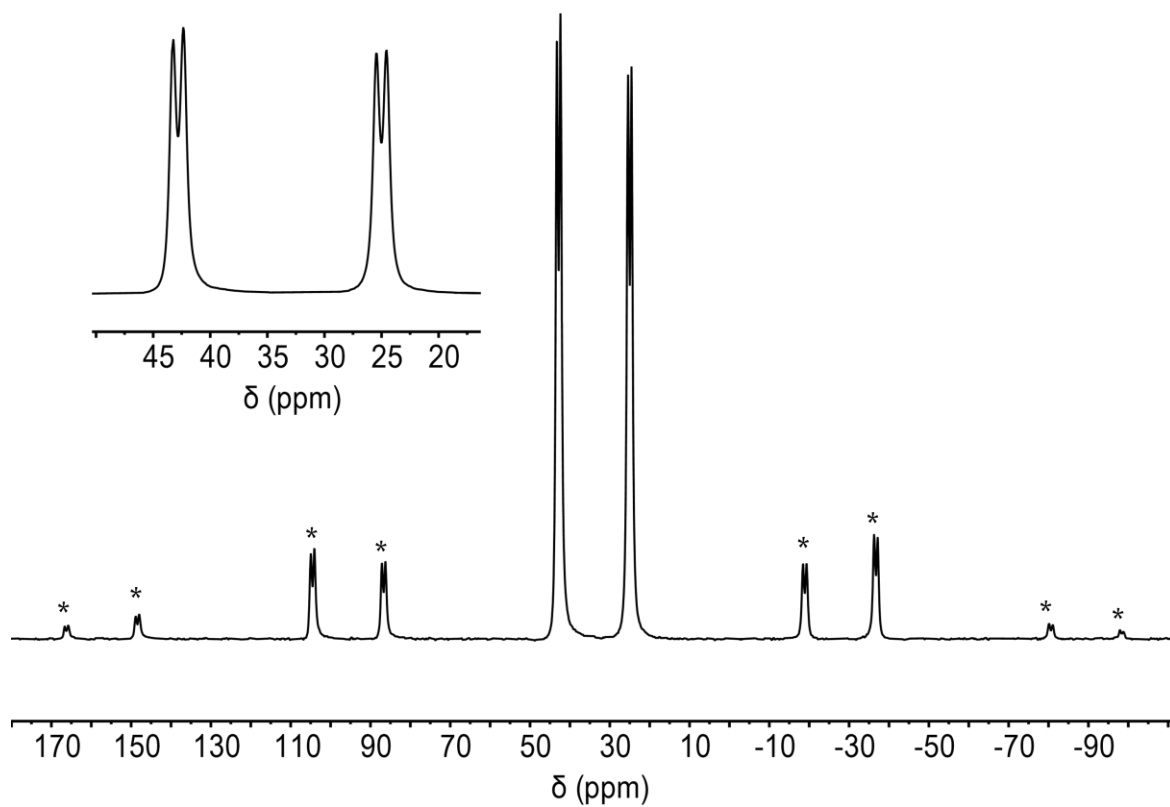
Figure 3.7: Solid-state $^{31}P\{^{1}H\}$ CP MAS NMR (162.04 MHz, 10 kHz spin rate, 298 K) spectrum of **1-NBD**. Inset depicts isotropic chemical shift. Spinning side bands are noted with asterisks.
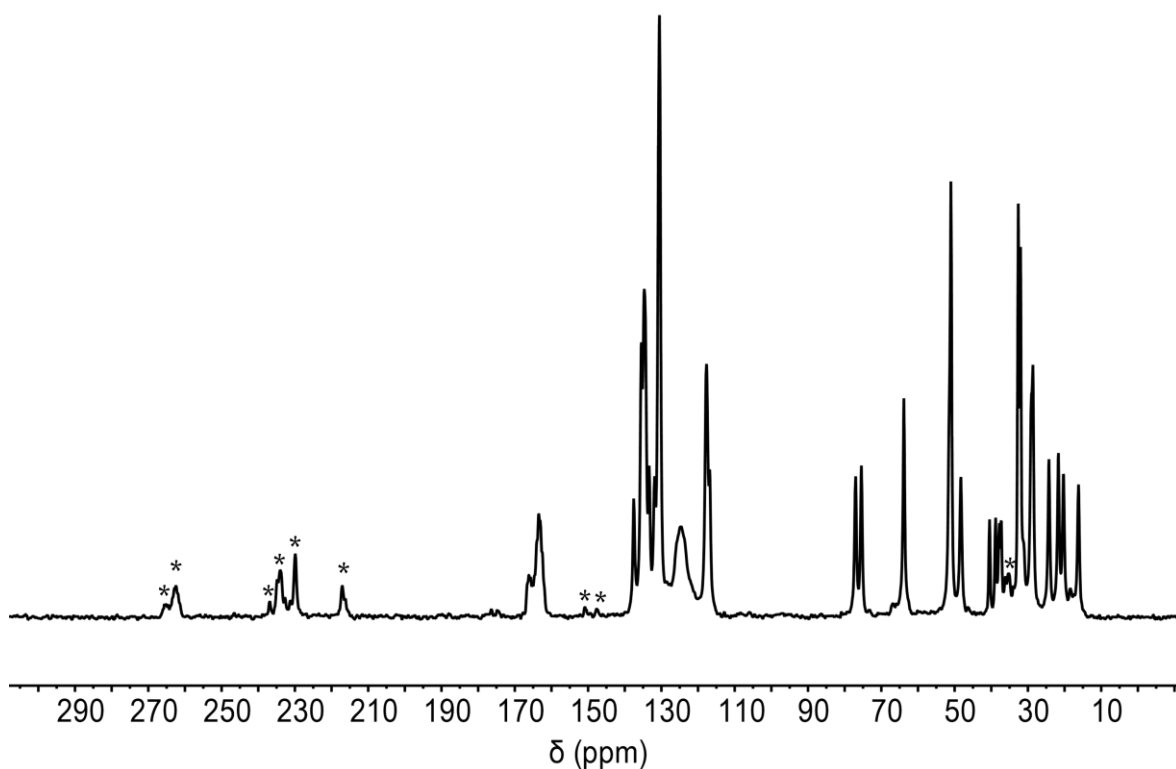
Figure 3.8: Solid-state $^{13}C\{^1H\}$ CP MAS NMR (100.66 MHz, 10 kHz spin rate, 298 K) spectrum of **1-NBD**. Spinning side bands are noted with asterisks.

3.2cii. Single-Crystal X-Ray Diffraction Analysis of 1-NBD

Single-crystals of **1-NBD** suitable for analysis *via* single-crystal X-Ray diffraction techniques were grown from layering a CH_2Cl_2 solution of **1-NBD** with hexane at room temperature. **1-NBD** crystallises in the $P\,2_1/n$ space group ($Z' = 1$, $Z = 4$), with a unit cell volume of 5954.40(7) $Å^3$. Consistent with the SSNMR data, there is no crystallographically-imposed symmetry in the cation. The cation is twisted away from a true square planar complex (**Figure 3.9**), with an angle of 33.808(9)° between the P1-Rh1-P2 plane and the NBD ligand. This twist towards tetrahedral is likely due to the steric bulk of the ^tBu groups and the wide natural bite angle of the

chelating phosphine. The cation also features relatively short[53, 60] Rh-alkene bonds [average Rh–C distance = 2.1769(18) Å] and relatively long[53, 65, 66] Rh-P bond lengths [average Rh–P distance = 2.4333(5) Å].
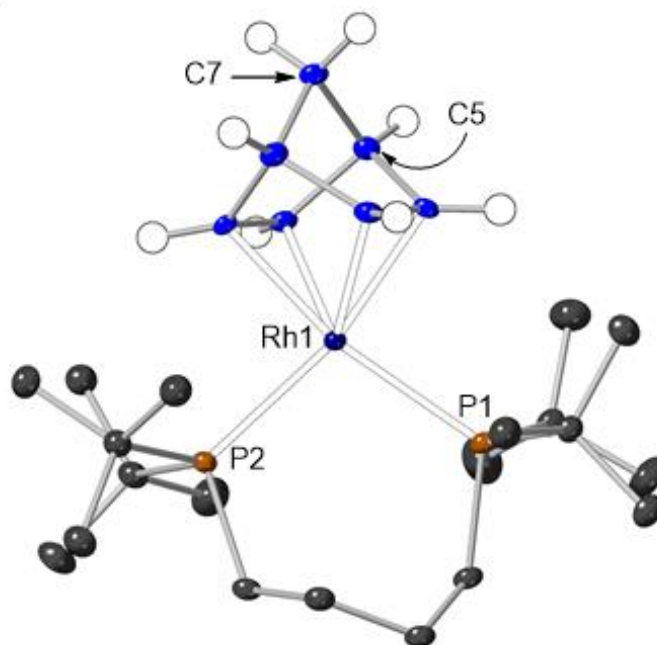
Figure 3.9: Single-crystal X-Ray structure of the cation of **1-NBD**. Thermal displacement ellipsoids are displayed at 50%. Protons associated with the chelating phosphine are omitted for clarity. NBD ligand shown in blue. Selected bond lengths and angles: Rh1-P1 2.4413(5) Å; Rh1-P2 2.4252(5) Å; P1-Rh1-P2 102.116(17)°; Rh1-C1-4 2.1922(19) Å, 2.1720(18) Å, 2.1653(18) Å and 2.1782(17) Å, respectively.

The cation lies within an approximately octahedral cage of six [BArF₄]⁻ anions (**Figure 3.10**). Similar to previously reported complex, [Rh(dtbpprop)(NBD)][BArF₄],[60] the cation of **1-NBD** is non-symmetrically placed within the octahedron, with the NBD bridge CH₂ pointed towards one anion-aryl

ring (**Figure 3.10**). The NBD alkene protons also have short C–H···F contacts with a neighbouring Ar^F CF$_3$ group [C1···F22 3.248(2) Å; C2···F21 3.276(2) Å; **Figure 3.10**].
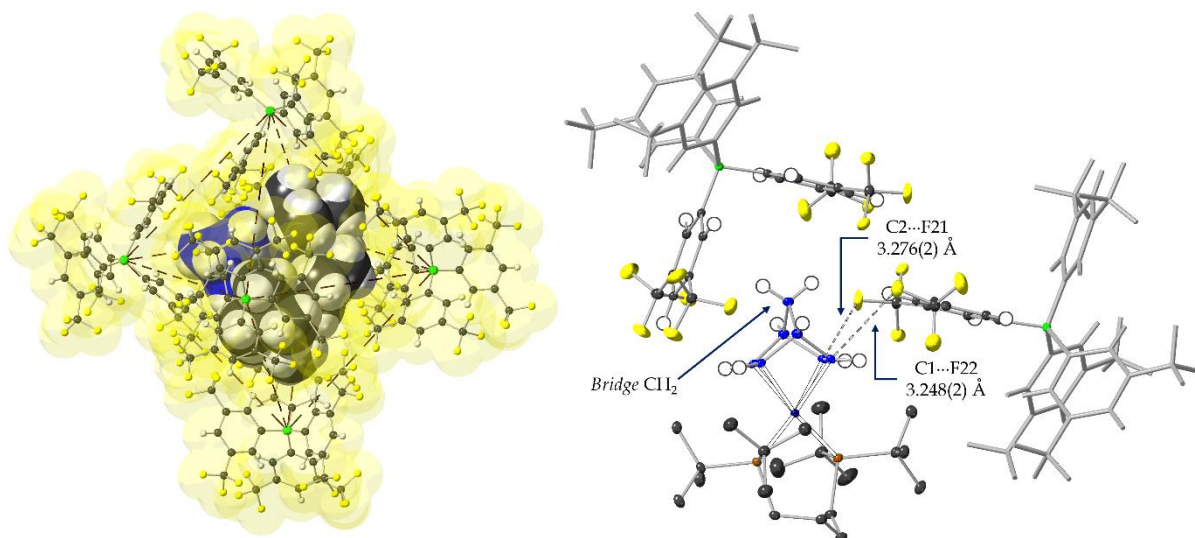
Figure 3.10: Solid-state structure of **1-NBD**. Carbon atoms of the NBD ligand are displayed in blue. *Left*: The {Rh(dtbpb)(NBD)}$^+$ cation is located within an approximately octahedral arrangement of six [BAr$^F_4$]$^-$ anions. *Right*: The cation is non-symmetrically placed within the octahedral arrangement, with the bridge CH$_2$ pointed towards an aryl ring. Close C–H···F contacts are noted with a neighbouring anion. Displacement ellipsoids are displayed at 50%. Selected hydrogen atoms omitted for clarity.

3.2ciii. Single-Crystal to Single-Crystal Hydrogenation of 1-NBD

Addition of H$_2$ (1 bar gauge) to single-crystalline samples of **1-NBD** (up to 200 mg scale) causes the crystals to change in colour from plum red to sandy yellow (**Figure 3.11**), enabling the reaction progress to be followed by optical microscopy. Reaction times varied considerably from batch to batch, ranging from 30 minutes to 120

minutes. For consistency between samples, crystals were thus lightly crushed with a spatula to introduce surface fractures and increase surface area[67-69] to increase efficiency of hydrogen diffusion into the lattice and always hydrogenated for 120 minutes. This hydrogenation time is significantly longer than previously reported SCSC hydrogenations of {Rh(NBD)}[BAr$^F_4$] complexes, which typically require 5 – 10 minutes.[53, 59, 62] The increased hydrogenation time is hypothesised to be due to the tetrahedral distortion of **1-NBD** favouring the formation of Rh(III), which increase the energy barrier of the reductive elimination step of alkene hydrogenation.[44, 70-72]
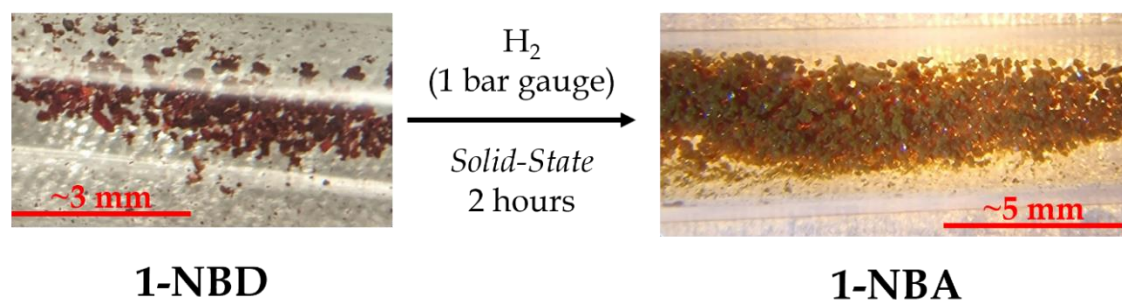
Figure 3.11: The *in-crystallo* reaction of **1-NBD** with H$_2$ gas can be visually tracked with optical microscopy due to the colour change from bright red (*left*, **1-NBD**), to sandy-yellow (*right*, **1-NBA**).

3.2civ. Single-Crystal X-Ray Diffraction Analysis of 1-NBA

The addition of H$_2$ to **1-NBD** induces a single-crystal to single-crystal transformation (**Scheme 3.11**),[73] which was studied by single-crystal X-Ray diffraction. At 110 K, a good model (R_1 = 5.58%, R_{int} = 3.73%) is reached for a complex where the NBD has been hydrogenated and one of the central CH$_2$ positions on the chelating phosphine backbone has been C–H activated to form an

asymmetric *trans*-spanning PCP pincer ligand [**1-NBA**; P1-Rh-P2 angle = 154.86(4)°

cf. 102.116(17)° in **1-NBD**; **Figure 3.12**]. The resultant alkyl ligand is disordered

above and below the plane of the rhodium in approximately a 60:40 ratio (**Figure**

3.13).
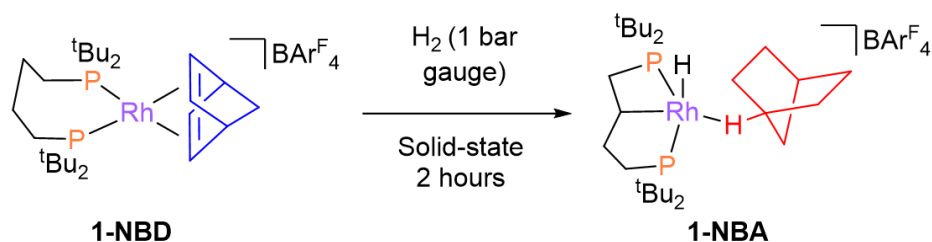
Scheme 3.11: Reaction scheme of the *in-crystallo* hydrogenation of **1-NBD** to form **1-NBA**.

The reaction proceeds as a single-crystal to single-crystal transformation.
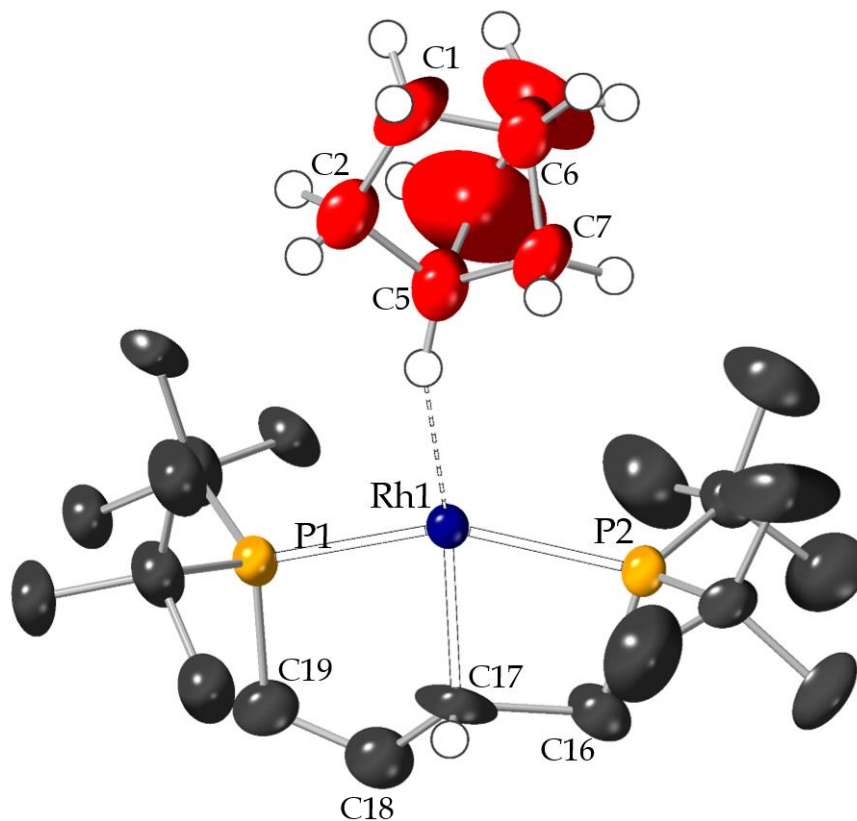
Figure 3.12: Single-crystal X-Ray structure of the cation of **1-NBA**. The NBA ligand was treated with light distance and angle restraints (see full text for detailed discussion). Carbon atoms of the NBA ligand are shown in red. Besides the cyclometalated carbon, all other protons associated with the phosphine are omitted for clarity. Displacement ellipsoids displayed at the 30% probability level. Selected bond lengths and angles: Rh1-P1 2.2969(9) Å; Rh1-P2 2.3292(11) Å; Rh1-C17 2.081(11) Å; Rh1-C5 2.980(5) Å; P1-Rh1-C17 82.0(4)°; P2-Rh1-C17 74.1(4)°.
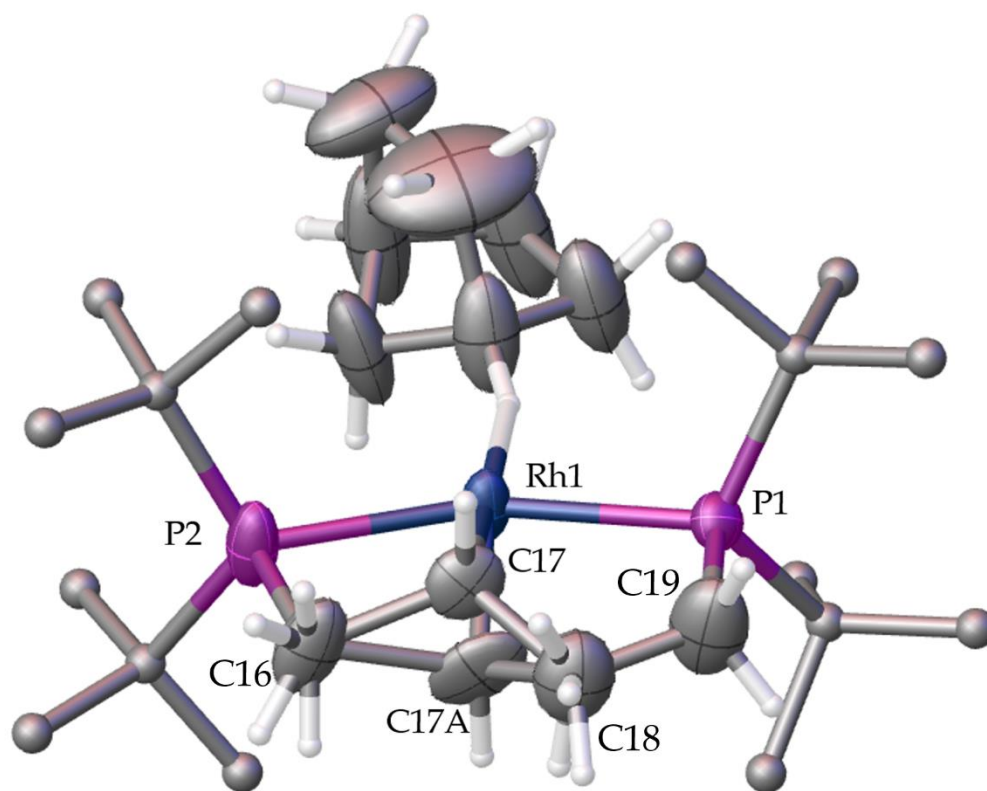
Figure 3.13: The alkyl ligand of **1-NBA** is disordered above and below the P-Rh-P plane in the solid-state structure in an approximately 60:40 ratio. The *tert*-butyl groups have had protons omitted and are represented as isotropic spheres for clarity. Displacement ellipsoids displayed at 50%.

The hydride ligand(s) could not be located in the electron difference map of the SC-XRD data. This is expected based on the 60:40 disorder model and proximity to the heavy rhodium atom. However, knowing the number of hydride ligands is important as onward reactivity of the alkyl ligand can be envisaged: α-hydride abstraction from the alkyl ligand to form a P-C(carbene)-P ligand and a dihydride (**Figure 3.14**, Complex K);[48, 49] β-hydride elimination to form a P-(olefin)-P ligand

framework and a dihydride (**Figure 3.14**, Complex L);[52] or a Rh(I) derivative of Complex L, where H_2 has been reductively eliminated (**Figure 3.14**, Complex M).
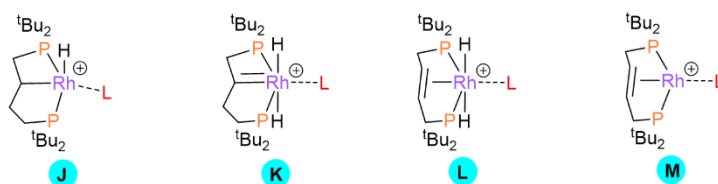
Figure 3.14: Potential binding motifs between the alkyl phosphine backbone and the rhodium centre.

The formation of the P-(olefin)-P ligand framework can be discounted based on the solid-state structure, as the olefin would be expected to coordinate to the low coordinate metal centre.[14, 49, 52] The C18⋯Rh1 distance of 2.973(6) Å and Rh1-C17-C18 angle of 119.2(11)° argues against this coordination (**Figures 3.12 and 3.13**). The non-planar geometry of the cyclometalated carbon atom (C17) also suggests C_{sp3} hybridisation (**Figures 3.12 and 3.13**), contrary to the C_{sp2} geometry of proposed P-C(carbene)-P or P-(olefin)-P ligand frameworks.

The alkene positions of the NBD ligand of **1-NBD** have been hydrogenated to norbornane, and the resulting alkane is coordinated to the Rh centre through the methine bridgehead C–H bond to form a tertiary η1-σ-alkane complex. Consistent with a η1-σ-alkane complex, the Rh⋯C distance is found to be 2.982(5) Å, which compares well to the only previously reported, crystallographically well-defined η1-σ-alkane complex, [Rh{Cy$_2$P(CH$_2$)$_2$CH(CH$_2$)$_2$}(η1-σ-COA)][BAr$^F_4$] [Rh⋯C 2.90(3) Å],[53] and contrasts to reported η2-σ-NBA complexes (2.169 – 2.408 Å).[53, 59, 62]

While [Rh(dcpe)(η^2;η^2-σ-isobutane)][BAr$^F_4$] [74] exhibits an η^2-σ-C–H⋯Rh interaction with the methine position of isobutane (**Figure 3.15**), a second η^2-σ-C–H⋯Rh interaction is found with the methyl position. We believe that **1-NBA** is the first example of a σ-alkane complex supported solely by a tertiary alkane C–H bond, characterised either in the solution- or solid-state.

η²;η²-NBA   η²;η²-isobutane

η¹-COA   η¹-NBA
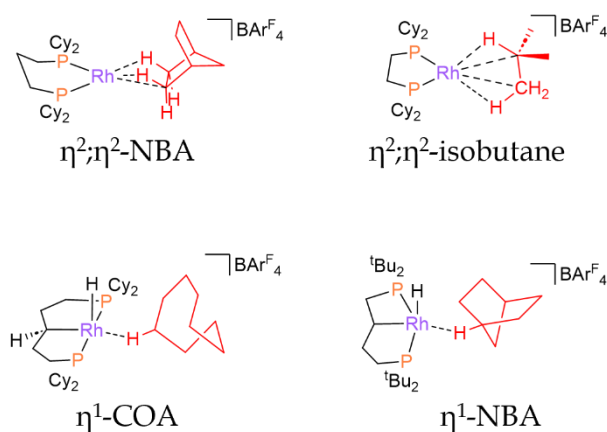
Figure 3.15: Comparison of Rh⋯alkane binding motifs.

The protons on the NBA fragment of **1-NBA** were placed in calculated positions and allowed to ride on their parent atoms. Bond lengths and angles of the NBA ligand were lightly restrained to provide sensible C–C bond metrics. The necessity of inclusion of restraints on the NBA fragment is due to unresolved disorder of the NBA fragment. The disorder of the NBA fragment becomes exacerbated in the single-crystal X-Ray diffraction data as the temperature increases (110 K, 215 K, and 298 K; **Figure 3.16**), which suggests a dynamic disorder process is occurring causing the electron density to smear.
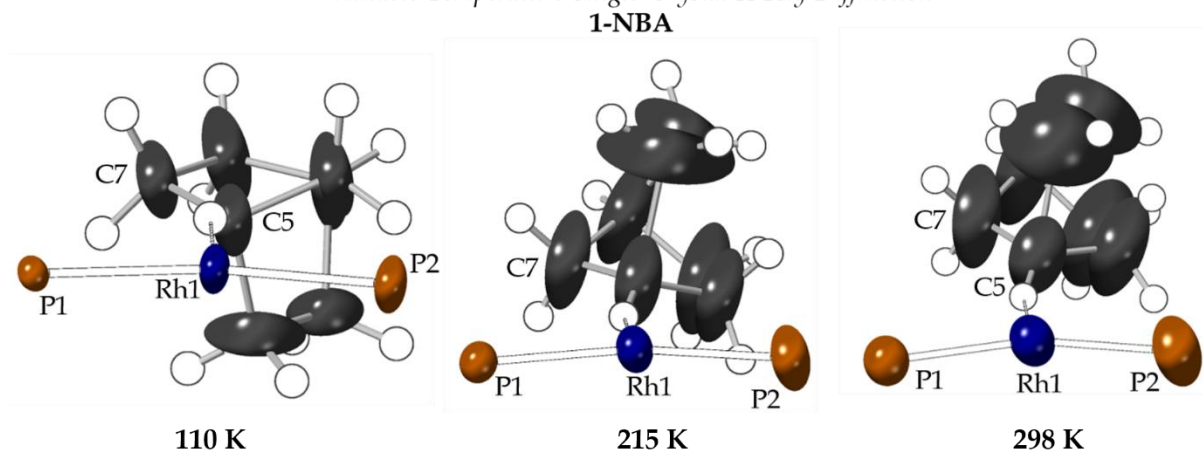
Figure 3.16: Variable temperature (110 K, *left*; 215 K, *middle*; 298 K, *right*) single-crystal X-Ray diffraction data of **1-NBA**. A truncated cation is shown in each case for clarity. Displacement ellipsoids displayed at 50%.

Despite the wealth of reports of C–H activation at C_5-phosphine backbones,[48-53] we are only aware of one publication involving activation of a C_4-phosphine backbone, by a ruthenium silylene complex (**Scheme 3.12**).[75] This example reaction is a base-promoted reaction, which will drive the reaction towards the alkylated product. This difference in number of reported examples of C_4- and C_5-phosphine backbone activation is likely due to the reduced degrees of freedom of the alkyl chain in approaching the metal, the decreased phosphine bite-angle, and the unfavourable formation of a four-membered ring.
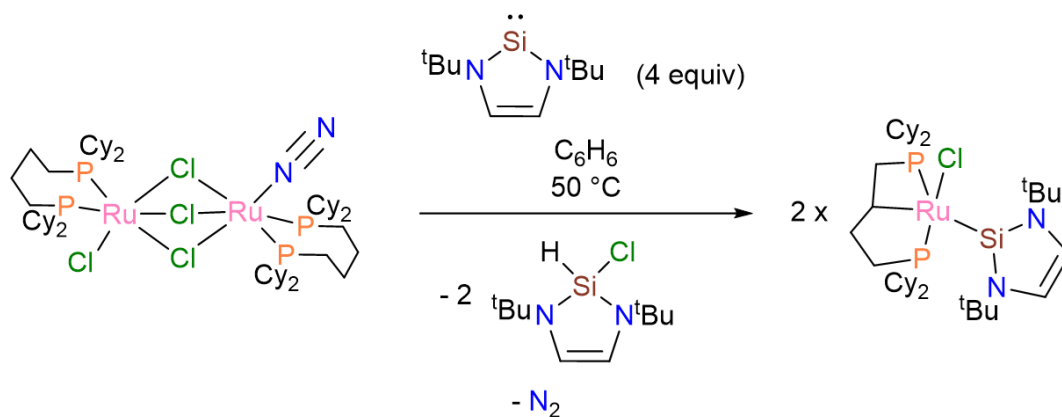
Scheme 3.12: Reaction scheme of the C–H activation, and subsequent deprotonation, of a C_4-backbone within a ruthenium silylene complex, reported by the Fogg group.[75]

In all previous reports of the solid-state synthesis of rhodium σ-alkane complexes, the unit cell volume increase from the alkene precursor has been less than 2%.[53, 60, 62, 74, 76-79] In the example reported here, the unit cell volume increase is approximately 5% [**1-NBD** V = 5954.40(7) Å^3; **1-NBA** V = 6251.67(16) Å^3], with no increase in void volume (as determined by PLATON).[80] This is suggested to be due to the significantly increased Rh···C bond lengths between the alkene groups in **1-NBD** to the η^1-σ-NBA fragment in **1-NBA**.

The octahedral arrangement of [BAr$^F_4$]$^-$ anions is retained throughout the SCSC transformation, and close C–H···F contacts are found between the bridge and methylene units with a neighbouring Ar^F CF$_3$ [C6···F9 3.377(7) Å; C7···F9 3.358(7) Å; **Figure 3.17**]. The structural-response of the phosphine and the hydrogenation of the alkene therefore does not significantly alter the geometry of the neighbouring [BAr$^F_4$]$^-$ microenvironment.
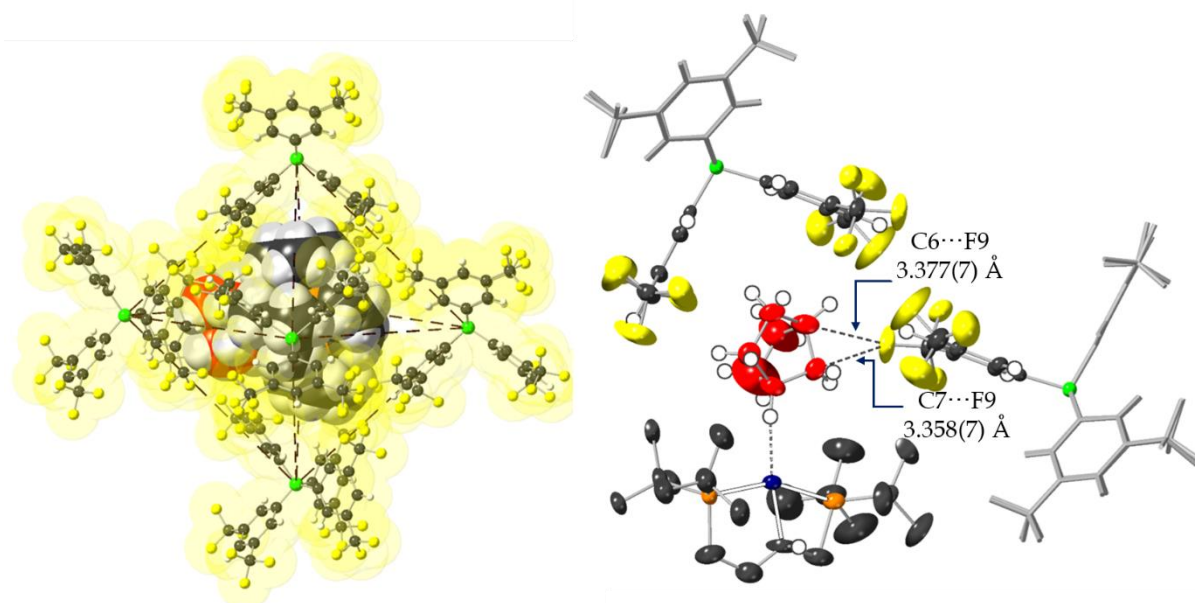
Figure 3.17: Solid-state structure of **1-NBA**. Carbons of NBA ligand displayed in red. *Left*: Approximately octahedral arrangement of [BAr$^F_4$]$^-$ anions around the cation in **1-NBA**. *Right*: The NBA ligand is non-symmetrically placed within the cleft of Ar^F aryl rings. Close C–H···F contacts between the NBA bridge and methylene protons and a neighbouring Ar^F CF$_3$ are noted. Ellipsoids displayed at 50% probability. Selected hydrogen atoms omitted for clarity.

3.2cv. Solid-State NMR Spectroscopic Characterisation of 1-NBA

The solid-state ^{13}C{^{1}H} CP MAS NMR (298 K, 10 kHz spin rate; **Figure 3.18**) spectrum of **1-NBA** is devoid of resonances between δ$_C$ 110 to 45. This indicates full hydrogenation of the NBD alkene groups in the bulk material (*cf.* **Figure 3.8**). Consistent with the SC-XRD model, this also gives further evidence the P-C(alkyl)-P ligand framework has not undergone β-hydride elimination to form a P-(olefin)-P framework, even as a minor impurity.[48, 49, 52] The spectrum is also devoid of

resonances downfield from δ_C 167 ([BAr$^F_4$] resonance) which is further evidence against the formation of a P-C(carbene)-P complex in the solid-state, as carbene ^{13}C resonances are usually observed downfield of δ_C 200.[15, 52, 81-83]
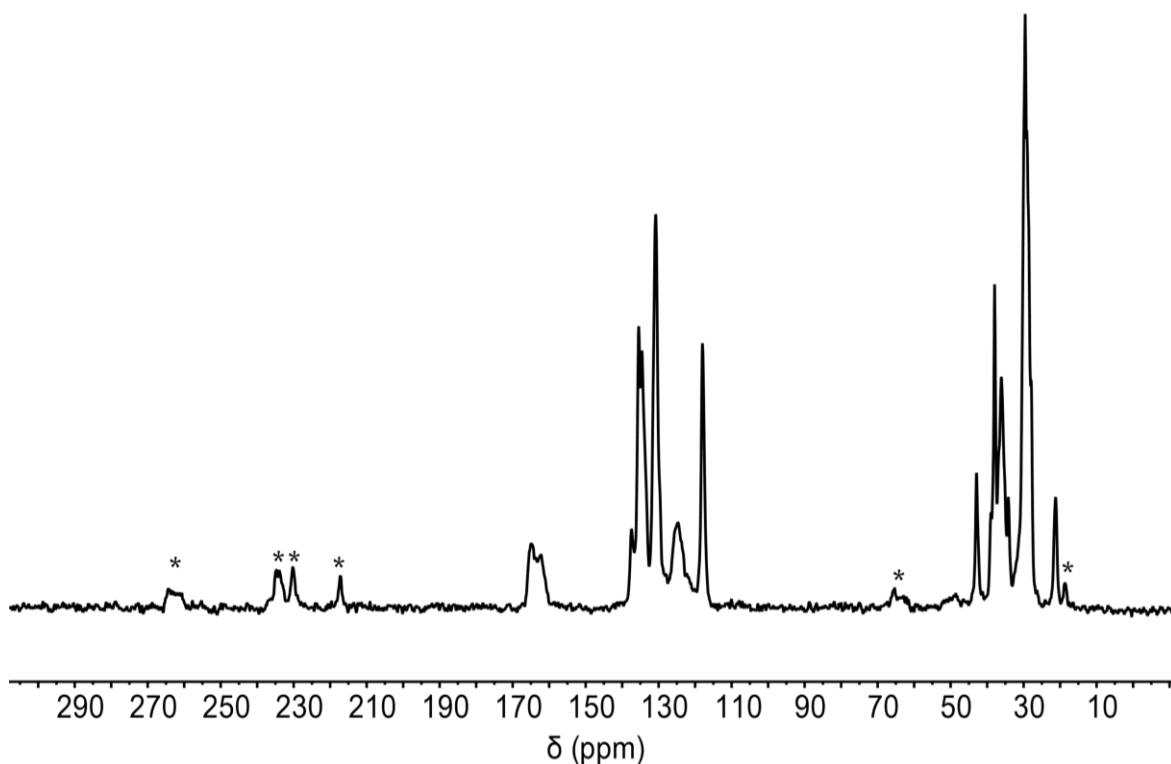
Figure 3.18: Solid-state ^{13}C{^{1}H} CP MAS NMR (100.66 MHz, 10 kHz spin rate, 298 K) spectrum of **1-NBA**. Spinning side bands are marked with asterisks.

In the solid-state ^{31}P{^{1}H} CP MAS NMR (298 K, 10 kHz spin rate) spectrum of **1-NBA** two environments are observed (F**igure 3.19**): δ_P 100.6 [dd, J(RhP) ~ 115 Hz; J(PP) ~ 280 Hz] and -8.7 [apparent triplet, J_{app} = 300 Hz]. These resonances are consistent with the solid-state X-Ray structure of **1-NBA** involving 5- and 4-membered rings.[84-87] The ^{103}Rh-^{31}P coupling observed for the resonance at δ_P 100.6 is consistent with the reduction in coupling constant from moving from a Rh(I) to Rh(III) manifold.[53, 88, 89] The broad (FHWM = 800 Hz) apparent triplet of the

resonance at δ_P -8.7 is rationalised by two overlapping doublets of doublets, caused by the crystallographically independent disordered components which are coincident in the resonance at δ_P 100.6.
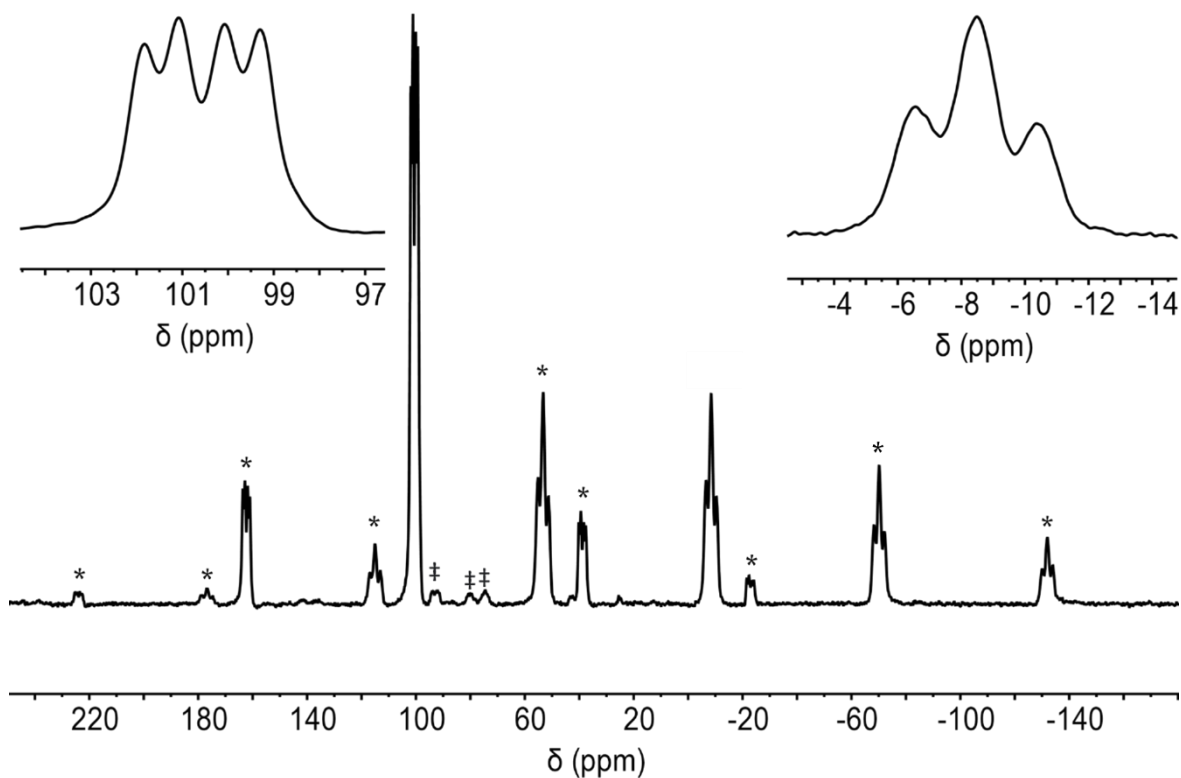
Figure 3.19: Solid-state ^{31}P{^{1}H} CP MAS NMR (162.04 MHz, 10 kHz spin rate, 298 K) spectrum of **1-NBA**. The insets depict the isotropic chemical shifts at δ_P 100.6 (*top left*) and -8.7 (*top left*). Spinning side bands are marked with asterisks. Unidentified impurities are denoted by ‡.

3.2cvi. Solution NMR Spectroscopic Characterisation of 1-NBA/1-CD$_2$Cl$_2$

As with all reported solid-state syntheses of σ-alkane complexes,[53, 62, 74, 76-78, 90] dissolution into CD$_2$Cl$_2$ at 193 K caused instantaneous loss of the coordinated alkane. In contrast to the majority of the previous studies where a zwitterionic arene complex formed through coordination of the [BAr$^F_4$]$^-$ anion, or chloride-bridged hydride dimer species are formed,[53, 59, 62, 76] dissolution of **1-NBA** in CD$_2$Cl$_2$ formed a stable (below 243 K) product, **1-CD$_2$Cl$_2$** (**Scheme 3.13**), which could be examined by solution NMR spectroscopic studies. The relative stability of **1-CD$_2$Cl$_2$** is suggested to be due to the increased steric bulk of the ligand framework precluding arene coordination, while the Rh(III) centre is unable to undergo oxidative cleavage of CD$_2$Cl$_2$. The solution ^{31}P{^{1}H} NMR (CD$_2$Cl$_2$, 193 K) spectrum of **1-CD$_2$Cl$_2$** reveals two mutually coupled doublets of doublets at δ_P 98.8 [J(RhP) = 127 Hz; J(PP) = 289 Hz] and -16.5 [J(RhP) = 90 Hz; J(PP) = 289 Hz; **Figure 3.20**].
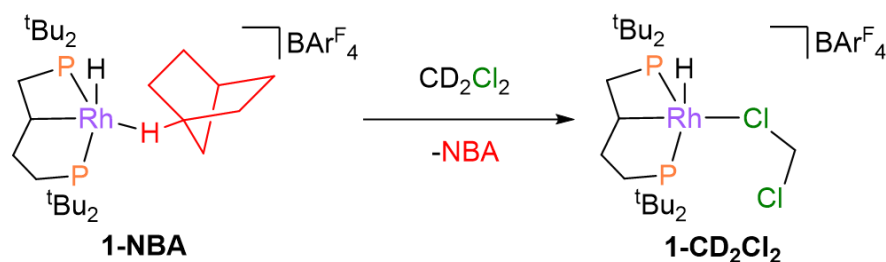
Scheme 3.13: When **1-NBA** is exposed to CD$_2$Cl$_2$, the coordinated alkane is lost, and CD$_2$Cl$_2$ is coordinated to the Rh(III).
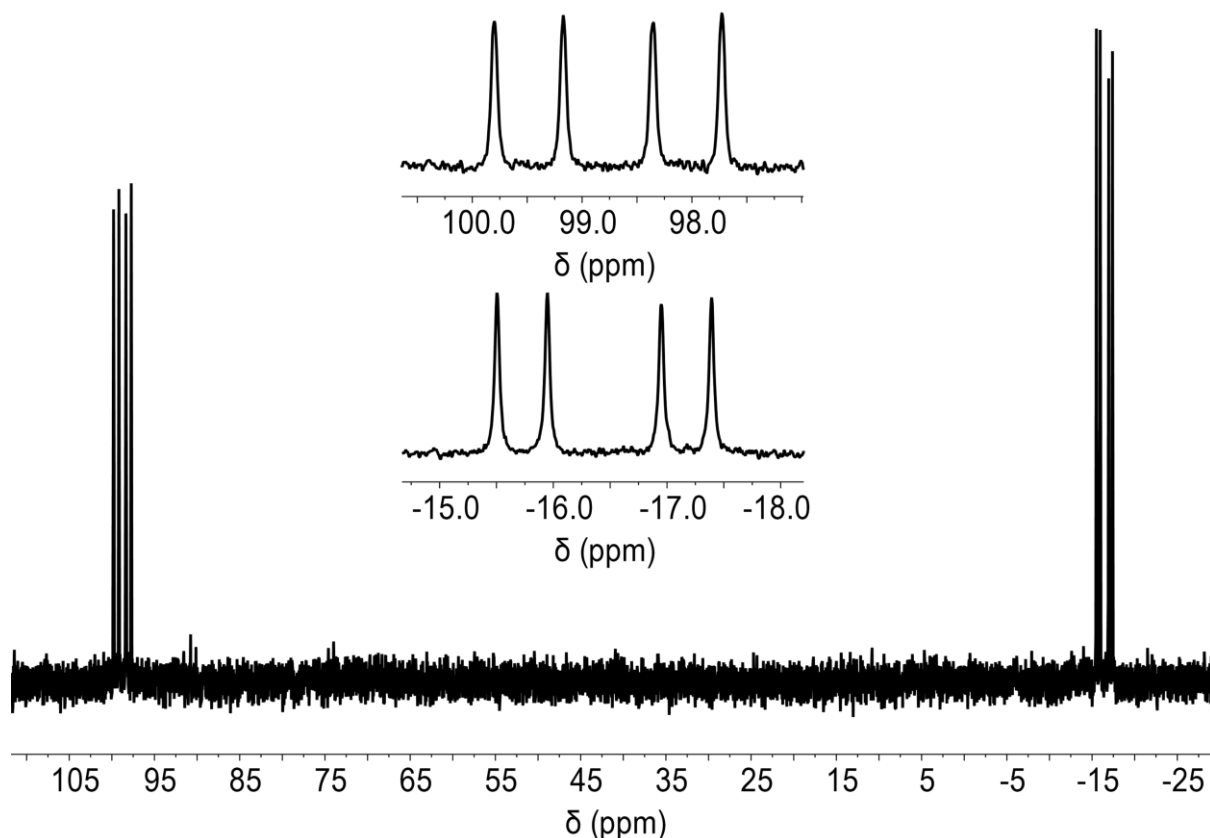
Figure 3.20: Solution $^{31}P\{^1H\}$ NMR (202.49 MHz, CD_2Cl_2, 193 K) spectrum of **1-CD$_2$Cl$_2$**.
Insets depict the doublet of doublets resonances at δ_P 98.9 (*middle, top*) and -16.5 (*middle, bottom*).

As noted in *Section 3.3civ*, the hydride could not be located in the single-crystal X-Ray diffraction difference map of **1-NBA**. The solution ^1H NMR (CD_2Cl_2, 193 K) spectrum reveals a single resonance indicative of a hydride *trans* to a vacant site[49, 53, 91]: an overlapping doublet of doublet of doublets, which collapses to a doublet upon ^{31}P decoupling at δ_H –28.43 [J(RhH) = 64.0 Hz; J(PH) ≈ 7 Hz; J(PH) ≈ 12 Hz; 1 H; **Figure 3.21**]. This compares well to the reported hydride resonance of [Rh{Cy$_2$P(CH$_2$)$_2$CH(CH$_2$)$_2$}H(ClCH$_2$Cl)][BAr$^F_4$] which is observed as a broad (FWHM = 40 Hz) doublet at δ_H -27.24.[53] Free NBA is noted in the solution ^1H NMR

spectrum by the bridge CH_2 resonance at δ_H 2.07, however the remaining methylene

and bridgehead proton resonances are overlapped with the phosphine backbone

and tBu methyl resonances.
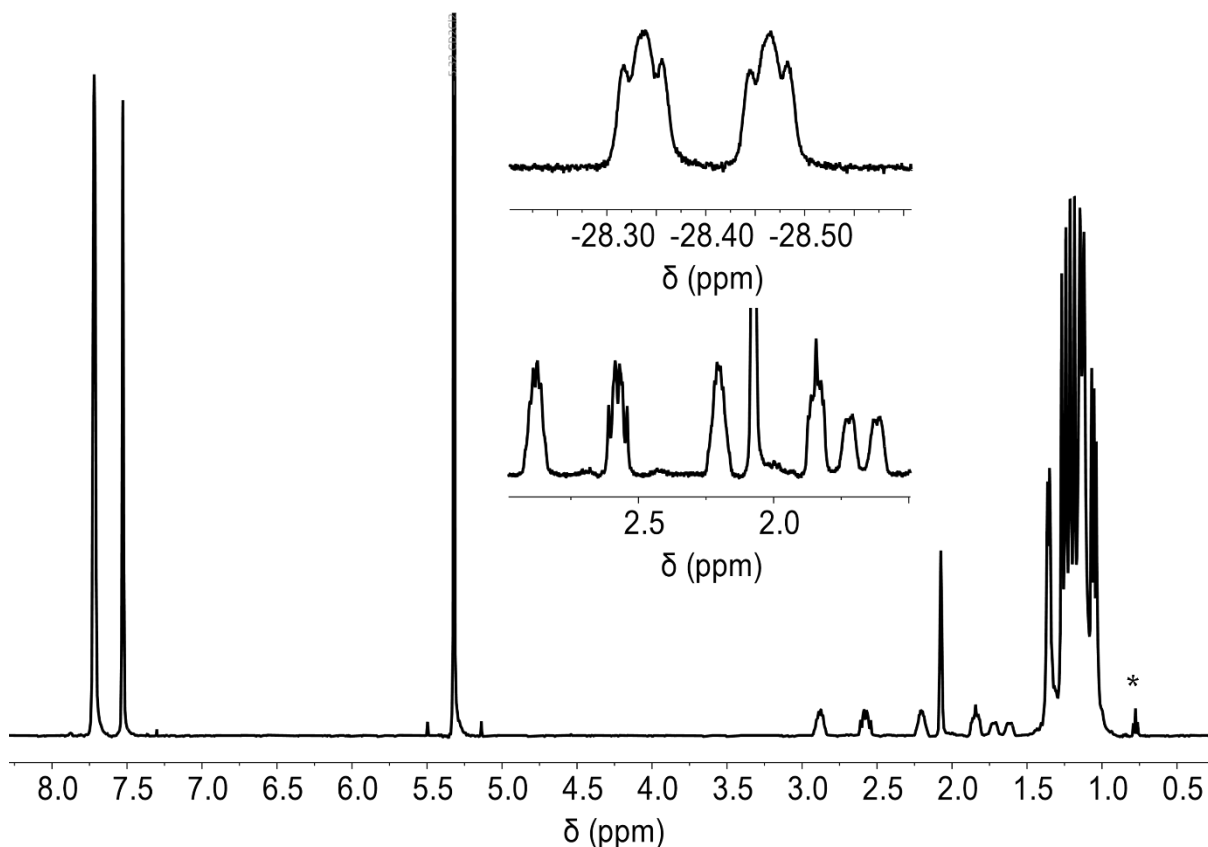
Figure 3.21: Solution ^{1}H NMR (500 MHz, CD_2Cl_2, 193 K) spectrum of **1-CD₂Cl₂**. Insets

depicts the hydride resonance at δ_H -28.43 (*middle, top*) and the phosphine backbone protons

between δ_H 3.0 and 1.5 (*middle, bottom*). Asterisk denotes minor pentane solvent impurity.

3.2.cvii. Single-Crystal X-Ray diffraction Analysis of 1-CD₂Cl₂

Small, light-yellow crystals of **1-CD₂Cl₂** were obtained from layering a solution of

1-CD₂Cl₂ in CD_2Cl_2 with heptane at -30 °C. **1-CD₂Cl₂** crystallises in the monoclinic

space group $P\,2_1/c$, with two independent molecules in the asymmetric unit (ASU,

Z = 8). One equivalent of heptane co-crystallises in the ASU which could not be

appropriately modelled, and the electron density was treated with the Olex2[92] implementation of the BYPASS solvent mask.[93]

Both of the independent molecules in the ASU confirm the κ^3-coordination of the P-C(alkyl)-P ligand framework is retained and the κ^1-coordination of the CD_2Cl_2 ligand to the Rh(III) centre through a chlorine lone pair (**Figure 3.22**). The methine proton and hydride were located in the electron density difference map for *one* of the independent cations in the ASU. The hydride is found to be *anti* with respect to the methine proton on the C–H activated alkyl ligand. Unlike in **1-NBA**, the C–H activated alkyl ligand is not disordered in the SC-XRD model of **1-CD₂Cl₂**. The hydride associated with the other cation in the ASU could not be located in the electron difference map, and a 3-part disorder model of the CD_2Cl_2 ligand was established for this cation.
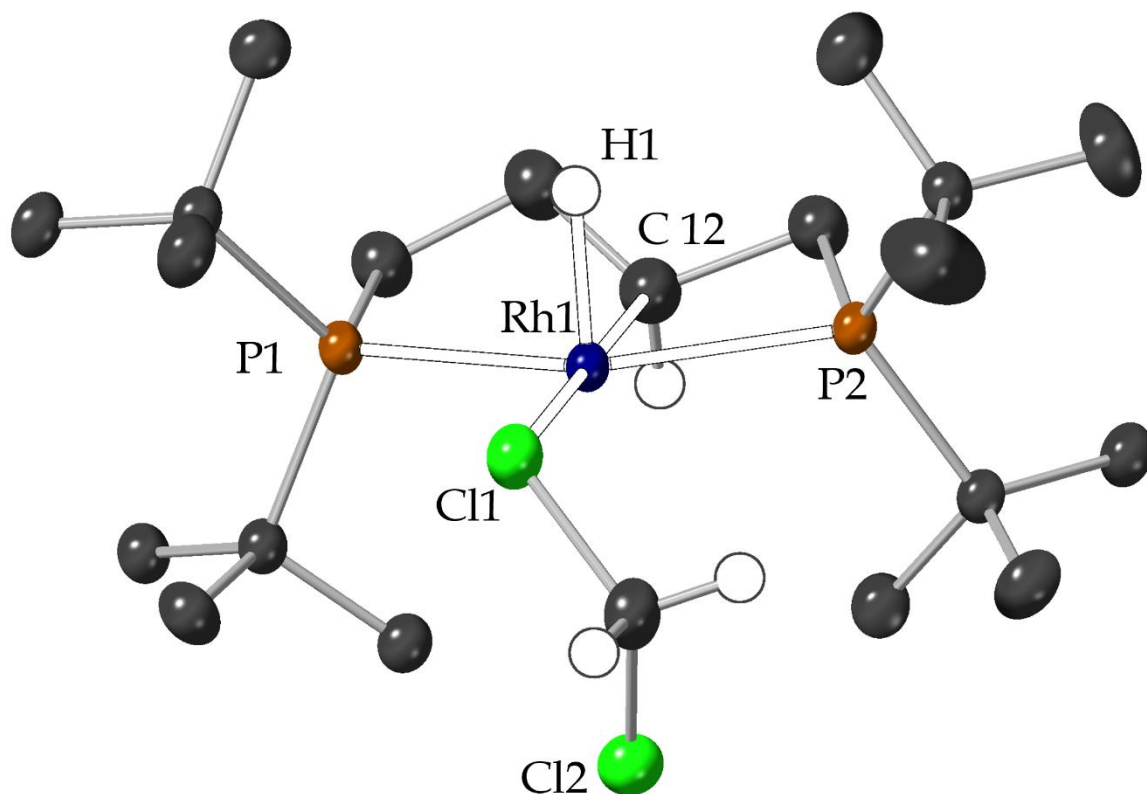
Figure 3.22: Solid-state structure of a well-resolved cation of **1-CD₂Cl₂**. The majority of hydrogen atoms are omitted for clarity. Thermal displacement ellipsoids displayed at 50%. Selected bond lengths and angles: Rh1-H 1.58(6) Å; Rh1-C12 2.045(5) Å; Rh1-Cl1 2.5692(13) Å; Rh1-P1 2.3033(9) Å; Rh1-P2 2.3365(9) Å; P1-Rh1-P2 154.50(4)°; P1-Rh1-Cl1 97.64(4)°; P1-Rh1-C12 83.56(12)°; P2-Rh1-Cl1 107.32(4)°; P2-Rh1-C12 71.38(11)°.

3.2cviii. (Periodic) DFT Calculations of 1-NBA

Due to the ambiguity of the single-crystal X-Ray diffraction data as to the location of the hydride ligand in **1-NBA**, models where the hydride is both *syn* and *anti* with respect to the alkyl ligand were investigated by DFT calculations (**Figure 3.23**). Gas phase calculations [PBE-D3//SDD(Rh/P)//6-31G(Rh/P/C/H)][94] show that the *anti*-isomer is the lowest in energy by 1.62 kcal mol⁻¹, consistent with the SC-XRD

model of **1-CD₂Cl₂**. Owing to the increased computational demands of periodic DFT calculations,[95, 96] only this isomer was studied using periodic DFT.

Anti-isomer   *Syn*-isomer
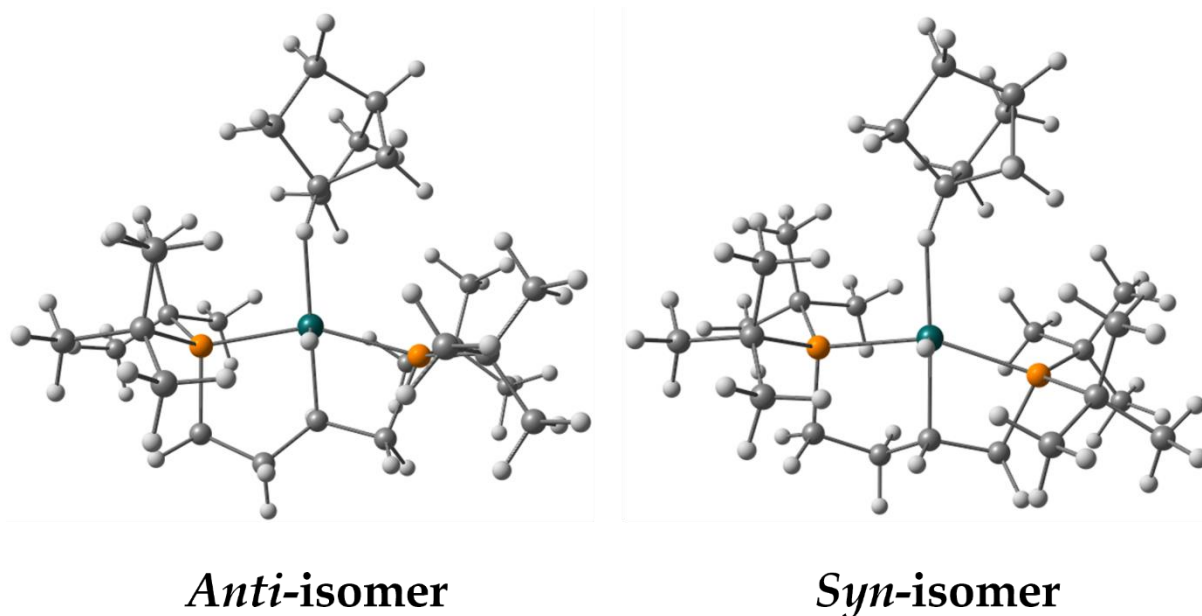
Figure 3.23: The models of the *anti-* (*left*) and *syn*-isomers (*right*) of **1-NBA** investigated by gas phase DFT calculations. The *anti*-isomer was found to be lower in energy by 1.62 kcal mol⁻¹.

The DFT-optimised geometry of **1-NBA** was investigated by Quantum Theory of Atoms in Molecules (QTAIM)[97] which locates bond paths between atoms based on electron density (ρ).[98] A bond path is located between the rhodium and the bridgehead methine proton on the NBA fragment (**Figure 3.24**). This bond path is directed into the hydrogen of the C–H bond, confirming the η^1-assignment of this interaction. A significant decrease in electron density at the bond critical point (ρ) of the coordinated C–H bond (0.2494 e bohr⁻³) is noted compared to the 'spectator' methine C–H bond on the opposite side of the NBA fragment (0.2761 e bohr⁻³). This

suggests there is a decrease in the C–H bond order upon coordination to the Rh(III) centre, as expected based on the models of σ(C–H) donation and Rh donation into the σ*(C–H) orbital (*Section 1.5a*).
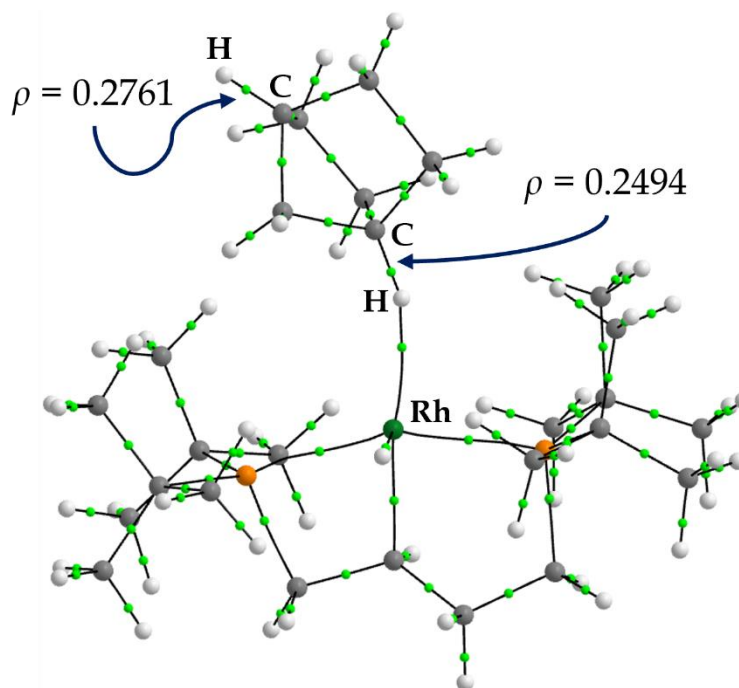
Figure 3.24: QTAIM plot of **1-NBA**. Electron density at the bond critical points of both bridgehead C–H bonds of the NBA fragment are displayed. Bond critical points shown in green. Ring critical points are omitted for clarity. Units of ρ = e bohr^{-3}.

A Natural Bond Order (NBO)[99-101] analysis was conducted on **1-NBA**, which found that the σ(C–H) donation and Rh backdonation into the σ*(C–H) contributions to the Rh-NBA σ-bonding are rather balanced, but Rh-σ*-backdonation slightly dominates (total σ-donation = 11.38 kcal mol^{-1}; total σ*-backdonation = 14.73 kcal mol^{-1}, **Figure 3.25**, **Table 3.1**). This contrasts from previous studies of [Rh(PP)(η²;η²-σ-NBA)][BAr$^F_4$] complexes where the alkane σ-donation dominants, by a factor of approximately 3.[53, 59, 62]

$$\sigma_{C-H} \text{ to } \sigma^*_{Rh-C}$$
10.61 kcal mol^{-1}

$$\sigma_{Rh-C} \text{ to } \sigma^*_{C-H}$$
5.43 kcal mol^{-1}
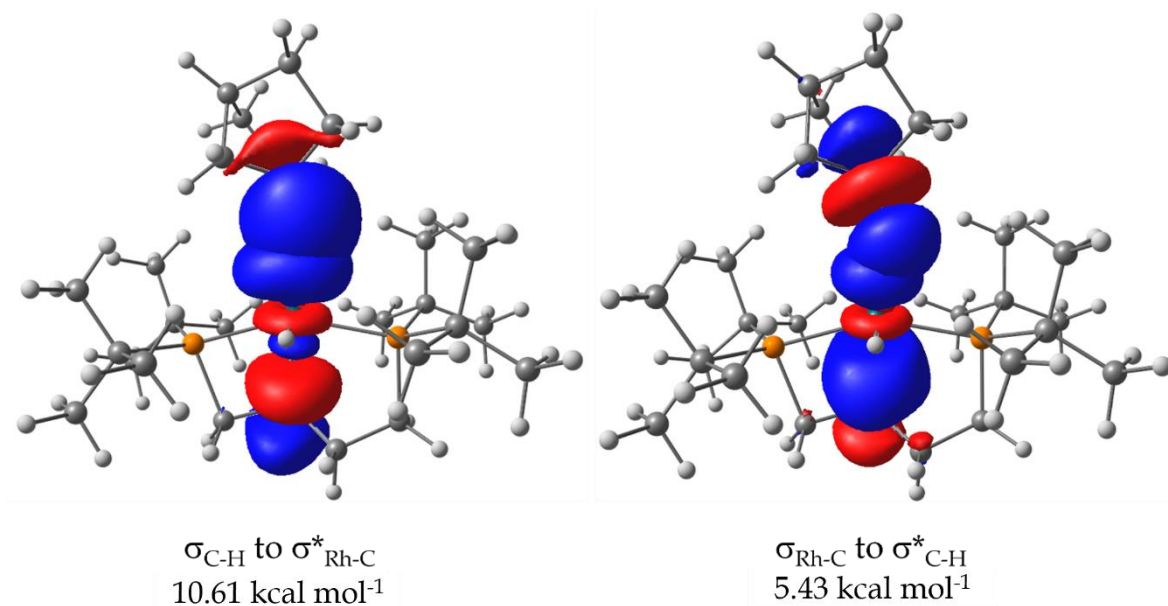
Figure 3.25: The two molecular orbitals which are the main contributors to the σ-donation (*left*) and σ-backdonation (*right*) associated with the Rh-NBA σ-bonding in **1-NBA**.

Table 3.1: Donor-acceptor orbitals and their respective energies from NBO calculations for **1-NBA**.

Donor-Acceptor Orbitals	Energy (kcal mol^{-1})
σ-donation	
σ(C–H) → σ*(Rh–C)	10.61
σ(C–H) → σ*(Rh–P)	0.53
σ(C–H) → σ*(Rh–H)	0.24
Total σ-donation	**11.38**
σ-backdonation	
σ(Rh–C) → σ*(C–H)	5.43
σ(Rh–P) → σ*(C–H)	4.95
σ(Rh–H) → σ*(C–H)	3.01
Rh LP(1) → σ*(C–H)	0.41
Rh LP(2) → σ*(C–H)	0.93
Total σ-backdonation	**14.73**

A similar degree of Rh σ-backdonation compared to σ(C–H)-donation was noted for [RhH{Cy$_2$P(CH$_2$)$_2$CH(CH$_2$)$_2$PCy$_2$}(η^1-σ-cyclooctane)][BAr$^F_4$], where the total σ-

(C–H)-donation was found to be 12.5 kcal mol^{-1} and the Rh σ-backdonation was 11.1 kcal mol^{-1}.[53] The degree of σ-backdonation was noted as similar in strength to '*pregostic*'[102-105] interactions (previously known as pseudo-agostic, or preagostic interactions; **Figure 3.26**). Pregostic interactions are considered to be short (M···H–C ≈ 2.4 Å), electrostatic interactions where the onset of covalency, especially M σ*-backdonation, becomes relevant.[105] They differ from *anagostic* interactions which are topologically enforced and due to ring-current effects at the metal, rather than formation of a M···H-C bond path (**Figure 3.26**).[105-108]

Agostic	*Pregostic*	*Anagostic*
3-centre-2-electron	Largely electrostatic, significant σ*-backdonation	Ring-current effects
d(M···H) ≈ 1.8 – 2.3 Å	d(M···H) ≈ 2.4 Å	d(M···H) ≈ 2.5 – 2.9 Å
δ_H upfield of uncoordinated C-H	δ_H downfield of uncoordinated C-H	δ_H downfield of uncoordinated C-H
M←σ(C-H) dominates	M→σ*(C-H) dominates	M→σ*(C-H) *very* small, but dominates
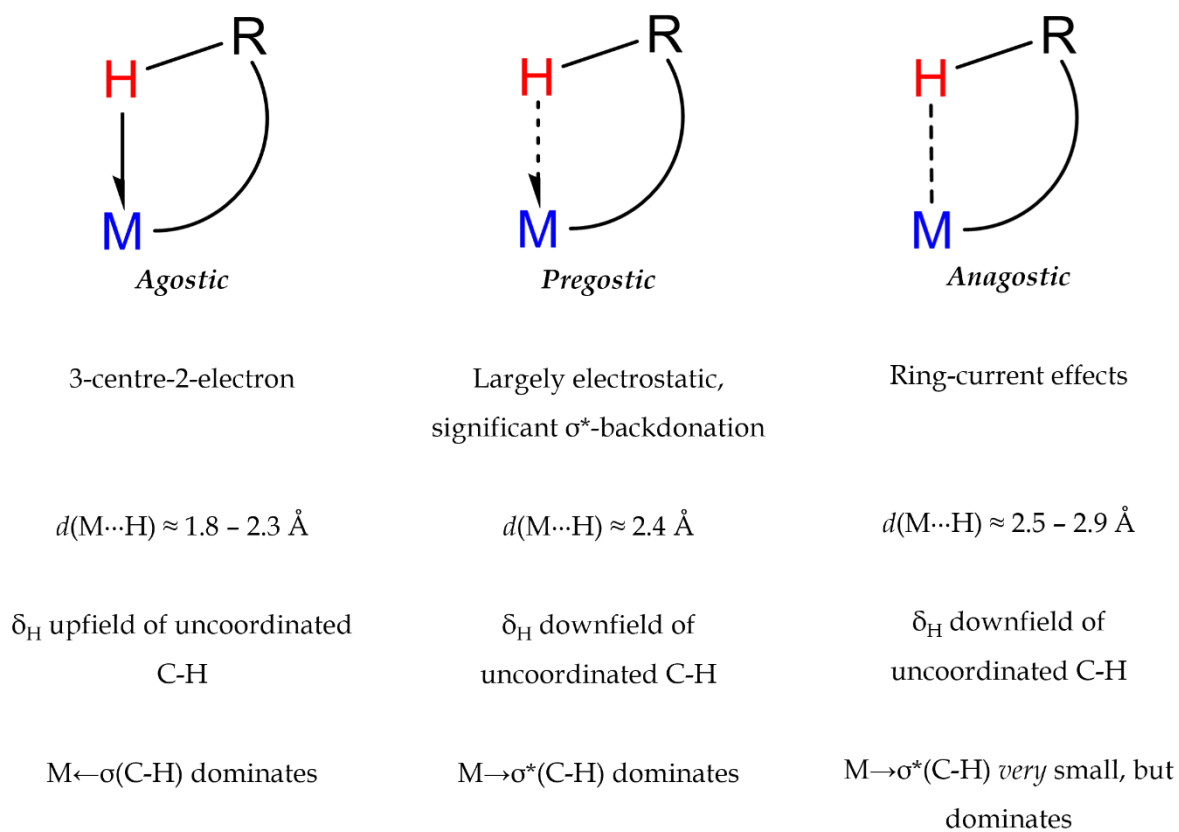
Figure 3.26: Comparison between agostic (*left*), pregostic (*middle*) and anagostic (*right*) interactions, with their variations in physical and spectroscopic properties.

As noted in ***Section 3.3civ***, the SC-XRD model of the σ-norbornane fragment of **1-NBA** exhibits significantly large atomic displacement ellipsoids, even at 110 K. Therefore, there is potential for ambiguity in the binding mode due to ambiguity in the precise location of the NBA being unresolved. Computational conformational searching analysis[109, 110] (GFN2-xTB)[111] has explored each potential η^1-σ-interaction of the alkane fragment, with 14 conformations explored, with isomers of η^1-σ-interactions from each of the methylene bridge, methine bridgehead, and methylene *endo* and *exo* positions (**Figures 3.27 - 3.30**). These are compared to the experimental conformer, obtained from SC-XRD data collected at 110 K.
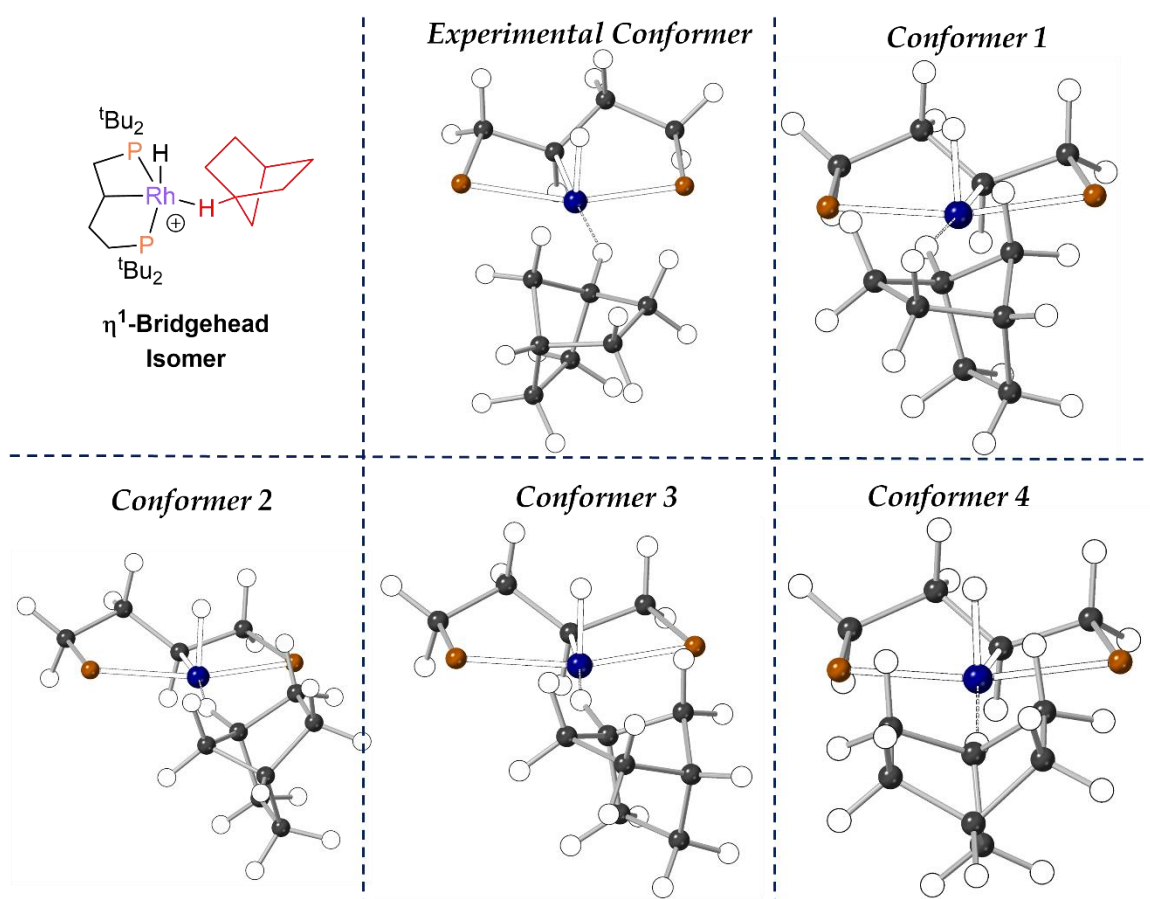
Figure 3.27: Conformers (*Experimental, 1-4*) of the Rh···η^1-Methine Bridgehead isomer of **1-NBA** studied by computational conformational searching analysis. *Tert*-Butyl environments omitted for clarity.
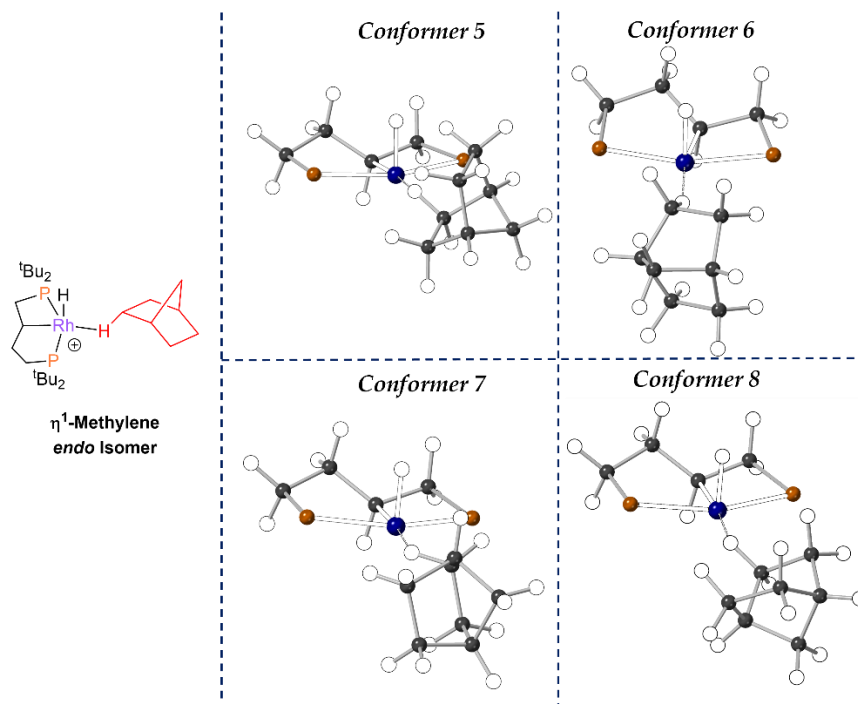
Figure 3.28: Conformers (*5-9*) of the Rh···η¹-Methylene *endo* isomer of **1-NBA** studied by computational conformational searching analysis. *Tert*-Butyl environments omitted for clarity.
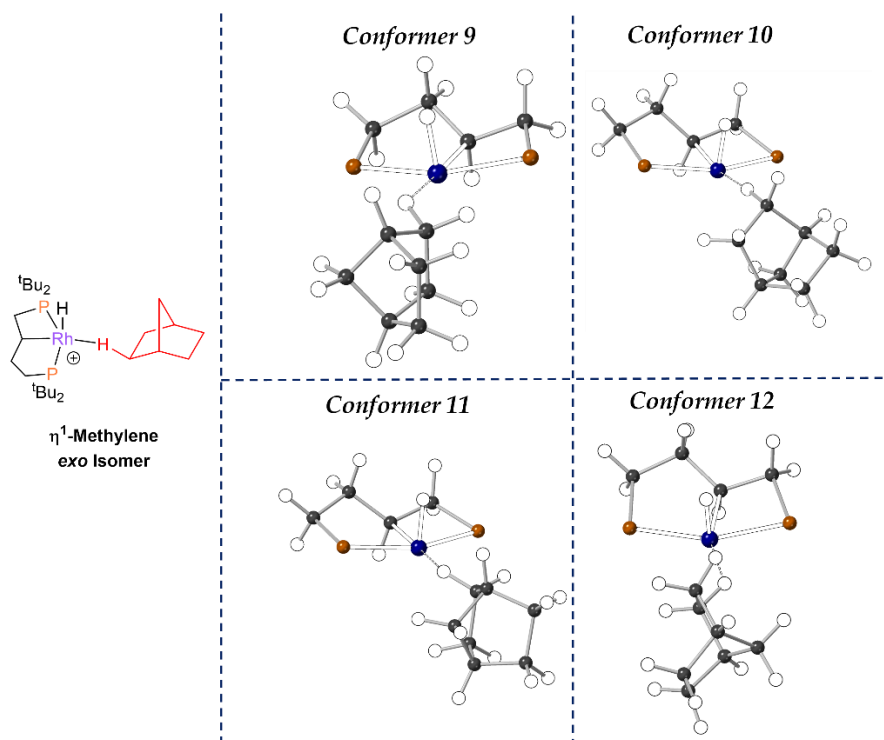
Figure 3.29: Conformers (*9-12*) of the Rh···η1-Methylene *exo* isomer of **1-NBA** studied by computational conformational searching analysis. *Tert*-Butyl environments omitted for clarity.
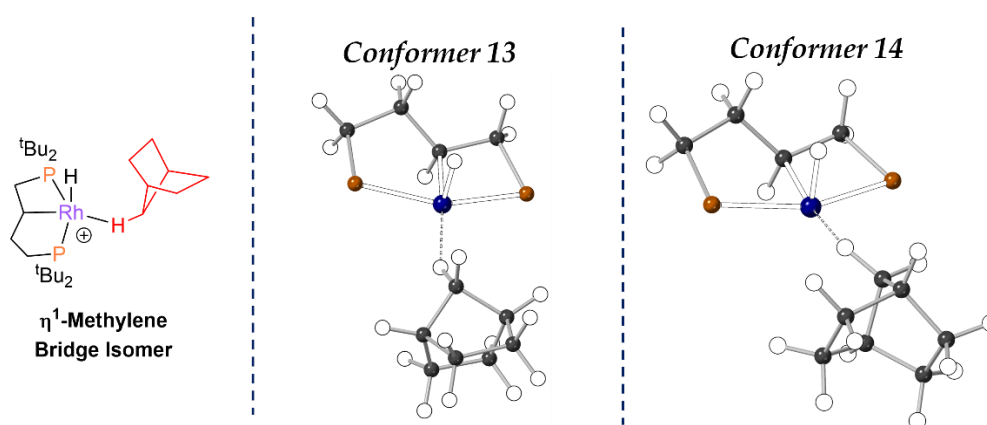
Figure 3.30: Conformers (*13 and 14*) of the Rh···η1-Methylene Bridge isomer of **1-NBA** studied by computational conformational searching analysis. *Tert*-Butyl environments omitted for clarity.

For each *in silico* experiment, the unit cell of **1-NBA** ($P\ 2_1/n$, $Z = 4$) was optimised with one cation substituted for the desired conformer. The energies of these conformations range from -1.71 to 7.62 kcal mol^{-1} compared to the experimentally observed conformation (**Table 3.2**). Due to computational demands, the barrier to the interconversion between these conformers has not been calculated but is assumed to be small based on the energy of the weak interactions which will be broken during each transition state.

Table 3.2: Relative energies of the η^1-isomers and conformers of **1-NBA**.

Isomer	Conformer	Relative Energy (kcal mol^{-1})
Bridgehead	*Experimental* (110 K)	0.00
	1	0.02
	2	-1.71
	3	-1.23
	4	3.79
Endo	5	0.23
	6	1.29
	7	3.89
	8	6.34
Exo	9	2.07
	10	3.27
	11	5.50
	12	7.62
Methylene bridge	13	4.79
	14	6.14

Conformer 2 and *Conformer 3* are remarkably similar to the model of the SC-XRD data. Therefore, the conformational searching analysis matches the experimental data, with the lowest energy isomer (Rh···η^1-Methine Bridgehead) being the sole observed isomer in the SC-XRD model. The NBA orientation of the NBA fragment in *Conformer 4*, which is the highest energy conformer of this isomer, does not fit

with the experimental SC-XRD data. No evidence of the other isomers (η^1-*Endo*-Methylene, η^1-*Exo*-Methylene, or η^1-Methylene bridge) is observed in the SC-XRD data. Therefore, it is suggested that interconversion between these isomers is not kinetically accessible in the solid-state. The facile interconversion between the conformers of the η^1-Methine bridgehead reflects the enlarged displacement ellipsoids observed in the SC-XRD data.

The energy associated with overall alkane binding in **1-NBA** was investigated through periodic-DFT calculations [PBE-D3//SDD(Rh/P)//6-31G(Rh/P/C/H)].[112-114] These calculations allow for the total energy to be deconvoluted into the Rh-alkane binding energy (molecular interaction energy) and the stabilisation provided in the solid-state through non-covalent and electrostatic interactions. The energy provided by non-covalent interactions can be separated from the electrostatic interactions through calculating the overall energy of the system with, and without, Grimme's dispersion corrections.[115]

Despite previous research from the Chaplin group,[89] and others,[53, 106] suggesting that the relatively long Rh···C distance [2.982(5) Å] in **1-NBA** should represent only a weak σ-interaction in comparison to shorter η^2-σ-C–H interactions, the molecular interaction energy of **1-NBA** was found to be 15.96 kcal mol^{-1}. This energy is approximately 50% of the *total* molecular interaction energies of previously reported η^2;η^2-σ-NBA complexes which possess much shorter Rh···C distances.[78] **1-NBA** differs from these earlier reports by having only one σ-interaction, whereas the previously reported values come from complexes with two σ-interactions. This

therefore implies that the η^1-σ-interaction observed in **1-NBA** is of comparable strength to previously reported η^2-σ-interactions.

The stabilisation energy of **1-NBA** provided by the 2° microenvironment is found to be 15.21 kcal mol^{-1} which is comparable to the previously reported values for σ-alkane complexes.[78] The non-covalent interactions contributing to the molecular interaction energy and solid-state stabilisation, have been mapped with an Independent Gradient Model with Hirshfeld Partitioning (IGMH) plot (**Figure 3.31**).[116] Stabilising C–H···H hydrogen bonds are found between the NBA fragment and the *tert*-butyl groups which have been thrust towards the alkane through the structural-response of the ligand backbone. Non-covalent C–H···π and C–H···F interactions are found between the NBA fragment and the neighbouring [BAr$^F_4$]$^-$ anion are also observed.
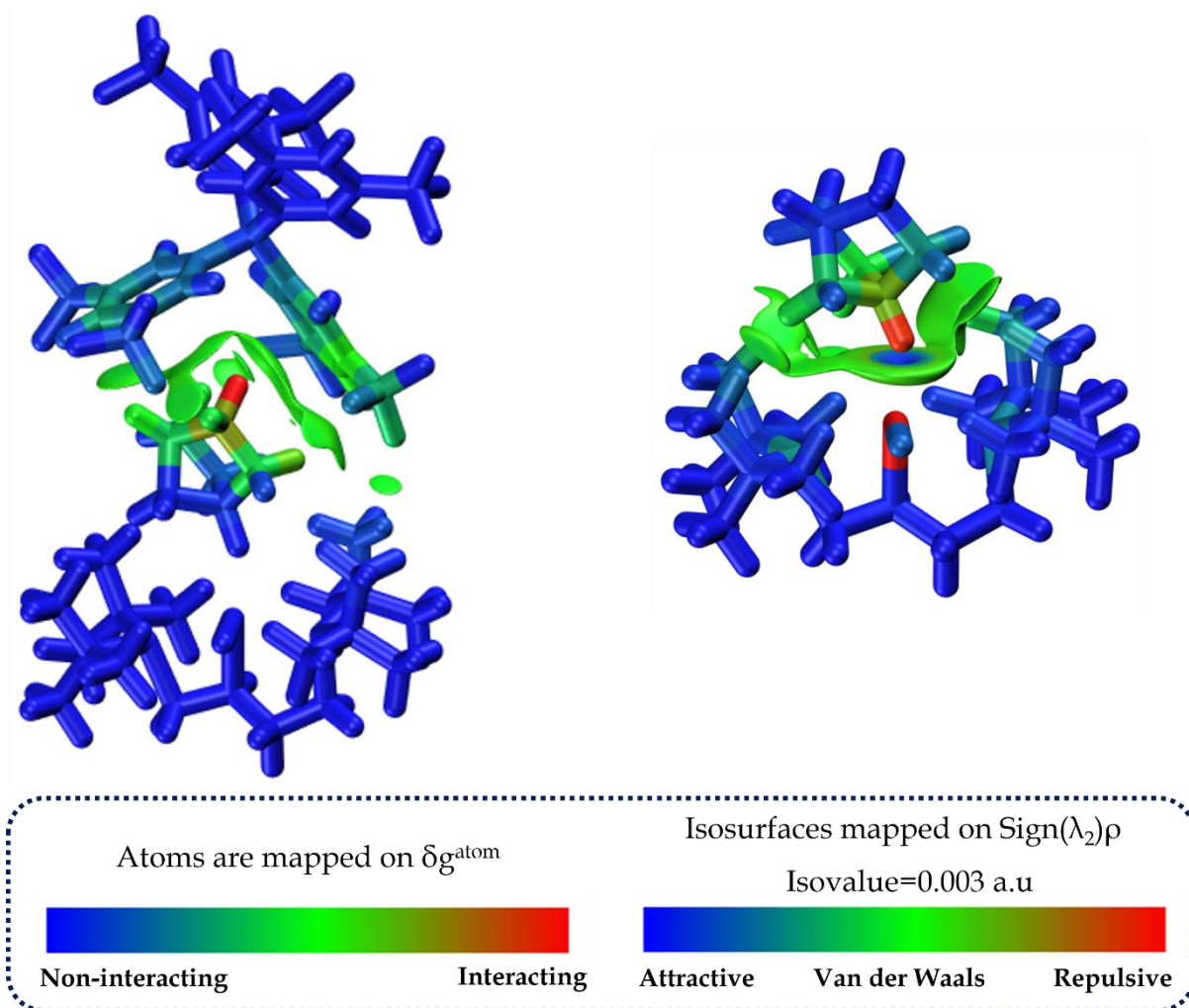
Figure 3.31: IGMH plots of **1-NBA**. *Left*: Isosurfaces map the non-covalent interactions between the NBA fragment and the neighbouring [BArF₄]⁻ anion. *Right*: The Rh-alkane σ-interaction, and intramolecular non-covalent interactions between the NBA and the *tert*-butyl groups, are mapped by the isosurfaces. *Note: The colour scheme for the degree of attraction between atoms, and the isosurfaces, are the same but use opposite signs.*

3.2d. Selective H/D Exchange in the Solid-State

3.2di. Previous Studies on Selective H/D Exchange with {Rh(dcpe)}+ in the Solid-State

As briefly discussed in *Section 1.7*, the {Rh(dcpe)}+ framework has been shown to enable selective H/D exchange on bound σ-alkane fragments. For example, the σ-NBA complex can undergo H/D exchange at the *exo* positions, which can be selected for by variation of the experimental conditions.[96, 117] Likewise, addition of D$_2$ to [Rh(dcpe)($\eta^2;\eta^2$-σ-cyclohexane)][BAr$^F_4$] or [Rh(dcpe)($\eta^2_\Pi;\eta^2_{CH}$-isobutylene)][BAr$^F_4$] results in rapid perdeuteration of cyclohexane to cyclohexane-d_{12} and a distribution of isotopologues of isobutane-$d_{6\text{-}10}$, respectively (**Scheme 3.14**).[74]
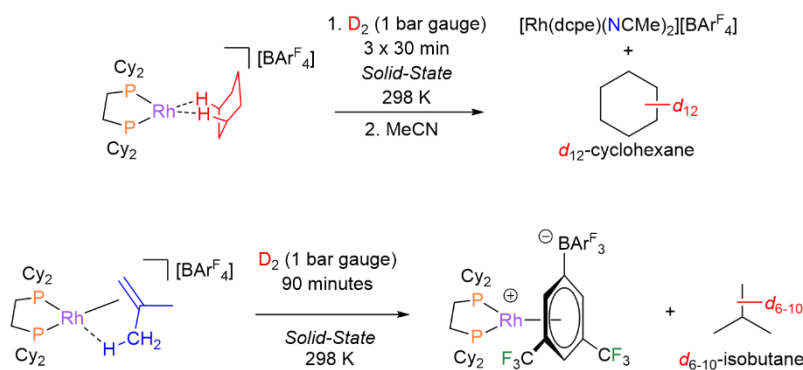
Scheme 3.14: Previously reported examples of H/D exchange into Rh σ-alkane complexes.[74]

3.2dii. Solid-State Deuteration of 1-NBD

No prior studies have reported on the *in-crystallo* reactivity of Rh(III) σ-alkane complexes, or η^1-σ-alkane complexes. Therefore, the *in-crystallo* reactivity of **1-NBD**

with D_2 was investigated to shed light on the whether H/D exchange would occur with Rh(III) η^1-σ-alkane complexes.

Addition of D_2 (1 bar gauge, 120 minutes) to single-crystalline samples of **1-NBD** leads to an analogous single-crystal to single-crystal transformation as addition of H_2, to form **2-NBA**. The gross structure is found to be essentially unchanged from **1-NBA** in the SC-XRD model (R_1 = 9.52%, R_{int} = 12.08%). Likewise, the solid-state $^{31}P\{^1H\}$ CP MAS NMR (162.06 MHz, 20 kHz spin-rate, 298 K) spectrum is similar to **1-NBA**, with two resonances, which are shifted from those of **1-NBA** by the isotopic perturbation of chemical shift[74] (δ_P 101.1 and –7.4 *cf.* **1-NBA** δ_P 100.6 and -8.5, **Figure 3.32**). The observed coupling of these peaks is also similar to that of **1-NBA**, with the resonance at δ 101.1 observed as a doublet of doublets [J(RhP) = 118 Hz; J(PP) = 285 Hz; *cf.* **1-NBA** J(RhP) = 115 Hz; J(PP) = 280 Hz] and the resonance at δ -7.4 as an apparent triplet (J_{app} = 310 Hz; *cf.* **1-NBA** J_{app} = 300 Hz).
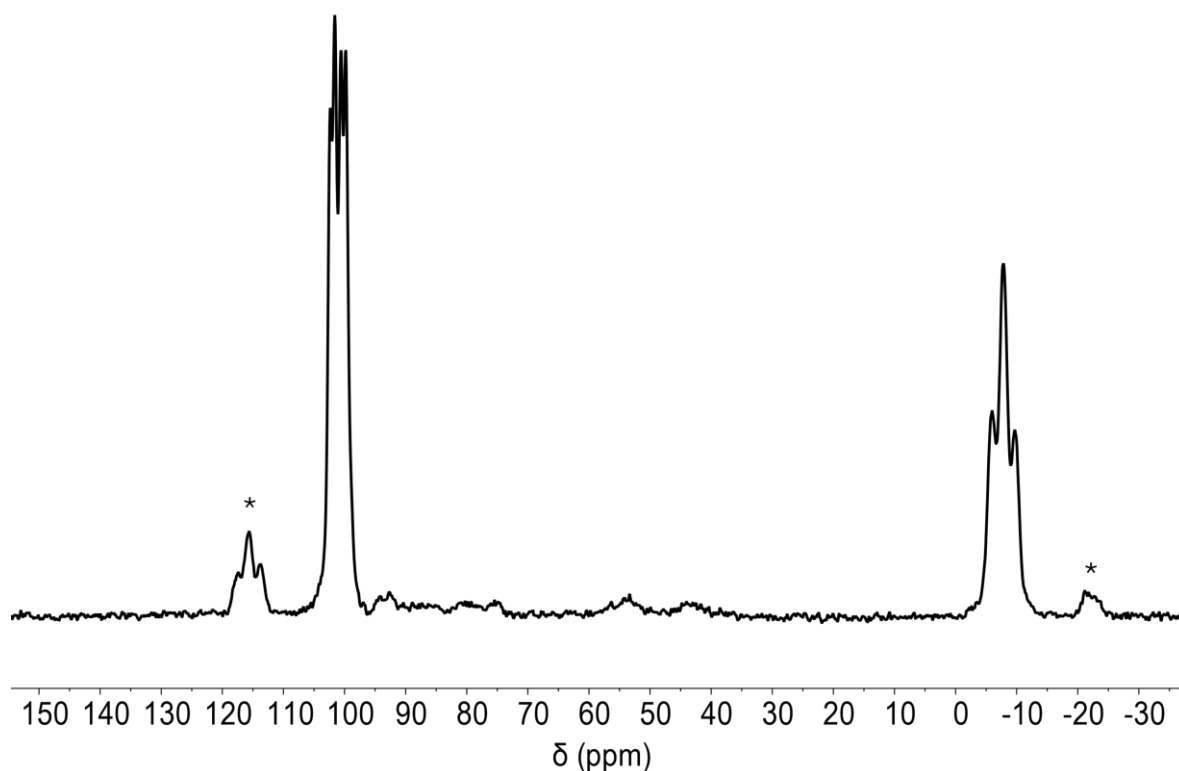
Figure 3.32: $^{31}P\{^{1}H\}$ CP MAS NMR (162.06 MHz, 20 kHz spin-rate, 298 K) spectrum of a sample of **1-NBD** exposed to D_2 for 2 hours. Asterisks denote spinning side bands.

However, dissolution of **2-NBA** into CD_2Cl_2 and analysis of the resultant CD_2Cl_2-adduct *via* solution $^{31}P\{^{1}H\}$ NMR (CD_2Cl_2, 193 K) spectroscopy highlights a large disparity in the solution- and solid-state $^{31}P\{^{1}H\}$ NMR spectra for **2-NBA/2-CD₂Cl₂**. Whereas the solution $^{31}P\{^{1}H\}$ NMR spectrum of **1-CD₂Cl₂** shows two mutually coupled, doublet of doublet resonances at δ_P 98.8 and -16.5 (**Figure 3.20**), the deuterated sample shows two sets of complex, overlapping sets of peaks, centred at δ_P 97.9 and -17.4 (**Figure 3.33**). The approximate *J*-couplings of the overlapping signals compare well to that of **1-CD₂Cl₂** [**1-CD₂Cl₂:** δ_P 98.8; *J*(RhP) = 127 Hz; *J*(PP) = 289 Hz; δ_P -16.5; *J*(RhP) = 90 Hz; *J*(PP) = 289 H; **2-CD₂Cl₂**: δ_P 97.9; *J*(RhP) = 124 -

128 Hz; *J*(PP) = 291 – 295; δ_P -17.4; *J*(RhP) *undetermined*; *J*(PP) = 289 – 295 Hz]. The

resonances of **1-CD₂Cl₂** are seen within this complex mixture as the most downfield

resonances in both sets of the overlapping signals (**Figure 3.33**). The remaining

signals in these complex clusters of resonances are assigned to isotopologues of **1-CD₂Cl₂**, which result from sequentially increased H/D exchange, where the signals

are isotopically shifted upfield with each further deuterium for proton substitution.

Extended exposure times, or repeated recharges of D_2, does not lead to differences

in the deuterium incorporation into **2-CD₂Cl₂** as determined by solution NMR

spectroscopy. Instead, **1-NBD** is sensitive to hydrogenation and deuteration

timeframes, and decomposition becomes evident with formation of unidentified

hydride products after extended periods under H_2 or D_2.
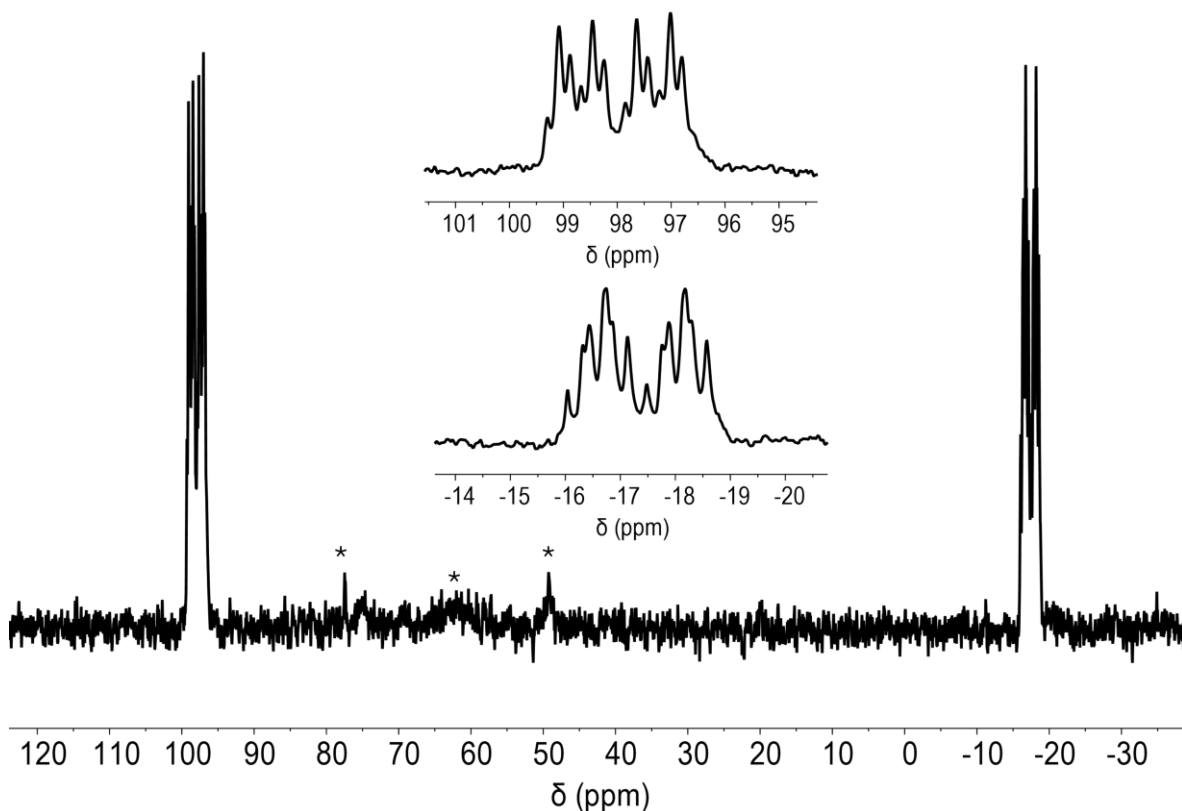
Figure 3.33: Solution $^{31}P\{^1H\}$ NMR (202.52 MHz, CD_2Cl_2, 193 K) spectrum of **2-CD₂Cl₂**. Insets depict fine structure of the downfield (*middle, top*) and upfield (*middle, bottom*) environments. Asterisks denote undetermined decomposition products.

The solution ^1H NMR (CD_2Cl_2, 193 K) spectrum of **2-CD₂Cl₂** also underscores the difference between deuteration and hydrogenation of **1-NBD**. The resonances associated with the phosphine backbone protons markedly decrease in intensity (relative to the *ortho*-[BAr$^F_4$]⁻ resonance of 8 H). and their chemical shifts slightly change (**Table 3.3**). The hydride resonance (δ_H -28.42) integration also decreases (0.61 H *cf*. **1-CD₂Cl₂** 0.73 H; d1 time of 10 seconds used throughout for consistency). The overall integral of the region of δ_H 1.44 to 1.34 where the ᵗBu methyl environments and liberated norbornane overlap decreases by slightly more than

234

the expected 4 H for NBA-d_4 formation (41.04 H *cf.* **1-CD$_2$Cl$_2$** 45.70 H). These data suggest that the ligand framework and associated hydride, are being substituted by deuterium during the *in-crystallo* reaction. It must be noted that the NMR spectroscopic data of **2-CD$_2$Cl$_2$** exhibits small levels of decomposition which are not observed in **1-CD$_2$Cl$_2$**, which will impact the accurate integration of the resonances.

Table 3.3: Comparison between the chemical shifts and integration of the phosphine backbone and hydride resonances in **1-CD$_2$Cl$_2$** and **2-CD$_2$Cl$_2$**. Integrations relative to *ortho*-[BAr$^F_4$]$^-$ resonance.

1-CD$_2$Cl$_2$		2-CD$_2$Cl$_2$	
Chemical Shift (δ$_H$)	*Integration*	*Chemical Shift (δ$_H$)*	*Integration*
2.87	0.74	2.85	0.28
2.58	0.75	2.55	0.32
2.20	0.72	2.18	0.57
1.85	0.74	1.81	0.37
1.67	0.80	1.64	0.91
-28.43	0.73	-28.42	0.61

The mixture of deuterated isotopologues produced through this reaction shall be referred to as **2-NBA** or **2-CD$_2$Cl$_2$** in the remainder of **Chapter 3**. Due to overlap of signals in the solution ^{1}H NMR spectrum, detailed interpretation of the NBA resonances is not possible. Deuterium incorporation into the NBA fragment was investigated by addition of CH$_2$Cl$_2$ (0.6 mL) to **2-NBA**, followed by distillation of the volatiles into an NMR tube and analysis *via* solution ^{2}H NMR spectroscopy (298 K, CH$_2$Cl$_2$). The solution ^{2}H NMR spectrum shows two resonances at δ$_H$ 1.39 and 1.09 (**Figure 3.34**). These resonances are indicative of the *exo* and *endo* methylene

positions on the NBA, respectively.[117, 118] It is not possible to distinguish whether

this is sample contains a mixture of NBA fragments separately deuterated in *exo*

and *endo* positions, or each molecule is deuterated in both the *exo* and *endo* positions.
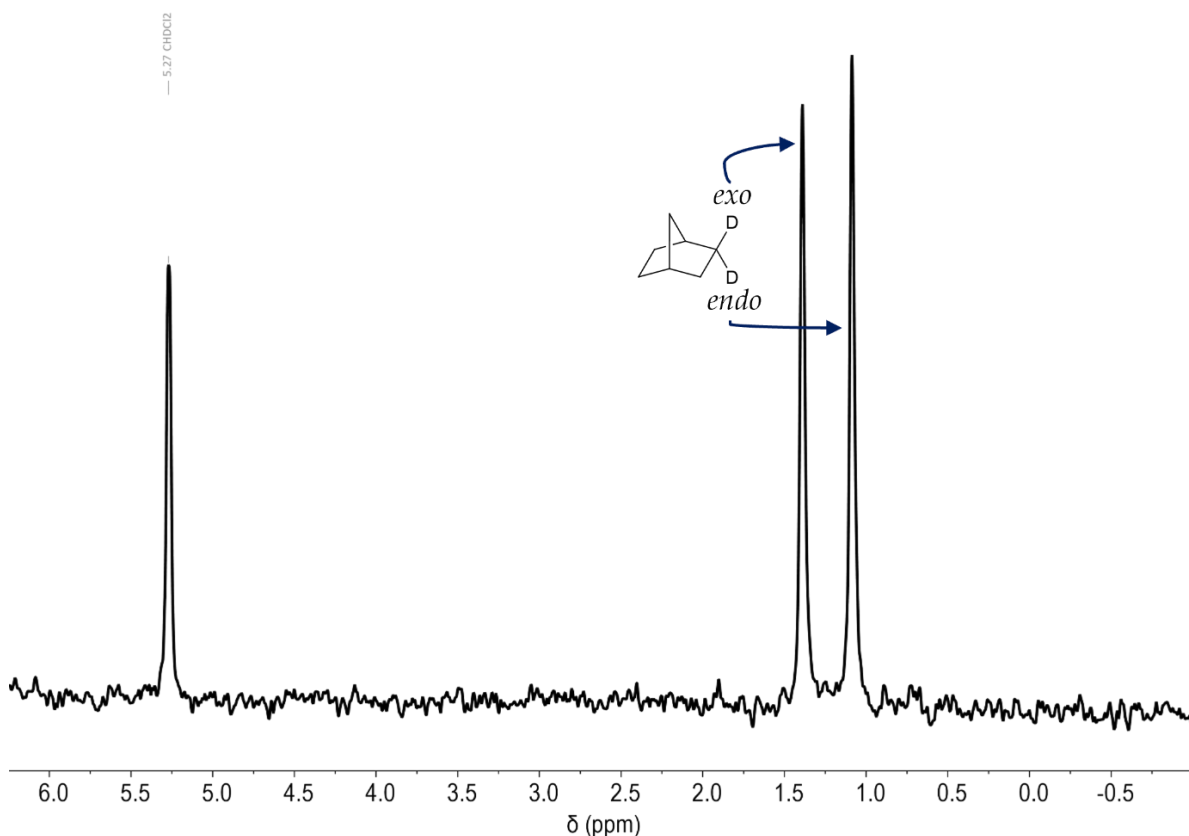
Figure 3.34: ^{2}H NMR (76.79 MHz, CH$_2$Cl$_2$, 298 K) spectrum of NBA-d_4, formed through solid-state deuteration of **1-NBD**.

The sample of volatiles assessed by solution ^{2}H NMR spectroscopy was analysed

by gas chromatography electron-ionisation mass spectrometry (GC/EI-MS).

Consistent with the solution ^{1}H and ^{2}H NMR spectroscopic data, the EI-MS

spectrum shows exclusively the presence of NBA-d_4 (m/z *found*: 100.12090; *calc.*

100.11901), with no further (or less) incorporation of deuterium than four per

fragment, to the detection limit of mass spectrometry (**Figure 3.35**). These data are

consistent with the deuteration of both alkene bonds of NBD. Unfortunately, **2-CD$_2$Cl$_2$** was found to be unstable under a range of mass spectrometry conditions, so the deuterium incorporation into the metal-phosphine fragment could not be investigated through this technique.
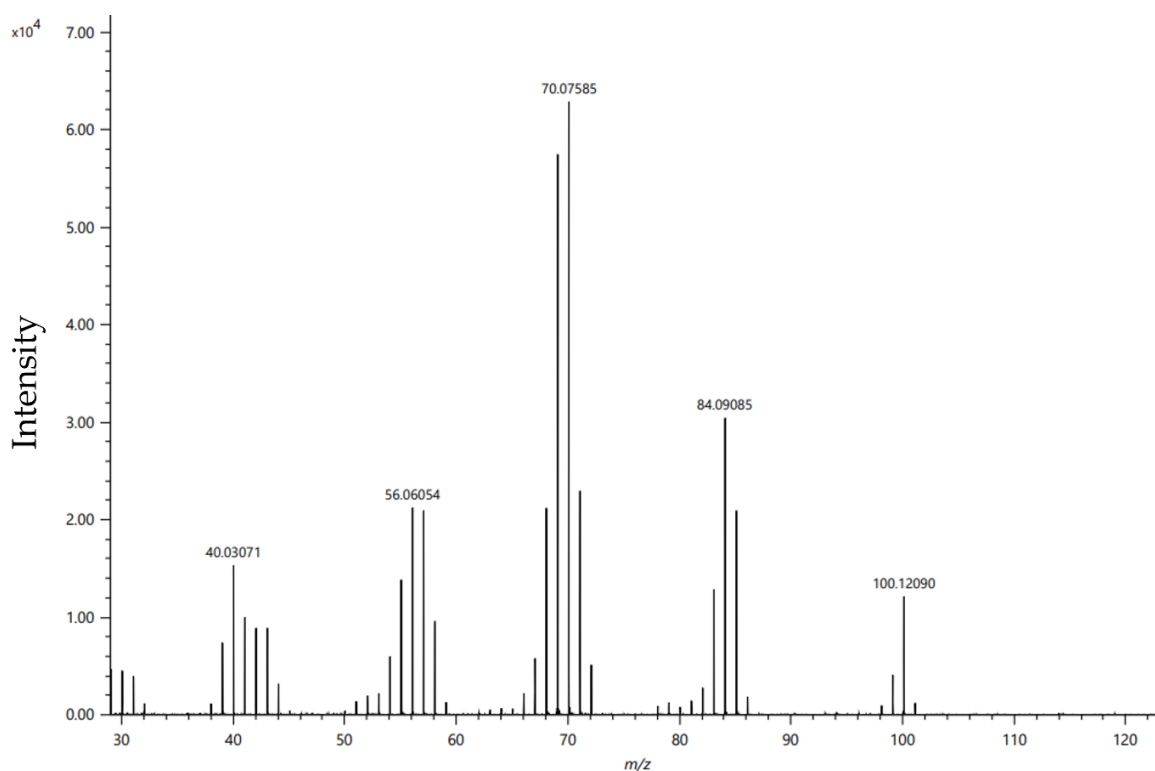
Figure 3.35: Gas chromatography electron-ionisation mass spectrum (GC/EI-MS) of the norbornane fragment from addition of D$_2$ gas to **1-NBD**. The peak at 100.12090 m/z is consistent with NBA-d_4 (calculated: 100.11901).

3.2diii. Solid-State Deuteration of 1-NBA

To probe whether H/D exchange also occurs into the σ-norbornane fragment of **1-NBA**, D$_2$ was added to single-crystals of **1-NBA** (1 bar gauge, 2 hours) to form **3-NBA**. As before, the solids were quenched with CH$_2$Cl$_2$, the volatiles were distilled and analysed by GC/EI-MS. Here, exclusively NBA-H_{12} was found (m/z *found*:

96.09401; *calc.* 96.09390) to the detection limit of mass spectrometry (**Figure 3.36**). This shows that the σ-bound alkane does not undergo H/D exchange in the solid-state, and that the d_4-incorporation of **2-NBA** must occur through D_2 addition across the alkene bonds in the formation of **2-NBA** from **2-NBD**.
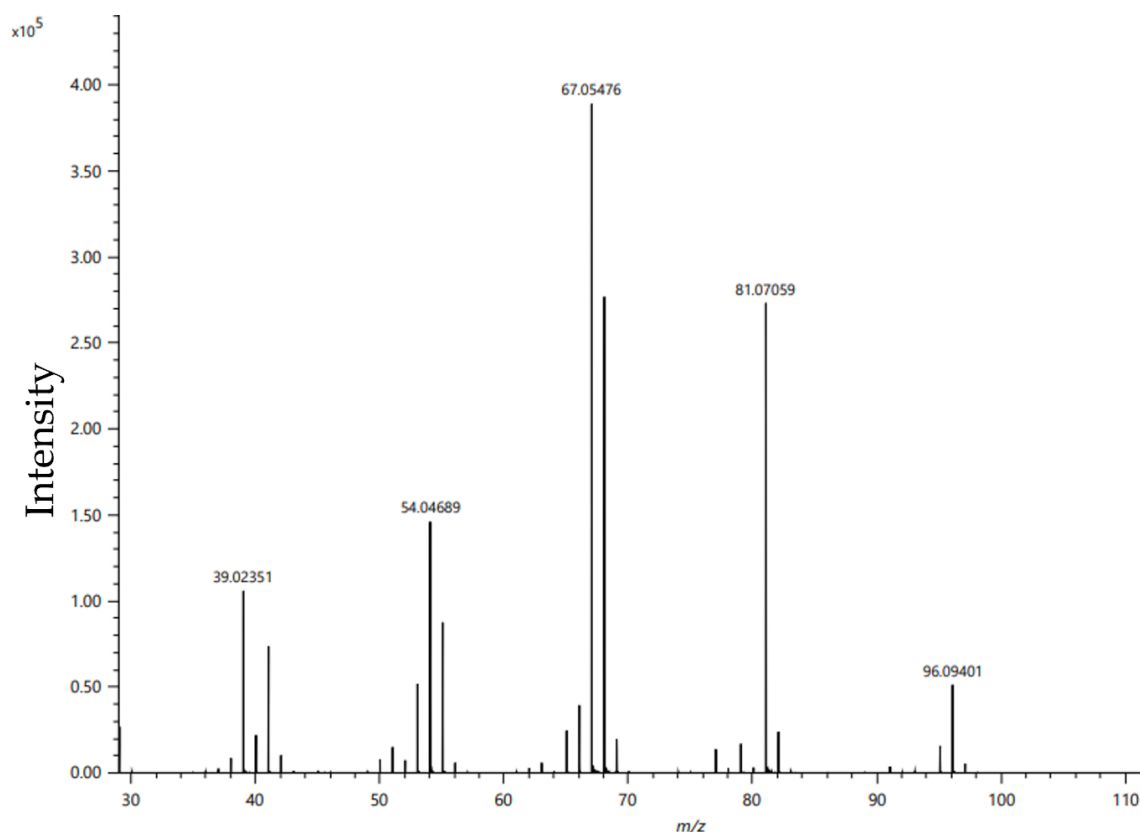
Figure 3.36: GC/EI-MS spectrum of the norbornane fragment produced from deuteration of **1-NBA** in the solid-state. The m/z peak at 96.09401 corresponds to NBA-H_{12} (*calc.* 96.09390).

3.2div. Synthesis of a Stable Analogue

As discussed in *Section 3.2dii*, investigation into the location, and extent, of deuterium incorporation into the metal-phosphine fragment was complicated due to the instability of **2-CD₂Cl₂** under mass spectrometry conditions, and peak overlap in the solution ¹H NMR spectra. For these reasons, a more robust analogue

was sought, bound by stronger ligands than CD_2Cl_2. Several ligands (dimethyl sulphoxide, pyridine, 4-dimethylaminopyridine, acetonitrile) were screened through addition to **1-CD₂Cl₂** followed by recrystallisation, and 2,2′-bipyridine (bpy, **Scheme 3.15**) was found to form the most stable complex under the required conditions. The single-crystal X-Ray structure of the resultant **1-bpy** shows the backbone activation is retained, forming a six-coordinate species with the κ³-PCP pincer, κ²-bpy and a hydride ligand (**Figure 3.37**).
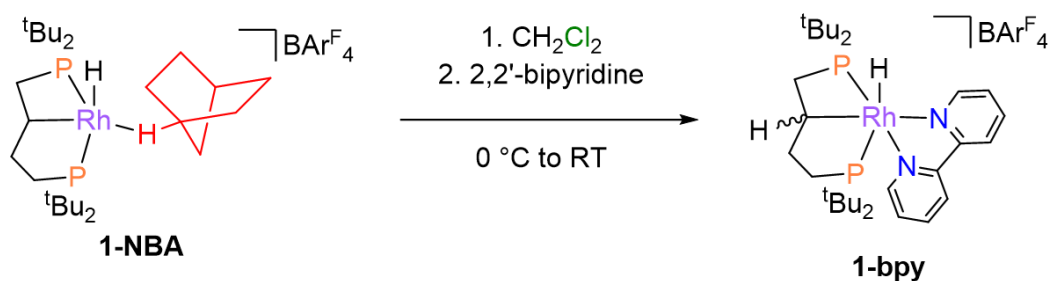
Scheme 3.15: Reaction scheme for the solution synthesis of **1-bpy** from **1-NBA** in CH_2Cl_2.
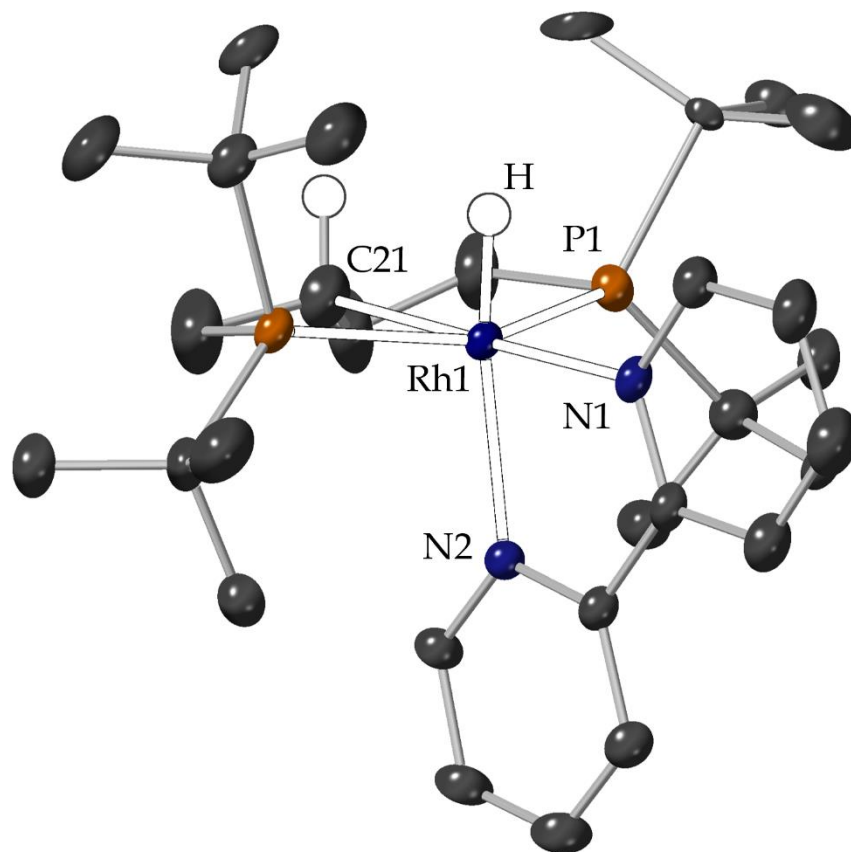
Figure 3.37: Solid-state structure of one cationic component within the ASU of **1-bpy**. Thermal displacement ellipsoids displayed at 50% occupancy. All protons except for the metal hydride and the activated phosphine backbone, are omitted for clarity. Selected bond lengths and angles: Rh1-H = 1.26(9) Å; Rh1-P1 = 2.3458(11) Å; Rh1-P2 = 2.386(8) Å; Rh1-C21 = 2.095(5) Å; Rh1-N1 = 2.150(3) Å; Rh1-N2 = 2.197(3) Å; P1-Rh1-P2 = 148.89(18)°; N1-Rh1-N2 = 75.75(13)°; P1-Rh1-C21 = 82.32(18)°; P2-Rh1-C21 = 68.0(3)°.

The solution ^{1}H NMR spectrum of **1-bpy** shows well resolved separation in the majority of the peaks of interest, including the backbone protons and the hydride resonances (**Figure 3.38**). Of note, however, is that two isomers are present and observed in all solution NMR spectra. These are assigned to presence of both the *syn-* and *anti*-isomers with respect to the proton on the alkyl ligand and the hydride

ligand. These are chemically inseparable but have been individually fully assigned through solution 2D NMR experiments (^{1}H-^{1}H NOESY, COSY, TOCSY and ^{1}H-^{31}P HMBC, **Figures 3.39 – 3.42**). The ratio of these isomers has been found to be highly sample dependent, which may be due to an isomerisation process occurring over the timescale of recrystallisation which will vary between samples, which has not been studied further.
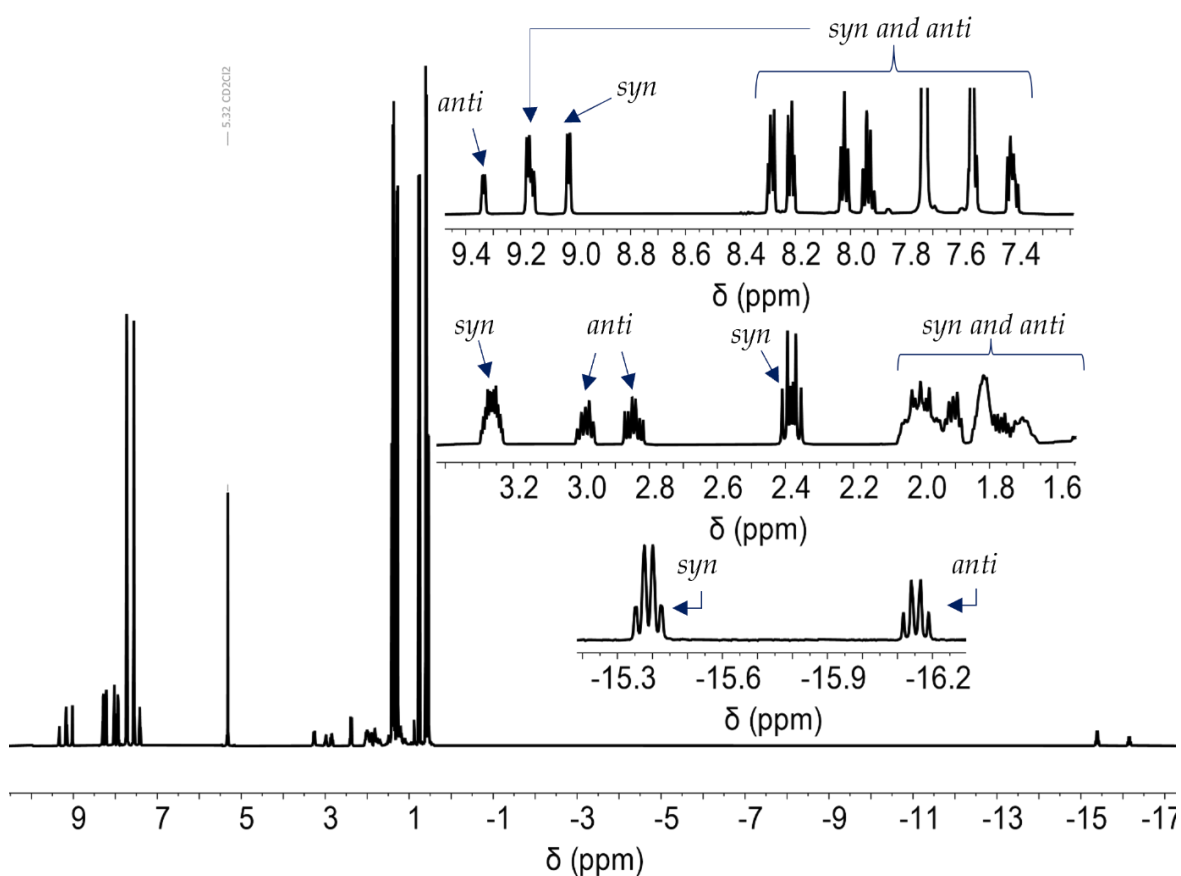
Figure 3.38: Solution ^{1}H NMR (500 MHz, CD$_2$Cl$_2$, 298 K) spectrum of **1-bpy**. Insets depict the aromatic (*top*), phosphine backbone (*middle*), and hydride (*bottom*) regions.
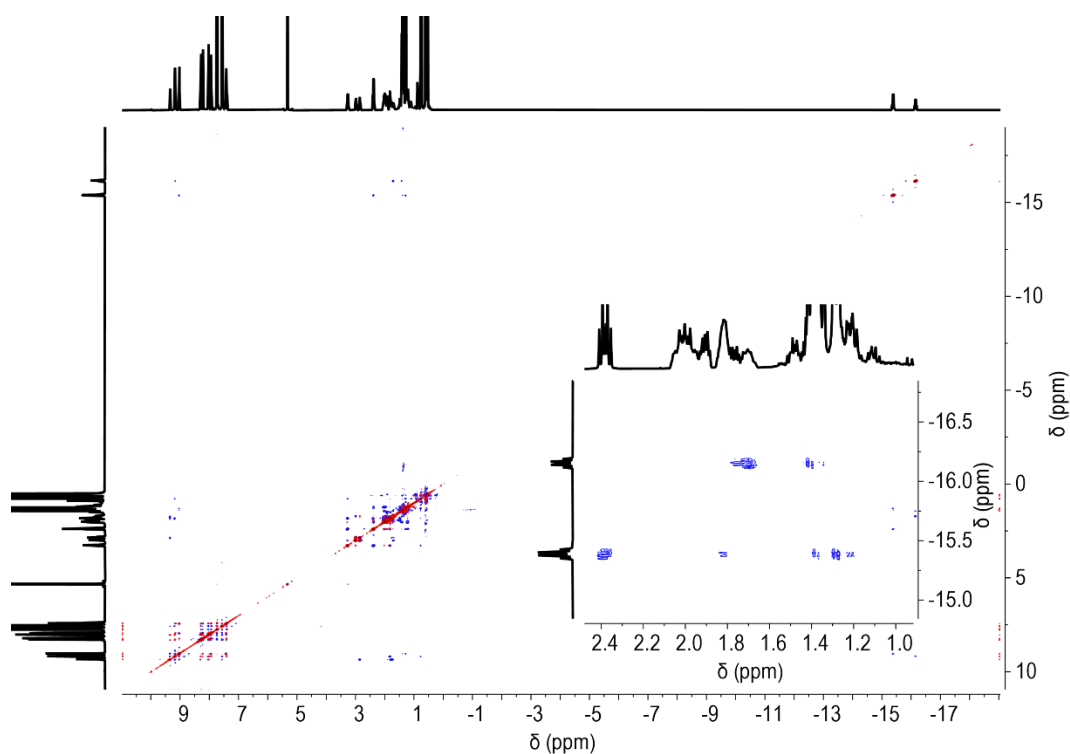
Figure 3.39: Solution ¹H-¹H NOESY spectrum of **1-bpy**. Inset depicts NOE peaks between the hydrides and the phosphine alkyl backbone.
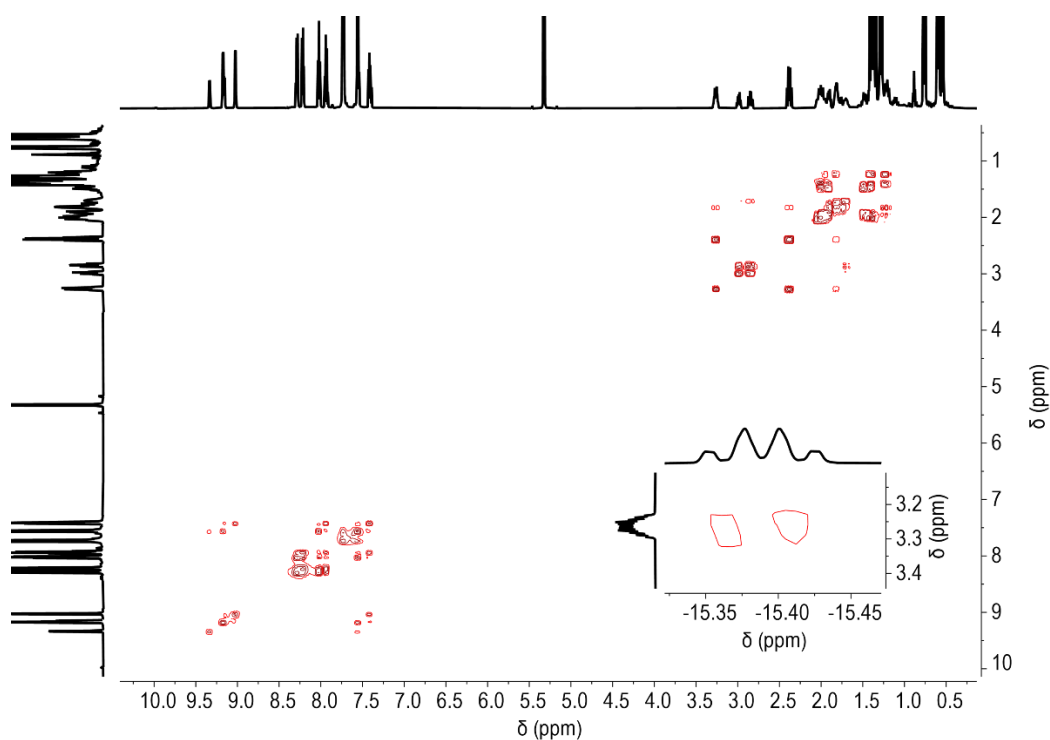
Figure 3.40: Solution ¹H-¹H COSY spectrum of **1-bpy**. Inset depicts COSY peak between hydride and proton on phosphine alkyl backbone, indicating *syn*-arrangement.

242
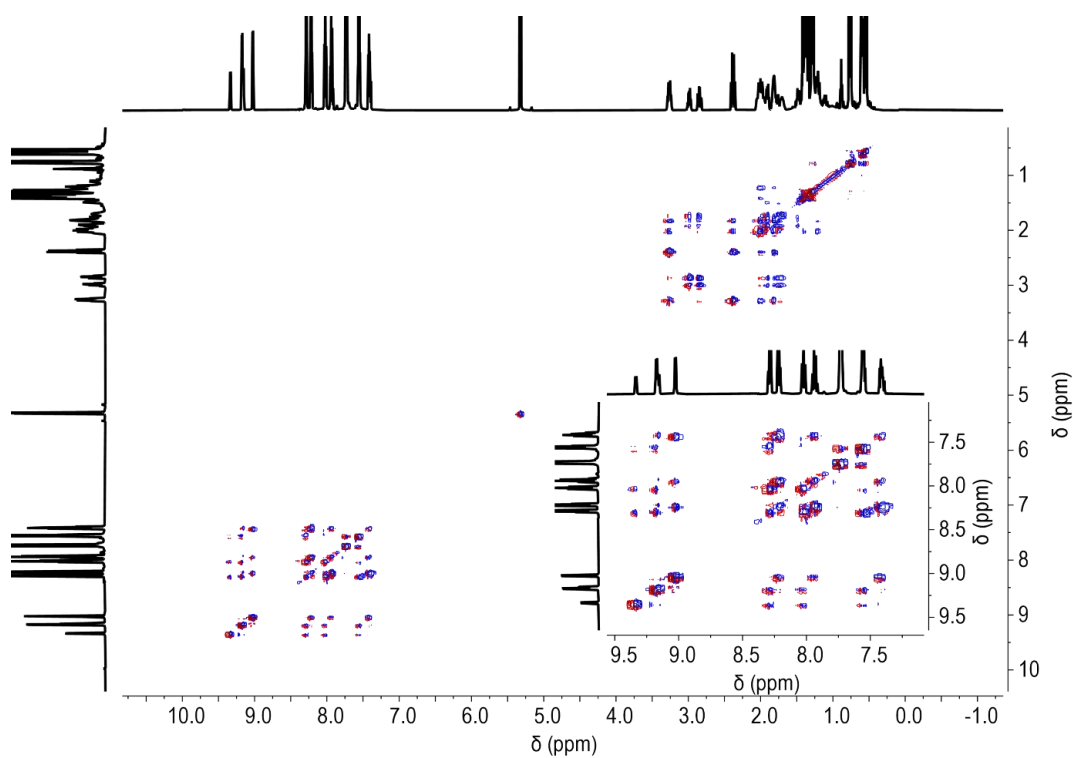
Figure 3.41: Solution ¹H-¹H TOCSY spectrum of **1-bpy**. Inset depicts the aromatic region.
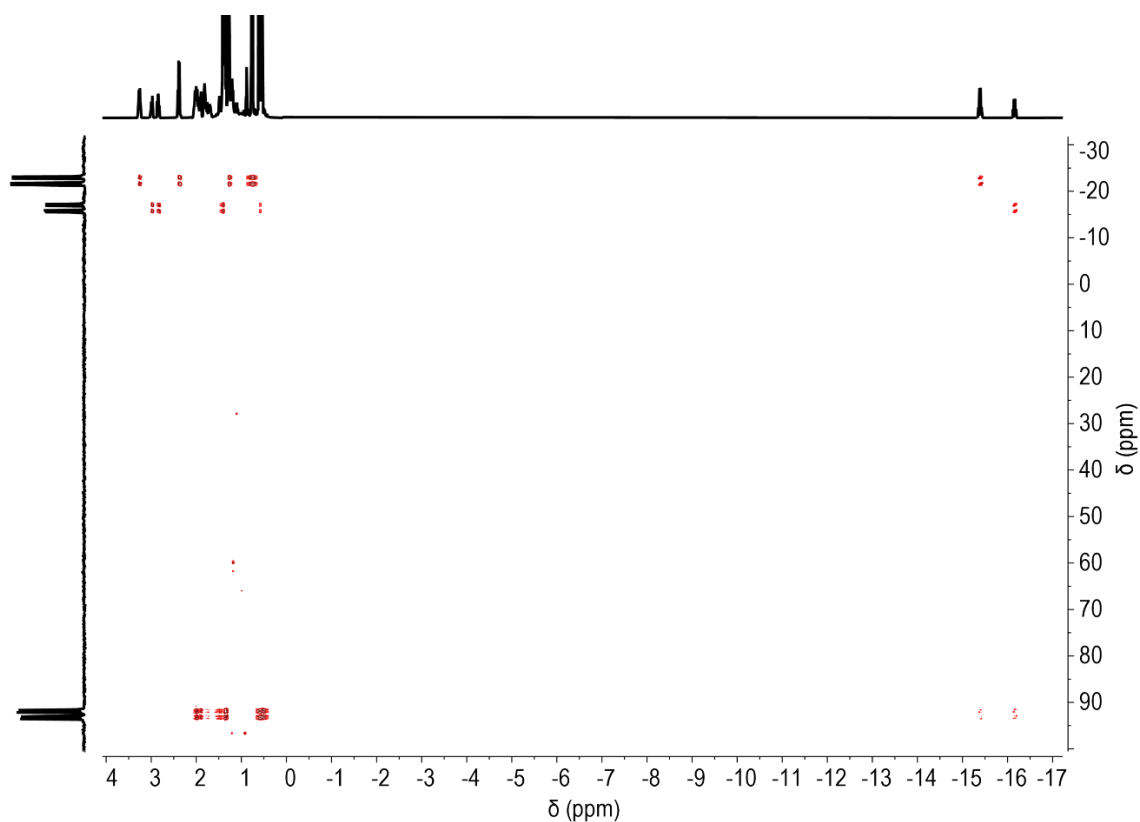
Figure 3.42: Solution ¹H-³¹P HMBC spectrum of **1-bpy**.

243

1-bpy is stable under electrospray-ionisation mass spectrometry (ESI-MS) conditions, with only one major fragmentation product, which is the $\{Rh(dtbpb)\}^+$ fragment (m/z *found*: 449.2038; *calc.*: 449.1973; **Figure 3.43**). Furthermore, **1-bpy** is air stable for at least 24 hours as determined by solution multinuclear NMR spectroscopy. For the combination of these benefits over **1-CD$_2$Cl$_2$**, the bpy adduct was used as a surrogate for investigations into deuterium incorporation into the metal-phosphine fragment.
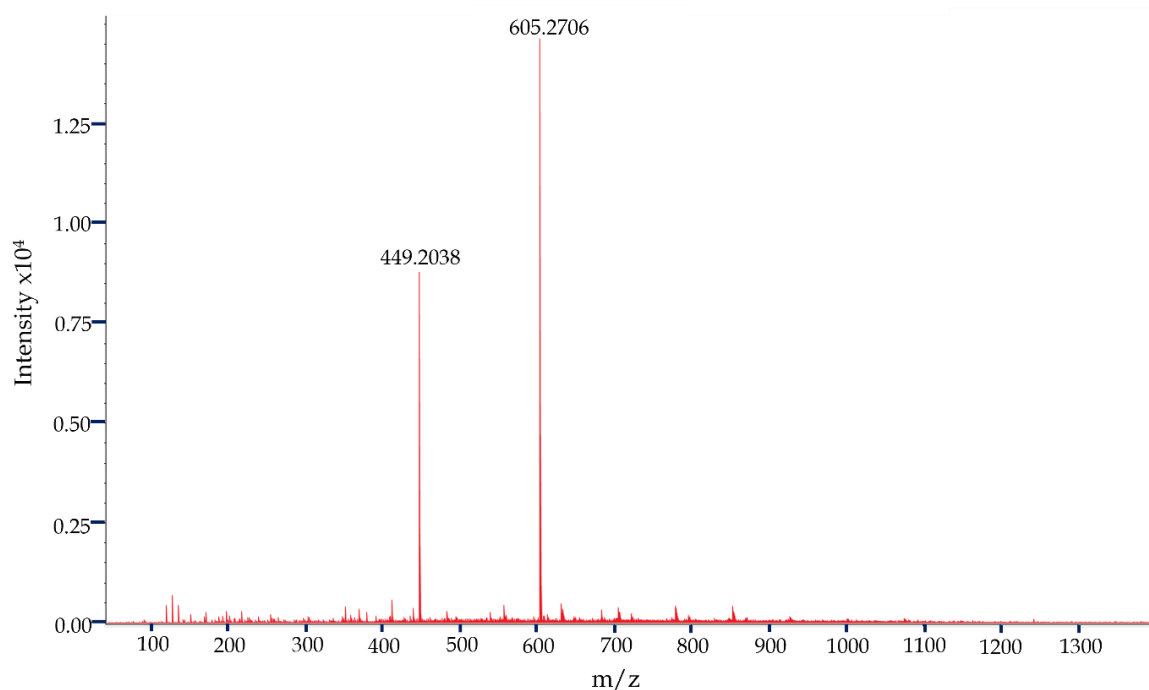
Figure 3.43: ESI-MS spectrum of **1-bpy** (*found*: 605.2706; *calc.*: 605.2661). The m/z peak at 449.2038 corresponds to $\{Rh(dtbpb)\}^+$ (*calc.*: 449.1973).

3.2dv. Location and Extent of Deuterium Incorporation

The ESI-MS (CH$_2$Cl$_2$, positive mode) spectra of **2-bpy** and **3-bpy** (the bpy adduct of **3-NBA**) are remarkably similar (**Figure 3.44**). In agreement with the solution NMR

spectroscopic data for **2-CD₂Cl₂**, a wide distribution of deuterated isotopologues of the metal-phosphine fragment is revealed in the ESI-MS data for **2-bpy** and **3-bpy** . The distribution of deuterium incorporation ranges from d_0 (m/z *found*: 605.26419; *calc*. 605.26553) to d_{27} (m/z *found*: 632.43186; *calc*. 632.43554) for **3-bpy**, and d_{38} (m/z *found*: 643.50204; *calc*.: 643.50405; full lists of peaks and relative intensities are given in **Section 3.5**) for **2-bpy**. By far the most dominant products are found to be the d_2, d_3 and d_4 isotopologues in the ESI-MS data. It is important to note that the negative mode ESI-MS spectra do not show any H/D exchange occurring with the [BArᶠ₄]⁻ anions in the solid-state, to the detection limit of mass spectrometry.
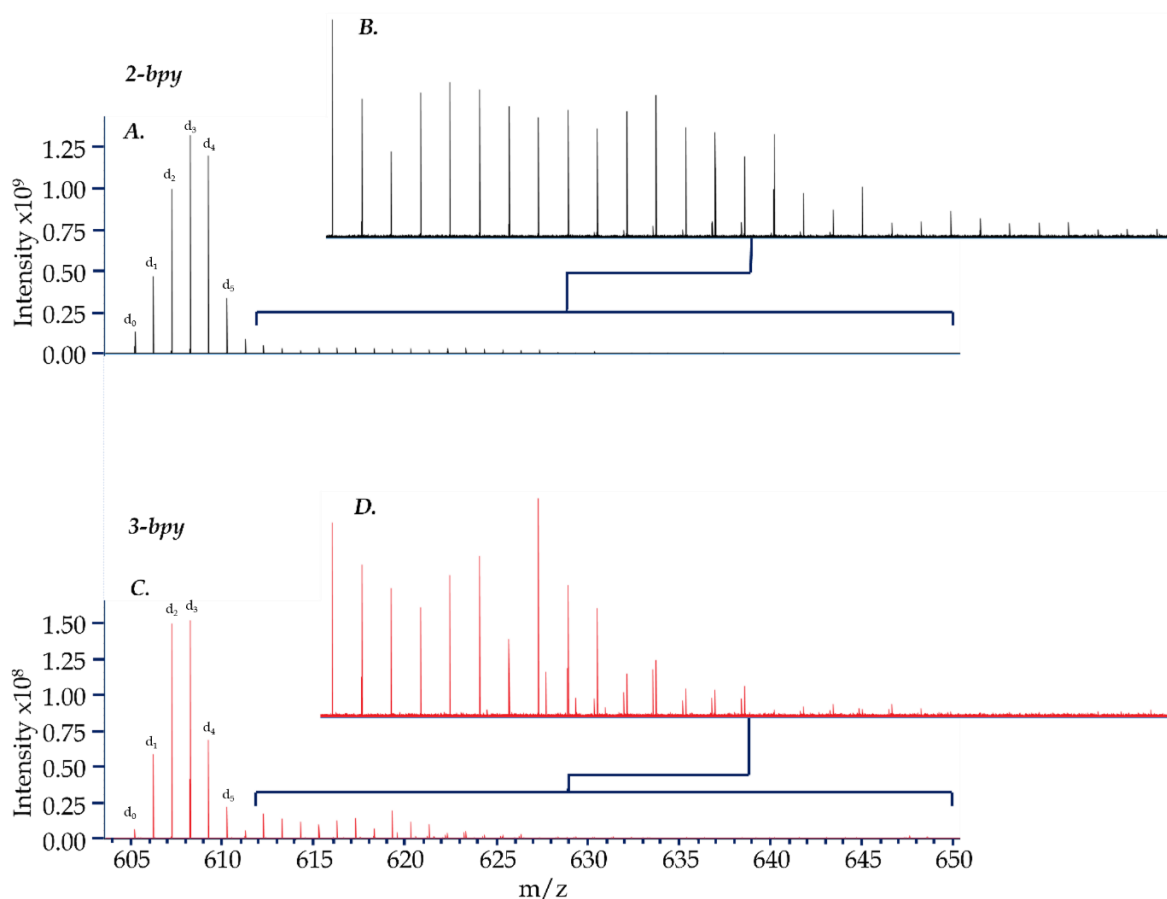
Figure 3.44: ESI-MS data for **2-bpy** and **3-bpy**. *A.* ESI-MS spectrum for **2-bpy**. *B.* Inset depicts intensity scaled m/z peaks beyond d_6. *C.* ESI-MS spectrum of **3-bpy**. *D.* Inset depicts intensity scaled m/z peaks beyond d_6.

Like the ESI-MS data, the solution NMR spectroscopic data for **2-bpy** and **3-bpy** are largely identical. It is important to note that the NMR spectroscopic data for **2-bpy** and **3-bpy** do not contain the unidentified decomposition products observed in **2-CD₂Cl₂** and **3-CD₂Cl₂**, therefore the resonance integrations can be assumed to be more accurate. The solution ³¹P{¹H} NMR spectra (CD₂Cl₂, 298 K; **Figures 3.45** and **3.46**) of both samples reveal two complex, overlapping resonances for the two isomers. A broad set of overlapping signals centred at δ_P 92.3, where the five-membered rings of both of the isomers are coincident, δ_P -16.8 for the four-membered ring of the *anti*-isomer and δ_P -22.6 for the *syn*-isomer.
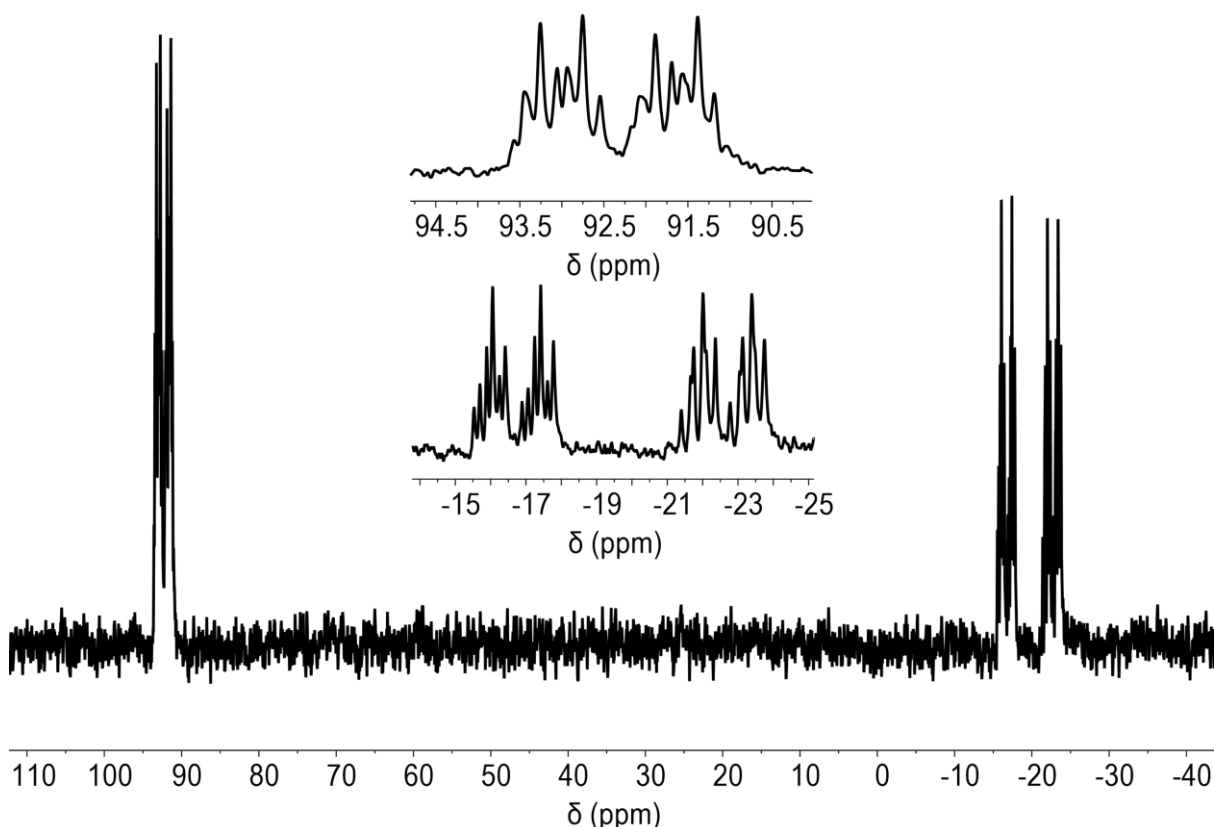
Figure 3.45: Solution ³¹P{¹H} NMR (242.93 MHz, CD₂Cl₂, 298 K) spectrum of **2-bpy**. Insets depict the downfield, five-membered ring phosphorus environments, and the upfield, four-membered ring phosphorus environments (*top* and *bottom*, respectively).
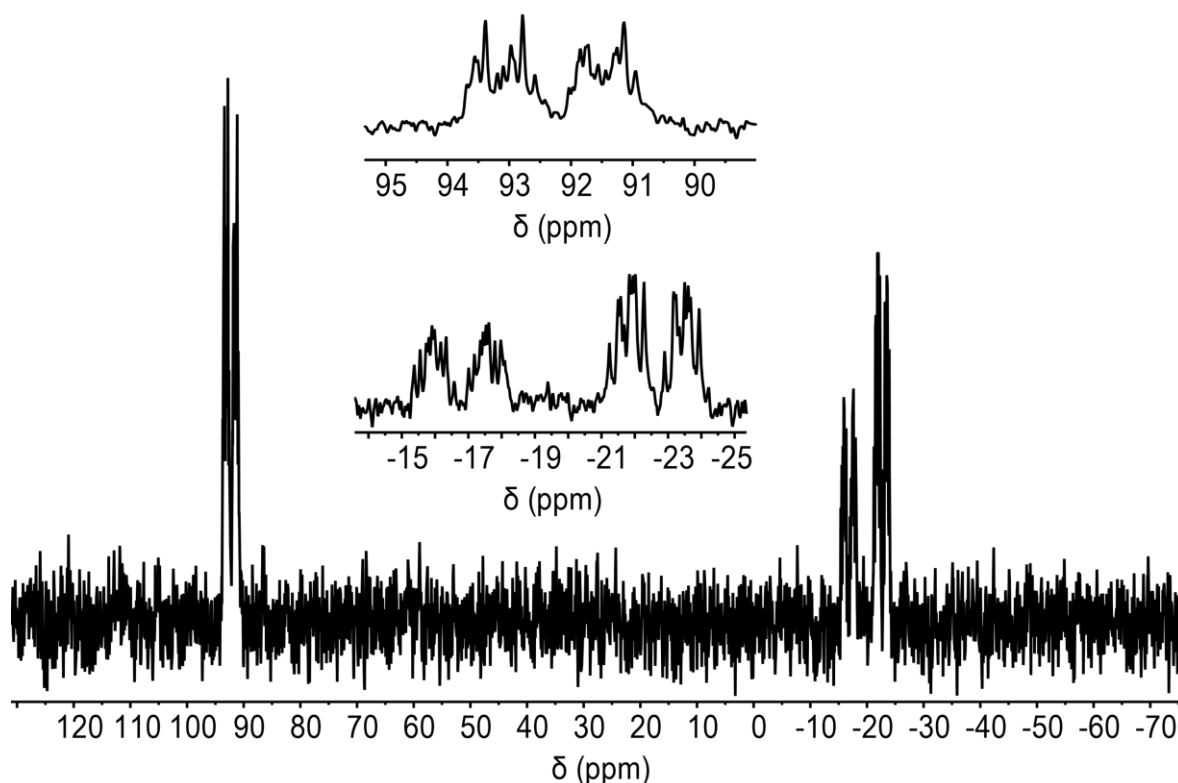
Figure 3.46: Solution $^{31}P\{^{1}H\}$ NMR (202.50 MHz, CD_2Cl_2, 298 K) spectrum of **3-bpy**. Insets depict the downfield, five-membered ring phosphorus environments, and the upfield, four-membered ring phosphorus environments (*top* and *bottom*, respectively).

In the solution ^{1}H NMR spectra of the complexes, the relative concentrations of the individual isomers can be referenced internally against the *ortho*-BAr^F_4 proton resonance (δ_H 7.72) and the proton on the 6-position of the pyridyl *trans* to the hydride (*anti*-isomer δ_H 9.33; *syn*-isomer δ_H 9.02; **Figure 3.47**). This position is unaffected by the H/D exchange process (*vide infra*) and the resonance is separated in each isomer by 0.31 ppm. The resonances associated with the C_2 and C_3 backbone protons for both isomers decrease (**Figure 3.48**, **Table 3.4**) and the coupling becomes less resolved compared to **1-bpy**. Interestingly, the hydride resonance integration

also decreases, but less markedly than that for the backbone protons. Considering the extent of deuterium incorporation highlighted in the ESI-MS data, the relatively low decrease in integration in the hydride resonance is noteworthy. This suggests an isotopic perturbation of equilibrium,[119] as the incorporated deuterium prefers to lie in the stronger C–D bond rather than the Rh–D bond.
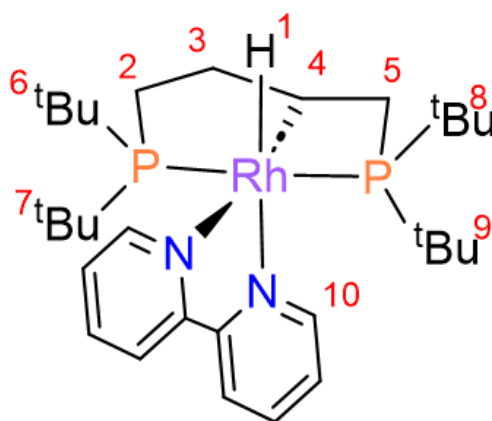
Figure 3.47: Labelled figure of **1-bpy** for ease of ¹H NMR assignments in **Table 3.4.**

Table 3.4: ¹H NMR chemical shifts in **1-bpy**, **2-bpy** and **3-bpy**, with their respective assignments and integrations.

Chemical shift (δ_H)	Assignment	Integrations		
		1-bpy	**2-bpy**	**3-bpy**
9.33	*anti*-H10	0.30	0.44	0.29
9.02	*syn*-H10	0.60	0.49	0.51
3.26	*syn*-H3a	0.60	0.15	0.17
2.99	*anti*-H3a	0.31	0.14	0.09
2.85	*anti*-H3b	0.31	0.14	0.07
2.38	*syn*-H4	0.60	0.15	0.17
2.07-1.88	*anti*-H2, *syn*-H3b, *syn*-H5a	1.71	0.87	0.76
1.86-1.66	*syn*-H5b, *anti*-H4, *anti*-H5	1.49	1.34	1.04
-15.39	*syn*-H1	0.60	0.38	0.37
-16.15	*anti*-H1	0.31	0.35	0.20
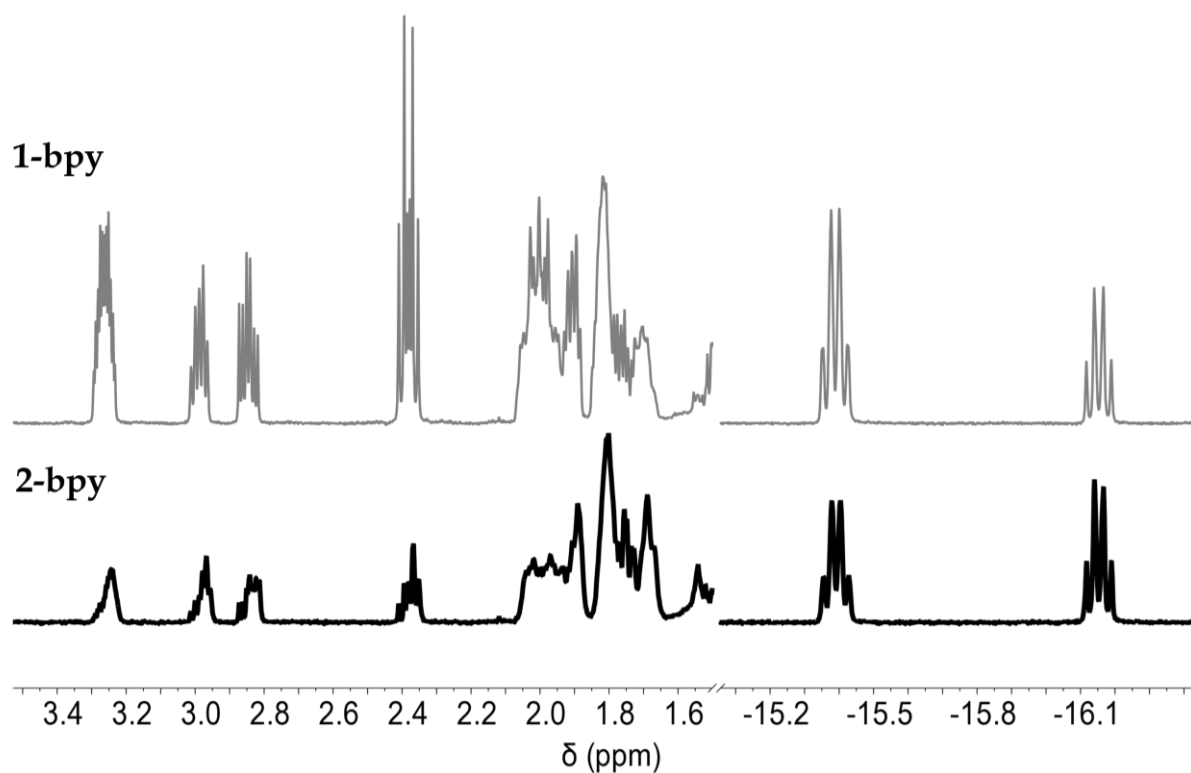
Figure 3.48: ^{1}H NMR (500 MHz, CD$_2$Cl$_2$, 298 K) spectra of **1-bpy** (*top*) and **2-bpy** (*bottom*), in the phosphine backbone and hydride regions. Spectra are normalised in intensity with respect to the [BAr$^F_4$]$^-$ resonances.

The solution ^{2}H NMR (CH$_2$Cl$_2$, 298 K) spectrum of **2-bpy** is consistent with the decrease in ^{1}H NMR integrals due to deuterium incorporation. All phosphine backbone positions, ^{t}Bu methyl environments, and hydride resonances, are observed in the solution ^{2}H NMR spectrum (**Figure 3.49**). Importantly, no resonances are observed in the aromatic region of the solution ^{2}H NMR spectrum, validating that no onward H/D exchange occurs into these positions.
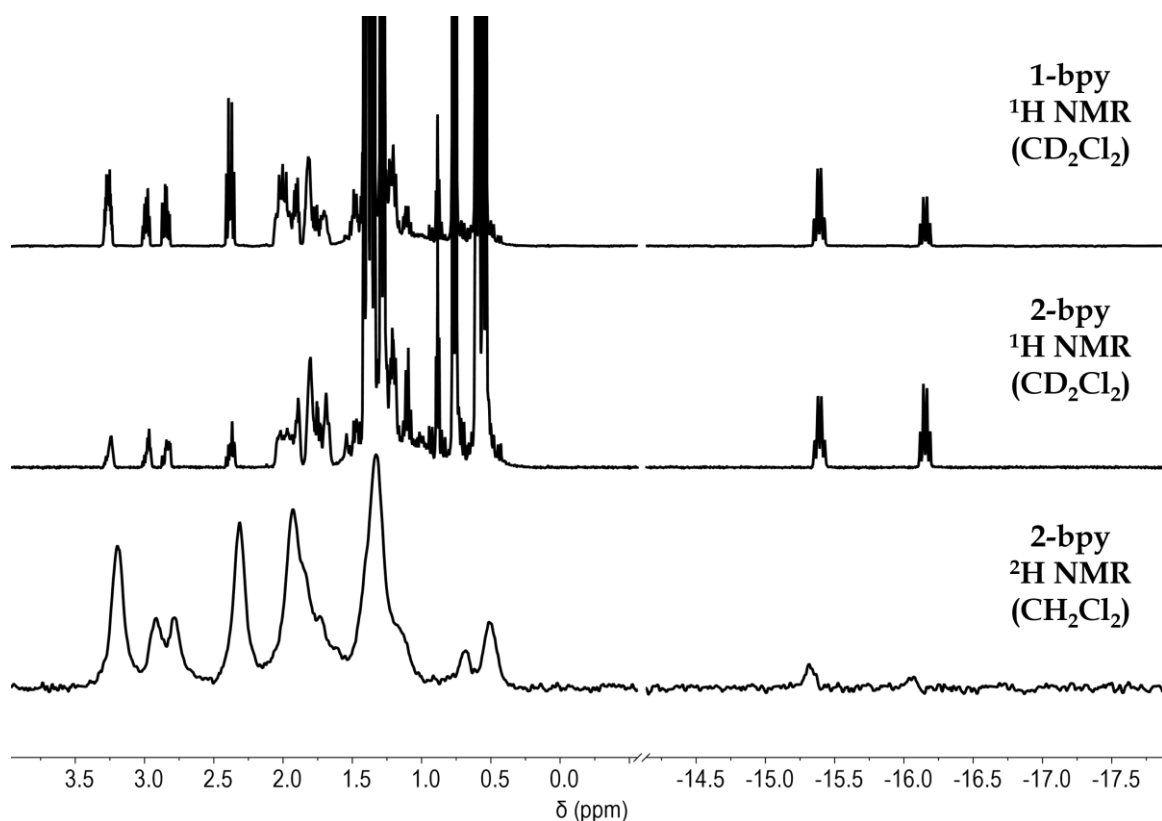
Figure 3.49: Comparison between the solution NMR spectroscopic data for **1-bpy** and **2-bpy**. *Top*: Solution ^{1}H NMR spectrum of **1-bpy**. *Middle*: Solution ^{1}H NMR spectrum of **2-bpy**. *Bottom*: Solution ^{2}H NMR spectrum of **2-bpy**.

As with **1-NBD**, extended exposure times of D_2 or repeated D_2/vacuum cycles does not increase the deuterium incorporation as determined by solution NMR spectroscopy. Similarly to **1-NBD**, **1-NBA** is sensitive to hydrogenation and deuteration timeframes, forming unidentified hydride decomposition products.

3.2dvi. Proposed Mechanism for Intramolecular H/D Exchange

Two potential mechanisms for the intramolecular H/D exchange could be occurring: an oxidative addition/reductive elimination pathway (**Scheme 3.16**), or a σ-complex-assisted-metathesis pathway (σ-CAM, **Scheme 3.17**).[57] The principal of

σ-CAM mechanisms is the exchange of a σ-(E–H) bond with a σ-bond, to metathesise to a new σ-(E′–H) bond and σ-bond, without change of metal oxidation state. This occurs through a single transition state, otherwise known as a concerted mechanism. This mechanism is similar to the LLHT mechanism shown in **Scheme 3.7** but differs as there is no change in metal oxidation state. It is suggested that the σ-CAM pathway is most likely to operate due to the absence of the Rh(III)/Rh(V) couple, as Rh(V) is a less common oxidation state.[120]
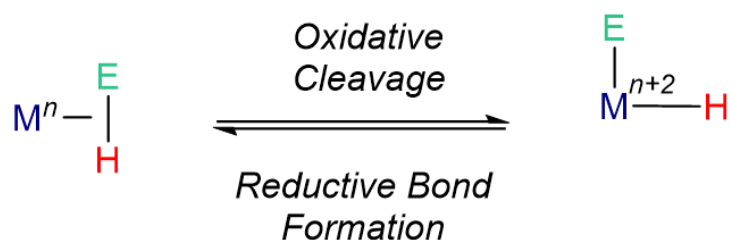
Scheme 3.16: General scheme for oxidative cleavage and reductive bond formation.
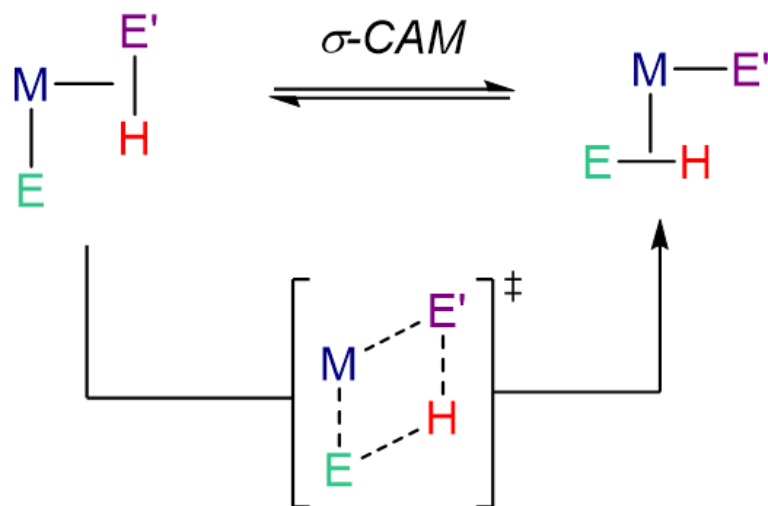
Scheme 3.17: General scheme and transition state of a σ-complex-assisted-metathesis (σ-CAM) mechanism.[57]

In the oxidative addition/reductive elimination pathway, D_2 will bind to the vacant site of the rhodium (**Scheme 3.18**, Complex N), undergo oxidative cleavage to form a Rh(V) hydride dideuteride (Complex O), followed by reductive elimination of the alkyl ligand and deuteride to form the Rh(III) hydride deuteride with a CHD unit in the phosphine backbone (Complex P). A C–H activation of the backbone would follow to form a Rh(V) dihydride deuteride (Complex Q), then reductive elimination of H_2 to form the Rh(III) deuteride which can then bind D_2 and further incorporate deuterium into the alkyl backbone (Complex R). Other sterically accessible C–H bonds in the phosphine backbone and ^tBu methyl groups can undergo the oxidative addition step to introduce deuterium into all accessible sites.
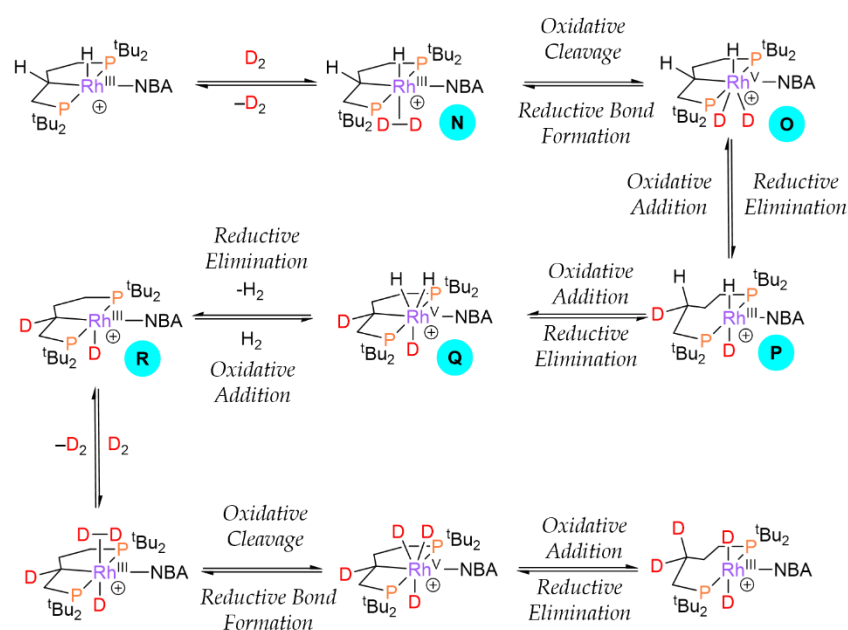
Scheme 3.18: Proposed oxidative addition/reductive elimination mechanism for H/D exchange into the ligand framework of **1-NBA**. $[BAr^F_4]^-$ anions omitted in all cases for clarity.

In the σ-CAM pathway, D_2 will bind through the vacant site at Rh (**Scheme 3.19**, Complex S) and follow a σ-CAM step to form the Rh(III) hydride deuteride, with a C–D bond installed in the phosphine backbone (Complex T). A sterically accessible C–H bond in the backbone or ^tBu methyl groups can then undergo a σ-CAM step with the hydride ligand to form a σ-H_2 complex (Complex U), which is subsequently substituted by D_2 to further incorporate deuterium into the remaining C–H positions. As a σ-CAM pathway is being followed throughout all mechanistic steps, no change in oxidation state is required.[57]
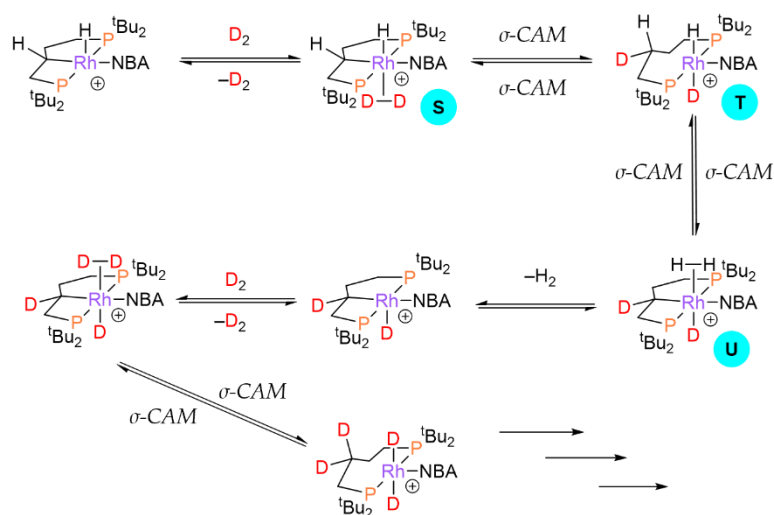
Scheme 3.19: Proposed σ-CAM[57] mechanism for the selective H/D exchange into the ligand framework of **1-NBA**. The [BAr$^F_4$]$^-$ anions are omitted for clarity.

3.2f. A Potential Intermediate in the Solid-State Hydrogenation Pathway

There are multiple opportunities in the mechanism of NBD hydrogenation to NBA where the backbone structural-response could occur. However, it is challenging to probe when this occurs in the solid-state: no intermediate complexes are observed

in the single-crystal X-Ray diffraction or solid-state NMR spectroscopic data, and *in silico* examination of reaction mechanisms in the solid-state is extremely computationally demanding.[95, 96, 121, 122] As the alkene groups of the NBD must be hydrogenated in sequence, it was logical to attempt to synthesise the proposed intermediate complex [Rh(dtbpb)(NBE)][BAr$^F_4$] (NBE = norbornene, **1-NBE**) to attempt to answer at which stage the phosphine backbone activation occurs.

3.2fi. Synthesis and NMR Characterisation of 1-NBE

A sample of **1-NBD** was dissolved in the weakly-coordinating solvent 1,2-F$_2$C$_6$H$_4$ with a large excess of NBE (>50 equivalents) into a 50 mL J Youngs ampoule, and the flask was back-filled with H$_2$ (1 bar gauge at 78 K, **Scheme 3.20**). This represents a slight excess of H$_2$ to NBE (approximately 35 equivalents of H$_2$ to **1-NBD**). The reaction mixture was warmed to room temperature and stirred for 2 minutes. The reaction mixture changes colour from a plum red to wine-red/purple during this time. After 2 minutes, the reaction mixture was rapidly frozen (78 K) and thoroughly degassed through three freeze-pump-thaw cycles. Precipitation of the reaction mixture with hexane and recrystallisation (1,2-F$_2$C$_6$H$_4$/hexane, ~0.5 equivalents of NBE, -30 °C) produced a small crop of crystals of **1-NBE** in poor yields (15%).
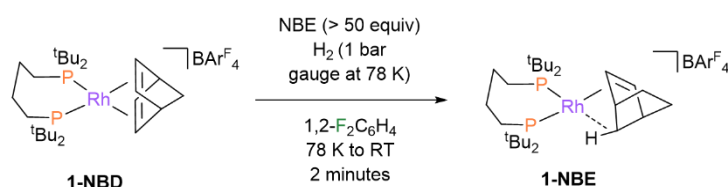
Scheme 3.20: Synthetic scheme for the solution synthesis of **1-NBE** from **1-NBD**.

1-NBE is not stable in solution at room temperature in CD_2Cl_2 and decomposes into unidentified products. Therefore, all solution NMR studies of **1-NBE** were carried out at 193 K. The solution $^{31}P\{^1H\}$ NMR (CD_2Cl_2, 193 K, **Figure 3.50**) spectrum shows two mutually-coupled, doublet of doublet resonances at δ_P 90.3 [^1J(RhP) = 220 Hz, ^2J(PP) = 19 Hz] and 30.0 [^1J(RhP) = 142 Hz, ^2J(PP) = 18 Hz]. The J(PP) coupling constant is consistent with *cis-*, rather than *trans*-phosphorus coupling, which tends to be > 200 Hz. [53, 123] The magnitude of the chemical shifts, and the ^{103}Rh-^{31}P and ^{31}P-^{31}P coupling constants, show that in CD_2Cl_2 solution, at 193 K, the phosphine alkyl backbone has not undergone activation.
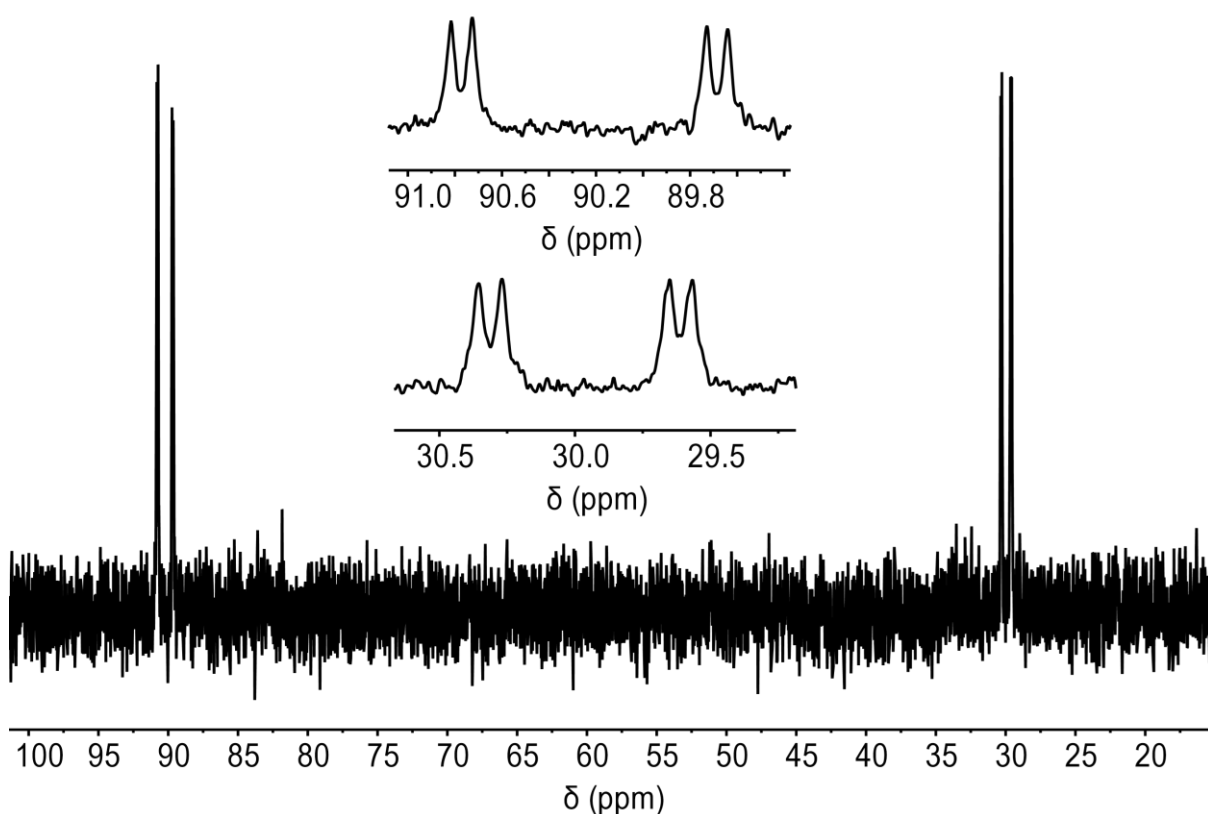
Figure 3.50: Solution $^{31}P\{^1H\}$ NMR (202.49 MHz, CD_2Cl_2, 193 K) spectrum of **1-NBE**. Insets depict the doublet of doublets resonances at δ_P 90.3 (*middle, top*) and 30.0 (*middle, bottom*).

The solution ^{1}H NMR (193 K, CD$_2$Cl$_2$, 500 MHz) spectrum reveals a broad resonance at δ_H -5.67 (1 H, **Figure 3.51**). The upfield ^{1}H resonance and large ^{31}P-^{103}Rh coupling constant in the ^{31}P{^{1}H} NMR (220 Hz) implies a persistent agostic σ(C–H)···Rh interaction in solution at 193 K.[89, 106, 108] Persistent agostic σ(C–H)···Rh interactions in Rh-NBE complexes have been previously reported, where a C–H from the methylene bridge provides the agostic interaction.[62] Due to the instability and poor yields of **1-NBE**, sufficient quantities for solid-state NMR spectroscopic studies could not be obtained.
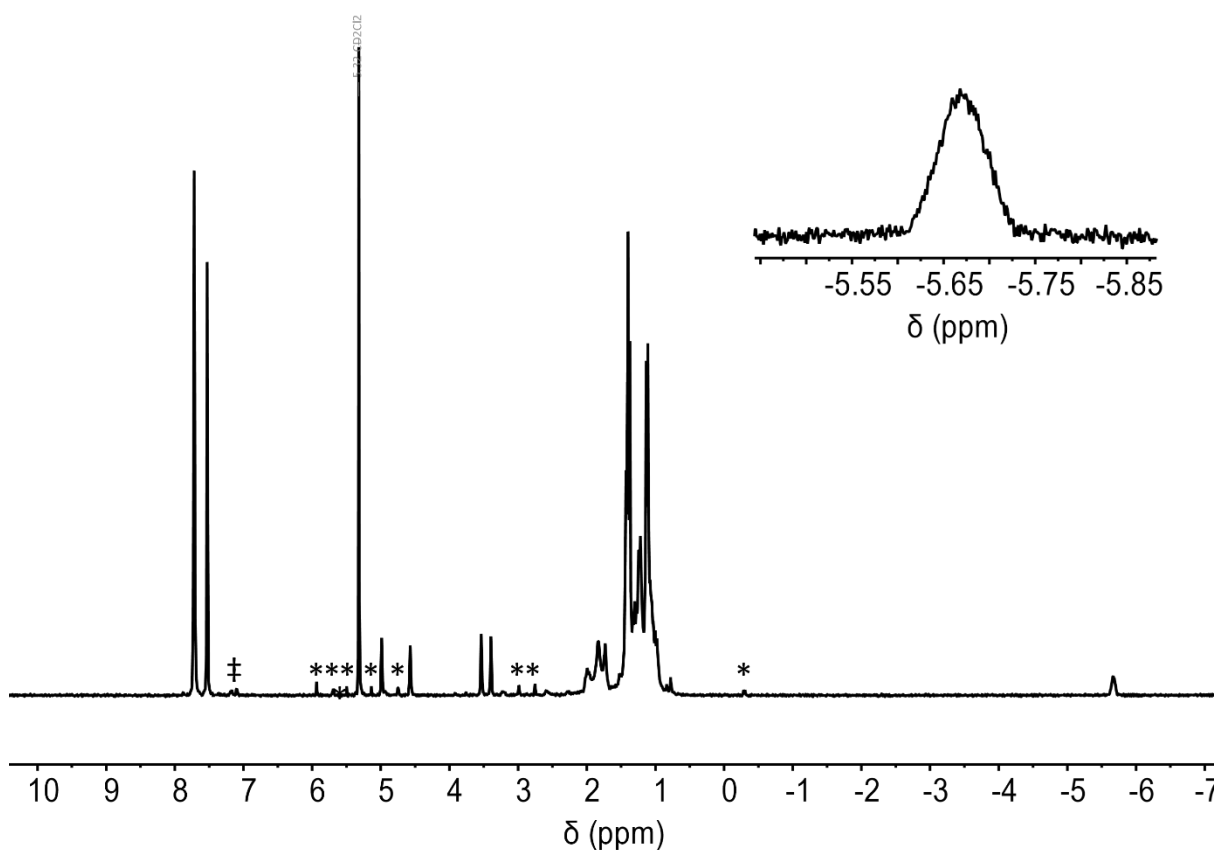
Figure 3.51: Solution ^{1}H NMR (500 MHz, CD$_2$Cl$_2$, 193 K) spectrum of **1-NBE**. Inset depicts the upfield resonance at δ_H -5.67 which is assigned to a σ(C–H) agostic interaction. Asterisks denote unidentified side products.

3.2fii. Single-Crystal X-Ray Diffraction Analysis of 1-NBE

The single-crystal structure of **1-NBE** shows that the NBE ligand is coordinated to the Rh centre in a $\eta^2;\eta^2$-($\pi_{CC};\sigma_{CH}$) fashion, through the alkene π-framework, and a σ(C–H) agostic interaction from the methylene bridge [Rh1···C7 = 2.368(6) Å, **Figure 3.52**]. Importantly, the phosphine alkyl backbone has not undergone C–H oxidative addition in **1-NBE** in the single-crystal structure.
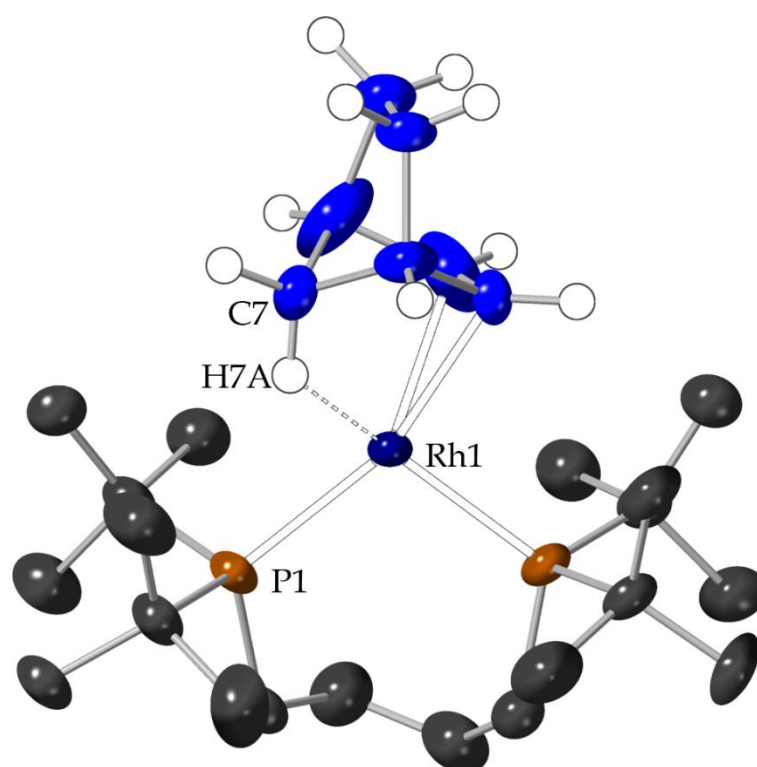
Figure 3.52: The solid-state structure of the cationic fragment of **1-NBE**. The NBE fragment is bound to the Rh(I) through the alkene framework and a σ(C–H) agostic interaction with the bridgehead methylene. Ellipsoids displayed at 50% occupancy. The carbon atoms of the NBE ligand are displayed in blue. All phosphine-based protons are omitted for clarity. Selected bond lengths and angles: Rh1-P1 = 2.3677(11) Å; Rh1-P2 = 2.3223(12); Rh1-C7 = 2.365(6) Å; P1-Rh1-P2 = 102.03(5)°.

The approximately octahedral arrangement of anions around the cation observed in **1-NBD** is also observed in **1-NBE** (**Figure 3.53**). As with **1-NBD**, the cation of **1-NBE** is non-symmetrically placed within the octahedral arrangement, with the NBE methylene groups facing an Ar^F aryl ring (**Figure 3.53**). Close contacts between the NBE fragment and neighbouring Ar^F CF$_3$ groups are also noted [C1···F15 3.274(16) Å; C2···F18 3.621(10) Å; **Figure 3.53**).
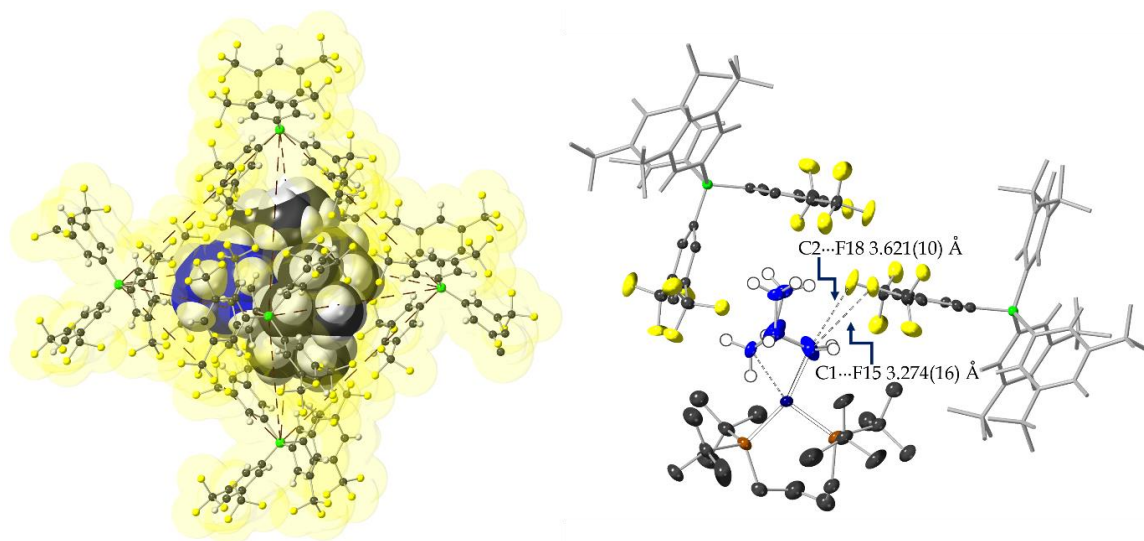
Figure 3.53: Solid-state structure of **1-NBE**. Carbon atoms of the NBE ligand are displayed in blue. *Left*: The {Rh(dtbpb)(NBE)}$^+$ cation is located within an approximately octahedral arrangement of six [BAr$^F_4$]$^-$ anions. *Right*: The cation is non-symmetrically placed within the octahedral arrangement. Close C–H···F contacts are noted with a neighbouring anion. Displacement ellipsoids are displayed at 50%. Selected hydrogen atoms omitted for clarity.

Therefore, although **1-NBE** is obtained through solution methods, the similarity between the solid-state structures of **1-NBD**, **1-NBE** and **1-NBA** suggests that this species is a valid intermediate in the **1-NBD** → **1-NBA** hydrogenation pathway.

Interestingly, the unit cell volume of **1-NBE** has only increased by 1.6% compared to **1-NBD** [**1-NBE** V = 6049.14(11) Å^3; **1-NBD** V = 5954.40(7) Å^3]. This unit cell volume increase is comparable to other solid-state σ-alkane complex syntheses, where two alkene groups, rather than just one, have been hydrogenated. The remaining 3.5% of the unit cell volume increase must therefore occur when the NBE ligand is hydrogenated to NBA and is followed by the ligand structural-response. The structural-response and the necessity to form an η^1-σ-NBA, with an elongated Rh⋯C bond distance is suggested to be responsible for the large overall unit cell volume change from **1-NBD** to **1-NBA**.

3.2g. Reaction of 1-NBA with Propylene

Addition of propylene gas (1 bar gauge) to single-crystals of **1-NBA** causes a single-crystal to single-crystal transformation to occur over the course of 24 hours. The crystals do not change colour, but become coated with a viscous, oily solid (presumably NBA and condensed propylene) which can be removed by application of vacuum (< 1 x10^{-3} mbar) for 18 hours.

3.2gi. Solution NMR Spectroscopic Data of 1-Allyl

After addition of propylene to **1-NBA** and application of vacuum for 18 hours to remove residual NBA, CD$_2$Cl$_2$ (0.6 mL) was vacuum transferred onto the solids and the sample analysed by solution NMR spectroscopy. The solution ^{31}P{^{1}H} NMR (CD$_2$Cl$_2$, 193 K) spectrum reveals a doublet at δ_P 65.3 [^1J(RhP) = 131 Hz; **Figure 3.54**]. This data suggests that both phosphorus environments have become chemically equivalent, necessitating that the phosphine structural-response be reversed from

1-NBA. However, the ^{31}P-^{103}Rh coupling constant is consistent with a Rh(III)

centre.[53, 89]
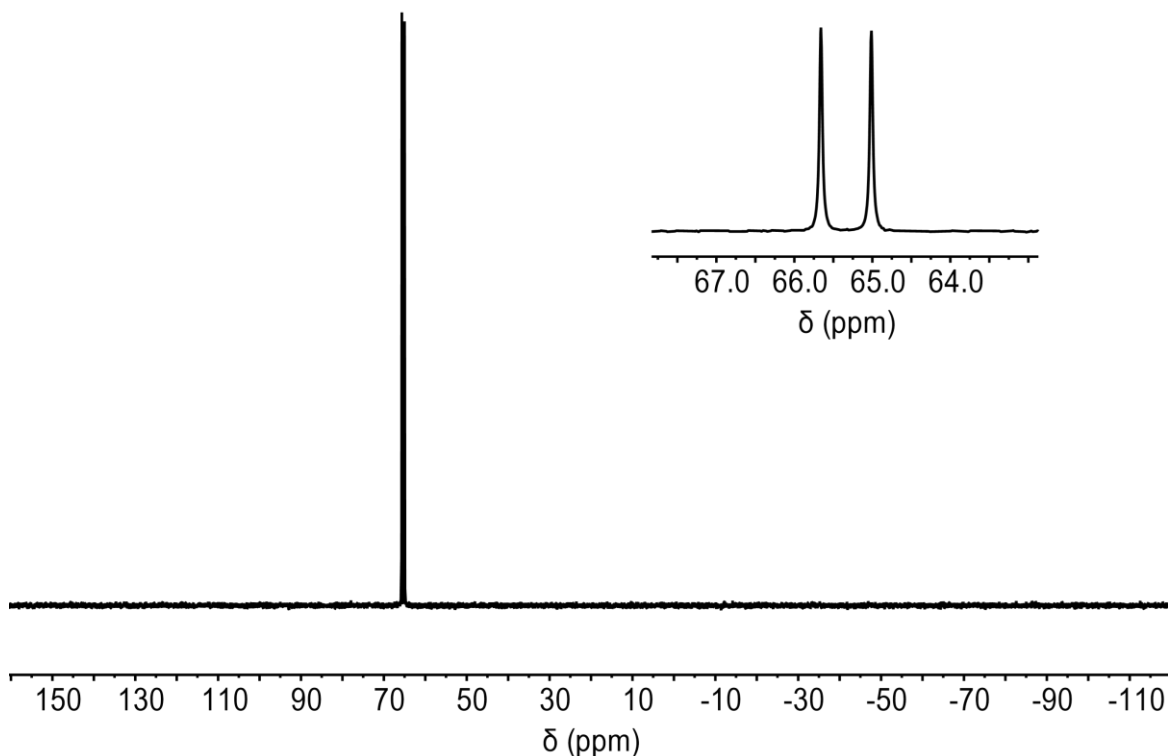
Figure 3.54: Solution $^{31}P\{^1H\}$ NMR (202.49 MHz, CD$_2$Cl$_2$, 193 K) spectrum of **1-Allyl**. Inset

depicts doublet character of isotropic chemical shift (δ_P 65.3).

The solution ^1H NMR (CD$_2$Cl$_2$, 193 K) spectrum shows a doublet of triplets at δ_H -

32.55 [1 H, ^1J(RhH) = 39.5 Hz; ^2J(PH) = 11.8 Hz]. Three mutually coupled resonances

are observed at δ_H 5.09 (1 H), 4.82 (2 H) and 2.36 (2 H; **Figure 3.55**). The combination

of the solution $^{31}P\{^1H\}$ and ^1H NMR spectroscopic data suggests that the backbone

activation has been reversed, indicating hydrogen transfer from the propylene, and

the phosphorus environments being equivalent implies that the C$_3$ ligand must be

symmetrical. The product is assigned from these data as [RhH(η³-C$_3$H$_5$)(dtbpb)][BAr$^F_4$] (**1-Allyl**, **Scheme 3.21**).
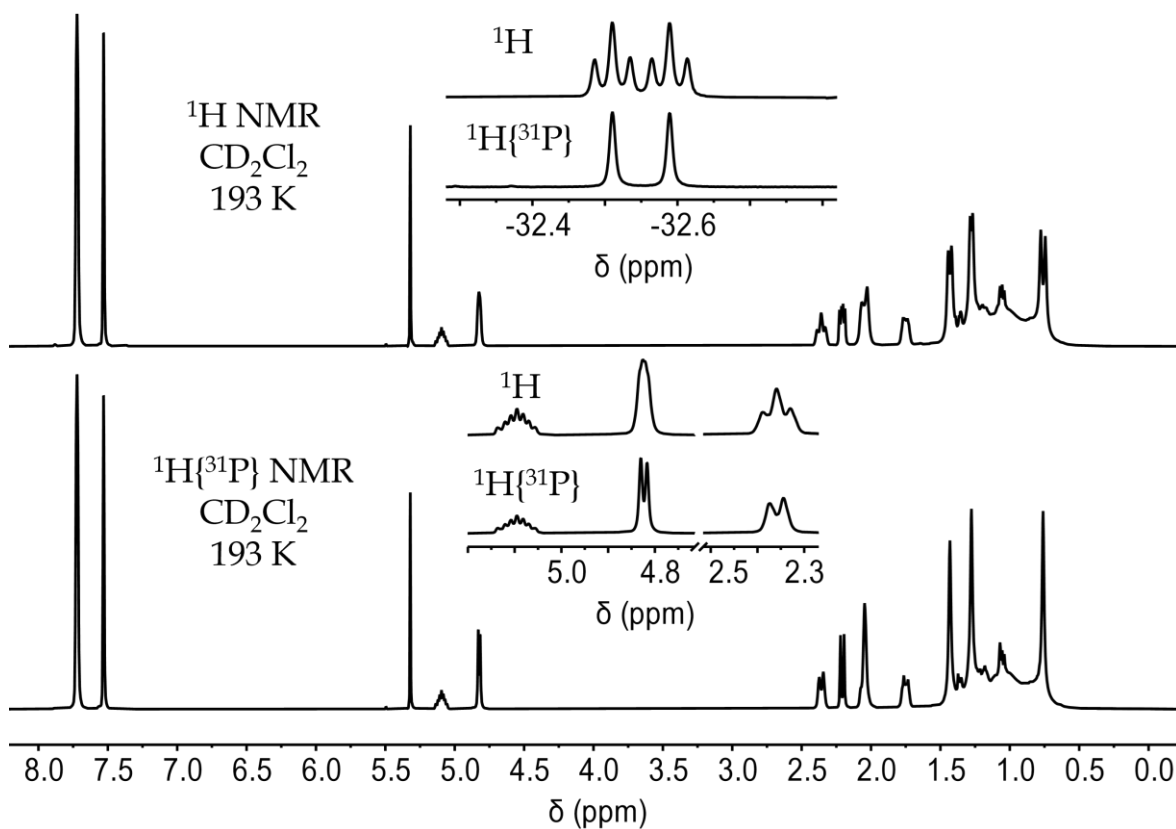
Figure 3.55: Solution ¹H NMR (500 MHz, CD$_2$Cl$_2$, 193 K) spectra of **1-Allyl**. Insets depict the hydride resonance (δ_H -32.55; *top*) and the allyl resonances (δ_H 5.09, 4.82 and 2.36; *bottom*).
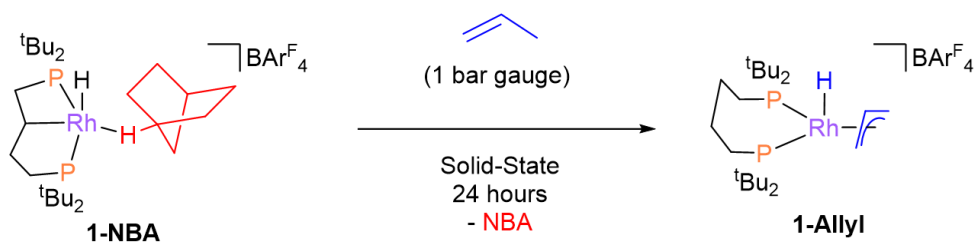
Scheme 3.21: Reaction scheme of the reaction between **1-NBA** and propylene gas in the solid-state. The NBA ligand is displaced, the asymmetric P-C(alkyl)-P pincer ligand is reductively eliminated, and the propylene is oxidatively cleaved to form **1-Allyl**.

3.2gii. Single-Crystal X-Ray Diffraction Analysis of 1-Allyl

Crystals of **1-NBA** exposed to propylene (1 bar gauge, 24 hours) were analysed by single-crystal X-Ray diffraction techniques. The reaction occurs in a single-crystal to single-crystal transformation[73] and exhibits a change in space group from $P\,2_1/n$ to $C\,2/c$. The cation and anion both lie on crystallographic 2-fold rotation centres (special positions). Considering that two single-crystal to single-crystal transformation events have occurred to reach this material, and a two-component twin model was necessitated for structural analysis, a reasonable model (**Figure 3.56**, R_1 = 9.74 %, $w\mathrm{R}_2$ = 29.76%) is achieved where a $\eta^2_\pi;\eta^2_{\sigma(C-H)}$-propylene or η^3-allyl unit is coordinated to the Rh centre [C1-C2 1.45(5) Å; C2-C3 1.46(3) Å; Rh1-C1 2.21(3) Å; Rh1-C2 2.18(2) Å; Rh1-C3 2.21(3) Å; **Figure 3.56**). The hydride is not observed in the difference map, which is to be expected based on the 50% occupancy model, high electron density of the proximate rhodium centre, and weak X-Ray diffraction data.
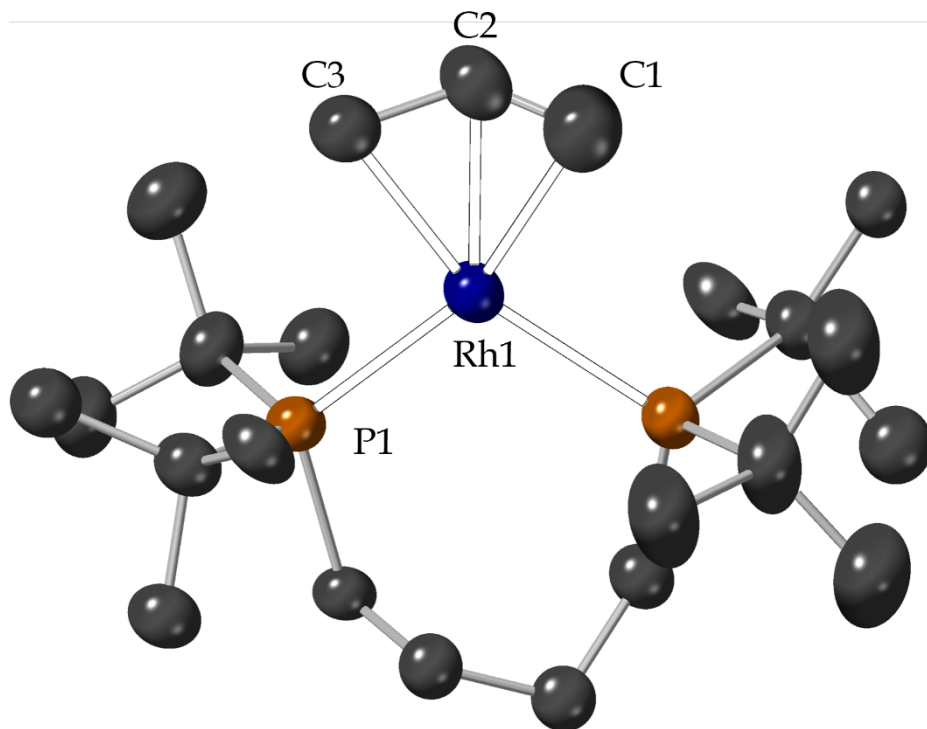
Figure 3.56: Solid-state structure of **1-Allyl**. All protons are omitted for clarity. The hydride is not observed in the difference map. The phosphorous centres and tBu groups are rotation-symmetry-related. Displacement ellipsoids displayed at 50% occupancy. Selected bond lengths and angles: C1-C2 1.45(5) Å; C2-C3 1.46(3) Å; Rh1-C1 2.21(3) Å; Rh1-C2 2.18(2) Å; Rh1-C3 2.21(3) Å; Rh1-P1 2.363(5) Å; P1-Rh1-P1 105.39(15)°.

1-Allyl can be recrystallised from slow cooling a saturated CH_2Cl_2 solution from 0 °C to -78 °C. The crystals grown from this recrystallisation show the same space group, and rotation symmetry-associated crystallographic issues, as material from the single-crystal to single-crystal transformation.

The solution NMR spectroscopy and SC-XRD data are both consistent with the formation of the Rh(III) η^3-allyl hydride complex, **1-Allyl**. This further highlights the *in-crystallo* responsive nature of the **dtbpb** ligand, enabling reversible C–H

activation of the phosphine backbone through SC-SC transformations. Furthermore, with the oxidative cleavage of the C_3 position of propylene, three separate C–H activations have occurred through a sequence of *in-crystallo* events.

3.2giii. Attempted Hydrogenation of 1-Allyl

In 2021, the Weller group published the first example of a Rh(I) σ-propane complex, $[Rh(dcpe)(\eta^2;\eta^2-\sigma-C_3H_8)][BAr^F_4]$ (**Scheme 3.21**).[78] This complex was synthesised on the I19 beamline at Diamond Light Source. Hydrogen gas was dosed into the gas cell while simultaneously cooling the sample to 150 K. The σ-propane complex rapidly decomposes (30 minutes) to the zwitterionic complex, $[Rh(dcpe)(\eta^6-(3,5-CF_3C_6H_3)Ar^F_3)]$ (**Scheme 3.21**), at 298 K.
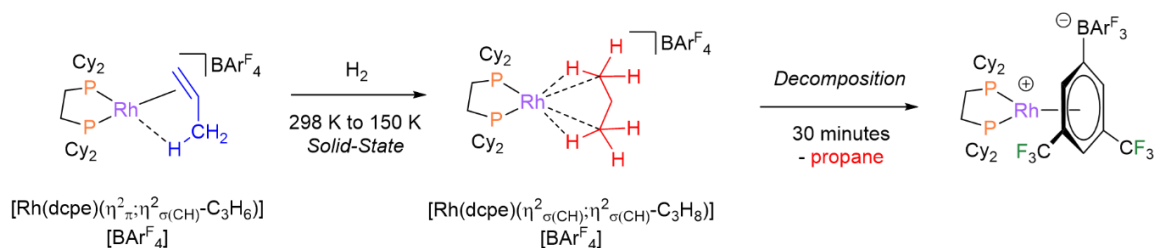
Scheme 3.21: Solid-state synthesis of a Rh(I) σ-propane complex, reported by Weller and co-workers.[78] The complex undergoes rapid (30 minute) decomposition to a zwitterionic arene complex.

The ligand structural response observed through hydrogenation of **1-NBD** to form **1-NBA** provides significant stabilisation of the σ-alkane complex through non-covalent interactions with the ᵗBu groups which are thrust towards the alkane fragment. We reasoned that a similar response may be observed through

hydrogenation of **1-Allyl** to provide stability to a proposed η^1-σ-propane complex,

[RhH(dtbpb*)(η^1-σ-C_3H_8)][BAr$^F_4$] (**Scheme 3.22**).
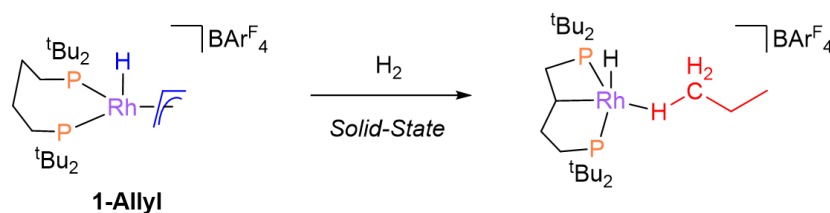
Scheme 3.22: Proposed solid-state hydrogenation of **1-Allyl** to form a Rh(III) η^1-σ-propane complex.

The optimum hydrogenation time of **1-Allyl** was investigated by solution NMR spectroscopy. Hydrogen gas (1 bar gauge) was added to crystals of **1-Allyl** at 0 °C or ambient temperature for varied durations. CD_2Cl_2 was then vacuum transferred onto the solids to observe the formation of **1-CD₂Cl₂** from **1-Allyl**. Hydrogenation of **1-Allyl** for 5 seconds at ambient temperature led to complete loss of **1-Allyl** by solution $^{31}P\{^1H\}$ NMR spectroscopy. The formation of **1-CD₂Cl₂** is noted, as well as an unknown decomposition product at δ$_P$ 51.2 (**Figure 3.57**).
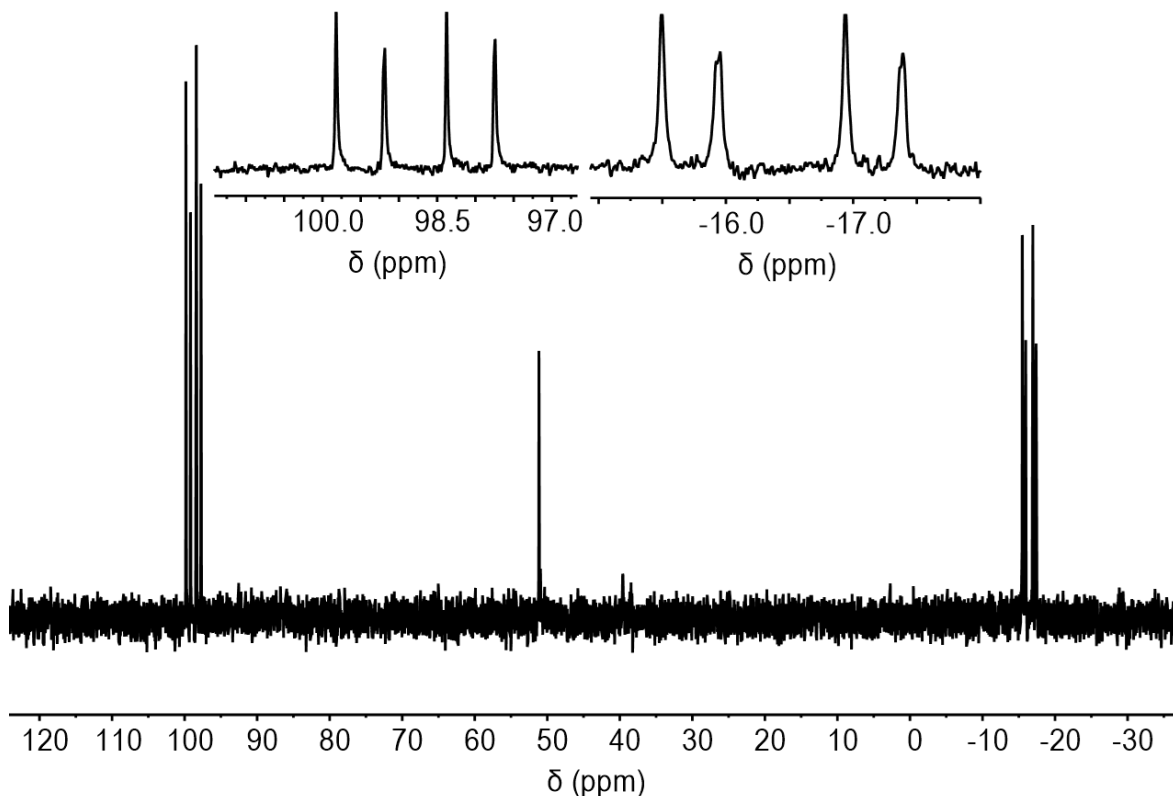
Figure 3.57: Solution ^{31}P{^{1}H} NMR (202.49 MHz, CD$_2$Cl$_2$, 193 K) spectrum of a sample of **1-Allyl** after exposure to H$_2$ (1 bar gauge) for 5 seconds at ambient temperature. Insets depict the resonances of the resultant **1-CD$_2$Cl$_2$** complex.

Recrystallised samples of **1-Allyl** were loaded into gas cells on I19 beamline at Diamond Light Source. Hydrogen gas (1 bar gauge) was dosed into the gas cells under a range of conditions, including: 298 K with simultaneous cooling to 150 K; 273 K with simultaneous cooling to 150 K; 150 K, collecting a new SC-XRD structure with 10 K temperature increase increments. Unfortunately, no new diffraction pattern could be found under these conditions, with only a decrease in intensity of the diffraction peaks of **1-Allyl** observed. This suggests that hydrogenation of **1-Allyl** rapidly causes the formation of an amorphous species.

3.3. Conclusions

The work reported in this Chapter shows that the wide-bite angle phosphine, **dtbpb**, undergoes a structural-response upon *in-crystallo* hydrogenation of **1-NBD**. The structural-response causes C–H oxidative addition of the C2-position of the alkyl backbone to form an asymmetrical, anionic PCP-pincer ligand. The structural-response induces stability of a highly reactive η^1-σ-alkane complex through non-covalent interactions between the ^{t}Bu-methyl groups and the σ-NBA. The structural-response of **dtbpb** *in-crystallo* is suggested to occur after full hydrogenation of the bound alkene positions, due to the (solution) synthesis of **1-NBE**, where the structural-response has not occurred. The structural-response is also shown to be reversible *in-crystallo* by the substitution of norbornane by propylene gas, synthesising **1-Allyl**, where the PCP-pincer ligand has been reductively eliminated to form the bidentate chelating phosphine.

The PCP-pincer ligand has been shown to undergo metal-ligand cooperation *in-crystallo* to produce selective H/D exchange into unactivated alkyl C–H positions of **1-NBA**. The reaction contains a wide-range of isotopologues, ranging from d_0 to d_{38}, where deuterium incorporates into the phosphine backbone and ^{t}Bu methyl groups.

3.4 Future Work

To further understand the increase in non-covalent interactions induced by the ligand structural-response, chemical modifications of **1-NBD** could be explored. For instance, methylating the C2/C3 C–H positions of **dtbpb** to form 1,4-bis(di-*tert*-

butylphosphino)-2,2,3,3-tetramethylbutane (**Figure 3.58**), which cannot undergo C–H activation at the C2/C3-positions. This could lead to an $\eta^2;\eta^2$-σ-NBA complex as a direct comparison, or an alternative ligand structural-response could be envisioned: ^{t}Bu-methyl cyclometallation, or phosphine backbone C-C bond oxidative addition.

Figure 3.58: Chemical formula of a methylated variant of **dtbpb**.

As mentioned in *Section 3.1c*, Hartwig has studied catalytic H/D exchange into vinylic compounds by a complex furnished with a cyclometalated wide bite-angle phosphine.[14] **2-NBA/3-NBA** may also be active for (stoichiometric) H/D exchange into gaseous alkenes through a similar mechanism.

Due to the related phosphine bite-angle, the previously reported [Rh(dcpb)($\eta^2;\eta^2$-σ-NBA)][BAr$^F_4$] [dcpb = 1,4-bis(di-cyclohexylphosphino)butane] should be investigated for H/D exchange. Although the solid-state structure does not show the formation of the related asymmetric PCP-pincer ligand, the transient formation of this framework could be achieved to induce selective H/D exchange into this phosphine. This would establish another example of *in-crystallo* metal-ligand cooperation, which would necessitate an alternative mechanism.

3.5 Experimental

3.5a. General Experimental

All manipulations, unless otherwise stated, were performed under standard Schlenk line and glovebox (<0.5 ppm O_2/H_2O) techniques under an argon (BOC, N4.8 purity), hydrogen (CK Gases, N5.0 purity), deuterium (CK Gases, N2.8 purity), propylene (CK Gases, N2.5 purity) or nitrogen atmosphere. Glassware was dried overnight at 140 °C and flame dried under vacuum before use. Pentane, hexane, CH_2Cl_2 and toluene were dried using a commercially available Grubbs-type purification system (Innovative Technology) and degassed with three freeze-pump-thaw cycles and stored over 3 Å molecular sieves (CH_2Cl_2 and toluene) under argon in resealable glass ampoules fitted with PTFE high vacuum stopcocks (Rotaflo HP or J. Young). 1,2-$C_6H_4F_2$ (pre-treated with alumina) and CD_2Cl_2 were dried over CaH_2, vacuum transferred, degassed with three freeze-pump-thaw cycles, and stored over 3 Å molecular sieves. Tetrahydrofuran (THF) was dried over Na/benzophenone, distilled, degassed with three freeze-pump-thaw cycles and stored over 3 Å molecular sieves. [Rh(NBD)$_2$][BAr$^F_4$][60] was synthesised according to literature methods. All other chemicals were from commercial sources and used without further purification. Solution-state NMR data were collected on a Bruker AVIIIHD 500 MHz or AVIIIHD 600 MHz Widebore spectrometer at the temperatures specified. The solution ^1H and $^{13}C\{^1H\}$ NMR spectra were referenced to the residual solvent peaks. Assignments were aided with $^1H\{^{31}P\}$ and 2-D solution NMR data. $^{31}P\{^1H\}$ solution NMR spectra were referenced externally to 85% H_3PO_4 in D_2O. Solid-state NMR samples were prepared in an argon-filled glovebox

by pre-loading 15-30 mg or 60-100 mg of crushed material into 1.9 mm or 4.0 mm zirconia solid-state NMR rotors, respectively, and sealed with Kel-F, vespel or zirconia caps. Solid-state NMR data were obtained on Bruker Avance III HD spectrometers, operating at 100.63 MHz ($^{13}C\{^1H\}$), 100.56 MHz ($^{13}C\{^1H\}$), 162.04 MHz ($^{31}P\{^1H\}$), 161.99 MHz ($^{31}P\{^1H\}$) or 376.5 MHz ($^{19}F\{^1H\}$) at the MAS rates and temperatures specified. All $^{13}C\{^1H\}$ CP MAS spectra were referenced to adamantane where the upfield methine resonance was taken to be δ_C = 29.5 ppm, secondarily referenced to $\delta_C(SiMe_4)$ = 0.0 ppm. $^{31}P\{^1H\}$ CP MAS spectra were referenced to triphenylphosphine (δ_P = -9.3 ppm relative to H_3PO_4) or calcium hydrogen phosphate (δ_P = 1.4 ppm relative to H_3PO_4). Solid-state NMR spectra were recorded at varied MAS rates to determine isotropic chemical shifts. Gas chromatography electron-ionisation mass spectrometry data were obtained by Mr Karl Heaton at the *University of York* Centre of Excellence in Mass Spectrometry. Electrospray ionisation mass spectrometry data for complexes **2-bpy** and **3-bpy** were recorded on a Bruker solariX XR FTMS operating at 9.4 T. Elemental analyses were collected by Ms Orfhlaith McCullough at *London Metropolitan University*.

3.5bi. Synthesis of 1,4-bis(di-tert-butylphosphino)butane (dtbpb)

A solution of di-*tert*-butylphosphine (2.5 mL, 1.98 g) in THF (20 mL) was cooled to -78 °C. A solution of *n*-butyllithium in hexanes (2.1 M, 6.4 mL) was added dropwise to cooled solution. After full addition of *n*-butyllithium, the reaction mixture changed colour from colourless to pale yellow. The reaction mixture was stirred at -78 °C before warming to ambient temperature. The solution was stirred at ambient

temperature for 18 hours, then cooled back to -78 °C. A solution of 1,4-dibromobutane (800 μL, 1.45 g) in THF (5 mL) was then added to the reaction mixture, dropwise *via* syringe. After full addition, the reaction mixture had turned cloudy white. The reaction mixture was stirred at -78 °C for 15 minutes before stirring at ambient for 18 hours. The volatiles were then removed *in vacuo* and the product extracted into hexane (3 x 30 mL) and isolated through filtration through two thick pads of celite. The volatiles were then removed *in vacuo* to yield a white powder (1.97 g, 85 % yield).

Solution ^{1}H NMR (500 MHz, C$_6$D$_6$, 298 K): δ_H 1.80 (second-order m, 4 H), 1.41 (second-order m, 4H), 1.11 [d, ^3J(PH) = 10.6 Hz, 36 H].

Solution ^{1}H{^{31}P} NMR (500 MHz, C$_6$D$_6$, 298 K): δ_H 1.80 (second-order m, 4 H), 1.41 (second-order m, 4H), 1.11 (s, 36 H).

Solution ^{31}P{^{1}H} NMR (202.49 MHz, C$_6$D$_6$, 298 K): δ_P 27.3.

Solution ^{13}C{^{1}H} NMR (125.80 MHz, C$_6$D$_6$, 298 K): δ_C 32.8 (second-order m, *C*H$_2$), 31.3 [d, ^1J(CP) = 22 Hz, *C*H$_2$], 29.9 [d, ^2J(CP) = 15 Hz, C(*C*H$_3$)$_3$], 21.8 [d, ^1J(CP) = 23 Hz, *C*(CH$_3$)$_3$].

Elemental Analysis *calc* for C$_{20}$H$_{44}$P$_2$: C 69.32; H 12.80; N 0; *found*: 69.15; H 12.42; N 0.

3.5bii. Synthesis of [Rh(dtbpb)(NBD)][BAr$^F_4$] (1-NBD)

To a rapidly stirring solution of [Rh(NBD)$_2$][BAr$^F_4$] (1 g) in CH$_2$Cl$_2$ (50 mL) was dropwise added a solution of **dtbpb** (321 mg) in CH$_2$Cl$_2$ (15 mL). The reaction

mixture was stirred at ambient temperature for 2 hours. The reaction mixture took a slight colour change from red to plum red. The reaction mixture was precipitated by addition of hexane (300 mL) to form a bright red, microcrystalline solid. The supernatant was removed *via* cannula filtration. The product was extracted into CH$_2$Cl$_2$ (2 x 30 mL), cannula filtered and layered at ambient temperature to yield bright-red, block-like crystals of **1-NBD** (897 mg, 80% yield).

Solution ^{1}H NMR (500 MHz, CD$_2$Cl$_2$, 298 K): δ$_H$ 7.72 (br s, 8 H, *ortho*-BAr$^F_4$), 7.56 (s, 3 H, *para*-BAr$^F_4$), 5.05 (second-order m, 4 H, NBD C=C*H*), 3.89 (m, 2 H, NBD bridge C*H$_2$*), 1.91 (br s, FWHM = 27 Hz, 4 H, C*H$_2$*), 1.78 (br m, FWHM = 30 Hz, 4 H, C*H$_2$*), 1.56 (s, 2 H, NBD bridge C*H*), 1.40 [d, ^2J(CP) = 13.2 Hz, 36 H, C(C*H$_3$*)$_3$].

Solution ^{31}P{^{1}H} NMR (202.49 MHz, CD$_2$Cl$_2$, 298 K): δ$_P$ 34.6 [d, ^1J(RhP) = 148 Hz].

Solid-state ^{31}P{^{1}H} CP MAS NMR (162.04 MHz, 10 kHz spin rate, 298 K): δ$_P$ 48.2 [d, ^1J(RhP) = 144 Hz], 25.0 [d, ^1J(RhP) = 144 Hz].

Solid-state ^{13}C{^{1}H} CP MAS NMR (100.66 MHz, 10 kHz spin rate, 298 K): δ$_C$ 166.4, 163.6, 137.7, 135.2, 130.5, 125.1, 117.2 (BAr$^F_4$ resonances), 77.1, 75.8, 64.4, 51.8, 48.7 (NBD alkene resonances), 40.5, 38.8, 38.8, 37.3, 32.6, 32.0, 29.0, 28.7, 24.3, 21.7, 20.3, 16.2 (NBD and phosphine resonances).

ESI-MS m/z (CH$_2$Cl$_2$) *found* (*calc*): C$_{27}$H$_{52}$P$_2$Rh$_1$ 541.2587 (541.2599).

Elemental Analysis *calc* for C$_{59}$H$_{64}$B$_1$F$_{24}$P$_2$Rh$_1$: C 50.44; H 4.59; N 0; *found*: C 50.48; H 4.54; N 0.

3.5biii. Synthesis of [Rh(dtbpb)(NBE)][BAr$^F_4$] (1-NBE)

An ampoule was charged with **1-NBD** (50 mg), norbornene (NBE, 200 mg) and 1,2-$F_2C_6H_4$ (7 mL) to form a bright red solution. The solution was degassed *via* three freeze-pump-thaw cycles and backfilled with H_2 gas (1 bar gauge pressure at -196 °C). The reaction mixture was warmed to ambient and stirred for 2 minutes when the reaction mixture became wine-red/purple in colour. The reaction mixture was rapidly cooled to -196 °C and degassed *via* three freeze-pump-thaw cycles after the 2 minutes stirring at ambient temperature. The volatiles were removed under reduced pressure to yield a wine-red solid which was washed with hexane (3 x 5 mL). The solids were extracted into solution of norbornene (2 mg) in 1,2-$F_2C_6H_4$ (3 mL). The solution was layered with hexane at -30 °C to yield a small crop of wine-red crystals (7 mg, 15% yield). *Notes: This reaction was found to be unpredictable. Trace impurities in the starting material or the 1,2-$F_2C_6H_4$ solvent may be responsible for variation in yields between repeats. **1-NBE** is unstable in CH_2Cl_2 solution at room temperature, decomposing within minutes to unidentified products. Solution NMR spectroscopic data for **1-NBE** is recorded at 193 K. At this temperature, **1-NBE** is quite insoluble in CD_2Cl_2.*

Solution ¹H NMR (500 MHz, CD$_2$Cl$_2$, 193 K): 7.72 (s, 8 H, *ortho*-BAr$^F_4$), 7.52 (s, 4 H, *para*-BAr$^F_4$), 4.99 (s, 1 H, C=C*H*), 4.57 (s, 1 H, C=C*H*), 3.53 (s, 1 H, NBE bridgehead), 3.39 (s, 1 H, NBE bridgehead), 2.06-1.66 (m, 7 H, overlapping phosphine backbone), 1.58-0.88 (m, 45 H, overlapping NBE methylene and bridge, and ᵗBu methyl resonances), -5.68 (s, 1 H, *agostic* NBE bridge C*H*).

Solution ^{31}P{^{1}H} NMR (202.49 MHz, CD$_2$Cl$_2$, 193 K): δ_P 90.3 [^1J(RhP) = 220 Hz, ^2J(PP) = 19 Hz] and 30.0 [^1J(RhP) = 142 Hz, ^2J(PP) = 18 Hz]

3.5biv. Synthesis of [RhH(dtbpb)(η¹-σ-NBA)][BAr$^F_4$] (1-NBA)*

An ampoule was charged with **1-NBD** (54 mg), evacuated (1 x 10^{-3} mbar) and back-filled with H$_2$ gas (1 bar gauge). The bright red crystals gradually became sandy yellow over the course of 2 hours. After 2 hours, the ampoule was degassed under vacuum and back-filled with Ar (0.2 bar gauge pressure) to yield **1-NBA** as a sandy-yellow solid (50 mg, 93%). *Reaction is quantitative by solid-state NMR spectroscopy, mass losses are due to glassware.*

Solid-state ^{31}P{^{1}H} NMR (162.05 MHz, 10 kHz spin rate, 298 K): δ_P 100.5 [dd, ^1J(RhP) = 125 Hz, ^2J(PP) = 289 Hz], -8.5 (apparent t, J_{app} = 300 Hz).

Solid-state ^{13}C{^{1}H} NMR (100.66 MHz, 10 kHz spin rate, 298 K): δ_C 164.8, 163.0, 137.4, 135.4, 130.7, 125.4, 117.8, 117.9 (BAr$^F_4$ resonances), 43.3, 38.6, 37.8, 33.9, 30.0, 21.3 (phosphine and NBA resonances).

Solution ^{1}H NMR (500 MHz, CD$_2$Cl$_2$, 193 K): δ_H 7.72 (s, 8 H, *ortho*-BAr$^F_4$), 7.53 (s, 4 H, *para*-BAr$^F_4$), 2.88 (m, 1 H, phosphine backbone), 2.57 (m, 1 H, phosphine backbone), 2.20 (m, 1 H, phosphine backbone), 2.07 (m, 2 H, NBA methylene bridge), 1.67 (m, 1 H, phosphine backbone), 1.41-0.97 (m, 46 H, overlapping phosphine ^{t}Bu methyl, backbone and NBA resonances), -28.43 [m, ^1J(RhH) = 64.0 Hz, 1 H, Rh-*H*].

Solution ^{31}P{^{1}H} NMR (202.49 MHz, CD$_2$Cl$_2$, 193 K): δ_P 98.8 [dd, ^1J(RhP) = 127 Hz, ^2J(PP) = 289 Hz], -16.5 [dd, ^1J(RhP) = 90 Hz, ^2J(PP) = 289 Hz].

*Due to the sensitivity of **1-NBA**, the complex repeatedly failed to produce satisfactory elemental analyses.*

3.5bv. Synthesis of [RhH(dtbpb*-d)(η¹-σ-NBA-d₄)][BAr^F₄] (2-NBA)

An ampoule was charged with **1-NBD** (x mg), evacuated (1 x 10⁻³ mbar) and back-filled with D_2 gas (1 bar gauge pressure). After 2 hours, the ampoule was degassed under vacuum and back-filled with Ar (0.2 bar gauge pressure).

Solid-state ³¹P{¹H} NMR (162.06 MHz, 20 kHz spin rate, 298 K): δ_P 101.1 [dd, ¹J(RhP) = 125 Hz, ²J(PP) = 287 Hz], -7.8 (apparent triplet, J_{app} = 300 Hz).

Solid-state ¹³C{¹H} NMR (100.66 MHz, 20 kHz spin rate, 298 K): δ_C 164.3, 137.4, 135.5, 134.6, 130.8, 126.1, 123.5, 117.9 (BAr^F₄ resonances), 42.8, 39.0, 38.5, 37.8, 36.7, 36.3, 35.7, 35.1, 34.2, 30.4, 29.0, 28.0, 21.0 (overlapping NBA and phosphine resonances).

Solution ¹H NMR (500 MHz, CD₂Cl₂, 193 K): δ_H 7.72 (s, 8 H, *ortho*-BAr^F₄), 7.52 (s, 4 H, *para*-BAr^F₄), 2.85 (m, 0.29 H, phosphine backbone), 2.56 (m, 0.33 H, phosphine backbone), 2.19 (m, 0.60 H, phosphine backbone), 2.06 (s, 1.66 H, NBA methylene bridge), 1.82 (m, 0.40 H, phosphine backbone), 1.76-1.54 (m, 0.91 H, phosphine backbone), 1.37-0.97 (m, 40.63 H, overlapping phosphine ᵗBu methyl, backbone and NBA resonances), -28.42 (m, 0.60 H, Rh-***H***).

Solution ³¹P{¹H} NMR (202.49 MHz, CD₂Cl₂, 193 K): δ_P 99.3, 99.1, 98.9, 98.7, 98.4, 98.2, 97.8, 97.7, 97.4, 97.2, 97.0, 96.8, -16.1, -16.3, -16.4, -16.7, -16.9, -17.1, -17.5, -17.8, -17.9, -18.2, -18.3, -18.6.

3.5bvi. Synthesis of [RhH(dtbpb*-d)(η^1-σ-NBA-H$_{12}$)][BAr$^F_4$] (3-NBA)

An ampoule was charged with **1-NBA** (24 mg), evacuated (1 x 10^{-3} mbar) and back-filled with D$_2$ gas (1 bar gauge pressure). After 2 hours, the ampoule was degassed under vacuum and back-filled with Ar (0.2 bar gauge pressure).

Solid-state ^{31}P{^{1}H} NMR (162.04 MHz, 20 kHz spin rate, 298 K): δ_P 101.1 [dd, J(RhP) = 115 Hz, J(PP) = 290 Hz], -7.9 (app. t, J_{app} = 285 Hz).

Solid-state ^{13}C{^{1}H} NMR (100.66 MHz, 20 kHz spin rate, 298 K): δ_C 164.2, 162.0, 137.3, 135.7, 134.7, 130.9, 126.0, 123.8, 118.0 (BAr$^F_4$ resonances), 42.7, 38.9, 38.0, 36.2, 29.6, 29.2, 20.9 (phosphine and NBA resonances).

Solution ^{1}H NMR (500 MHz, CD$_2$Cl$_2$, 193 K): δ_H 7.72 (s, 8 H, *ortho*-BAr$^F_4$), 7.52 (s, 4 H, *para*-BAr$^F_4$), 2.85 (br, 0.35 H, phosphine backbone), 2.55 (m, 0.34 H, phosphine backbone), 2.18 (br, 0.55 H, phosphine backbone), 2.07 (s, 1.55 H, NBA methylene bridge), 1.81 (br, 0.48 H, phosphine backbone), 1.64 (br d, 0.90 H, phosphine backbone), 1.42-0.92 (m, 41.72 H, overlapping phosphine ^{t}Bu methyl, backbone and NBA resonances), -28.43 (br d, 0.62 H, Rh-*H*).

Solution ^{31}P{^{1}H} NMR (202.52 MHz, CD$_2$Cl$_2$, 193 K): δ_P 99.8, 99.6, 99.3, 99.2, 98.9, 98.7, 98.3, 98.1, 97.9, 97.7, 97.5, 97.3, -15.5, -15.8, -15.9, -16.2, -16.3, -16.6, -17.0, -17.3, -17.4, -17.7, -17.8, -18.1.

3.5bvii. Synthesis of [RhH(dtbpb*)(2,2'-bipyridine)][BAr$^F_4$] (1-bpy)

An ampoule was charged with **1-NBA** (46 mg) and cooled to 0 °C. The solids were then taken up in CH_2Cl_2 (3 mL) to form a pale-yellow solution. A solution of 2,2'-bipyridine (5.5 mg) in CH_2Cl_2 (1 mL) was then added to the solution. The solution was agitated, allowed to warm to ambient temperature, and layered with hexane to yield bright yellow crystals of **1-bpy** (21 mg, 44% yield).
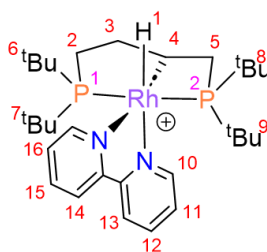
Figure 3.59: Labelled figure of **1-bpy** to aid with NMR atom assignments.

Solution ¹H NMR (600 MHz, CD₂Cl₂, 298 K): δ_H 9.33 [d, ^1J(HH) = 5.6 Hz, 0.32 H, *anti*-10], 9.17 [d, ^1J(HH) = 5.4 Hz, 0.60 H, *syn*-17], 9.16 [d, ^1J(HH) = 5.3 Hz, 0.32 H, *anti*-17], 9.03 [d, ^1J(HH) = 5.1 Hz, 0.61 H, *syn*-10], 8.29 (m, 0.93 H, overlapping *syn*-14 and *anti*-14), 8.22 (m, 0.98 H, overlapping *syn*-13 and *anti*-13), 8.02 (m, 0.98 H, overlapping *syn*-15 and *anti*-15), 7.93 (m, 0.93 H, overlapping *syn*-12 and *anti*-12), 7.73 [br sept, ^4J(HF) = 2.0 Hz, 8 H, *ortho*-BAr$^F_4$], 7.56 (br s, 4.87 H, overlapping *para*-BAr$^F_4$, *syn*-16 and *anti*-16), 7.41 (m, 0.98 H, overlapping *syn*-11 and *anti*-11), 3.26 (m, 0.60 H, *syn*-3a), 2.99 (m, 0.31 H, *anti*-3a), 2.85 (m, 0.31 H, *anti*-3b), 2.38 (m, 0.60 H, *syn*-4), 2.07-1.88 (m, 1.71 H, overlapping *anti*-2, *syn*-3b, *syn*-5a), 1.86-1.66 (m, 1.49 H, overlapping *anti*-4, *syn*-5b, *anti*-5), 1.43-1.33 (m, 11.99 H, overlapping *syn*-6, *anti*-6

and *anti*-8), 1.28 [d, ^2J(HP) = 13.8 Hz, 5.96 H, *syn*-8], 0.76 [d, ^2J(HP) = 13.4 Hz, 5.64 H, *syn*-9], 0.61-0.58 (m, 8.24 H, overlapping *syn*-7 and *anti*-9), 0.55 [d, ^2J(HP) = 12.3 Hz, 2.95 H, *anti*-7], -15.39 (m, 0.60 H, *syn*-1), -16.15 (m, 0.31 H, *anti*-1).

Solution ^{31}P{^{1}H} NMR (242.93 MHz, CD$_2$Cl$_2$, 298 K): δ_P 92.9 [dd, ^1J(RhP) = 120 Hz, ^2J(PP) = 337 Hz, *syn*-1], 92.5 [dd, ^1J(RhP) = 123 Hz, ^2J(PP) = 329 Hz, *anti*-1], -16.4 [dd, ^1J(RhP) = 89 Hz, ^2J(PP) = 330 Hz, *anti*-2], -22.3 [dd, ^1J(RhP) = 89 Hz, ^2J(PP) = 336 Hz, *syn*-2].

Solution ^{13}C{^{1}H} NMR (150.91 MHz, CD$_2$Cl$_2$, 298 K): δ_C 162.2 [q, ^1J(CB) = 50 Hz, *ipso*-BAr$^F_4$], 156.4, 155.9, 154.3, 154.3, 154.1, 153.9, 152.4, 138.3, 135.2 [sept., ^3J(CF) = 1.6 Hz, *ortho*-BAr$^F_4$], 129.3 [qq, ^2J(CF) = 31 Hz, ^3J(CF) = 3 Hz, *meta*-BAr$^F_4$], 127.7, 126.2, 126.1, 125.9, 125.7, 125.4, 124.1, 124.1, 123.7, 123.3, 123.3, 122.3, 117.9 [quint., ^3J(CF) = 4 Hz, *para*-BAr$^F_4$], 43.1, 43.0, 43.0, 42.9, 38.5 (m), 38.4 (m), 38.1, 37.8, 37.7, 37.6, 37.5, 37.5, 35.2, 33.3, 33.2, 32.0, 31.0 [d, ^2J(CP) = 4 Hz, C(*C*H$_3$)$_3$], 30.8 [d, ^2J(CP) = 4 Hz, C(*C*H$_3$)$_3$], 30.5 [d, ^2J(CP) = 3 Hz, C(*C*H$_3$)$_3$], 30.1 [d, ^2J(CP) = 4 Hz, C(*C*H$_3$)$_3$], 30.0 (dd, J = 4 Hz, J = 1 Hz), 29.8-29.6 (overlapping signals), 29.3 [d, ^2J(CP) = 4 Hz, C(*C*H$_3$)$_3$], 25.9 (dt, J = 22 Hz, J = 2 Hz), 24.9 (dt, J = 23 Hz, J = 2 Hz), 23.1, 20.4, 20.3, 20.1, 15.9, 15.7, 15.7, 15.6, 14.3.

ESI-MS m/z (CH$_2$Cl$_2$) *found* (*calc*): C$_{30}$H$_{52}$N$_2$P$_2$Rh$_1$ 605.2706 (605.2661); C$_{20}$H$_{44}$P$_2$Rh$_1$ 449.2038 (449.1973).

3.5bviii. Synthesis of [RhH(dtbpb*-d)(2,2'-bipyridine)][BAr$^F_4$] (2-bpy)

The synthesis of **1-bpy** was repeated, replacing **1-NBA** for **2-NBA**. Yield: 15 mg, 41%.

Solution ¹H NMR (600 MHz, CD₂Cl₂, 298 K): δ_H 9.33 (m, 0.44 H, *anti*-10), 9.16 (m, 0.90 H, overlapping *syn*-17 and *anti*-17), 9.02 [d, *J*(HH) = 5.6 Hz, 0.49 H, *syn*-10], 8.29 (m, 0.93 H, overlapping *syn*-14 and *anti*-14), 8.22 (m, 0.97 H, overlapping *syn*-13 and *anti*-13), 8.03 (m, 0.96 H, overlapping *syn*-15 and *anti*-15), 7.94 (m, 0.92 H, overlapping *syn*-12 and *anti*-12), 7.73 (s, 8 H, *ortho*-BAr$^F_4$), 7.56 (s, 4.92 H, overlapping *para*-BAr$^F_4$, *syn*-16 and *anti*-16), 7.41 (m, 0.98 H, overlapping *syn*-11 and *anti*-11), 3.26 (m, 0.15 H, *syn*-3a), 2.99 (m, 0.14 H, *anti*-3a), 2.85 (m, 0.14 H, *anti*-3b), 2.38 (m, 0.14 H, *syn*-4), 2.07-1.88 (m, 0.87 H, overlapping *anti*-2, *syn*-3b and *syn*-5a), 1.86-1.66 (m, 1.34 H, overlapping *anti*-4, *syn*-5b and *anti*-5), 1.43-1.33 (m, 12.08 H, overlapping *syn*-6, *anti*-6 and *anti*-8), 1.28 [d, ²*J*(PH) = 13.6 Hz, 4.92 H, *syn*-8], 0.76 [d, ²*J*(PH) = 13.6 Hz, 4.19 H, *syn*-9], 0.62-0.52 (m, 11.98 H, overlapping *syn*-7 and *anti*-9), -15.39 [m, ¹*J*(RhH) = 15 Hz, 0.38 H, *syn*-1], -16.15 [m, ¹*J*(RhH) = 17 Hz, 0.35 H, *anti*-1].

Solution ²H NMR (76.79 MHz, CH₂Cl₂, 298 K): δ_D 3.2, 2.9, 2.8, 2.3, 1.9, 1.3, 1.2, 0.7, 0.5, -15.3, -16.0.

Solution ³¹P{¹H} NMR (242.93 MHz, CD₂Cl₂, 298 K): δ_P 93.5, 93.4, 93.2, 93.0, 92.9, 92.7, 92.5, 92.2, 92.0, 91.9, 91.7, 91.6, 91.4, 91.2 (overlapping isotopologues of *syn*-1 and *anti*-1), -15.5, -15.7, -15.9, -16.1, -16.3, -16.4, -16.9, -17.1, -17.3, -17.4, -17.6, -17.8

(overlapping isotopologues of *anti*-2), -21.4, -21.6, -21.7, -22.0, -22.1, -22.4, -22.8, -23.1, -23.2, -23.4, -23.8 (overlapping isotopologues of *syn*-2).

ESI-MS m/z *found* (*calc* **m/z, deuterium content, abundance rel. to [M]⁺**):

605.26628 (605.26607, d_0, 10.0%); 606.27213 (606.27235, d_1, 34.9%); 607.27909 (607.27863, d_2, 75.3%); 608.28313 (608.28490, d_3, 100%); 609.29058 (609.29118, d_4, 90.2%); 610.29514 (610.29746, d_5, 23.1%); 611.30185 (611.30373, d_6, 6.6%); 612.30776 (612.31001, d_7, 4.0%); 613.31402 (613.31629, d_8, 2.5%); 614.32100 (614.32256, d_9, 1.6%); 615.32876 (615.32884, d_{10}, 2.6%); 616.33325 (616.33512, d_{11}, 2.8%); 617.33946 (617.34139, d_{12}, 2.7%); 618.34799 (618.34767, d_{13}, 2.4%); 619.35167 (619.35395, d_{14}, 2.2%); 620.36073 (620.36022, d_{15}, 2.3%); 621.36427 (621.36650, d_{16}, 2.0%); 622.37328 (622.37278, d_{17}, 2.3%); 623.37709 (623.37905, d_{18}, 2.6%); 624.38345 (624.38533, d_{19}, 2.0%); 625.38900 (625.39161, d_{20}, 1.9%); 626.39562 (626.39788, d_{21}, 1.5%); 627.40131 (627.40416, d_{22}, 1.9%); 628.41109 (628.41044, d_{23}, 0.8%); 629.41509 (629.41671, d_{24}, 0.5%); 630.42082 (630.42299, d_{25}, 0.9%); 631.42765 (631.42927, d_{26}, 0.3%); 632.43314 (632.43554, d_{27}, 0.3%); 633.43987 (633.44182, d_{28}, 0.5%); 634.44522 (634.44810, d_{29}, 0.4%); 635.45146 (635.45437, d_{30}, 0.3%); 636.45779 (636.46065, d_{31}, 0.3%); 637.45779 (637.46693, d_{32}, 0.3%); 638.47106 (638.47320, d_{33}, 0.2%); 639.47742 (639.47948, d_{34}, 0.2%); 640.48478 (640.48576, d_{35}, 0.2%); 641.49062 (641.49203, d_{36}, 0.1%); 642.49622 (642.49831, d_{37}, 0.1%); 643.50204 (643.50459, d_{38}, 0.2%).

3.5bix. Synthesis of [RhH(dtbpb*-d)(2,2′-bipyridine)][BAr$^F_4$] (3-bpy)

The synthesis of **1-bpy** was repeated, replacing **1-NBA** for **3-NBA**. Yield: 10 mg, 38%.

Solution ^{1}H NMR (500 MHz, CD$_2$Cl$_2$, 298 K): δ_H 9.33 (m, 0.29 H, *anti*-10), 9.16 (m, 0.80 H, overlapping *syn*-17 and *anti*-17), 9.02 (m, 0.51 H, *syn*-10), 8.30 (m, 0.87 H, overlapping *syn*-14 and *anti*-14), 8.23 (m, 0.92 H, overlapping *syn*-12 and *anti*-12), 8.03 (m, 0.92 H, overlapping *syn*-15 and *anti*-15), 7.95 (m, 0.87 H, overlapping *syn*-12 and *anti*-12), 7.72 (s, 8 H, *ortho*-BAr$^F_4$), 7.55 (s, 4.83 H, overlapping *para*-BAr$^F_4$, *syn*-16 and *anti*-16), 7.43 (m, 0.84 H, overlapping *syn*-11 and *anti*-11), 3.25 (m, 0.17 H, *syn*-3a), 2.97 (m, 0.09 H, *anti*-3a), 2.83 (m, 0.07 H, *anti*-3b), 2.36 (m, 0.17 H, *syn*-4), 2.09-1.87 (m, 0.76 H, overlapping *anti*-2, *syn*-3b, and *syn*-5a), 1.84-1.63 (m, 1.04 H, overlapping *anti*-4, *syn*-5b and *anti*-5), 1.44-1.32 (m, 9.97 H, overlapping *syn*-6, *anti*-6 and *anti*-8), 1.29 [d, ^2J(PH) = 13.3 Hz, 6.29 H, *syn*-8], 0.76 [d, ^2J(PH) = 13.4 Hz, 4.61 H, *syn*-9], 0.62-0.52 (m, 9.74 H, overlapping *syn*-7 and *anti*-9), -15.39 (m, 0.37 H, *syn*-1), -16.15 (m, 0.20 H, *anti*-1).

Solution ^{31}P{^{1}H} NMR (202.50 MHz, CD$_2$Cl$_2$, 298 K): δ_P 93.7, 93.6, 96.5, 93.4, 93.2, 93.1, 93.0, 92.9, 92.8, 92.6, 92.4, 92.0, 91.9, 91.9, 91.8, 91.8, 91.7, 91.6, 91.6, 91.4, 91.3, 91.2, 91.1, 91.0 (overlapping isotopologues of *syn*-1 and *anti*-1), -15.4, -15.6, -15.7, -15.8, -15.9, -16.0, -16.1, -16.2, -16.3, -16.6, -17.0, -17.2, -17.4, -17.4, -17.5, -17.6, -17.8, -18.0 (overlapping isotopologues of *anti*-2) -21.2, -21.5, -21.6, -21.7, -21.8, -21.9, -22.0, -22.3, -22.9, -23.2, -23.2, -23.3, -23.5, -23.6, -23.7, -23.9 (overlapping isotopologues of *syn*-2).

ESI-MS m/z *found* (**calc m/z, deuterium content, abundance rel. to [M]$^+$**):

605.26279 (605.26607, d_0, 4.2%); 606.26900 (606.27235, d_1, 38.5%); 607.27521

(607.27863, d_2, 98.6%); 608.28143 (608.28490, d_3, 100%); 609.28778 (609.29118, d_4,

45.0%); 610.29424 (610.29746, d_5, 14.2%); 611.29991 (611.30373, d_6, 3.7%); 612.30640

(612.31001, d_7, 11.3%); 613.31281 (613.31629, d_8, 8.8%); 614.31852 (614.32256, d_9, 7.5%);

615.32456 (615.32884, d_{10}, 6.4%); 616.33181 (616.33512, d_{11}, 8.2%); 617.33726

(617.34139, d_{12}, 9.3%); 618.34375 (618.34767, d_{13}, 4.5%); 619.35005 (619.35395, d_{14},

12.6%); 620.35585 (620.36022, d_{15}, 7.3%); 621.36265 (621.36650, d_{16}, 6.3%); 622.36861

(622.37278, d_{17}, 2.5%); 623.37492 (623.37905, d_{18}, 3.3%); 624.38097 (624.38533, d_{19},

1.7%); 625.38797 (625.39161, d_{20}, 1.6%); 626.39389 (626.39788, d_{21}, 1.8%); 627.39997

(627.40416, d_{22}, 0.5%); 628.40664 (628.41044, d_{23}, 0.6%); 629.41280 (629.41671, d_{24},

0.8%); 630.41860 (630.42299, d_{25}, 0.5%); 631.42527 (631.42927, d_{26}, 0.8%); 632.43186

(632.43554, d_{27}, 0.5%).

3.5bx. Synthesis of [RhH(dtbpb*)(κ^1-ClCH$_2$Cl)][BAr$^F_4$]•½ hexane

An ampoule was charged with **1-NBA** (55 mg) and CH$_2$Cl$_2$ (3 mL) was added to the

solids to form a pale-yellow solution. The complex was precipitated with hexane

(15 mL) and isolated by cannula filtration to afford a pale-yellow, microcrystalline

solid (20 mg, 37% yield).

Solution NMR spectroscopic data for **1-CD$_2$Cl$_2$** are reported under the synthesis for

1-NBA.

Elemental Analysis *calc* for C$_{56}$H$_{65}$B$_1$F$_{24}$Rh$_1$P$_2$Cl$_2$: C 46.69; H 4.55; N 0; *found*: C 46.33;

H 4.33; N 0.

3.5bxi. Synthesis of [RhH(η³-C₃H₅)(dtbpb)][BArᶠ₄] (1-Allyl)

An ampoule was charged with **1-NBA** (125 mg) and evacuated (1 x 10⁻³ mbar). The ampoule was back-filled with propylene gas (1 bar gauge pressure) and sealed for 24 hours. After 24 hours, the ampoule was evacuated and placed under dynamic vacuum (1 x 10⁻³ mbar) for 18 hours. The product was directly isolated as a crystalline, tan solid. Yield: 108 mg (90%).

Note: The addition of propylene gas causes the crystalline material to aggregate together, likely due to the egressed NBA. Ensure the solids are evenly dispersed to allow to even gas diffusion throughout the crystals.

Solution ¹H NMR (500 MHz, CD₂Cl₂, 193 K): δ_H 7.72 (s, 7 H, *ortho*-BArᶠ₄), 7.53 (s, 4 H, *para*-BArᶠ₄), 5.09 (m, 1 H, allyl C*H*), 4.82 (m, 2 H, allyl C*H₂*), 2.36 (apparent triplet, 2 H, allyl C*H₂*), 2.21 (m, 2 H, phosphine backbone C*H₂*), 2.04 (m, 2 H, phosphine backbone C*H₂*), 1.75 (m, 2 H, phosphine backbone C*H₂*), 1.52-0.65 (36 H, overlapping ᵗBu methyl environments), -32.55 [dt, ¹*J*(RhH) = 40 Hz, ²*J*(PH) = 20 Hz, 1 H, Rh*H*].

Solution ³¹P{¹H} NMR (202.49 MHz, CD₂Cl₂, 193 K): δ_P 65.3 [d, ¹*J*(RhP) = 131 Hz]

Elemental Analysis *calc* for C₅₅H₆₂B₁F₂₄P₂Rh₁: C 48.76; H 4.61; N 0; *found*: C 48.82; H 4.71; N 0.

3.6 References

1.   J. R. Khusnutdinova and D. Milstein, *Angew. Chem. Int. Ed.*, 2015, **54**, 12236-12273.

2.   M. R. Elsby and R. T. Baker, *Chem. Soc. Rev.*, 2020, **49**, 8933-8987.

3.   A. Kumar and D. Milstein, in *Metal-Ligand Co-operativity: Catalysis and the Pincer-Metal Platform*, eds. G. van Koten, K. Kirchner and M.-E. Moret, Springer International Publishing, Cham, 2021, DOI: 10.1007/3418_2020_67, pp. 1-23.

4.   Y. Nicolet, A. L. de Lacey, X. Vernède, V. M. Fernandez, E. C. Hatchikian and J. C. Fontecilla-Camps, *J. Am. Chem. Soc.*, 2001, **123**, 1596-1601.

5.   H.-J. Fan and M. B. Hall, *J. Am. Chem. Soc.*, 2001, **123**, 3828-3829.

6.   B. E. Barton, M. T. Olsen and T. B. Rauchfuss, *J. Am. Chem. Soc.*, 2008, **130**, 16834-16835.

7.   J. Zhang, G. Leitus, Y. Ben-David and D. Milstein, *Angew. Chem. Int. Ed.*, 2006, **45**, 1113-1115.

8.   C. Gunanathan, Y. Ben-David and D. Milstein, *Science*, 2007, **317**, 790-792.

9.   B. Gnanaprakasam, J. Zhang and D. Milstein, *Angew. Chem. Int. Ed.*, 2010, **49**, 1468-1471.

10.   S. N. Ege, *Organic chemistry*, Cengage Learning, 1998.

11.   P.-Q. Huang, H.-Q. Lan, X. Zheng and Y.-P. Ruan, *J. Org. Chem.*, 2004, **69**, 3964-3967.

12.   C. P. Prasanth, J. Ebbin, A. Abhijith, D. S. Nair, I. Ibnusaud, J. Raskatov and B. Singaram, *J. Org. Chem.*, 2018, **83**, 1431-1440.

13.   M. Kishino, S. Takaoka, Y. Shibutani, S. Kusumoto and K. Nozaki, *Dalton Trans.*, 2022, **51**, 5009-5015.

14.   J. Zhou and J. F. Hartwig, *Angew. Chem. Int. Ed.*, 2008, **47**, 5783-5787.

15.   L. J. Donnelly, J.-B. Lin, B. S. Gelfand, C. Y. Chang and W. E. Piers, *Dalton Trans.*, 2024, **53**, 1862-1869.

16.   S. Musa, I. Shaposhnikov, S. Cohen and D. Gelman, *Angew. Chem. Int. Ed.*, 2011, **50**, 3533-3537.

17.   A. M. Poitras, S. E. Knight, M. W. Bezpalko, B. M. Foxman and C. M. Thomas, *Angew. Chem. Int. Ed.*, 2018, **57**, 1497-1500.

18.   M. R. Elsby and R. T. Baker, *Chem. Commun.*, 2019, **55**, 13574-13577.

19.   Z. K. Sweeney, J. L. Polse, R. G. Bergman and R. A. Andersen, *Organometallics*, 1999, **18**, 5502-5510.

20.   J. M. Blacquiere, *ACS Catal.*, 2021, **11**, 5416-5437.

21.   A. J. Hart-Davis and R. J. Mawby, *J. Chem. Soc. A*, 1969, 2403-2407.

22.   B. M. Trost and M. C. Ryan, *Angew. Chem. Int. Ed.*, 2017, **56**, 2862-2879.

23.   J. M. O'Connor and C. P. Casey, *Chem. Rev.*, 1987, **87**, 307-318.

24.   M. A. Bennett, Z. Lu, X. Wang, M. Bown and D. C. R. Hockless, *J. Am. Chem. Soc.*, 1998, **120**, 10409-10415.

25.   T. R. Dugan, X. Sun, E. V. Rybak-Akimova, O. Olatunji-Ojo, T. R. Cundari and P. L. Holland, *J. Am. Chem. Soc.*, 2011, **133**, 12418-12421.

26.   M. H. Al-Afyouni, E. Suturina, S. Pathak, M. Atanasov, E. Bill, D. E. DeRosha, W. W. Brennessel, F. Neese and P. L. Holland, *J. Am. Chem. Soc.*, 2015, **137**, 10689-10699.

27.   C. P. Casey, J. M. O'Connor, W. D. Jones and K. J. Haller, *Organometallics*, 1983, **2**, 535-538.

28.   E. A. Bielinski, W. Dai, L. M. Guard, N. Hazari and M. K. Takase, *Organometallics*, 2013, **32**, 4025-4037.

29.   E. M. Miller and B. L. Shaw, *J. Chem. Soc., Dalton Trans.*, 1974, 480-485.

30.   J. C. Jeffrey and T. B. Rauchfuss, *Inorg. Chem.*, 1979, **18**, 2658-2666.

31.   C. Bolzati, A. Boschi, L. Uccelli, F. Tisato, F. Refosco, A. Cagnolini, A. Duatti, S. Prakash, G. Bandoli and A. Vittadini, *J. Am. Chem. Soc.*, 2002, **124**, 11468-11479.

32.   A. Wu, B. O. Patrick, E. Chung and B. R. James, *Dalton Trans*, 2012, **41**, 11093-11106.

33.   G. M. Adams and A. S. Weller, *Coord. Chem. Rev.*, 2018, **355**, 150-172.

34.   M. J. Cross, C. N. Brodie, D. G. Crivoi, J. C. Goodall, D. E. Ryan, A. J. Martínez-Martínez, A. Johnson and A. S. Weller, *Chem. Eur. J.*, 2023, **29**, e202302110.

35.   M. R. Kita and A. J. M. Miller, *J. Am. Chem. Soc.*, 2014, **136**, 14519-14529.

36.   Z. Cai and L. H. Do, *Organometallics*, 2017, **36**, 4691-4698.

37.   T. V. Tran, E. Lee, Y. H. Nguyen, H. D. Nguyen and L. H. Do, *J. Am. Chem. Soc.*, 2022, **144**, 17129-17139.

38.   S. Acosta-Calle and A. J. M. Miller, *Acc. Chem. Res.*, 2023, **56**, 971-981.

39.   Y. Guari, G. P. F. van Strijdonck, M. D. K. Boele, J. N. H. Reek, P. C. J. Kamer and P. W. N. M. van Leeuwen, *Chem. Eur. J.*, 2001, **7**, 475-482.

40.   A. J. M. Miller, *Dalton Trans.*, 2017, **46**, 11987-12000.

41.   C. Yoo, H. M. Dodge and A. J. M. Miller, *Chem. Commun.*, 2019, **55**, 5047-5059.

42.   M. R. Kita and A. J. M. Miller, *Angew. Chem. Int. Ed.*, 2017, **56**, 5498-5502.

43.   R. M. Izatt, J. S. Bradshaw, S. A. Nielsen, J. D. Lamb, J. J. Christensen and D. Sen, *Chem. Rev.*, 1985, **85**, 271-339.

44.   A. D. Wilson, A. J. M. Miller, D. L. DuBois, J. A. Labinger and J. E. Bercaw, *Inorg. Chem.*, 2010, **49**, 3918-3926.

45.   J. A. B. Abdalla, A. Caise, C. P. Sindlinger, R. Tirfoin, A. L. Thompson, A. J. Edwards and S. Aldridge, *Nat. Chem.*, 2017, **9**, 1256-1262.

46.   R. H. Crabtree, *The Organometallic Chemistry of the Transition Metals*, John Wiley & Sons, Inc., Hoboken, New Jersey, 6 edn., 2014.

47.   J. F. Hartwig, *Organotransition Metal Chemistry: From Bonding to Catalysis*, University Science Books, California, 2010.

48.   H. D. Empsall, E. M. Hyde, R. Markham, W. S. McDonald, M. C. Norton, B. L. Shaw and B. Weeks, *J. Chem. Soc., Chem. Commun.*, 1977, 589-590.

49.   C. Crocker, R. J. Errington, W. S. McDonald, K. J. Odell, B. L. Shaw and R. J. Goodfellow, *J. Chem. Soc., Chem. Commun.*, 1979, 498-499.

50.   J. M. Brown, P. A. Chaloner, A. G. Kent, B. A. Murrer, P. N. Nicholson, D. Parker and P. J. Sidebottom, *J. Organomet. Chem.*, 1981, **216**, 263-276.

51.   D. J. Cole-Hamilton, *Coord. Chem. Rev.*, 1981, **35**, 113-142.

52.   D. G. Gusev and A. J. Lough, *Organometallics*, 2002, **21**, 2601-2603.

53.   A. J. Martínez-Martínez, B. E. Tegner, A. I. McKay, A. J. Bukvic, N. H. Rees, G. J. Tizzard, S. J. Coles, M. R. Warren, S. A. Macgregor and A. S. Weller, *J. Am. Chem. Soc.*, 2018, **140**, 14958-14970.

54.   M. L. G. Sansores-Paredes, T. T. T. Nguyen, M. Lutz and M. E. Moret, *Organometallics*, 2023, **42**, 3418-3427.

55.   M. L. G. Sansores-Paredes, M. Lutz and M. E. Moret, *Nat. Chem.*, 2024, **16**, 417-425.

56.   J. Guihaumé, S. Halbert, O. Eisenstein and R. N. Perutz, *Organometallics*, 2012, **31**, 1300-1314.

57.   R. N. Perutz, S. Sabo-Etienne and A. S. Weller, *Angew. Chem. Int. Ed.*, 2022, **61**, e202111462.

58.   A. I. McKay, T. Krämer, N. H. Rees, A. L. Thompson, K. E. Christensen, S. A. Macgregor and A. S. Weller, *Organometallics*, 2017, **36**, 22-25.

59.   S. D. Pike, F. M. Chadwick, N. H. Rees, M. P. Scott, A. S. Weller, T. Krämer and S. A. Macgregor, *J. Am. Chem. Soc.*, 2015, **137**, 820-833.

60.   S. K. Furfari, B. E. Tegner, A. L. Burnage, L. R. Doyle, A. J. Bukvic, S. A. Macgregor and A. S. Weller, *Chem. Eur. J.*, 2021, **27**, 3177-3183.

61.   A. I. McKay, A. J. Martínez-Martínez, H. J. Griffiths, N. H. Rees, J. B. Waters, A. S. Weller, T. Krämer and S. A. Macgregor, *Organometallics*, 2018, **37**, 3524-3532.

62.   S. D. Pike, A. L. Thompson, A. G. Algarra, D. C. Apperley, S. A. Macgregor and A. S. Weller, *Science*, 2012, **337**, 1648-1651.

63.   J. Huber and S. Mecking, *Macromolecules*, 2010, **43**, 8718-8723.

64.   C. H. Low, J. D. Nobbs, M. van Meurs, L. P. Stubbs, E. Drent, S. Aitipamula and M. H. L. Pung, *Organometallics*, 2015, **34**, 4281-4292.

65.   M. D. Fryzuk, W. E. Piers, F. W. B. Einstein and T. Jones, *Can. J. Chem.*, 1989, **67**, 883-896.

66.   L. Zámostná, T. Braun and B. Braun, *Angew. Chem. Int. Ed.*, 2014, **53**, 2745-2749.

67.   M. Oliván, A. V. Marchenko, J. N. Coalter and K. G. Caulton, *J. Am. Chem. Soc.*, 1997, **119**, 8389-8390.

68.   A. J. Martinez-Martinez, C. G. Royle, S. K. Furfari, K. Suriye and A. S. Weller, *ACS Catal*, 2020, **10**, 1984-1992.

69.   I. Halasz, *Cryst. Growth Des.*, 2010, **10**, 2817-2823.

70.   A. Miedaner, R. C. Haltiwanger and D. L. DuBois, *Inorg. Chem.*, 1991, **30**, 417-427.

71.   J. W. Raebiger, A. Miedaner, C. J. Curtis, S. M. Miller, O. P. Anderson and D. L. DuBois, *J. Am. Chem. Soc.*, 2004, **126**, 5502-5514.

72.   D. E. Berning, B. C. Noll and D. L. DuBois, *J. Am. Chem. Soc.*, 1999, **121**, 11432-11447.

73.   K. A. Reid and D. C. Powers, *Chem. Commun.*, 2021, **57**, 4993-5003.

74.   A. I. McKay, A. J. Bukvic, B. E. Tegner, A. L. Burnage, A. J. Martínez-Martínez, N. H. Rees, S. A. Macgregor and A. S. Weller, *J. Am. Chem. Soc.*, 2019, **141**, 11700-11712.

75.   D. Amoroso, M. Haaf, G. P. A. Yap, R. West and D. E. Fogg, *Organometallics*, 2002, **21**, 534-540.

76.   F. M. Chadwick, N. H. Rees, A. S. Weller, T. Krämer, M. Iannuzzi and S. A. Macgregor, *Angew. Chem. Int. Ed.*, 2016, **55**, 3677-3681.

77.   T. M. Boyd, B. E. Tegner, G. J. Tizzard, A. J. Martínez-Martínez, S. E. Neale, M. A. Hayward, S. J. Coles, S. A. Macgregor and A. S. Weller, *Angew. Chem. Int. Ed.*, 2020, **59**, 6177-6181.

78.   A. J. Bukvic, A. L. Burnage, G. J. Tizzard, A. J. Martínez-Martínez, A. I. McKay, N. H. Rees, B. E. Tegner, T. Krämer, H. Fish, M. R. Warren, S. J. Coles, S. A. Macgregor and A. S. Weller, *J. Am. Chem. Soc.*, 2021, **143**, 5106-5120.

79.   C. G. Royle, L. Sotorrios, M. R. Gyton, C. N. Brodie, A. L. Burnage, S. K. Furfari, A. Marini, M. R. Warren, S. A. Macgregor and A. S. Weller, *Organometallics*, 2022, **41**, 3270-3280.

80.   A. Spek, *J. Appl. Crystallogr.*, 2003, **36**, 7-13.

81.   W. Weng, C.-H. Chen, B. M. Foxman and O. V. Ozerov, *Organometallics*, 2007, **26**, 3315-3320.

82.   R. J. Burford, W. E. Piers and M. Parvez, *Organometallics*, 2012, **31**, 2949-2952.

83.   J. A. Love, J. P. Morgan, T. M. Trnka and R. H. Grubbs, *Angew. Chem. Int. Ed.*, 2002, **41**, 4035-4037.

84.   M. D. Fryzuk, T. Jones and F. W. B. Einstein, *Organometallics*, 1984, **3**, 185-191.

85.   V. F. Kuznetsov, G. P. A. Yap, C. Bensimon and H. Alper, *Inorg. Chim. Acta*, 1998, **280**, 172-182.

86.   I. Pernik, J. F. Hooper, A. B. Chaplin, A. S. Weller and M. C. Willis, *ACS Catal.*, 2012, **2**, 2779-2786.

87.   A. L. Colebatch, A. I. McKay, N. A. Beattie, S. A. Macgregor and A. S. Weller, *Eur. J. Inorg. Chem.*, 2017, **2017**, 4533-4540.

88.   C. N. Iverson and W. D. Jones, *Organometallics*, 2001, **20**, 5745-5750.

89.   R. C. Knighton, J. Emerson-King, J. P. Rourke, C. A. Ohlin and A. B. Chaplin, *Chem. Eur. J.*, 2018, **24**, 4927-4938.

90.   F. M. Chadwick, A. I. McKay, A. J. Martinez-Martinez, N. H. Rees, T. Krämer, S. A. Macgregor and A. S. Weller, *Chem. Sci.*, 2017, **8**, 6014-6029.

91.   N. M. Scott, R. Dorta, E. D. Stevens, A. Correa, L. Cavallo and S. P. Nolan, *J. Am. Chem. Soc.*, 2005, **127**, 3516-3526.

92.   O. V. Dolomanov, L. J. Bourhis, R. J. Gildea, J. A. K. Howard and H. Puschmann, *J. Appl. Crystallogr.*, 2009, **42**, 339-341.

93.   P. van der Sluis and A. L. Spek, *Acta Crystallogr. A.*, 1990, **46**, 194-201.

94.   Gassium 16, Revision C.01, M. J. Frisch, G. W. Trucks, H. B. Schlegel, G. E. Scuseria, M. A. Robb, J. R. Cheeseman, G. Scalmani, V. Barone, G. A. Petersson, H. Nakatsuji, X. Li, M. Caricato, A. V. Marenich, J. Bloino, B. G. Janesko, R. Gomperts, B. Mennucci, H. P. Hratchian, J. V. Ortiz, A. F. Izmaylov, J. L. Sonnenberg, Williams,

F. Ding, F. Lipparini, F. Egidi, J. Goings, B. Peng, A. Petrone, T. Henderson, D. Ranasinghe, V. G. Zakrzewski, J. Gao, N. Rega, G. Zheng, W. Liang, M. Hada, M. Ehara, K. Toyota, R. Fukuda, J. Hasegawa, M. Ishida, T. Nakajima, Y. Honda, O. Kitao, H. Nakai, T. Vreven, K. Throssell, J. A. Montgomery Jr., J. E. Peralta, F. Ogliaro, M. J. Bearpark, J. J. Heyd, E. N. Brothers, K. N. Kudin, V. N. Staroverov, T. A. Keith, R. Kobayashi, J. Normand, K. Raghavachari, A. P. Rendell, J. C. Burant, S. S. Iyengar, J. Tomasi, M. Cossi, J. M. Millam, M. Klene, C. Adamo, R. Cammi, J. W. Ochterski, R. L. Martin, K. Morokuma, O. Farkas, J. B. Foresman and D. J. Fox, Gassian, Inc., Wallingford CT, 2016.

95.   T. J. Goncalves, P. N. Plessow and F. Studt, *ChemCatChem*, 2019, **11**, 4368-4376.

96.   T. Krämer, F. M. Chadwick, S. A. Macgregor and A. S. Weller, *Helv. Chim. Acta*, 2023, **106**, e202200154.

97.   AIMAll, http://aim.tkgristmill.com (accessed 22/03/24).

98.   F. Cortés-Guzmán and R. F. W. Bader, *Coord. Chem. Rev.*, 2005, **249**, 633-662.

99.   J. P. Foster and F. Weinhold, *J. Am. Chem. Soc.*, 1980, **102**, 7211-7218.

100.   J. E. Carpenter, University of Wisconsin, 1987.

101.   NBO Version 6.0, E. D. Glendening, J. K. Badenhoop, A. E. Reed, J. E. Carpenter, J. A. Bohmann, C. M. Morales, C. R. Landis and F. Weinhold.

102.   D. Braga, F. Grepioni, E. Tedesco, K. Biradha and G. R. Desiraju, *Organometallics*, 1997, **16**, 1846-1856.

103.   P. Marcazzan, C. Abu-Gnim, K. N. Seneviratne and B. R. James, *Inorg. Chem.*, 2004, **43**, 4820-4824.

104.   Y. Zhang, J. C. Lewis, R. G. Bergman, J. A. Ellman and E. Oldfield, *Organometallics*, 2006, **25**, 3515-3519.

105.   A. J. Nielson, J. A. Harrison, M. A. Sajjad and P. Schwerdtfeger, *Eur. J. Inorg. Chem.*, 2017, **2017**, 2255-2264.

106.   M. Brookhart, M. L. H. Green and G. Parkin, *Proc. Natl. Acad. Sci. U.S.A.*, 2007, **104**, 6908-6914.

107.   J. E. Barquera-Lozada, A. Obenhuber, C. Hauf and W. Scherer, *J. Phys. Chem. A.*, 2013, **117**, 4304-4315.

108.   J. J. Race, A. L. Burnage, T. M. Boyd, A. Heyam, A. J. Martínez-Martínez, S. A. Macgregor and A. S. Weller, *Chem. Sci.*, 2021, **12**, 8832-8843.

109.   P. Pracht, F. Bohle and S. Grimme, *Phys. Chem. Chem. Phys.*, 2020, **22**, 7169-7192.

110.   S. Grimme, *J. Chem. Theory Comput.*, 2019, **15**, 2847-2862.

111.   C. Bannwarth, S. Ehlert and S. Grimme, *J. Chem. Theory Comput.*, 2019, **15**, 1652-1671.

112.   T. D. Kühne, M. Iannuzzi, M. Del Ben, V. V. Rybkin, P. Seewald, F. Stein, T. Laino, R. Z. Khaliullin, O. Schütt, F. Schiffmann, D. Golze, J. Wilhelm, S. Chulkov, M. H. Bani-Hashemian, V. Weber, U. Borštnik, M. Taillefumier, A. S. Jakobovits, A. Lazzaro, H. Pabst, T. Müller, R. Schade, M. Guidon, S. Andermatt, N. Holmberg, G. K. Schenter, A. Hehn, A. Bussy, F. Belleflamme, G. Tabacchi, A. Glöß, M. Lass, I. Bethune, C. J. Mundy, C. Plessl, M. Watkins, J. VandeVondele, M. Krack and J. Hutter, *J. Chem. Phys.*, 2020, **152**, 194103.

113.   J. VandeVondele, M. Krack, F. Mohamed, M. Parrinello, T. Chassaing and J. Hutter, *Comput. Phys. Commun.*, 2005, **167**, 103-128.

114.   J. Hutter, M. Iannuzzi, F. Schiffmann and J. VandeVondele, *Wiley Interdiscip. Rev. Comput. Mol. Sci.*, 2014, **4**, 15-25.

115.   S. Grimme, J. Antony, S. Ehrlich and H. Krieg, *J. Chem. Phys.*, 2010, **132**, 154104.

116.   T. Lu and Q. Chen, *J. Comput. Chem.*, 2022, **43**, 539-555.

117.   F. M. Chadwick, T. Krämer, T. Gutmann, N. H. Rees, A. L. Thompson, A. J. Edwards, G. Buntkowsky, S. A. Macgregor and A. S. Weller, *J. Am. Chem. Soc.*, 2016, **138**, 13369-13378.

118.   B. Nguyen and J. M. Brown, *Adv. Synth. Catal.*, 2009, **351**, 1333-1343.

119.   J. Bigeleisen, M. W. Lee and F. Mandel, *Annu. Rev. Phys. Chem.*, 1973, **24**, 407-440.

120.   J. L. McBee, J. Escalada and T. D. Tilley, *J. Am. Chem. Soc.*, 2009, **131**, 12703-12713.

121.   Y. Zhao and D. G. Truhlar, *J. Phys. Chem. A*, 2005, **109**, 5656-5667.

122.   S. Svelle, C. Tuma, X. Rozanska, T. Kerber and J. Sauer, *J. Am. Chem. Soc.*, 2009, **131**, 816-825.

123.   S. O. Grim and R. A. Ference, *Inorg. Chim. Acta*, 1970, **4**, 277-282.

Chapter 4 – Conclusions

Chapter 4 - Conclusions

4.1 Conclusions

This thesis reports on adaptivity occurring in the solid-state throughout solid/gas single-crystal to single-crystal (SCSC) transformations, with reactivity inducing adaptions of the 2° microenvironment and 3° periodic structure, (**Chapter 2**) and structurally-responsive metal-ligand cooperation (**Chapter 3**). Together, these results provide a degree of insight into the freedom of movement and reorganisation of reagents within the solid-state, as well as the plasticity of the solid-state, which has not been as rigorously investigated previously. While the majority of successful SCSC transformations are associated with very minor changes in unit cell dimensions,[1-5] the work presented in this thesis adds to the growing body of work regarding SCSC transformations with significant impact on the crystallographic dimensions.[6-8] The deepened understanding and quantification of the underpinning non-covalent interactions in the solid-state sheds light on the potential mechanisms by which the solid-state may be used to facilitate synthesis of unstable complexes,[1, 2, 9-11] impart topological control of reactions,[12, 13] or application for energy transduction to mechanical or thermal energy through crystalline reorganisation.[14, 15]

The findings reported in this thesis supply information from which a set of approximate guidelines which may be applied when designing a system for SCSC transformations may be formed. Firstly, as has been previously noted,[16-18] it appears to be important for the crystalline material to contain a significant halogen content.

This is crucial for reactant ingress and product egress from the crystalline material,[18, 19] in addition to providing stability to the long-range order of the single-crystal, through non-specific and non-directional interhalogen bonds.[20-22] Secondly, where considerable unit cell dimension changes do occur, or are likely to occur due to large changes at the coordination sphere, solvent of crystallisation may enable retention of single-crystalline material through phase rebuilding of damaged crystals.[8] Thirdly, where steric clashes are likely to be formed due to a reaction in the solid-state, energetic compensation is required by the formation of strong bonds in the products. Finally, periodic DFT calculations, including the concept of proto-structures, can be insightful predictive tools for the potential of a system to undergo reorganisation due to reduced non-covalent interactions, or formation of steric clashes. It should be noted that these are simply guidelines, for which exceptions are inevitable. For example, this work highlights two exceptions to previously reported guidelines of SCSC transformations, which is that retention of crystallinity is generally associated with a cell volume change of less than 4%.[1]

The report of utilisation of MicroED methods to circumvent problems with crystal cracking in SCSC transformations included in this thesis is of importance for characterisation of reactions exhibiting further exceptions to these new guidelines, which may impact crystalline integrity, forming microcrystalline material which previously necessitated structural analysis by (synchrotron) powder X-Ray or neutron diffraction.[23-25] This approach may also find application in structural analysis of material synthesised through mechanochemical methods.[24]

4.2 References

1.   S. D. Pike and A. S. Weller, *Philos. Trans. R. Soc. A*, 2015, **373**, 20140187.

2.   L. E. Hatcher, J. M. Skelton, M. R. Warren and P. R. Raithby, *Acc. Chem. Res.*, 2019, **52**, 1079-1088.

3.   A. J. Bukvic, A. L. Burnage, G. J. Tizzard, A. J. Martínez-Martínez, A. I. McKay, N. H. Rees, B. E. Tegner, T. Krämer, H. Fish, M. R. Warren, S. J. Coles, S. A. Macgregor and A. S. Weller, *J. Am. Chem. Soc.*, 2021, **143**, 5106-5120.

4.   K. A. Reid and D. C. Powers, *Chem. Commun.*, 2021, **57**, 4993-5003.

5.   L. E. Hatcher, L. K. Saunders and B. A. Coulson, *Faraday Discuss.*, 2023, **244**, 370-390.

6.   M. K. Panda, R. Centore, M. Causà, A. Tuzi, F. Borbone and P. Naumov, *Sci. Rep.*, 2016, **6**, 29610.

7.   A. I. Vicente, A. Joseph, L. P. Ferreira, M. de Deus Carvalho, V. H. N. Rodrigues, M. Duttine, H. P. Diogo, M. E. Minas da Piedade, M. J. Calhorda and P. N. Martinho, *Chem. Sci.*, 2016, **7**, 4251-4258.

8.   Y. Li, B. Zhao, J. P. Xue, J. Xie, Z. S. Yao and J. Tao, *Nat. Commun.*, 2021, **12**, 6908.

9.   A. Das, J. H. Reibenspies, Y.-S. Chen and D. C. Powers, *J. Am. Chem. Soc.*, 2017, **139**, 2912-2915.

10. A. Das, C.-H. Wang, G. P. Van Trieste, III, C.-J. Sun, Y.-S. Chen, J. H. Reibenspies and D. C. Powers, *J. Am. Chem. Soc.*, 2020, **142**, 19862-19867.

11. M. I. Gonzalez, D. Gygi, Y. Qin, Q. Zhu, E. J. Johnson, Y.-S. Chen and D. G. Nocera, *J. Am. Chem. Soc.*, 2022, **144**, 1464-1472.

12. F. M. Chadwick, T. Krämer, T. Gutmann, N. H. Rees, A. L. Thompson, A. J. Edwards, G. Buntkowsky, S. A. Macgregor and A. S. Weller, *J. Am. Chem. Soc.*, 2016, **138**, 13369-13378.

13. F. Hu, X. Bi, X. Chen, Q. Pan and Y. Zhao, *Chem. Lett.*, 2021, **50**, 1015-1029.

14. E. Ahmed, D. P. Karothu and P. Naumov, *Angew. Chem. Int. Ed.*, 2018, **57**, 8837-8846.

15. P. Naumov, D. P. Karothu, E. Ahmed, L. Catalano, P. Commins, J. Mahmoud Halabi, M. B. Al-Handawi and L. Li, *J. Am. Chem. Soc.*, 2020, **142**, 13256-13272.

16. S. Libri, M. Mahler, G. Mínguez Espallargas, D. C. N. G. Singh, J. Soleimannejad, H. Adams, M. D. Burgard, N. P. Rath, M. Brunelli and L. Brammer, *Angew. Chem. Int. Ed.*, 2008, **47**, 1693-1697.

17. I. J. Vitórica-Yrezábal, G. Mínguez Espallargas, J. Soleimannejad, A. J. Florence, A. J. Fletcher and L. Brammer, *Chem. Sci.*, 2013, **4**, 696-708.

18. A. J. Martínez-Martínez, N. H. Rees and A. S. Weller, *Angew. Chem. Int. Ed.*, 2019, **58**, 16873-16877.

19. Z. Huang, P. S. White and M. Brookhart, *Nature*, 2010, **465**, 598-601.

20. S. Saha, M. K. Mishra, C. M. Reddy and G. R. Desiraju, *Acc. Chem. Res.*, 2018, **51**, 2957-2967.

21.   D. Braga, F. Grepioni, E. Tedesco, K. Biradha and G. R. Desiraju, *Organometallics*, 1997, **16**, 1846-1856.

22.   M. K. Panda, S. Ghosh, N. Yasuda, T. Moriwaki, G. D. Mukherjee, C. M. Reddy and P. Naumov, *Nat. Chem.*, 2015, **7**, 65-72.

23.   M. Albrecht, M. Lutz, A. L. Spek and G. van Koten, *Nature*, 2000, **406**, 970-974.

24.   I. J. Vitorica-Yrezabal, R. A. Sullivan, S. L. Purver, C. Curfs, C. C. Tang and L. Brammer, *CrystEngComm*, 2011, **13**, 3189-3196.

25.   M. K. Panda, T. Runcevski, S. C. Sahoo, A. A. Belik, N. K. Nath, R. E. Dinnebier and P. Naumov, *Nat. Commun.*, 2014, **5**, 4811.

<u>*Appendix 1 – Crystallographic Data Tables*</u>

Table A1: Crystallographic Data for **[Mn-CO]**, **[Mn-THF]** and **[Mn-CO]** (MicroED)

	[Mn-CO] (recrystallised)	**[Mn-THF]**	**[Mn-CO]** (MicroED)
Formula	$C_{52}H_{43}BNO_5F_{24}P_2Mn$	$C_{58}H_{58}BNO_5F_{24}P_2Mn$	$C_{52}H_{43}BNO_5F_{24}P_2Mn$
M_w	1345.56	1432.754	1345.56
Crystal System	Triclinic	Monoclinic	Triclinic
Space Group	$P\bar{1}$	$P\,2_1/n$	$P\bar{1}$
T / K	149.95(10)	150.00(10)	80(2)
a / Å	12.9543(6)	19.6838(4)	13.0245(6)
b / Å	14.1111(6)	23.8631(6)	14.1722(9)
c / Å	17.0692(8)	13.4251(3)	17.0849(12)
α / °	105.704(4)	90	105.823(5)
β / °	106.445(4)	90	106.400(5)
γ / °	97.358(4)	90	97.542(3)
V / Å³	2809.2(2)	6306.0(2)	2835.6(3)
Z	2	4	2
ρ_{calc} / g cm^{-1}	1.591	1.509	1.576
μ / mm^{-1}	3.613	3.254	0.000
2Θ range / °	7.246 – 142.247	7.41 – 142.54	0.092 – 1.732
Reflns Collected	20116	44881	43604
R_{int}	0.0302	0.0675	0.1748
Completeness / %	100	100	95.3
Data/Restr/Param	10626 / 157 / 895	12038 / 121 / 953	9903 / 339 / 868
R_1 [I > 2σ(I)]	0.0415	0.0759	0.1514
wR_2 [all data]	0.1109	0.2171	0.4048
GooF	1.043	1.014	1.028
Largest pk/hole / e Å^{-3}	0.67 / -0.47	0.86 / -0.88	0.20 / -0.23
Flack Param	-	-	-

Table A2: Crystallographic Data for **[Re-Br]**, and **[Re]** at 110 K and 298 K.

	[Re-Br]	**[Re]** (110 K)	**[Re]** (298 K)
Formula	$C_{23}H_{39}BrNO_4P_2Re$	$C_{55}H_{51}BF_{24}NO_4P_2Re$	$C_{55}H_{51}BF_{24}NO_4P_2Re$
M_w	721.60	1504.43	1504.43
Crystal System	Orthorhombic	Triclinic	Triclinic
Space Group	$P\,na2_1$	$P\,\overline{1}$	$P\,\overline{1}$
T / K	110.05(10)	110.00(10)	298.0(2)
a / Å	24.3315(2)	12.74810(10)	12.87470(10)
b / Å	10.26090(10)	14.4679(2)	14.51620(10)
c / Å	11.21410(10)	17.4995(2)	17.7612(2)
α / °	90	107.7110(10)	106.7050(10)
β / °	90	94.0020(10)	93.6650(10)
γ / °	90	98.7510(10)	98.2320(10)
V / Å³	2799.75(4)	3015.62(6)	3127.18(5)
Z	4	2	2
ρ_{calc} / g cm^{-1}	1.712	1.657	1.598
μ / mm^{-1}	11.464	5.526	5.329
2Θ range / °	7.266 – 153.866	7.07 – 153.976	6.978 – 153.96
Reflns Collected	32487	36432	37887
R_{int}	0.0383	0.0401	0.0356
Completeness / %	100	100	100
Data/Restr/Param	5693 / 1 / 301	12178 / 77 / 889	12765 / 223 / 1029
R_1 [I > 2σ(I)]	0.0227	0.0407	0.0263
wR_2 [all data]	0.0597	0.1063	0.0671
GooF	1.092	1.051	1.058
Largest pk/hole / e Å^{-3}	1.17 / -0.96	1.80 / -2.28	0.30 / -0.86
Flack Param	-0.034(6)	-	-

Table A3: Crystallographic Data for **[Re-CO]**, **[1-NBD]** and **[1-NBA]**.

	[Re-CO]	[1-NBD]	[1-NBA] (110 K)
Formula	$C_{56}H_{51}BF_{24}NO_5P_2Re$	$C_{59}H_{64}BF_{24}P_2Rh$	$C_{59}H_{67}BF_{24}P_2Rh$
M_w	1532.92	1404.76	1407.78
Crystal System	Triclinic	Monoclinic	Monoclinic
Space Group	$P\bar{1}$	$P\,2_1/n$	$P\,2_1/n$
T / K	109.95(10)	110.00(10)	110.00(10)
a / Å	12.9529(4)	21.39780(10)	22.0393(3)
b / Å	14.1717(3)	12.92970(10)	12.96270(10)
c / Å	16.8449(5)	23.21930(10)	23.7552(3)
α / °	97.370(2)	90	90
β / °	94.209(3)	112.0440(10)	112.901(2)
γ / °	96.468(2)	90	90
V / Å³	3034.88(15)	5954.39(7)	6251.66(15)
Z	2	4	4
ρ_{calc} / g cm⁻¹	1.677	1.567	1.496
μ / mm⁻¹	5.517	3.856	3.673
2Θ range / °	6.896 – 155.206	7.104 - 153.998	6.998 – 142.916
Reflns Collected	33048	69849	45037
R_{int}	0.0935	0.0380	0.0373
Completeness / %	100	100	100
Data/Restr/Param	12259 / 0 / 823	12409 / 0 / 796	12063 / 95 / 906
R_1 [I > 2σ(I)]	0.0577	0.0315	0.0579
wR_2 [all data]	0.1584	0.0787	0.1614
GooF	1.082	1.052	1.049
Largest pk/hole / e Å⁻³	1.55 / -2.34	0.87 / -0.62	2.16 / -1.73
Flack Param	-	-	-

Table A4: Crystallographic Data for **[1-NBA]** (215 K and 298 K) and **[1-CD₂Cl₂]**.

	[1-NBA] (215 K)	**[1-NBA]** (298 K)	**[1-CD₂Cl₂]**
Formula	$C_{59}H_{67}BF_{24}P_2Rh$	$C_{59}H_{67}BF_{24}P_2Rh$	$C_{53}H_{57.5}BCl_2F_{24}P_2Rh$
M_w	1407.78	1407.78	1397.08
Crystal System	Monoclinic	Monoclinic	Monoclinic
Space Group	$P\,2_1/n$	$P\,2_1/n$	$P\,2_1/c$
T / K	214.95(10)	298.00(14)	110.15
a / Å	22.2413(5)	22.4113(8)	21.70260(10)
b / Å	13.0869(2)	13.1931(5)	27.81260(10)
c / Å	24.0201(5)	24.2050(6)	21.48550(10)
α / °	90	90	90
β / °	112.889(2)	112.732(3)	103.0890(10)
γ / °	90	90	90
V / Å³	6441.0(2)	6600.9(4)	12631.83(11)
Z	4	4	8
ρ_{calc} / g cm⁻¹	1.452	1.417	1.469
μ / mm⁻¹	3.565	3.478	4.391
2Θ range / °	7.848 – 136.492	7.784 – 155.524	7.31 – 136.502
Reflns Collected	24466	40937	150980
R_{int}	0.0438	0.0873	0.0458
Completeness / %	99.9	99.1	100
Data/Restr/Param	11775 / 133 / 908	13308 / 222 / 955	23135 / 332 / 1664
R_1 [I > 2σ(I)]	0.0757	0.0871	0.0570
wR_2 [all data]	0.2467	0.3216	0.1597
GooF	1.017	1.012	1.020
Largest pk/hole / e Å⁻³	2.28 / -0.56	1.83 / -0.75	1.93 / -1.01
Flack Param	-	-	-

Table A5: Crystallographic Data for **[1-bpy]**, **[1-NBE]** and **[1-Allyl]**.

	[1-bpy]	[1-NBE]	[1-Allyl]
Formula	$C_{62}H_{63.17}BF_{24}N_2P_2Rh$	$C_{59}H_{66}BF_{24}P_2Rh$	$C_{55}H_{61}BF_{24}P_2Rh$
M_w	1467.97	1406.77	1353.736
Crystal System	Triclinic	Monoclinic	Monoclinic
Space Group	$P\bar{1}$	$P\,2_1/n$	$C\,2/c$
T / K	110.00(10)	110.05(10)	110
a / Å	17.6320(3)	21.8071(2)	22.2481(4)
b / Å	19.4092(3)	12.76750(10)	12.4878(2)
c / Å	20.1617(3)	23.4341(3)	23.2951(6)
α / °	80.3640(10)	90	90
β / °	71.5470(10)	112.0080(10)	113.745(2)
γ / °	87.5090(10)	90	90
V / Å³	6452.36(18)	6049.13(11)	5924.2(2)
Z	4	4	4
ρ_{calc} / g cm^{-1}	1.511	1.545	1.518
μ / mm^{-1}	3.596	3.796	0.710
2Θ range / °	6.984 – 153.76	8.032 – 154.164	3.16 – 33.62
Reflns Collected	76736	40271	10427
R_{int}	0.0300	0.0519	N/A (twin)
Completeness / %	99.8	99.8	99.6
Data/Restr/Param	26133 / 83 / 1977	12371 / 187 / 968	10427 / 270 / 505
R_1 [I > 2σ(I)]	0.0828	0.0675	0.1206
wR_2 [all data]	0.2383	0.1749	0.3557
GooF	1.013	1.027	1.145
Largest pk/hole / e Å^{-3}	3.54 / -0.91	1.84 / -1.56	3.88 / -0.61
Flack Param	-	-	-